Experimental Study on Thermal Conductivity of Powdered Materials under Vacuum and Its Application to Thermal Evolution of Planetesimals

Naoya Sakatani

Doctor Thesis

Department of Space Science
School of Physical Science
The Graduate University for Advanced Studies

Abstract

Powdered materials have been ubiquitously existed from the past to the present of the solar system. For example, in early solar nebula, km-sized bodies so-called planetesimals are considered to have formed by accretion of μm-sized dust particles. At present, surface of the Moon and asteroids are covered with crushed rock powders called regolith. Thermal conductivity of such powdered materials under vacuum is known to be extremely lower than that of consolidated materials. Therefore, the powdered material act as a thermal insulator and its thermal conductivity is one of the essential parameters for thermal evolution of the planetary bodies.

The thermal conductivity of the powdered materials depends on many parameters (gas pressure, particle size and its distribution, porosity, temperature, compressional stress, material composition, particle shape, etc.). At atmospheric pressure, the effective thermal conductivity is primary determined by conduction and convection of the gas phase. On the other hand, under vacuum condition, the effective thermal conductivity is determined by the combination of solid conductivity (contribution of the conduction within the particles and across the inter-particle contacts) and radiative conductivity (contribution of the thermal radiation through void spaces between particle surfaces). Both conductivities vary by orders of magnitude depending on the parameters. Although their individual effects on the thermal conductivity have tried to be investigated, the integrative understanding on heat transfer mechanisms in the powdered media is still insufficient. The purpose of this study is to reveal the heat transfer mechanism in the powdered materials under vacuum and to develop an integrative thermal conductivity model describing the parameter dependences. In order to accomplish this purpose, the thermal conductivity of the powder samples, whose parameters were accurately controlled, was measured under vacuum, and the parameter dependences were systematically investigated. In this study, the thermal conductivity for all samples was divided into the solid and radiative conductivities using temperature-dependent thermal conductivity data. Determination of each contribution helps us to understand the heat transfer mechanism. Integrating the experimental results, the heat transfer mechanism was discussed and thermal conductivity model was constructed.

The powder samples used in this study were glass beads of six different sizes smaller than 1 mm in diameter. Titanium beads, copper beads, and lunar regolith simulant were also used. The thermal conductivity was measured by line heat source method under vacuum conditions (less than 0.01 Pa). To control extrinsic parameters, temperature and compressional stress, two different experimental systems were designed. The temperature was controlled from 250 to 330 K in

a thermostatic chamber. Using this experimental system, the solid and radiative conductivities were derived for all samples, and the dependences on particle size, porosity, material composition, and particle size distribution were investigated. Another experimental system for investigating compressional stress dependence of the thermal conductivity was developed. Sintered glass beads were also prepared, and the effect of the sintering on the thermal conductivity was investigated.

The major experimental results and inferred causes are the followings:

1. The solid conductivity of five glass beads larger than 50 μm increased from 0.001 to 0.003 W/mK with increasing the particle size. On the other hand, glass beads smaller than 10 μm had higher solid conductivity by an order of magnitude than the larger glass beads. The higher solid conductivity of the smallest glass beads sample would result from strong adhesive force, which enhances the contact area between the particles. It was found that the lower solid conductivity for the larger glass beads samples resulted from the constricted contact area by sub-μm scale roughness observed on the surface of the larger glass beads.
2. The solid conductivity of the glass beads smaller than 10 μm was strongly depends on the porosity. It decreased from 0.02 to 0.0007 W/mK with the porosity increasing from 0.5 to 0.86. This dependence would be explained by decrease of conduction path within unit volume.
3. As the compressional stress applied on the powders increased, the thermal conductivity was enhanced without variation of the porosity. The solid conductivities of the glass beads were proportional to 0.29 to 0.35 powers of the compressional stress. This result supported an idea that the solid conductivity of the powdered materials is proportional to radius of the contacting area.
4. The thermal conductivity of the sintered glass beads was orders of magnitude higher than the unconsolidated glass beads. It was found that the thermal conductivity of the sintered powders is characterized by the size of the contacting parts called necks. It was scaled by the ratio of the neck radius to the particle radius.
5. The radiative conductivity increased with increasing the particle size. This result indicated that the radiative conductivity is characterized by the radiative heat transfer distance scaled by void size between the particles.
6. As the porosity became higher, the radiative conductivity enhanced in the porosity range higher than 0.6. This can be interpreted as the result of the larger void size for the higher porosity samples. On the other hand, in the porosity range less than 0.6, the measured radiative conductivity was scattered, and therefore, the porosity dependence could not be defined in this porosity regime.

Based on heat transfer mechanisms inferred from the series of the experiments, a thermal conductivity model of the powdered materials for vacuum condition, which integratively describes the parameter dependences, was constructed for the first time. The solid conductivity was modeled as serial and parallel connections of thermal conductance at the contacts between the equal-sized elastic spheres. From the experimental results, surface roughness on particles was found to reduce the solid conductivity. Then, a factor representing the constriction of the contact radius between rough spheres from that between perfectly smooth spheres was newly introduced in the solid conductivity model. By comparing the developed solid conductivity model with the experimental data, it was found that the model could give higher solid conductivity than the experimental values, if assuming the perfectly smooth particles. The deviation was less than factor of three, which would mean the effect of the surface roughness. The radiative conductivity was modeled as thermal radiation between infinitely thin parallel planes. The modeled radiative conductivity is proportional to distance between the planes. It was scaled by the typical void length, which was calculated by assuming the homogeneous packing of equal-sized spheres. A scaling factor correlating the void length to effective radiative transfer distance (distance between the parallel planes) was introduced in the radiative conductivity model. Comparison between the radiative conductivity model and the experimental results revealed that, for the smallest glass beads less than 10 μm, the measured radiative conductivity was higher than the modeled one by a factor of 15. The smallest glass beads used in this study formed aggregates due to the adhesive force between the individual particles and large void spaces were found between the aggregates. The higher radiative conductivity than the model suggested that the radiative heat transfer dominantly took place through the inter-aggregates large voids.

As an example of application of the developed thermal conductivity model to the planetary science, the thermal conductivity of highly porous planetesimal was estimated and thermal evolution was numerically calculated. As the temeprature of the planetesimal increases by radioactive heating, the sintering or neck formation of the dust particles occurs. The resulting consolidated planetesimal would had different thermal and mechanical properties from the initial unconsolidated state, whcih could affect subsequent thermal and collisional evolutions. By solving the heat conduction equation together with equations for the sintering of the particles, the condition and beginning time for the sitnering of the planetesimal were constrained for the first time. As a result of the thermal caclulation, it was found that the temperature at the center of planetesimals could increase up to the sintering temperature, even if the radius of the planetesimal was as small as 400 meters radius due to the thermal insulating effect of the powdered materials. After the sintering oc-

curred, the temerature started to decrease because of enhenced thermal conductivity resulting from the neck formation.

It was also found that time delay between the planetesimal accretion and the beginning of the sintering was more than seventy thousands years, depending on the accretion age. In the previous study on evolution of the planetesimals, the thermal and collisional processes had been independently discussed. Because the planetesimals would be expected to acquire strength by the sintering, the collisional outcome would be different before and after the sintering. Then, the sintering time was compared to the collisional timescale. It was found that the collisional timescale was faster than the sintering timescale at the orbits of the Earth and Mars. Therefore, protoplanets would be formed by the collisions between the unconsolidated planetesimals. In the asteroid region, the collisional timescale was comparable with the sintering timescale. This means that the early collisional evolution of the parent bodies of the asteroids was dominated by the collisions of the consolidated planetesimals. Thus, this study first presented the temporal relation between the thermal and collisional process of the planetesimals.

Contents

1 Introduction **1**

1.1 Role of powdered materials in planetary evolution 1
1.2 Thermal evolution of the planetesimal 4
1.3 Thermal conductivity of planetary surface regolith 11
1.4 Purpose of this study 14

2 Thermal conductivity of powdered materials: Review of previous works **17**

2.1 Heat transfer in powdered materials 17
2.2 Thermal conductivity of powdered materials under vacuum 20

3 Thermal conductivity measurement of powder samples **41**

3.1 Sample selection 41
3.1.1 List of the measured sample 41
3.1.2 Physical properties of component materials 44
3.2 Method for thermal conductivity measurements 45
3.2.1 Principle of the line heat source measurement 45
3.2.2 Measurement system and error analysis 49
3.2.3 Protocol for derivation of solid and radiative conductivity . . 58
3.3 Particle size dependence 61
3.3.1 Experimental method 61
3.3.2 Results 61
3.4 Porosity dependence 68
3.4.1 Experimental method 68
3.4.2 Results 70
3.5 Thermal conductivity of metallic beads and regolith simulant 73
3.5.1 Experimental method 73
3.5.2 Results 74
3.6 Compressional stress dependence 78
3.6.1 Experimental method 78
3.6.2 Results 80

3.7 Effect of particle size distribution . . . 83
3.7.1 Experimental method . . . 83
3.7.2 Results . . . 84
3.8 Thermal conductivity of sintered glass beads . . . 86
3.8.1 Experimental method . . . 86
3.8.2 Results . . . 90
3.9 Summary of the experimental results . . . 95

4 Integrative model of thermal conductivity of powdered materials 101
4.1 Solid conductivity model . . . 101
4.2 Radiative conductivity model . . . 107
4.3 Comparison with the experimental results . . . 110
4.3.1 Solid conductivity . . . 110
4.3.2 Radiative conductivity . . . 118
4.4 Discussion . . . 122

5 Numerical simulation for thermal evolution of planetesimals 131
5.1 Thermal model . . . 131
5.1.1 Heat conduction equation . . . 135
5.1.2 Heat source . . . 136
5.1.3 Sintering of dust particles . . . 136
5.1.4 Thermal conductivity . . . 138
5.2 Thermal evolution of planetesimals . . . 141
5.3 Sintering condition of the planetesimals . . . 144
5.4 Implication to collisional process of planetesimals . . . 148

6 Summary and conclusion 153

A Thermal conductivity structure in lunar regolith layer 157

B Physical properties of regolith on small bodies inferred from thermal inertia 163

Acknowledegments 167

References 169

Chapter 1

Introduction

1.1 Role of powdered materials in planetary evolution

In the general theory of planetary formation, hypothetical km-sized objects, so-called planetesimals, were formed by coagulation of μm-sized dust particles in early solar nebula. Collisional accretion of the planetesimals resulted in the formation of larger planetary embryos, called protoplanets. Subsequent long-term evolutions of the protoplanets produced the planets seen in the present solar system. Remnant bodies that were not involved in the planetary growth, or fragments broken from larger parent bodies are considered to be asteroids and comets in present. Some fragments are seen as the meteorites whose parent bodies may accommodate to the current asteroids, satellites, and planets. Figure 1.1 shows a chronological overview of the planetary evolution.

Planetesimal formation is one of the key issues on the planetary evolution. Although their formation process has been studied, a concrete theory has not been established to explain how μm-sized dust particles grew into km-sized objects. In the nebula, dust particles grew into mm-sized aggregates through mutual hit-and-stick, and these aggregates settled on the mid-plane of the disk (*Weidenschilling*, 1980). Generally, two scenarios have been proposed for the planetesimal formation; mutual collisional growth of the dust aggregates (*Wada et al.*, 2007; *Okuzumi et al.*, 2012) and gravitational instability of dense dust layers (*Youdin and Shu*, 2002). In the former model, the dust aggregates gradually accreted into larger planetesimals via the mutual collision at low relative velocity (several m/s or higher). In the nebula, solid materials experienced gas drag so that they drifted toward the central Sun. The drift rate is the highest for meter-sized materials (1 AU in few hundred years, *Weidenschilling*, 1977; *Chambers*, 2006). The planetesimal formation would be

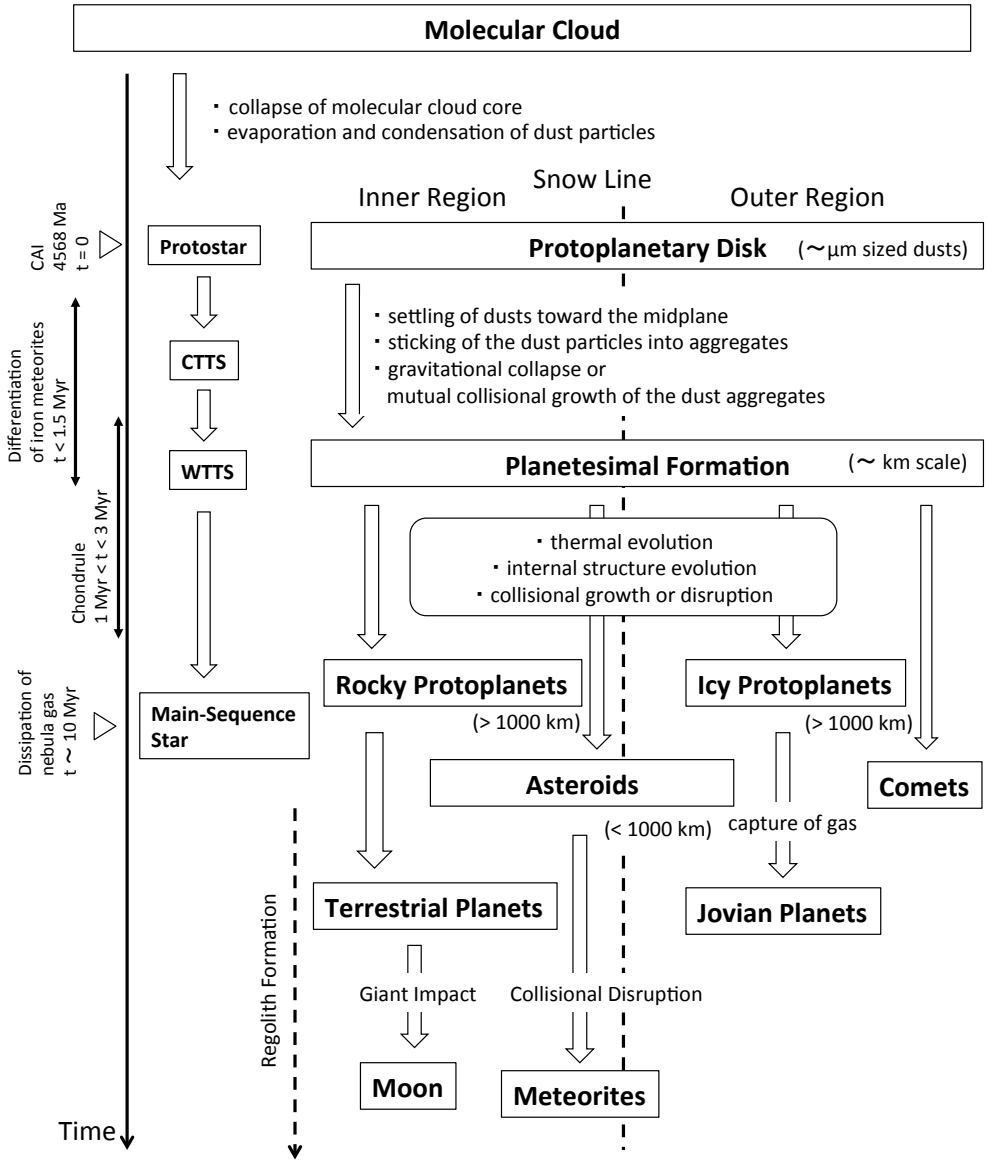

Figure 1.1: Chronological overview of the planetary evolution. CAI: Calcium-aluminum rich inclusions; CTTS: Classical T-Tauri star; WTTS: Weak-lined T-Tauri star.

prevented by this radial drift barrier, because the meter-sized bodies on the way of the growth were quickly fell onto the Sun. *Kataoka et al.* (2013) suggested that the density of icy dust aggregates increases from 10^{-5} g/cm^3 to 10^{-1} g/cm^3 with increasing the size of the aggregate due to compression by the gas pressure and the self-gravity. They stated that the planetesimals with such internal density evolution could avoid the radial drift barrier. However, another problem appears for the rocky planetesimal. The silicate dust aggregate is poorly sticky and easily disrupted by the collision (*Blum and Wurm*, 2008; *Wada et al.*, 2013). Thus, the rocky planetesimal growth via mutual collision of the silicate dust aggregates is still an open question.

The gravitational instability model allows instantaneous accretion of the km-sized planetesimals so as to overcome the radial drift barrier and disruption problem of the silicate dusts. However, turbulent flow in the nebula would mix the dust particles in the mid-plane and inhibit the gravitational instability. To overcome the turbulent mixing, local enhancement of dust-to-gas ratio higher than cosmic abundance is required in the mid-plane of the nebula (*Youdin and Shu*, 2002).

In any cases, the porous planetesimals consisted of μm-sized dust particles would be formed, although which scenario is plausible for the planetesimal formation is still under discussion. Outcome of the collisions between the planetesimals depends on physical properties of the planetesimal, such as planetesimal size, internal density, adhesive force between the dust particles, and mechanical strength. Moreover, these properties could significantly change by thermal processes, which is described in detail in Section 1.2. Therefore, it is essentially important to understand physical properties of assemblage of the dust particles for constraining the evolution of the planetesimals.

After the formation of the solid planetary embryos, collisional disruption of the bedrock of the planetary bodies and re-accumulation of the impact ejecta produced surface blanket of fine grains. These grains are observed on the surface of the Moon, Mercury, and Mars in present, as the so-called regolith. Spacecraft missions have revealed that asteroids are also covered with the regolith (*Carr et al.*, 1994; *Belton et al.*, 1994; *Miyamoto et al.*, 2007; *Sierks et al.*, 2011). Because such small bodies can not re-accumulate the high-speed impact ejecta, alternative mechanism of the regolith formation on the asteroids was reported by *Delbo et al.* (2014), in which the regolith on the small bodies was formed by the breakup of boulders by thermal fatigue due to diurnal temperature variation.

The surface regolith layer has highly significance from the perspective of several kinds of the planetary science and engineering. From the scientific standpoint, the regolith affects impact cratering, surface and internal temperature, or reflectance spectrum. Because the regolith layer forms the boundary between planetary interior and outer space, its thermal, elastic, and electrical properties serve as essential

information for in-situ exploration of planetary internal structure, such as heat flow, seismic, and electrical experiments. Thermal and mechanical properties of the surface regolith should be understood for feasibility study of the landing, touchdown, and night-time survivability.

As mentioned above, powdered materials, such as the dust particles constituting the initial planetesimals and the regolith covering the planets and asteroids, have existed universally in the solar system from the past to the present. Understandings of basic physical properties of the powdered materials are necessary for discussing the planetary evolution. In this thesis, thermal conductivity of powdered materials is focused on. It is known that the thermal conductivity of the powdered materials under vacuum is lower than that of the consolidated materials by several orders of magnitude. This is of interest to the planetary science as described below.

1.2 Thermal evolution of the planetesimal

Thermal process is one of the most fundamental events in the planetary evolution. It causes variable physical and chemical processes, such as aqueous alteration, thermal metamorphism, partial melting, metallic core formation, and volcanism. Many meteorites show the evidence of several degrees of the thermal evolution in the pre-existing parent bodies or planetesimals.

Several heat sources in the planetesimal are suggested; decay heat of radioactive isotopes (*Urey*, 1955), electromagnetic induction heating (*Herbert*, 1989), and/or impact heating (*Rubin*, 1995). The radioactive heating, especially by the decay of short-lived isotope ^{26}Al, is believed to be the primary heat source for the planetesimals in the early solar nebula (*McSween et al.*, 2002).

Many researchers have been attempted to examine the variety of the thermal metamorphism of chondritic meteorites by means of numerical thermal calculation of the planetesimal with ^{26}Al as a main heat source. The mass of the body of interest is generally assumed to be constant during the thermal evolution. The "formation" age of the body is defined by the time when attaining the terminal mass. The abundance of the short-lived radioactive isotopes ^{26}Al, which is often defined by the ratio to the stable nuclide ^{26}Al/^{27}Al, is calculated from the relative time of the planetesimal formation to the condensation age of calcium-aluminum-rich inclusions (CAIs) in the chondritic meteorites. The CAIs are believed to be the earliest materials formed in the solar system and their age would represent the age of the solar system. Pb-Pb dating of CAIs in carbonaceous chondrites (*Amelin et al.*, 2002; *Bouvier et al.*, 2007) revealed that the CAIs were formed at about 4568 million years ago (Ma). The ratio ^{26}Al/^{27}Al at the solar system formation was 5.1×10^{-5} (*Nyquist et al.*, 2009), which is also constrained from the CAI. The ^{26}Al abundance

decreased from this value with half-time of 0.73 million years (Myr).

The degree of the temperature rise in the planetesimal is controlled by competing effect between the internal heating efficiency and heat loss timescale to the surface. As the formation age of the planetesimals is shorter after the CAI formation, the temperature increases more easily because of the more abundant heat source ^{26}Al. In general, the internal temperature of a larger body becomes higher than smaller one, because it would take more time to conducting the heat from the center to the surface. The peak temperature decreases from the center to the surface.

Thermophysical properties, such as thermal conductivity and heat capacity, also control the heating and cooling efficiency. The lower thermal conductivity contributes to inefficient heat loss, by which the internal temperature becomes higher. The lower heat capacity reduces the heat energy required to increase the temperature, and in parallel, enhances the cooling rate.

The thermal conductivity is the most changeable parameter depending on the material condition. The thermal conductivity of silicate powdered materials under vacuum is roughly 0.001 W/mK (*Wechsler et al.*, 1972), while the intact rocks have those about 1 W/mK. If the planetary body contains the unconsolidated powdered materials, as is the case for the planetesimal, its temperature during the thermal evolution becomes significantly higher than that of consolidated body, due to the thermal insulating effect of the less conductive powdered materials.

Figure 1.2 shows the thermal evolution of a body of 1 km in radius formed at 2 Myr after the CAI formation. Four different thermal conductivity values of 1, 0.1, 0.01, and 0.001 W/mK are given. The heat source is the radioactive decay energy of a short-lived nuclide ^{26}Al. The more detailed information about the calculation method will be shown in Chapter 5. As seen in Figure 1.2, the temperature profile significantly changes by the thermal conductivity. When giving the thermal conductivity of 1 W/mK, the temperature remains nearly constant at initial temperature, and such bodies could not evolved thermally. The lower thermal conductivity makes the peak temperature higher. If the thermal conductivity of 0.001 W/mK is adopted as a typical value of powdered materials under vacuum, its internal temperature rises higher than 1000 K.

If the planetesimal composed of the dust particles undergoes such high temperature, sintering of the dust particles occurs. The sintering is a phenomenon of the consolidation of the powdered materials at high temperature below the melting temperature. As the sintering starts, physical connections between the particles are formed and the void space between the particles gradually contracts. The resultant thermal and mechanical properties differ from the original unconsolidated values. Thus, the sintering is one of the important thermal processes that changes the physical properties of the planetesimal. Condition for the sintering (size and formation

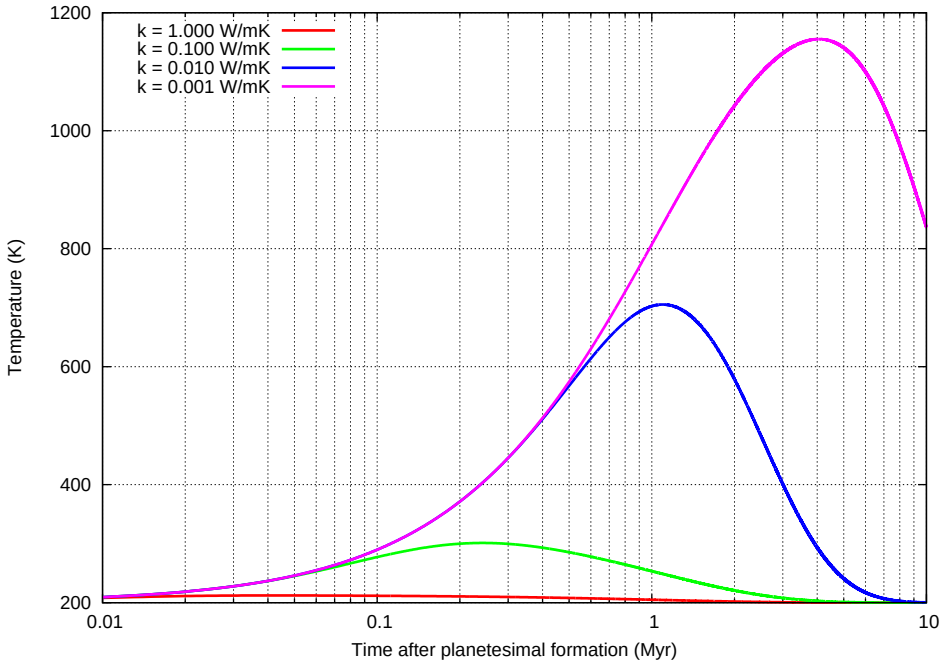

Figure 1.2: Temperature evolution at the center of planetesimals of 1 km in radius, formed at 2 Myr after CAI formation. The thermal conductivity is set at 1 W/mK (red), 0.1 W/mK (green), 0.01 W/mK (blue), and 0.001 W/mK (purple), respectively. The density and specific heat is assumed to be 3230 kg/m^3 and 800 J/kgK, respectively.

age of the planetesimal, onset timing of the sintering) is primary controlled by the initial thermal conductivity of the planetesimal as the assemblage of the powdered materials.

Table 1.1 shows the some previous works on the thermal evolution model of small body including the planetesimal, summarized with respet to the heat source, initial structure, thermal conductivity value, and with or wihtout the sintering. *Miyamoto et al.* (1981) analytically calculated the thermal evolution of parent body of the ordinary chondrites with internal heat source of ^{26}Al. According to their results, the chondritic materials were formed in a body of 85 km in radius which was formed after about 2.5 Myr after CAI formation. The thermal conductivity values for the parent body was constant at 1 W/mK, a typical value for the silicate rock. They stated that the ordinary chondrites with different petrologic types came from single large parent body, in which the degrees of the thermal metamorphism (peak temperature experienced during the thermal evolution) increased with depth. This model for the origin of the chondrites is called onion-shell model (Figure 1.3).

Yomogida and Matsui (1984) calculated the thermal evolution of the porous planetesimals, formed from unconsolidated powder materials. Their model took into account the sintering of powder materials in terms of the reduction of the porosity and the related change of the thermophysical properties. The heat source in their model included only long-lived isotopes. The thermal conductivity they used was given as a function of porosity and temperature. For the initial unconsolidated state, experimental data by *Fountain and West* (1970) was used, who measured thermal conductivity of basalt powder under vacuum. As the sintering (reduction of the porosity) proceeds, they used chondritic meteorite's data obtained by *Yomogida and Matsui* (1983). The modeled thermal conductivity increased from 0.002 W/mK to 3 W/mK by the sintering. Their results indicated that even small body of a few tens km in radius was heated by several hundred degrees and the temperature distribution inside the bodies became very homogeneous, due to thermally insulating effect of powders. The peak temperature was primary restricted by the temperature at which the sintering and the related thermal conductivity enhancement occurred. Their model predicted that the chondrite meteorites with different petrologic types were formed in different sizes of the parent body. This model is called multiple parent bodies model (Figure 1.3).

Table 1.1: Some previous studies on thermal evolution of small bodies.

Reference	Heat source	Initial strucuture	Thermal conductivity	Sintering [yes/no]
Miyamoto et al. (1981)	^{26}Al	Consolidated rock	1 W/mK	no
Yomogida and Matsui (1984)	^{40}K,^{232}Th, ^{235}U,^{238}U	Unconsolidated rock powder	0.002 to 3 W/mK dependent on temperature and porosity	yes
Akridge et al. (1998)	^{26}Al,^{40}K,^{232}Th, ^{235}U,^{238}U	Consolidated rock core with regolith blanket	0.1 to 3 W/mK	no
Henke et al. (2012a)	^{26}Al,^{60}Fe,^{40}K, ^{232}Th,^{235}U,^{238}U	Unconsolidated rock powder	0.005 to 4 W/mK dependent on porosity	yes

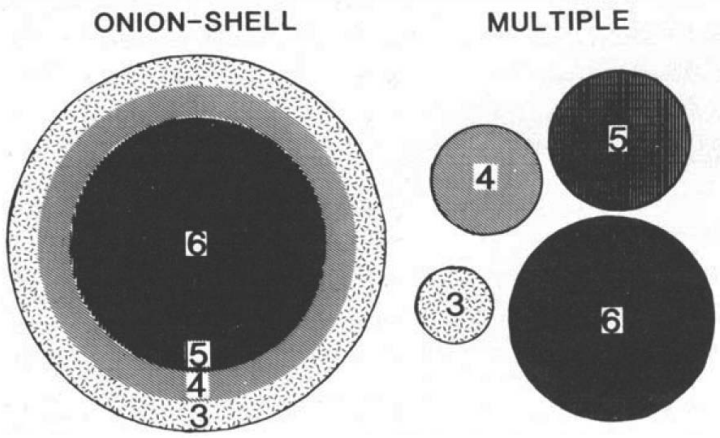

Figure 1.3: Onion shell model (left) and multiple parent body model (right) for ordinary chondrite parent bodies (*Yomogida and Matsui*, 1984). In the onion shell model, the petrologic types 3 to 6 (numbers in this figure) are originated from single body. The multiple parent body hypothesis predicts individual parent bodies for different petrologic types.

Akridge et al. (1998) investigated the effect of the surface regolith insulation on the temperature evolution of ordinary chondrite parent body of 100 km in radius, with ^{26}Al as the internal heat source. The thermal conductivity of about 0.1 W/mK was used for the surface regolith, which is higher than that for the lunar regolith *Langseth et al.* (1976). Comparison between the thermal models with and without the surface regolith layer revealed that the surface regolith made the internal temperature more uniform and the cooling rate slower.

Recently, *Henke et al.* (2012a) modeled the thermal history the porous planetesimals consisted of the dust particles including the sintering. The thermal conductivity used in their model is a function of the porosity, from the experimental data by *Krause et al.* (2011) for SiO_2 unconsolidated powders and by *Yomogida and Matsui* (1983) for the consolidated meteorites. The relation between the thermal conductivity and the porosity used in their thermal evolution model is shown in Figure 1.4. As the degree of the sintering increases, the thermal conductivity increases along the solid curve in this figure. *Henke et al.* (2012a) showed that initially porous planetesimals of a few km in radius formed shortly after the CAI formation experienced high degree of the heating sufficiently to melt at the center. To form the ordinary chondritic materials by the onion-shell model, a planetesimal of 100 km radius formed at 2.3 Myr after CAI formation could be appropriate.

As shown above, several values of the thermal conductivity from 0.001 to 1 W/mK have been used in the previous studies. This variation affects the thermal evolution, as shown in Figure 1.2. For the unconsolidated powdered planetesimals (*Yomogida and Matsui*, 1984; *Henke et al.*, 2012a), the thermal conductivity val-

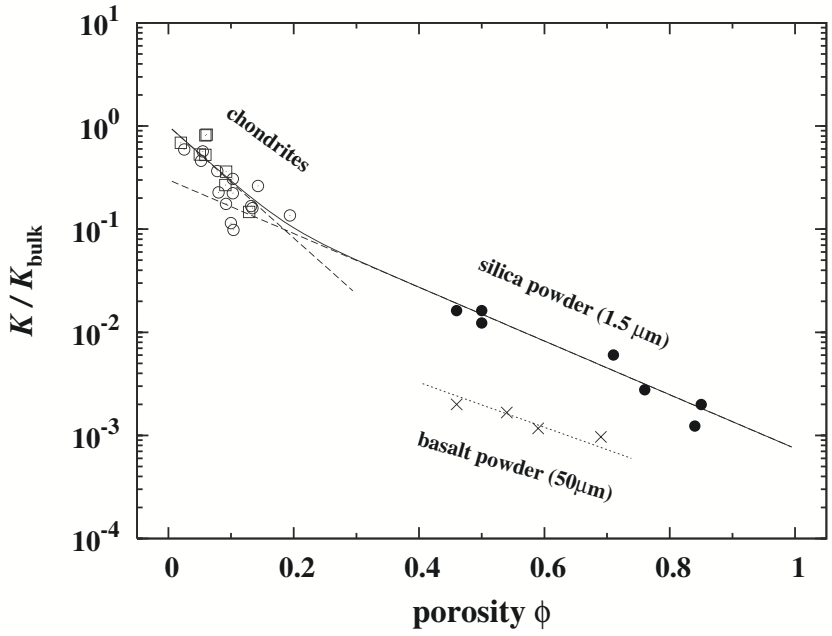

Figure 1.4: Thermal conductivity model of planetesimal as a function of the porosity, proposed by *Henke et al.* (2012a). The vertical axis represents the thermal conductivity relative to that of the intact material (they used 4.3 W/mK). The filled circles are the results for unconsolidated SiO_2 powders obtained by *Krause et al.* (2011). The open square and circles are experimental data for the ordinary chondrites by *Yomogida and Matsui* (1983). The crosses represent the thermal conductivity of basalt powder obtained by *Fountain and West* (1970), whose data were used for the thermal calculation by *Yomogida and Matsui* (1984).

ues used in their calculations differed by an order of magnitude (crosses and filled circles in Figure 1.4). Thus, the thermal conductivity of the unconsolidated porous planetesimal has not been constrained sufficiently.

1.3 Thermal conductivity of planetary surface regolith

The thermal conductivity of surface regolith layer on terrestrial bodies is of great interest for understanding their surface and interior thermal state. Crustal heat flow is a measure of heat production in planetary bodies. It can be estimated as a product of the thermal conductivity and vertical temeprature gradient in the surface material. On the Moon, heat flow experiments were conducted in Apollo 15 and 17 Heat Flow Experiments (*Langseth et al.*, 1972, 1973), and the thermal conductivity of the surface regolith was measured. Heat flow probes were emplaced in drilled borestems in the regolith layer (Figure 1.5). *Langseth et al.* (1973) estimated the thermal conductivity of the regolith from temperature increase rate during the heating of the probes. As a result, they reported that the thermal conductivity of subsurface regolith increases with depth; 0.0141 W/mK at 35 cm and 0.0295 W/mK at 233 cm below the surface. On the other hand, *Langseth et al.* (1976) estimated the thermal diffusivity of regolith using the data on annual temperature variations propagating into the lunar regolith. The deduced thermal diffusivities were independent of the depth. Assuming the constant density and specific heat of the underground regolith, they revised the thermal conductivity values between 0.009 W/mK to 0.013 W/mK dependent on the measurement sites. *Keihm and Langseth* (1973) reported that the thermal conductivity of upper few centimeters of the lunar surface regolith is about 0.001-0.0015 W/mK, based on microwave brightness temperature analyses around the landing sites. These in-situ measurement values are summarized as a function of depth in Figure 1.6.

The thermal conductivity values deduced by *Langseth et al.* (1973) are higher than those by *Langseth et al.* (1976). They argued that the short-time heater activated measurements (*Langseth et al.*, 1973) is sensitive to the regolith material near the probes, and the derived thermal conductivity was affected by regolith compaction during the drilling process. The compaction would enhance the thermal conductivity, due to increase in the packing density and compressional stress in the regolith. The thermal conductivity estimated from the annual temperature variations (*Langseth et al.*, 1976) are dependent on the bulk regolith properties far from the probes. *Grott et al.* (2010) showed that if the thermal conductivity of 0.01 W/mK is true for the undisturbed regolith, the temperature variation during the heating of the probe can be reproduced by taking account of effect of regolith compaction on the thermal conductivity according to the compaction model by *Pilbeam and Vaišnys*

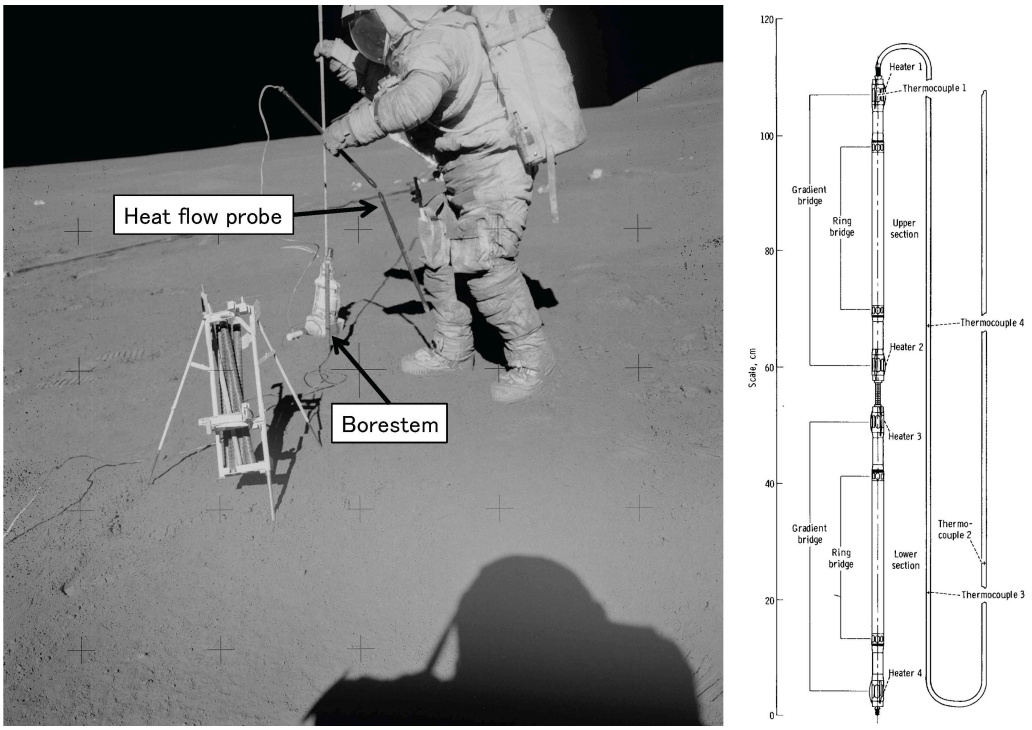

Figure 1.5: Photo during Apollo 15 Heat Flow Experiments (AS15-92-12407, `http://www.apolloarchive.com/apollo_gallery.html`) and illustration of heat flow probe (*Langseth et al.*, 1973). Borestem is emplaced in the regolith. A rod in the left hand of the astronaut is the heat flow probe, which was inserted in the borestem.

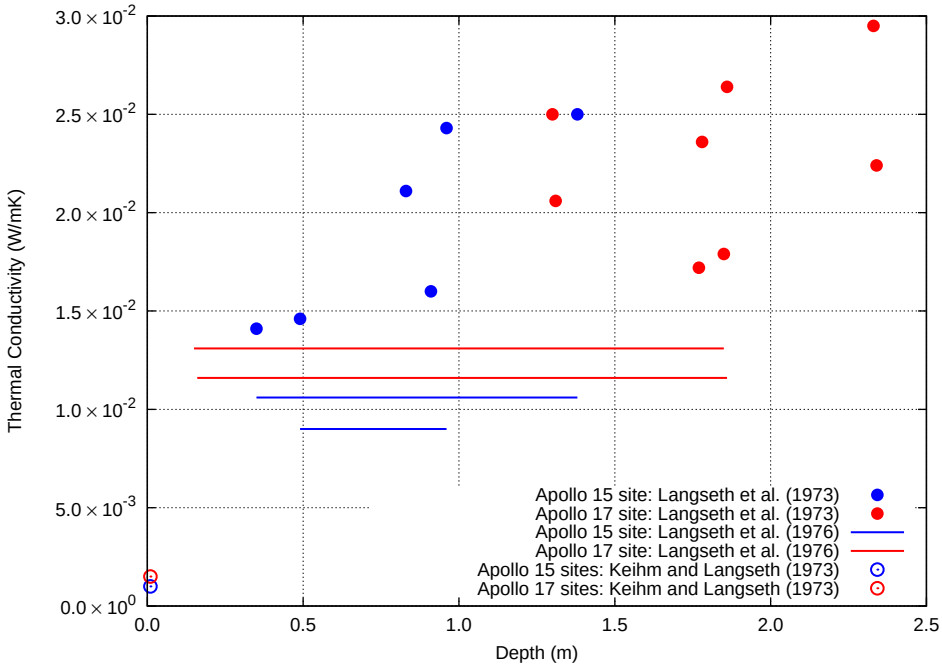

Figure 1.6: Thermal conductivity of lunar surface regolith estimated by Apollo Heat Flow Experiments. Filled circles represent the heater-activated measurements (*Langseth et al.*, 1973). Horizontal lines are deduced from thermal diffisivity values estimated from the attenuation of annual temperature variation along the depth (*Langseth et al.*, 1976). Hollow circles at the left of this graph are estimated from analyses of brightness surface temperatures (*Keihm and Langseth*, 1973). Blue and red symbols represent the landing sites of Apollo 15 and 17, respectively.

(1973). Then, the thermal conductivity around 0.01 W/mK is recently believed to be proper value for underground of the lunar regolith layer. The thermal conductivity of the lunar regolith would increase considerably within several tens centimeters in depth. The thermal infrared measurements by Diviner onboard the Lunar Reconnaissance Orbiter also indicated eightfold increase in the thermal conductivity from 0.001 to 0.008 W/mK within a few tens centimeters depth at lunar equatorial regions (*Vasavada et al.*, 2012). In the previous studies, the reason of this trend was deduced to be changes of bulk density (*Fountain and West*, 1970) and self-weighted stress (*Horai*, 1981; *Sakatani et al.*, 2012) with depth.

Beside the Moon, the regolith layer also exists on Mercury, Mars, asteroids, and comets. Surface temperature variation against the solar thermal radiation is strongly depends on thermal properties of surface materials. Degree of the periodic variation in the surface temperature is characterized by thermal inertia defined by the square root of the product of the thermal conductivity, specific heat, and density. Surface materials with low thermal inertia (low thermal conductivity) shows wide range of the temperature variation. For example on the Moon, the surface temperature varies from 100 K at lunar night to 380 K at lunar noon at Apollo 17 site (*Keihm and Langseth*, 1973), due to low thermal inertia about 40 J/m^{2}Ks$^{0.5}$ (*Wesselink*, 1948) of the lunar surface regolith. Thermal infrared measurements of the asteroids reveals that the thermal inertia varies widely between the bodies from 10 to 1000 J/m^{2}Ks$^{0.5}$ (*Delbo' et al.*, 2007). The thermal inertia depends on the nature of the surface materials as grain size, porosity, depth of the regolith layer, and larger rock abundance, all of which serve as key informations for the surface evolution of planetary body. These also help to choose landing and sample-return sites for future space missions to asteroids. To connect the thermal inertia value to the physical condition of the surface materials, parametric study on the thermal conductivity of regolith-like powdered materials is an essential work.

1.4 Purpose of this study

The thermal conductivity of the powdered materials under vacuum is one of the most important physical parameters in context of the thermal issues of the planetary bodies. However, heat transfer in the powdered material is complex phenomenon. Its thermal conductivity depends on many parameters (particle size and its distribution, porosity, temperature, compressional stress, material composition, particle shape, etc.), and these dependences have not still been understood integratively. A model of the thermal conductivity of the powdered materials must be established for application to the planetary sciences, such as the thermal evolution of the planetesimal and the thermal model of the planetary surface layer.

Table 1.2: Overview of our thermal conductivity measurements. GB: Glass beads. MB: Metalic beads. RS: Lunar regolith simulant.

Parameter	Sample	Parameter range
Temperature	GB, MB, RS	from 250 to 330 K
Particle size	GB	from 50 to 1000 μm
Porosity	GB	from 0.49 to 0.86
Compressional stress	GB	less than 20 kPa
Material type	GB, MB	-
Particle size distribution	GB	size ratio = 1:2
Degree of sintering	GB	neck radius ratio less than 0.3

This study aims at understanding the heat transfer mechanism in the powdered materials under vacuum and developing an integrative thermal conductivity model that describes the parameter dependences. In order to accomplish this purpose, the thermal conductivity of several powder samples, whose dependent parameters were accurately controlled, was measured experimentally and the parameter dependences were systematically investigated. Integrating the experimental results, the heat transfer mechanism, which caused the revealed parameter dependences, was verified. Then, a thermal conductivity model was constructed.

Theoretical background and previous experimental works on the thermal conductivity of the powdered materials are reviewed in Chapter 2. Chapter 3 is the main part of this thesis, in which the experimental method and results are described. Table 1.2 outlines the dependent parameters whose effect on the thermal conductivity were investigated experimentally in this study. The temperature dependence of the thermal conductivity was measured for all samples used in this study. The temperature-dependent data was utilized to determine conductive and radiative contributions, which helps us to understand the heat transfer mechanism. In Chapter 4, an thermal conductivity model is constructed based on the heat transfer mechanism inferred from the experimental results. The developed thermal conductivity model is finally applied to calculation of the thermal evolution of planetesimals in Chapter 5. The model is also applied to the surface regolith on the Moon (Appendix A) and asteroids (Appendix B). Chapter 6 shows summary and conclusion of this thesis.

Chapter 2

Thermal conductivity of powdered materials: Review of previous works

2.1 Heat transfer in powdered materials

The thermal conductivity is defined as amount of transported heat per unit time and per unit area as a result of unit temperature gradient in a material. According to Fourier's law of heat conduction,

$$q = -k\frac{dT}{dz}, \tag{2.1}$$

where k is the thermal conductivity, q is heat flux, and dT/dz is temperature gradient.

Heat transfer in powdered media attributes three mechanisms listed below.

1. Thermal conduction and convection of gas in void space between the particles.

2. Thermal conduction within the particles and through contact area between the particles.

3. Thermal radiation from a particle surface to next one through the void space.

Effective or total thermal conductivity of powdered materials k_{eff} can be written by the sum of these three contributions as (*Wechsler et al.*, 1972),

$$k_{\text{eff}} = k_{\text{gas}} + k_{\text{solid}} + k_{\text{rad}}, \tag{2.2}$$

where k_{gas}, k_{solid}, and k_{rad} are thermal conductivities attributed from the above mechanisms, respectively. These contributions are named as gas conductivity, solid

conductivity, and radiative conductivity, respectively. Under vacuum conditions, in which the gas conductivity can be neglected, Equation (2.2) reduces to,

$$k_{vac} = k_{\text{solid}} + k_{\text{rad}}. \tag{2.3}$$

At relatively high atmospheric pressure, the gas conductivity is dominant. The solid and radiative conductivities are important only under vacuum.

According to kinetic theory of gas molecules, the thermal conductivity of gas in free space, k_0, is represented by,

$$k_0 = \frac{n\bar{v}\lambda C_{\text{v}}}{3N_{\text{a}}}, \tag{2.4}$$

where n is number density of the gas molecules per unit volume, $\bar{v}$ is mean kinetic speed of the gas molecules, λ is mean free path, C_{v} is specific heat, and N_{a} is the Avogadro number. The mean free path of gas molecules is described as a function of the gas pressure, P, as,

$$\lambda = \frac{k_{\text{B}}T}{\sqrt{2}\pi\theta^2 P}, \tag{2.5}$$

where k_{B} is the Boltzmann constant, T is temperature, and θ is diameter of the gas molecules. Because the number density n is proportional to P, Equation (2.4) means that the thermal conductivity of the gas is independent of the gas pressure.

For powdered media, however, it is known that the effective thermal conductivity decreases with the gas pressure reducing. Experimental results by *Huetter et al.* (2008), who measured the thermal conductivity of five sizes of glass beads as a function of the gas pressure, are shown in Figure 2.1. As the pressure is reduced from the atmospheric pressure, the mean free path becomes longer and the gas density becomes lower. When the mean free path derived theoretically from Equation (2.5) becomes larger than the void size between the particles, the mean free path is restricted by the void size. Therefore, the mean free path λ remains to be a constant. The gas conductivity decreases with the gas pressure decreasing since the gas density n continues to decrease. If the gas pressure reduces enough so that the gas conductivity becomes negligible compared to the sum of the solid and radiative conductivities, the effective conductivity remains constant.

A meaningful dimensionless parameter, which characterizes the behavior of the gas molecules in porous materials is Knudsen number Kn. It is defined as a ratio of the mean free path λ to the typical void size L,

$$Kn = \frac{\lambda}{L} = \frac{k_{\text{B}}T}{\sqrt{2}\pi\theta^2 P}\frac{1}{L}. \tag{2.6}$$

For $Kn \ll 1$, collision among the gas molecules dominates (viscous flow regime). Collision between the void wall and the gas molecules becomes dominative when

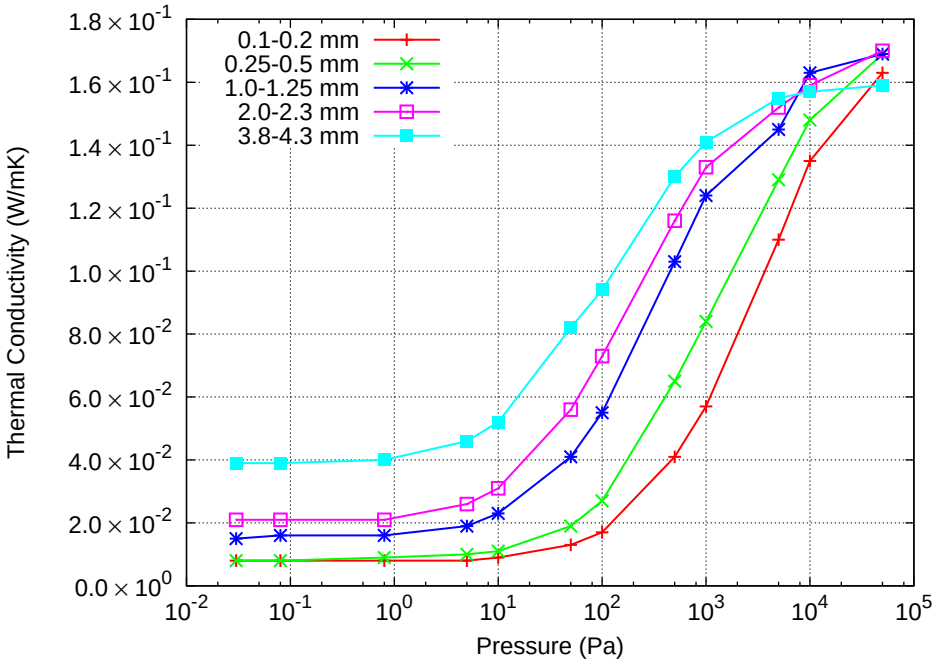

Figure 2.1: Thermal conductivity of glass beads as a function of gas pressure, cited from *Huetter et al.* (2008). The symbols represent the difference of the particle size from 0.1-0.2 mm to 3.8-4.3 mm.

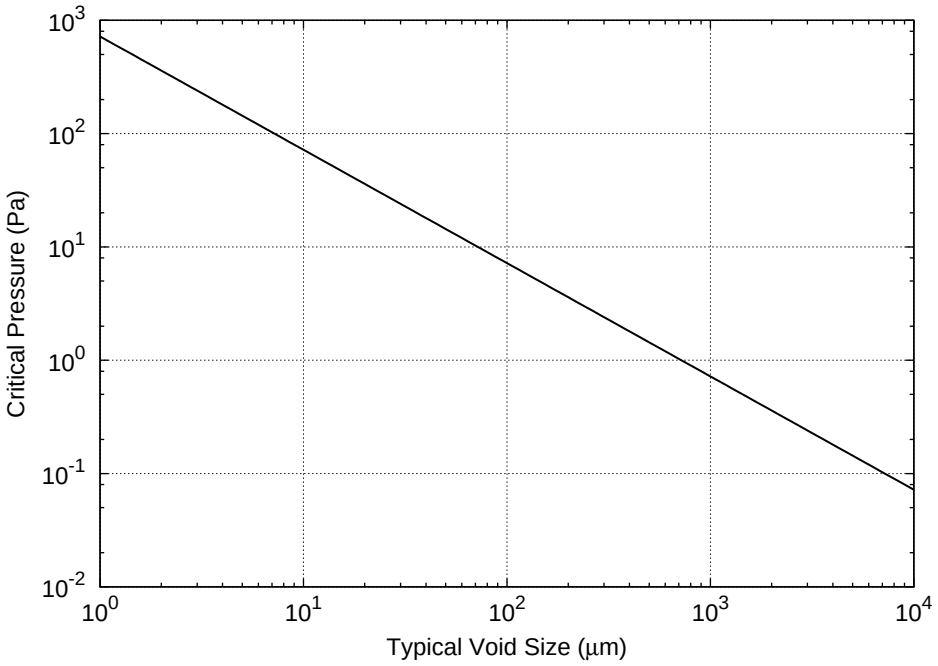

Figure 2.2: Critical gas pressure to neglecting the effect of gas heat transfer as a function of typical void size between the particles from Equation (2.7).

$Kn \gg 1$ (free molecular regime). The contribution of the gas conduction is negligible when $Kn > 10$ (*Kaviany*, 1998). Therefore, critical gas pressure, below which the gas heat transfer can be neglected and the thermal conductivity reaches a constant value dominated by the solid conduction and the radiation, can be calculated as,

$$P_{\mathrm{crit}} = \frac{1}{10}\frac{k_{\mathrm{B}}T}{\sqrt{2}\pi\theta^2 P}\frac{1}{L} = 7.2\times10^{-4}\frac{1}{L}. \tag{2.7}$$

Figure 2.2 shows the critical pressure P_{crit} as a function of typical void size L, when $\theta = 3.6\times10^{-10}$ m (nitrogen molecule) and $T = 300$ K are adopted, In Figure 2.1, the critical pressure differs by the particle size. This difference can be explained by the Knudsen number (*Piqueux and Christensen*, 2009).

2.2 Thermal conductivity of powdered materials under vacuum

When $Kn > 10$, the effective thermal conductivity is given by the sum of the solid and radiative conductivity as Equation (2.3). Both solid and radiative conductivities depend on several parameters. Table 2.1 shows the chronological overview of the previous experimental studies for the thermal conductivity of silicate powdered materials under vacuum conditions. In this section, the parameter dependences of the thermal conductivity under vacuum are reviewed. It should be noted again that the measured thermal conductivity contains the solid and radiative contributions.

Theoretical background

The solid conductivity is considered to depend on inter-particle contact area and networks of contacting particles. Since restricted contact area between the particles acts as strong thermal resistor, the thermal conductivity of the powdered materials under vacuum becomes extremely lower than the consolidated material. The inter-particle contact area and particle contact network depend on several physical parameters, such as particle size, applied load, surface roughness, shape of the particles, elastic modulus of the materials, and porosity. It is quite difficult to modeling the solid conductivity including the effect of these parameters. Therefore, previous studies for the solid conductivity had been focused on simple situations such as spheres of uniform size with regular packing structure.

Halajian and Reichman (1969) modeled the conductivity thorough the contact between spherical particles packed with the simple cubic lattice. They reported that the conductivity increases with depth, or applied force, which broads the contact

area due to elastic deformation of the spheres;

$$k_{\text{solid}} = k_{\text{m}} \left[\frac{\pi \rho_{\text{m}} g (1-\nu^2)}{2E} \right]^{1/3} z^{1/3}, \tag{2.8}$$

where k_{m} is thermal conductivity of the solid material, ρ_{m} is true density of the solid material, g is the gravitational constant, ν is Poisson's ratio, E is Young's modulus, and z is depth. Their theory predicted that k_{solid} is independent of the particle size.

The radiative conductivity depends strongly on temperature (*Watson*, 1964). The thermal radiation between the particles is often approximated by the radiation between two detached flat plates with small temperature difference. When two plates have temperature of T and $T + \Delta T$, radiative heat flux between the plates is approximated by the following equation if $\Delta T \ll T$,

$$q_{\text{rad}} \propto (T+\Delta T)^4 - T^4, \tag{2.9}$$

$$\propto T^3 \Delta T. \tag{2.10}$$

The radiative conductivity is defined using the Fourier's law of heat conduction as,

$$k_{rad} = q_{\text{rad}} \frac{L}{\Delta T}, \tag{2.11}$$

where L is distance between the two plates. From Equation (2.10) and (2.11), the radiative conductivity is modeled as,

$$k_{rad} \propto L T^3. \tag{2.12}$$

For the powdered media, L is representative of the typical void size. Equation (2.12) suggests that the radiative conductivity is proportional to the temperature cubic.

Table 2.1: Previous studies for the thermal conductivity of silicate powders under vacuum (less than 1 Pa).

Reference	Sample	Particle Size (μm)	Density (kg/m^3)	Temperature (K)	Thermal conductivity ($\times 10^{-3}$ W/mK)
Watson (1964) [(1)]	Glass beads	590-840	1590-1820	150-350	0.8-11.4
		250-350	1500-1610		0.5-5.8
		88-125	1570-1630		0.6-4.0
		53-74	1380-1680		0.8-2.2
		< 37	1170-1470		1.2-3.7
	Crushed glass beads	44-74	580-860		1.9-3.2
	Crushed quartz	44-74	1220-1460		3.5-5.1
		< 74	1100-1240		3.0-5.1
	Crushed hornblende	< 74	1100-1500		1.2-5.1
	Crushed olivine	< 74	1370		1.5-6.5
Wechsler and Glaser (1965)	Olivine powder	20	-	270-300	5.9-6.3
	Chondrite powder	20	-	220-440	3.4-4.6
	Tektite powder	20	-	280	2.3
	Basalt powder	20	-	290	1.8
	Glass beads	150	-	190-300	4.6-5.0
		50	-	190-300	1.7-3.2

1) Since *Watson* (1964) did not show the direct measurement results for the effective thermal conductivity, I calculated it from solid A and radiative B coefficients (Equation 2.13) with temperature range between 150 and 350 K.

Table 2.1: Continued.

Reference	Sample	Particle Size (μm)	Density (kg/m^3)	Temperature (K)	Thermal conductivity ($\times 10^{-3}$ W/mK)
Wechsler and Simon (1966)	Glass beads	44-62	1420	190-350	0.6-1.7
	Pumice powder	44-74	840	200-350	0.5-1.9
		10-37	820	160-380	0.6-2.1
	Basalt powder	44-74	1430	180-350	0.8-1.7
		10-37	1360	170-360	1.2-2.1
	Quartz powder	1-10	1000	160-400	2.4-4.3
Merrill (1969)	Glass beads	10-20	1210	320-510	1.2-4.9
		38-53	1130	100-500	0.4-4.8
		125-243	1490	100-490	0.2-6.0
Fountain and West (1970)	Basalt powder	37-62	790	180-370	0.6-1.3
			880	150-360	0.7-1.5
			980	160-360	0.6-1.4
			1130	140-370	0.8-1.8
			1300	150-360	1.3-2.6
			1500	140-360	1.7-3.1

Table 2.1: Continued.

Reference	Sample	Particle Size (μm)	Density (kg/m^3)	Temperature (K)	Thermal conductivity ($\times 10^{-3}$ W/mK)
Cremers et al. (1970)	Apollo 11 sample (10084)	-	1265	200-400	1.5-2.6
Cremers (1971)	Apollo 11 sample (10084)	-	1640	160-400	1.6-3.7
			1950	170-410	1.8-3.1
Cremers and Birkebak (1971)	Apollo 12 sample (12001)	-	1300	170-430	1.1-3.5
Cremers (1972a)	Apollo 12 sample (12001)	-	1640	210-420	1.1-2.8
Cremers (1972b)	Apollo 12 sample (12001)	-	1970	100-430	1.2-2.7
Cremers (1972c)	Apollo 14 sample (14163)	-	1100	120-350	0.7-1.7
			1300	110-400	0.7-2.4
Cremers and Hsia (1973)	Apollo 15 sample (15031)	-	1300	100-410	0.6-1.4
Cremers and Hsia (1974)	Apollo 16 sample (68501)	-	1500	100-390	0.5-1.5
Fountain and West (1974)	Basalt powder	74-149	1250	240-360	0.8-1.7
			1390	250-360	0.9-1.8
			1750	230-360	1.2-2.2
			1900	210-350	2.5-4.3
			1950	120-360	3.6-6.4

Table 2.1: Continued.

Reference	Sample	Particle Size (μm)	Density (kg/m^3)	Temperature (K)	Thermal conductivity ($\times 10^{-3}$ W/mK)
Cremers (1975)	Apollo 14 sample (14163)	-	1500	100-400	0.8-2.6
			1800	100-400	1.2-2.8
Fountain and West (1975) (2)	Lunar regolith simulant	-	1250	230-400	0.8-2.5
			1500	180-440	1.0-2.5
			1750	170-400	2.0-4.5
			1800	170-400	3.1-8.1
Fountain and West (1978) (2)	Apollo 15 sample (15031)	-	1350	290-420	2.2-4.5
Horai et al. (1980)	Lunar regolith simulant	-	1470	Room temp.	2.1
			1500		2.1
			1570		2.7
			1580		2.1
			1670		2.1
	Apollo 17 core sample (70002)	-	1740		1.9-3.5
	Apollo 17 core sample (70006)	-	1800		3.9-4.9

2) The thermal conductivity values were read out from their graphical plots, because they did not plot the experimental points.

Table 2.1: Continued.

Reference	Sample	Particle Size (μm)	Density (kg/m^3)	Temperature (K)	Thermal conductivity ($\times 10^{-3}$ W/mK)
Horai (1981)	Lunar regolith simulant	-	1700	Room temp.	8.8
			1850		10.9
Huetter and Koemle (2008)	Black glass beads	1000-1250	1550	Room temp.	22.6
	Clear glass beads				15.4
Huetter et al. (2008)	Glass beads	100-200	1550	Room temp.	8.0
		250-500			8.0
		1000-1250			15.0
		2000-2300			21.0
		3800-4300			39.0
	Glass beads mixture	1000-4300	1610		9.0

Table 2.1: Continued.

Reference	Sample	Particle Size (μm)	Density (kg/m^3)	Temperature (K)	Thermal conductivity ($\times 10^{-3}$ W/mK)
Krause et al. (2011) [3]	Silica powder	1.5	300	Room temp.	2.6
			320		1.6
			480		3.6
			580		7.8
			1000		16.0-21.0
			1080		21.0
Gundlach and Blum (2012) [3]	Silica powder	25-55	1340	Room temp.	12.2
		118-236	1270		8.2
		245-497	1380		7.4
		423-591	1370		6.7
		861-989	1380		6.2

3) The density was calculated from the volume filling factor and porosity assuming the true density of 2000 kg/m^3 for the silica.

Effect of temperature

Most of the previous studies on temperature dependence of the thermal conductivity of powdered materials showed the increase with the temperature. Figure 2.3 shows an experimental result by *Merrill* (1969) for the thermal conductivity of glass beads of 38-53 μm in diameter. The cause of the increase in the thermal conductivity with temperature was considered to be attributed to the enhancement of radiative conductivity, as represented by Equation (2.12). In the strict sense, the solid conductivity also depends on the temperature primarily through the thermal conductivity of solid materials. However, it would be negligible compared with the stronger dependence of the radiative conductivity, if the solid conductivity is not significantly larger than the radiative one. Assuming the solid conductivity is independent of the temperature, *Watson* (1964) represented the temperature dependence of the thermal conductivity as,

$$k(T) = k_{\text{solid}} + k_{\text{rad}} = A + BT^3, \tag{2.13}$$

where T is the temperature, and A and B are constants representing the solid and radiative conductivity coefficients, respectively. This equation can well fitted to the experimental data in Figure 2.3 (solid curves in Figure 2.3).

Determined fitting variables A and B provide meaningful informations about the solid and radiative conductivities, respectively. In Figure 2.3, $A = 4.5 \times 10^{-4}$ and $B = 3.2 \times 10^{-11}$ can be obtained by the fitting. It means that the solid and radiative conductivities of this sample at 300 K are $k_{\text{solid}} = A = 4.5 \times 10^{-4}$ W/mK and $k_{\text{rad}} = B \times 300^3 = 8.6 \times 10^{-4}$ W/mK, respectively. The resulting effective thermal conductivity at 300 K becomes $k = k_{\text{solid}} + k_{\text{rad}} = 1.3 \times 10^{-3}$ W/mK. In this manner, the solid and radiative conductivities of a powdered sample can be estimated independently by using the temperature dependence of the thermal conductivity, which gives essential understanding on heat transfer mechanism in the powdered material. As shown in Table 2.1, however, the temperature dependence had been measured only until 1970's, most of which is concerned with the temperature-dependent thermophysical property of the lunar surface materials. After 1980's, the temperature during the measurements was not controlled and was restricted only at room temperature.

Effect of particle size

The particle size dependence has been often tested using artificially-manufactured glassy spheres. Figure 2.4 shows comparison of the thermal conductivity of glass

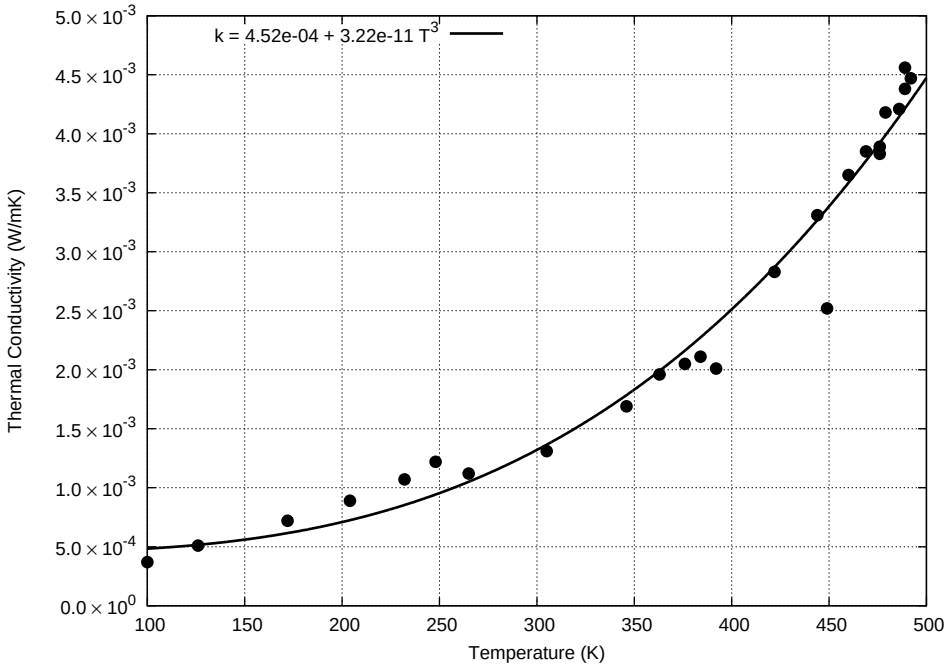

Figure 2.3: Temperature dependence of thermal conductivity of glass beads (38-53 μm in diameter), measured by *Merrill* (1969). A solid curve is a regression curve of Equation (2.13).

and silica beads from *Wechsler and Glaser* (1965), *Wechsler and Simon* (1966), *Merrill* (1969), *Huetter et al.* (2008), and *Gundlach and Blum* (2012) as a function of the particle diameter at about 300 K. As one can see form this figure, the thermal conductivity values were never definitive and differed by an order of magnitude even for the same sizes of the beads. *Merrill* (1969) and *Gundlach and Blum* (2012) observed lower thermal conductivity for large particles. On the other hand, the data from *Wechsler and Glaser* (1965) and *Huetter et al.* (2008) appeared to increase with the particle size. The cause of these differences has not been clear.

Merrill (1969) attempted to get the solid and radiative conductivities as a function of the particle size using the temperature-dependent thermal conductivity. These results are shown as a function of the particle diameter in Figure 2.5, together with the results by *Watson* (1964). Their results showed that the solid conductivity decreased with increasing the particle size, while the radiative conductivity increased.

Theoretically, the radiative conductivity increases with the particle size, because the typical void size L in Equation (2.12) becomes larger. If packing structure or porosiy remains constant, the void size, and therefore, the radiative conductivity is proportional to the particle diameter. This is consistent with the variation of B with the particle diameter in Figure 2.5. The theory of the solid conductivity by

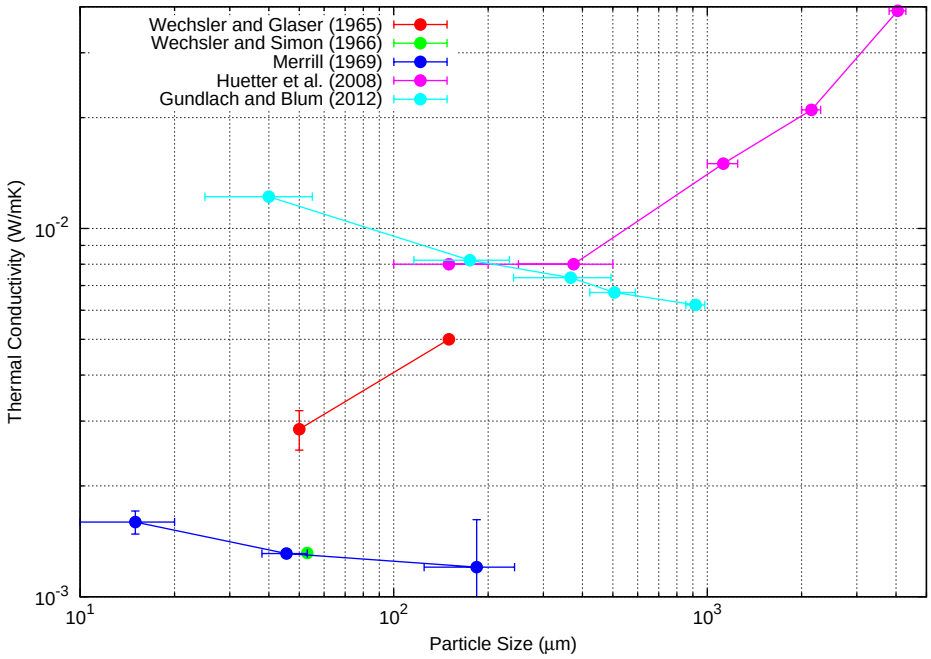

Figure 2.4: Thermal conductivity of glass and silica beads compiled from *Wechsler and Glaser* (1965), *Wechsler and Simon* (1966), *Merrill* (1969), *Huetter et al.* (2008), and *Gundlach and Blum* (2012) as a function of the particle diameter. For *Wechsler and Glaser* (1965), *Wechsler and Simon* (1966), and *Merrill* (1969), the data at the temperatures of 300 $\pm$ 30 K are shown.

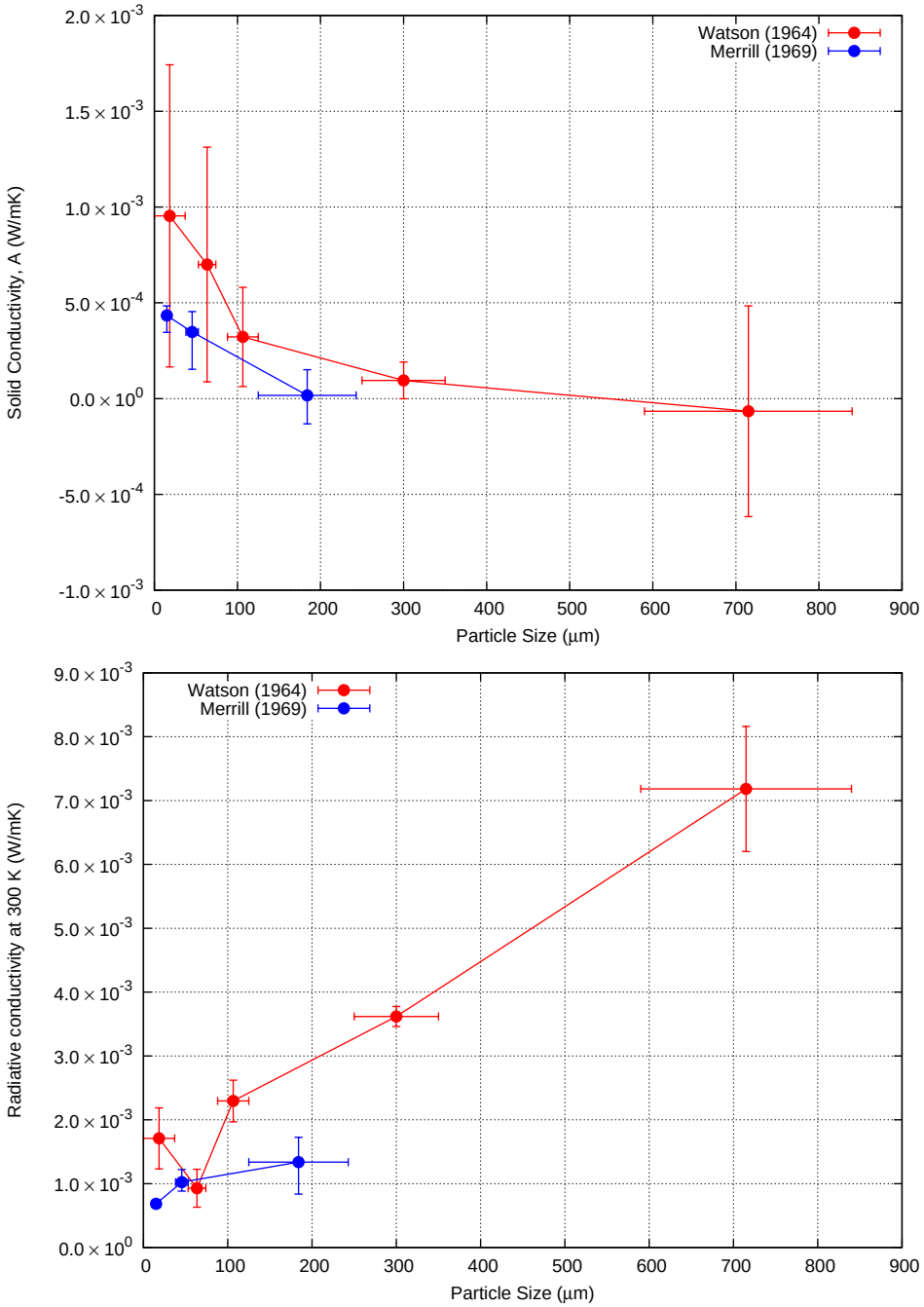

Figure 2.5: The solid (top) and radiative (bottom) conductivity of glass beads at 300 K, cited from *Watson* (1964) and *Merrill* (1969).

Halajian and Reichman (1969) in Equation (2.8) expects that the solid conductivity is independent of the particle diameter. This is inconsistent iwth the experimental results. *Gundlach and Blum* (2012) stated that the solid conductivity decreases with the particle diameter if the contact force betwen the particles is adhesive (van der Waals) force but the self-weight.

Note that the samples used by *Watson* (1964) and *Merrill* (1969) had wide range of the packing density or porosity, especially for *Watson* (1964) and *Merrill* (1969), as shown in Table 2.1. Since the density also affects the thermal conductivity, the trend shown in Figure 2.4 and 2.5 might represent the effect of not only the particle size but also the density.

Effect of porosity or bulk density

Fountain and West (1970) measured the thermal conductivity of terrestrial basalt powders (37-63 μm in diameter) as a function of bulk density ranged from 790 to 1500 kg/m^3 under vacuum. Similar experiments using the basalt powders were conducted by *Fountain and West* (1974) and *Fountain and West* (1975) for the particle sizes of 74-149 μm and less than 5 mm, respectively. *Krause et al.* (2011) measured 1.5 μm-sized SiO_2 powders with porosity ranging from 0.85 to 0.46. Their experimental results are compared in Figure 2.6 as a function of the porosity at temperature around 300 K. Figure 2.6 shows that the thermal conductivity is reduced when the porosity increases, in other words, the density decreases. The 1.5 μm silica powders had higher thermal conductivity by an order of magnitude than the basalt powders.

Fountain and West (1970, 1974, 1975) determined the solid and radiative conductivities of their samples, using the temperature-dependent data as *Merrill* (1969). The results are shown in Figure 2.7. The solid conductivity seems to decrease with the porosity. The solid conductivity is considered to primary depend on the packing arrangement of the particles. The porous sample has less number of contacting particles (coordination number), which reduces the efficiency of the thermal conduction. The radiative conductivity also seems to decrease with the porosity. For the higher porosity, the radiative conductivity is expected to increase because the void size L in Equation (2.12) becomes larger. This estimation contradicts their experimental results shown in Figure 2.7. *Wechsler et al.* (1972) suggested that part of this increase in the estimated radiative conductivity might be contributed from temperature-dependent increase in the solid conductivity, primary attributed to the temperature-dependent thermal conductivity of the composite material (basalt).

Thermal conductivity of lunar regolith samples

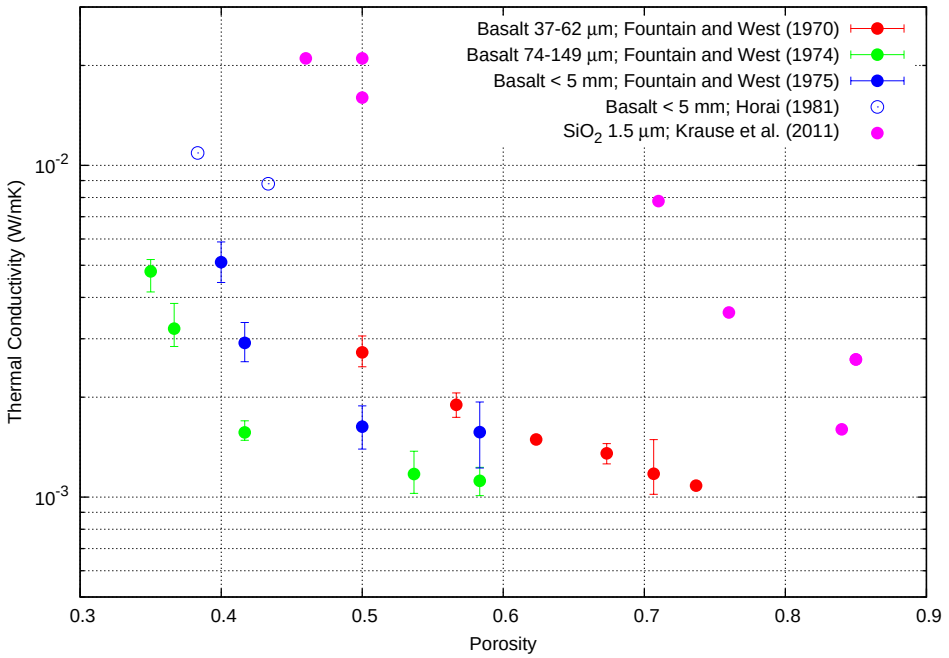

Figure 2.6: Porosity dependence of the thermal conductivity of powdered materials under vacuum by *Fountain and West* (1970, 1974, 1975) and *Krause et al.* (2011). Since the porosity of the basalt powders used by *Fountain and West* (1970, 1974, 1975) did not defined, it was calculated from the bulk density assuming the true density of 3000 kg/m^3 for the basalt. The thermal conductivity values obtained at the temperature of 300 $\pm$ 35 K are taken from the figures in the literature. The results by *Horai* (1981), who measured the same sample as used by *Fountain and West* (1975), are also plotted.

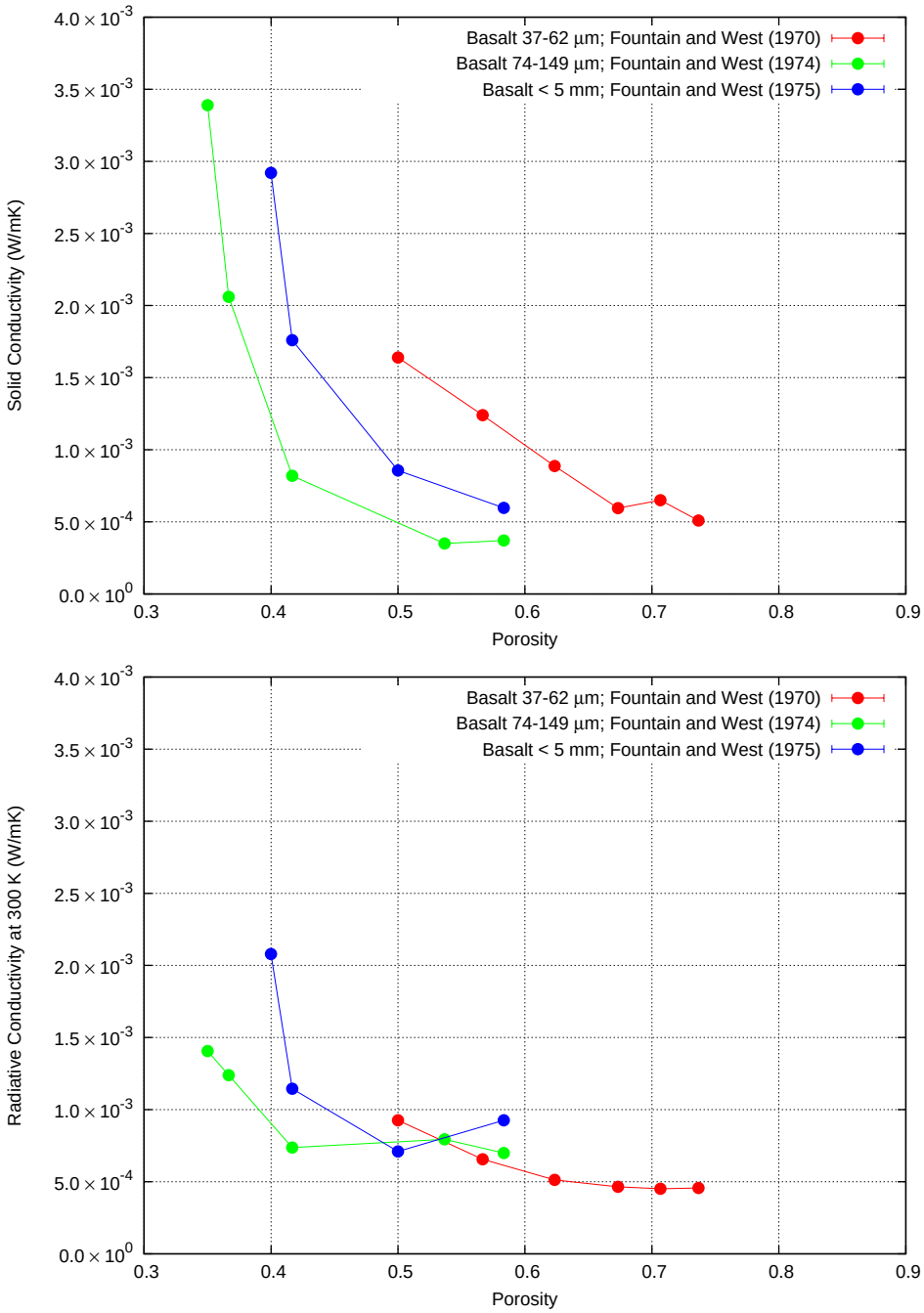

Figure 2.7: Estimated solid (top) and radiative (bottom) conductivities at 300 K for basalt powders (*Fountain and West*, 1970, 1974, 1975). Since *Fountain and West* (1974) did not show fitting results of Equation (2.13), the values of A and B are determined in this work. Only approximated curves of the thermal conductivity as a function of the temperature were shown in *Fountain and West* (1975), without the data points. Then, eight data points on their approximated curves were picked up, and the values of A and B were estimated by fitting Equation (2.13) into these data.

Lunar regolith samples collected in Apollo missions were measured in laboratories (*Cremers et al.*, 1970; *Cremers*, 1971; *Cremers and Birkebak*, 1971; *Cremers*, 1972a,b,c; *Cremers and Hsia*, 1973, 1974; *Cremers*, 1975) with the density range from 1100 to 1950 kg/m^3 as a function of the temperature. Figure 2.8 shows all of the available thermal conductivity data for the lunar samples. The obtained thermal conductivity ranges from 0.0005 to 0.0037 W/mK, which is consistent with the estimated values of the upper few centimeters of the lunar surface regolith (Figure 1.6, *Keihm and Langseth*, 1973). It should be noted that the higher thermal conductivity measured in-situ at the deeper depth ($\approx$ 0.01 W/mK *Langseth et al.*, 1973, 1976) was not reproduced in the laboratory experiments.

The solid and radiative conductivities of the lunar regolith samples are summarized in Figure 2.9. The solid conductivity is scattered from 0.0005 to 0.002 W/mK. The radiative conductivity at 300 K appears less scattered than the solid conductivity.

Effect of compressional stress

Fountain and West (1975) and *Horai* (1981) measured the thermal conductivity of the same basalt powders as a terrestrial analogue of the lunar soils. Their results are plotted in Figure 2.6. *Horai* (1981) observed the thermal conductivities of 0.0088 and 0.0109 W/mK at the densities of 1700 and 1850 kg/m^3, respectively, which were two times higher than those measured by *Fountain and West* (1975). One of the differences between these two experiments was the dimensions of sample containers. *Horai* (1981) used the vertically-elongated sample container (2.54 cm in diameter and 6.99 cm long), while *Fountain and West* (1975), as well as the other previous works on the basaltic powders and lunar regolith samples (e.g. *Fountain and West*, 1970; *Cremers et al.*, 1970), used horizontally-elongated containers. *Horai* (1981) argued that the higher conductivity resulted from elastic enhancement of inter-particle contact area by self-weighted stress in the sample. However, degree of thermal conductivity variation due to the compressional stress has not been verified experimentally.

In our previous works (*Sakatani et al.*, 2012), the thermal conductivity of glass beads were measured using a vertically-elongated sample container, and effect of the depth, at which the thermal conductivity is measured, was investigated. Within the depth from 1 cm to 30 cm, the thermal conductivity of the glass beads increased with the depth. This result was qualitatively consistent with the Horai's interpretation that the self-weighted stress enhances the thermal conductivity.

Horai (1981) obtained the thermal conductivity consistent with the in-situ mea-

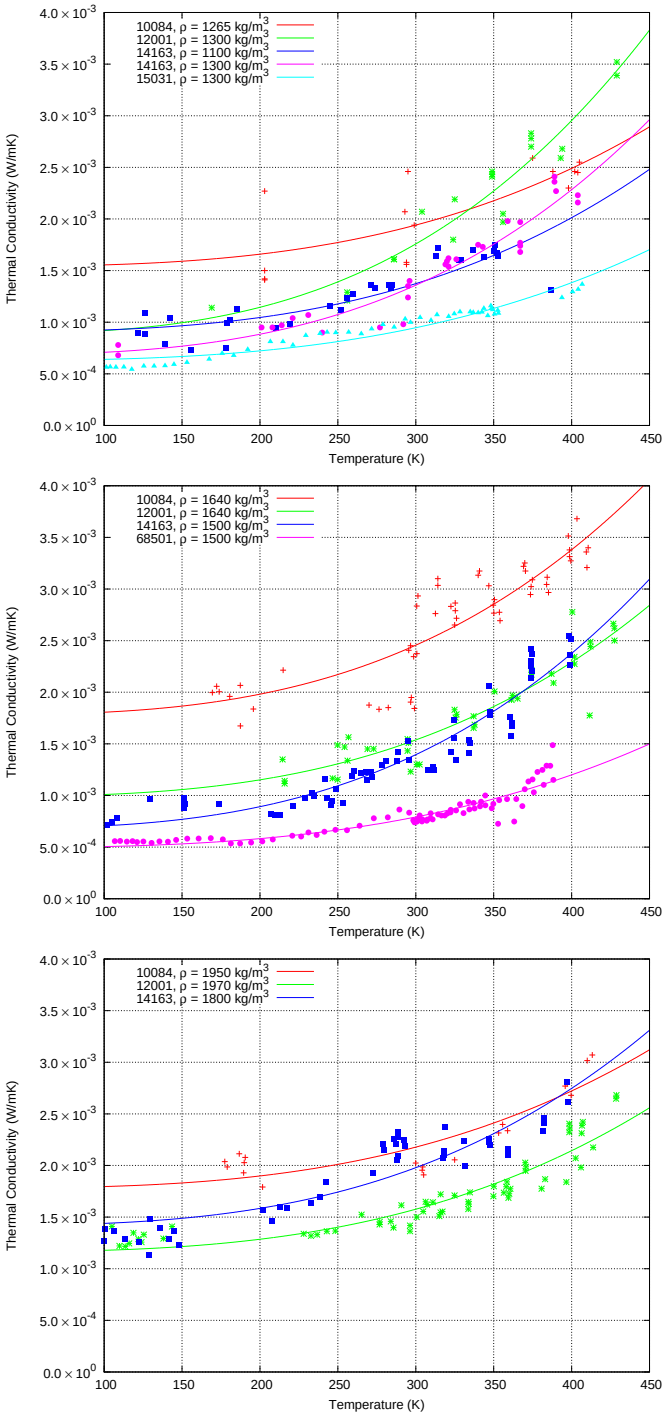

Figure 2.8: Thermal conductivity of Apollo lunar regolith samples at low (top, $\rho < 1400$ kg/m^3), intermediate (middle, 1400 kg/m^3 $< \rho <$ 1700 kg/m^3), and high (bottom, $\rho >$ 1700 kg/m^3) densities, compiled from (*Cremers et al.*, 1970; *Cremers*, 1971; *Cremers and Birkebak*, 1971; *Cremers*, 1972a,b,c; *Cremers and Hsia*, 1973, 1974; *Cremers*, 1975).

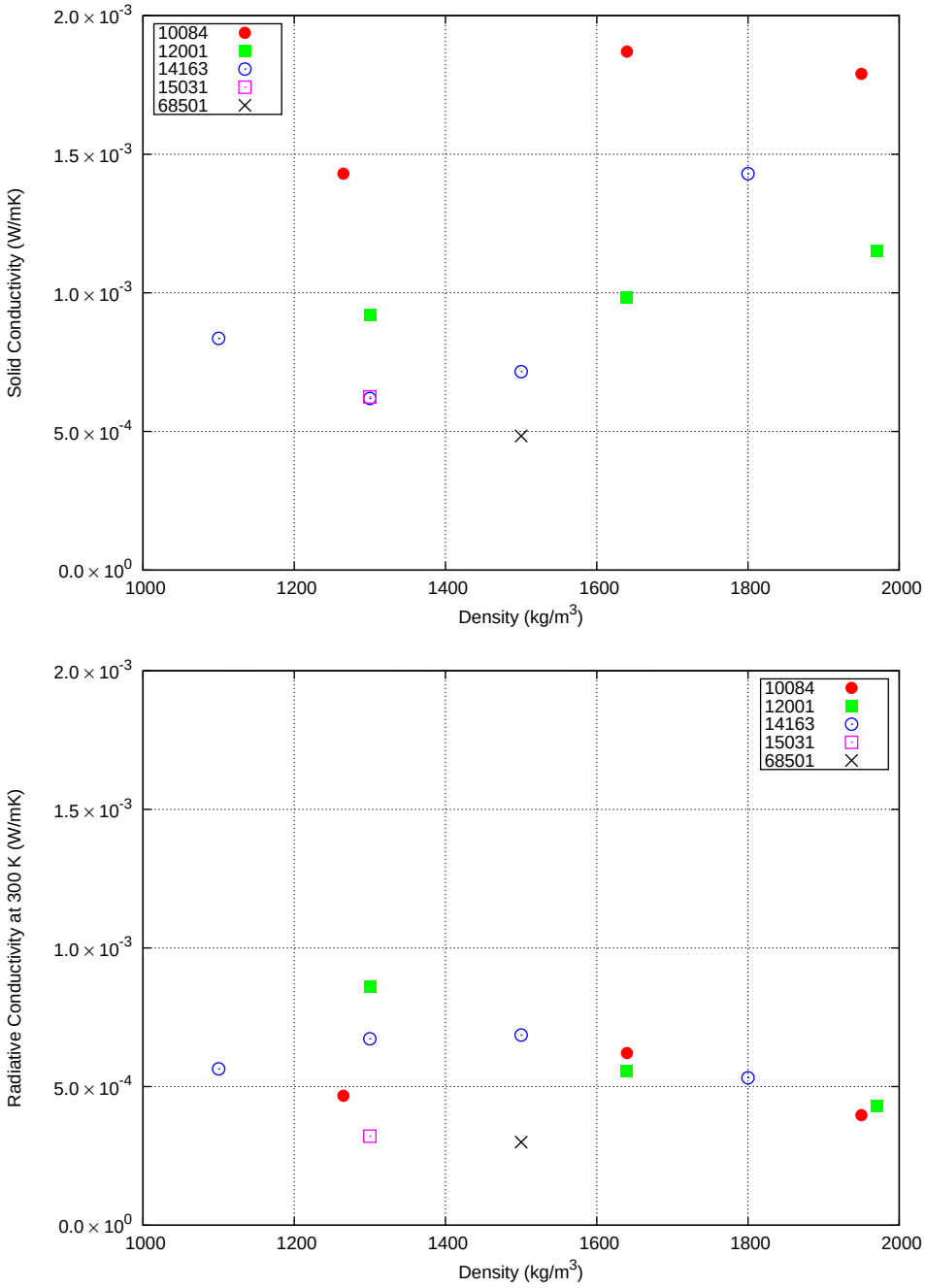

Figure 2.9: The solid (top) and radiative (bottom) conductivity at 300 K for Apollo lunar regolith samples as a function of bulk density (*Cremers et al.*, 1970; *Cremers*, 1971; *Cremers and Birkebak*, 1971; *Cremers*, 1972a,b,c; *Cremers and Hsia*, 1973, 1974; *Cremers*, 1975).

surements of the lunar subsurface regolith (*Langseth et al.*, 1976). This indicated that the rapid increase of the thermal conductivity of the lunar regolith within several tens centimeters depth (Figure 1.6) was essentially caused by the self-weighted compressional stress in the regolith.

Effect of particle size distribution and particle shape

Huetter et al. (2008) measured the thermal conductivity for a mixture of equal volumes of three glass beads with different particle sizes (1.0-1.25, 2.0-2.3, and 3.8-4.3 mm). The thermal conductivity of the mixture was lower than that for the single particle sizes. They stated that the lower thermal conductivity of the mixture would come from the smaller pore size between the particles, which made the radiative conductivity smaller. However, they did not determine the ratio of the solid and radiative contributions, so that their statement had no strong foundation.

Watson (1964) measured the spherical glass beads and crushed glass powders. He observed higher thermal conductivity of the crushed glass than the spherical glass beads. He argued that the irregular shape of the crushed particles provided larger coordination number, which could enhance the solid conductivity. However, the packing density of the crushed sample was twice lower than the spherical sample (Table 2.1). Therefore, his experimental results indicated not only the effect of the particle shape but also the density.

Issues on the previous works

According to the previous works, the thermal conductivity of the silicate powdered materials under vacuum condition varies significantly from 0.0005 to 0.021 W/mK, depending on the materials, the several parameters characterizing the powdered samples, and the temperature. However, integrative understanding on the parameter dependences and the heat transfer mechanism has not been established. For example, the particle size dependence of the thermal conductivity is still be an open question (Figure 2.4), even though the particle size is one of the fundamental parameters for characterizing the powdered materials.

Several methods for the thermal conductivity measurements have been utilized. Because of the less conductive nature of the powdered materials and possible heterogeneity of the packed samples, the measurement methods could also affect the measured values. Steady state methods (e.g. *Watson*, 1964; *Gundlach and Blum*, 2012) measure bulk properties of the samples, but it may not be suited for the thermal insulating materials. On the other hand, transient methods (e.g. *Fountain and West*, 1970; *Krause et al.*, 2011) measure local parts of the samples near the detec-

tor, so that the measurements would be affected by the heterogeneity.

The results by *Horai* (1981) and *Sakatani et al.* (2012) indicates that the depth for the thermal conductivity measurement also affects the thermal conductivity. Since the measurement depth differed by the researchers, the measured thermal conductivities can not be easily compared.

The inconsistency in the experimental results would arise from several factors; different methods for thermal conductivity measurements, packing conditions (e.g. porosity and compressional stress in the samples), or nature of the samples (e.g. particle shapes or microscopic surface roughness). They can be no longer verified. In order to understand the heat transfer mechanism experimentally, a systematic series of the experiments with the same experimental method and condition is absolutely required. Moreover, the determination of the solid and radiative conductivities contributing to the effective thermal conductivity provides key information for examining the conductive and radiative heat transfer mechanisms independently. There were a number of the studies that lacked this information (e.g., *Huetter et al.*, 2008; *Krause et al.*, 2011; *Gundlach and Blum*, 2012).

Chapter 3

Thermal conductivity measurement of powder samples

3.1 Sample selection

3.1.1 List of the measured sample

In order to investigate heat transfer mechanism in powdered media, it is appropriate to use a sample whose parameters, such as particle size and porosity, are well controlled. The samples used in this study are listed in Table 3.1.

Despite regolith simulant, powder samples have narrow ranges of the particle size and spherical shapes. The soda-lime glass beads, manufactured by Fuji Manufacturing Co. Ltd., were used for investigating the dependence on particle size, temperature, compressional stress, particle size distribution, and degree of sintering. These glass beads samples are called FGB glass beads. It is known that fine grains with several μm size can form porous aggregates due to strong adhesive force against the gravitational force. Therefore, the low-alkali glass beads with 5 μm in mean diameter, manufactured by Potters-Ballotini Co. Ltd., was selected in order to examine the porosity dependence of the thermal conductivity. This smallest glass beads sample is called EMB glass beads. The titanium and copper beads, manufactured by Fukuda Metal Foil & Powder Co. Ltd., were used for the effect of composite material. Regolith simulant is the same materials *Horai* (1981) used. According to his paper (*Horai*, 1981), this sample was prepared by Dr. W. D. Carrier, and consists of crashed basalt powders. Its particle size range is comparable with that of Apollo 12 soil samples.

Table 3.1: Samples used in this study.

Sample ID	Material	Particle Size (μm)	Porosity	Packing Method	Experiment Types [1]
FGB-20 [2,3]	Soda-lime Glass Beads	710-1000	0.42	free fall and tapped	A, B, C, H
FGB-40 [2, 3]		355-500	0.42	free fall and tapped	A, B, H
FGB-80 [2, 3]		180-250	0.40	free fall and tapped	A, B, F, H
FGB-180 [2, 3]		90-106	0.42	free fall and tapped	A, B, C, F[4]
FGB-300 [2, 3]		53-63	0.42	free fall and tapped	A, B
EMB-86.2 [2]	Low-alkali Glass Beads	2-10	0.862	free fall through a 53 μm sieve	A, B, D
EMB-77.9 [3]			0.779	free fall through a 53 μm sieve	A, B, D
EMB-75.3 [2]			0.753	free fall through a 500 μm sieve	A, B, D
EMB-69.5 [2]			0.695	free fall through a 53 μm sieve and tapped	A, B, D
EMB-58.5 [3]			0.585	compressed	A, B, D
EMB-49.5 [2]			0.495	compressed	A, B, D
FMF-Ti [2]	Titanium Beads	106-212	0.40	free fall and tapped	E
FMF-Cu [2]	Copper Beads	106-150	0.39	free fall and tapped	E
RS [2]	Regolith Simulant	average 74	0.43	free fall and tapped	B, C, F, G

[1] The sample used for investigating (A) particle size dependence, (B) temperature dependence, (C) compressional stress dependence, (D) porosity dependence, (E) material conductivity dependence, (F) particle size distribution dependence, (G) particle shape dependence (H) neck size ratio dependence during sintering.

[2] The thermal conductivity was measured by 1 point line heat source system using sample container A (see Section 3.2 and Figure 3.3).

[3] The thermal conductivity was measured by 3 point line heat source system using sample container B for investigating the heterogeneity of the thermal conductivity (see Section 3.2 and Figure 3.3).

[4] Since original sample of the FGB-180 has the particle size range wider than the cataloged value (90-106 μm), this sample was sieved again into 90 to 106 μm. Original sample that did not sieved was used only in the experiments for the particle size distribution dependence (F).

Table 3.2: Physical properties of the composite materials used in this study.

Material	FGB glass	EMB glass	Basalt	Titanium	Copper
Thermal conductivity, k_{m} (W/mK)	$8.5\times10^{-4}T+0.855$	$5.1\times10^{-4}T+1.406$	2.5	$1587/T+16.5$	$9784/T+365$
True density ρ_ρ (kg/m^3)	2480	2600	2990	4460	8750
Poisson's Ratio ν	0.23	0.23	0.25	0.32	0.34
Young modulus, E (GPa)	71.6	71.6	78	116	130
Emissivity, ε	0.89	0.89	0.9	0.21	0.28

Table 3.3: Composition of FGB and EMB glass beads (%).

Composition	Soda-lime glass (FGB)	Low-alkali glass (EMB)
SiO_2	70.0-73.0	55.5
$Na_2O + K_2O$	12.0-16.0	0.5
B_2O_3	0.0	5.7
Al_2O_3	1.0-2.5	14.0
CaO	7.0-12.0	23.1
Fe_2O_3	0.05-0.15	0.2
MgO	2.0-5.0	1.0
others	<1.0	0.0

3.1.2 Physical properties of component materials

One of the most fundamental properties for the thermal conductivity of powdered material is the thermal conductivity of the component material (named material thermal conductivity). Material thermal conductivity of glass depends on its composition and temperature (*Ratcliffe*, 1963). In order to determine the thermal conductivity of glass used in this study, the soda-lime FGB glass beads and the low-alkali EMB glass beads were sintered for 24 hours at 1120 K in electrical heating furnace, and thermal conductivity of each sintered glass plate was measured by line heat source method (see Section 3.2) within temperature range from 240 to 360 K. The sintered glass plates had the density of 2480 and 2510 kg/m^3, corresponding to the relative density of 1 and 0.97, for FGB and EMB. The thermal conductivity measurement results are shown in Figure 3.1. The thermal conductivity of the FGB and EMB glass increased with the temperature, which is accepted for glassy materials (*Ratcliffe*, 1963). Linear approximation of the material thermal conductivity k_{m} with the temperature T gives,

$$k_{\mathrm{m}}(T) = 8.50 \times 10^{-4} T + 0.855, \tag{3.1}$$

for the soda-lime FGB glass, and

$$k_{\mathrm{m}}(T) = 5.10 \times 10^{-4} T + 1.406, \tag{3.2}$$

for the low-alkali EMB glass.

Empirical values of the material thermal conductivity were adopted for the other samples. For the regolith simulant, a constant material conductivity of 2.5 W/mK, typical thermal conductivity of basalt rock from *Clauser and Huenges* (1995), is used. Metallic materials has higher thermal conductivity than electrically insulating

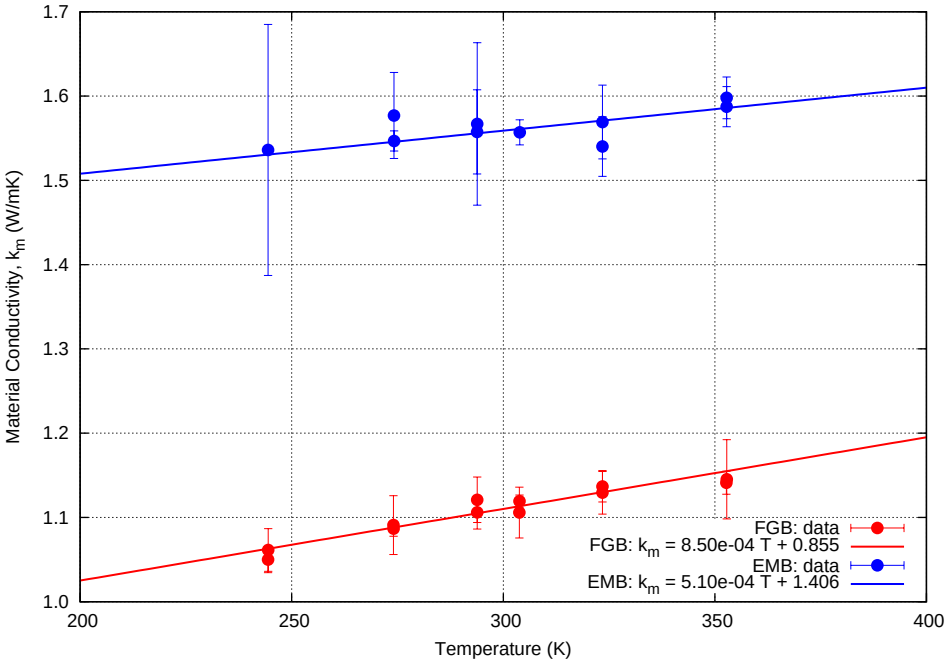

Figure 3.1: Material thermal conductivity of FGB (red) and EMB (blue) glass as a function of temperature. Solid lines represent linear fitting results shown in Equation (3.1) and (3.2)

materials as the glass. It is knwon that thermal conductivity of metals decreases with increasing the temperature. Approximate expressions of the material thermal conductivity are made as $k_{\mathrm{m}} = 1587/T + 16.5$ for the titanium beads, and $k_{\mathrm{m}} = 9784/T + 365$ for the copper beads, cited from *Nagashima et al.* (2008).

Other physical properties are listed in Table 3.2. True density of the particles was measured by using a pycnometer, for FGB glass, titanium, and copper beads and regolith simulant. It could not be measured for EMB glass beads, because of small size of the particles. Poisson's ratio and Young modulus are reference values for each material. Emissivity was measured by emissivity measurement device (A & D AERD, Kyoto Electronics Manufacturing Co. LTD.) on the top surface of the powder beds.

3.2 Method for thermal conductivity measurements

3.2.1 Principle of the line heat source measurement

There are several ways to measure the thermal conductivity (*Presley and Christensen*, 1997a). These methods fall into two broad categories; steady state and non-steady state methods. One of the advantages of the steady state method is ability to

estimate the thermal conductivity of bulk material. For guarded hot plate method (one of the steady state methods), a sample is placed between hot and cold plates, and the thermal conductivity is determined from heat flow thorough the sample, temperature difference between the plates, and sample thickness. *Gundlach and Blum* (2012) applied this method for measuring the thermal conductivity of powdered media under vacuum conditions, by substituting the halogen lamp heating for the hot plate of top surface of the sample. However, it is quite difficult to insulate powder sample because of its low thermal conductivity (the side of the sample needs to be surrounded by lower thermal conductivity material than the sample). Therefore, the steady state method might be inappropriate for measuring the thermal conductivity of low conductive powdered materials.

In non-steady state method, the thermal conductivity of local part in the sample can be measured. The basic idea of this method is heating the sample locally inside the sample or on the surface of the sample, and measuring the time-dependent temperature variation near the heating region. The thermal conductivity is estimated by comparing the temperature data with theoretical or numerical solutions. The method which has been often adopted for powdered materials is so-called line heat source method (*Carslaw and Jaeger*, 1959). The principle of this method is reviewed below.

The line heat source method is based on following assumptions: there is an infinitely thin and long heat source in a sample, heat diffuses into the sample only to radial direction from the line heat source, and the sample has infinite dimensions. The temperature field in the sample is represented by following equation of axisymmetrical heat conduction in circular cylindrical coordinate system,

$$\frac{\partial T}{\partial t} = \frac{\kappa}{r}\frac{\partial}{\partial r}\left(r\frac{\partial T}{\partial r}\right), \tag{3.3}$$

where κ is thermal diffusivity of the sample, T is temperature, and r is distance from the central axis. Initial and boundary conditions are taken as follows;

$$T = 0 \quad \text{for } t = 0 \text{ and } r > 0 \tag{3.4}$$

$$T = 0 \quad \text{for } t > 0 \text{ and } r \to \infty \tag{3.5}$$

$$-2\pi r k\frac{\partial T}{\partial t} = q \quad \text{for } t > 0 \text{ and } r \to 0 \tag{3.6}$$

where q is heat generation per unit length of the heat source. The first condition represents thermal equilibrium at $t = 0$, the second represents no heat flow infinitely far from the source, and the last represents heat conduction from the line heat source.

With these initial and boundary conditions, solution of Equation (3.3) becomes,

$$T = \frac{-q}{4\pi k}\left(\gamma + \ln\frac{r^2}{4\kappa t} - \frac{r^2}{4\kappa t} + \frac{r^4}{64\kappa^2 t^2} + \cdots\right), \tag{3.7}$$

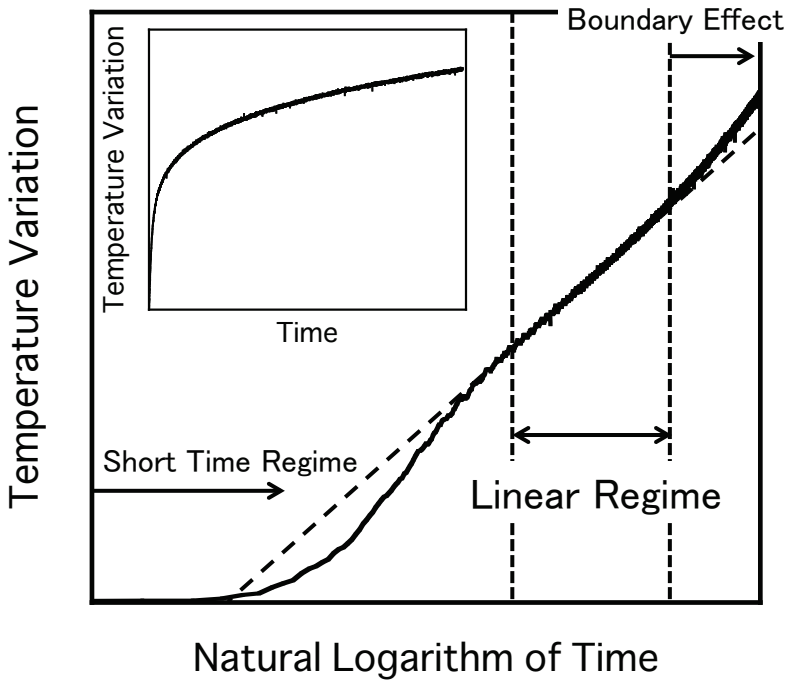

Figure 3.2: Typical temperature data as a function of natural logarithm of time during the line heat source measurement. Upper left legend shows temperature variation as a function of time.

where $\gamma = 0.577$ is the Euler constant. If $r^2/4\kappa t \ll 1$, Equation (3.7) reduces to

$$T = \frac{-q}{4\pi k}\left(\gamma + \ln\frac{r^2}{4\kappa t}\right). \tag{3.8}$$

If temperature T_1 and T_2 are measured at a point r at different times t_1 and t_2, respectively, one can obtain the following equation using Equation(3.8),

$$T_2 - T_1 = \frac{q}{4\pi k}\ln\frac{t_2}{t_1}. \tag{3.9}$$

Equation (3.9) implies that if the change of temperature at r is plotted as a function of the natural logarithm of the time, a straight line with the slope of $q/4\pi k$ can be observed.

In practice, however, a heating wire with finite diameter and length is used as the line heat source, the sample has finite dimensions, and there is thermal resistance between the heat source and the sample. Therefore, the experimental configuration somewhat differs from the ideal line heat source. Because of this discrepancy, the temperature typically yields an S-shaped curve as shown in Figure 3.2. This figure shows the temperature of the heating wire as a function of the logarithm of the heating time. In the short-time regime, the temperature of the heater increases rapidly,

which is mainly attributed to thermal resistance between the heating wire and the surrounding sample (*Blackwell*, 1954). Nevertheless, after sufficiently long heating time, the linear relation as in Equation (3.9) can be found. In this linear regime, the temperature can be written as

$$\Delta T = \frac{q}{4\pi k} \ln t + c_0, \tag{3.10}$$

where ΔT is temperature rise and c_0 is a constant. The thermal conductivity can be determined from the slope of the linear regime, s, if the heat generation q is known, as

$$k = \frac{q}{4\pi s}. \tag{3.11}$$

If the heating continues more, the relation between the temperature and time begins to deviate from the linear relation. This means that the heat from the heater gets to the inner wall of the sample container or top surface of the sample. Therefore, to determine the thermal conductivity, time range of the linear regime needs to be constrained. For this purpose, several analytical studies can be found in the literature, which are summarized by *Presley and Christensen* (1997a).

The time until the short-time regime ends, in other words, the linear regime appears, can be roughly estimated as follows, (*Jones*, 1988).

$$t \gg \frac{50{b_\mathrm{t}}^2}{\kappa}, \tag{3.12}$$

where t is heating time, κ is thermal diffusivity of the sample, and b_t is distance between the heat source and a temperature measurement point. The axial heat transfer can occur due to finite diameter and length of the line heater. This effect can be neglected if the following equation is satisfied (*Blackwell*, 1954).

$$t < \frac{0.0632{L_\mathrm{h}}^2}{\kappa}, \tag{3.13}$$

where L_h is length of the line heater. Finite volume of the sample causes the heat absorption or reflection at the sample boundary if the heating time is too long. When the following equation is satisfied, the effect of the sample boundary is negligible (*Andersson and Bäckström*, 1976).

$$t < \frac{0.25{R_\mathrm{s}}^2}{\kappa}, \tag{3.14}$$

where R_s is radial extent of the sample from the heater. The linear regime can be found when Equations (3.12) to (3.14) are satisfied.

3.2.2 Measurement system and error analysis

In this study, two types of the sample containers to measure the thermal conductivity by the line heat source method were prepared. Only difference between these containers is the number of the line heat source sensors in the container. In the sample container A (Figure 3.3a), single line heat source sensor consisting of a nichrome wire of 180 μm in diameter and a K-type thermocouple (alumel and chromel wires have diameter of 50 μm) is mounted. The thermocouple is fixed by glue at the mid-length point of the nichrome wire, by which the temperature of the nichrome wire was directly measured. Using this container, the thermal conductivity for all samples was determined (see below). Note that the line heat source method measures the conductivity locally around the heat source. Therefore, the measured value is affected by the local heterogeneity of packing arrangement of the particles. To investigate the resulting heterogeneity of the thermal conductivity, a sample container B (Figure 3.3b) with three line heat source sensors was used. The distance between the sensors of 2 cm is sufficiently larger than the heat transfer distance during the measurement (see below), and therefore, they do not interfere with each other.

Overview of the measurement system is shown in Figure 3.4. During the measurement, constant current is induced to the nichrome wire with a power supply device (ADCMT 6242). The heat generation per unit length along the nichrome wire is calculated by,

$$q = I^2 R_{\mathrm{h}}, \tag{3.15}$$

where I is induced constant current and R_{h} is electrical resistance per unit length. The thermocouple wires are connected to a zero degC standard device (ZEROCON, Coper Electronics Co.), as a reference temperature point of the thermocouple. A digital multimeter (Keithley 2002) measured the output voltage, from which the temperature of the nichrome wire was determined.

The appropriate linear fitting regime for this experimental system can be constrained by the following manner. The distance between the heat source and the temperature measurement point, b_{t} in Equation (3.12), corresponds to the radius of the nichrome wire, 9×10^{-5} m, because surface temperature of the nichrome wire was directly measured by the thermocouple. The length of the nichrome heater, L_{h} in Equation (3.13), is 0.08 m at the minimum. The radial distant of the sample, R_{s} in Equation (3.14), is nominally 0.01 m. The thermal diffusivity κ is unknown parameter. According to previous experimental studies, the thermal conductivity of the powder materials under vacuum conditions would be roughly from 10^{-3} to 10^{-2} W/mK. Given that the product of the bulk density and the specific heat is 10^6 J/m^{3}K, one can roughly estimate the thermal diffusivity between 10^{-9} to 10^{-8} m^2/s. Figure 3.5 shows plots of Equation (3.12), (3.13), and (3.14) as a function

(a) Sample container A

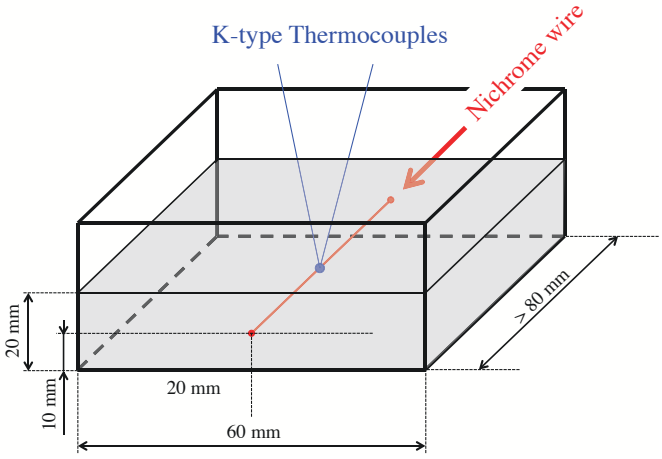

(b) Sample container B

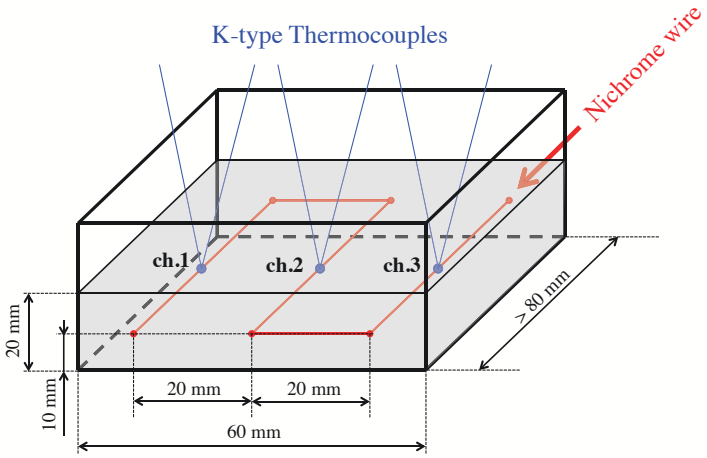

Figure 3.3: Sample containers for the thermal conductivity measurements with single line heat source sensor (container A, top) and three sensors (container B, bottom).

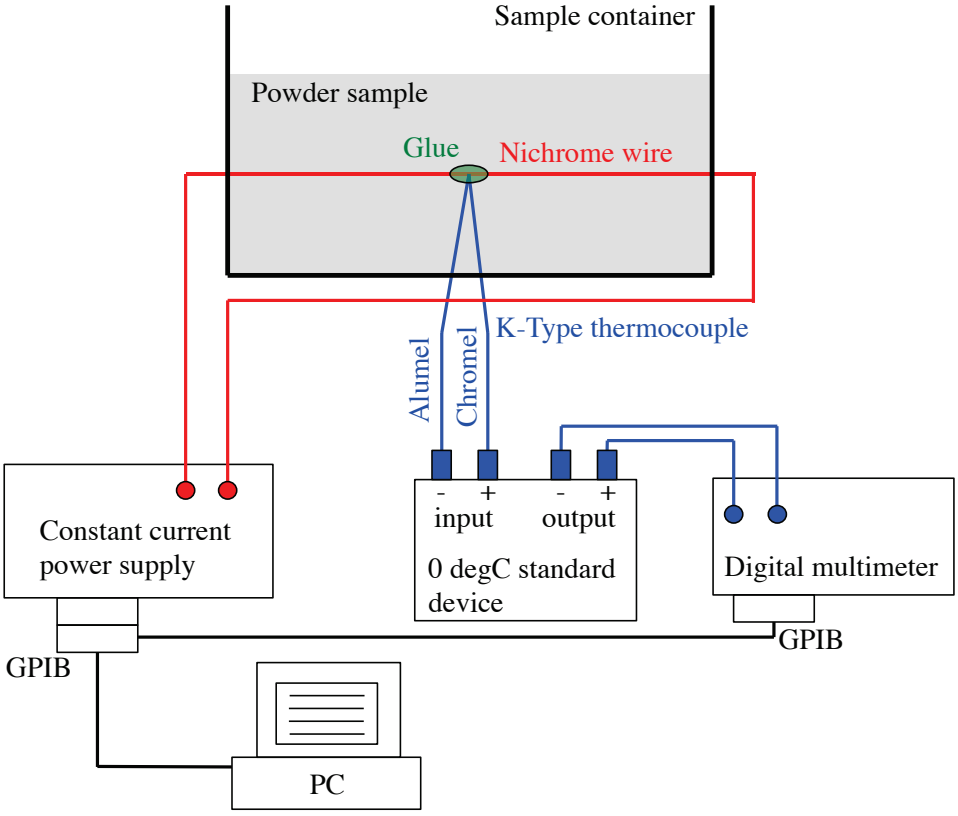

Figure 3.4: Overview of thermal conductivity measurement system.

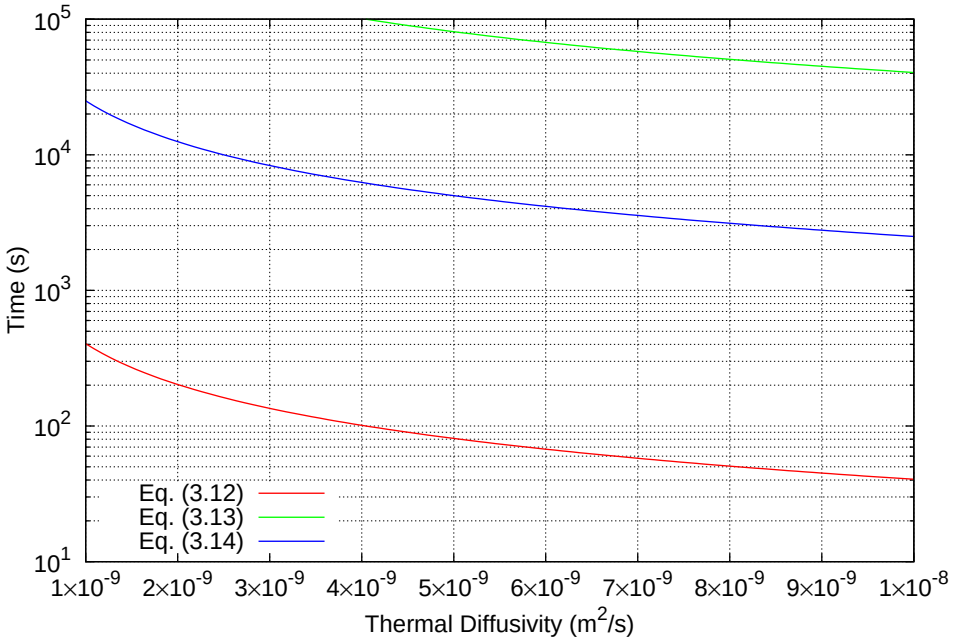

Figure 3.5: Constriction of time range of the linear regime in line heat source method. The time reduced from Equation (3.12) to (3.14) are drawn as a function of thermal diffusivity. The time range above the red curve and below the green or blue curves is appropriate.

of the thermal diffusivity. The linear regime would appear when the time is longer than that given by red curve (Eq. 3.12). It would be disturbed due to axial heat loss through the nichrome wire or sample boundary effect, when the time is longer than green or blue curves (Eq. 3.13 or 3.14). Then, the linear regime can be found above the red curve and below green or blue curves in Figure 3.5. From these estimates, the linear fitting regime was nominally fixed between 400 to 1000 seconds.

A protocol of the measurement error estimation for the line heat source method was summarized by *Presley and Christensen* (1997b). The thermal conductivity can be calculated from Equations (3.11) and (3.15) as,

$$k = \frac{I^2 R_\mathrm{h}}{4\pi s}. \tag{3.16}$$

If all human errors are assumed to be random, the propagation of the error can be written as,

$$\delta k \approx \frac{\partial k}{\partial I}\delta I + \frac{\partial k}{\partial R_\mathrm{h}}\delta R_\mathrm{h} + \frac{\partial k}{\partial s}\delta s. \tag{3.17}$$

Using Equation (3.16), then the relative error is,

$$\frac{\delta k}{k} = \sqrt{\left(2\frac{\delta I}{I}\right)^2 + \left(\frac{\delta R_\mathrm{h}}{R_\mathrm{h}}\right)^2 + \left(\frac{\delta s}{s}\right)^2}, \tag{3.18}$$

and the maximum relative error is,

$$\frac{\delta k}{k} = 2\left|\frac{\delta I}{I}\right| + \left|\frac{\delta R_{\mathrm{h}}}{R_{\mathrm{h}}}\right| + \left|\frac{\delta s}{s}\right|. \tag{3.19}$$

The uncertainty of the induced current comes from accuracy of the current source device. The relative error of the induced current is 0.05% from a catalog value.

The error in resistance R_{h} of the nichrome wire is divided into two sources. One is the measurement uncertainty of the resistance. The electrical resistance per unit length was estimated by linear slope of the measured resistance as a function of the length. The result for 180 μm nichrome wire used in the experiments at room temperature about 25 degC is shown in Figure 3.6. A slope of the fitting line represents the R_{h} value. The fitting error can be taken as the uncertainty of the resistance measurement. From Figure 3.6, the resistance per unit length of the 180 μm nichrome wire R_{h} is 42.35 (Ω/m), and its measurement error $(\delta R_{\mathrm{h}}/R_{\mathrm{h}})_{\mathrm{measure}}$ is 0.24%. The other source of the resistance error comes from temperature dependence of the resistance, since the temperature of the nichrome wire varies during the thermal conductivity measurements, although it was typically less than 5 K. The relation between the resistance and the temperature can be written as,

$$R_{\mathrm{h}}(T) = R_{\mathrm{h0}}[1 + \beta(T - T_0)], \tag{3.20}$$

where T is the temperature, R_{h0} is the resistance at a standard temperature T_0, and β is temperature coefficient of the resistance. The value of β was estimated experimentally. The resistance of the nichrome wire was measured with temperature sweeping from 360 K to 240 K at the temperature decreasing rate of 10 K/h in a thermostatic chamber. The temperature of the nichrome wire was measured by a thermocouple. Figure 3.7 shows the relation between the temperature variation $(T - T_0)$ and relative resistance difference $((R_{\mathrm{h}} - R_{\mathrm{h0}})/R_{\mathrm{h0}})$. The slope found in this plot is corresponds to β. Then, $\beta = 9 \times 10^{-5}$ was obtained. The relative resistance error due to the temperature variation can be estimated as,

$$\left(\frac{\delta R_{\mathrm{h}}}{R_{\mathrm{h}}}\right)_{\mathrm{temp}} = \beta \Delta T, \tag{3.21}$$

where ΔT is temperature variation during the measurement. Then, the error in the electrical resistance per unit length can be expressed as,

$$\frac{\delta R_{\mathrm{h}}}{R_{\mathrm{h}}} = \left(\frac{\delta R_{\mathrm{h}}}{R_{\mathrm{h}}}\right)_{\mathrm{measure}} + \left(\frac{\delta R_{\mathrm{h}}}{R_{\mathrm{h}}}\right)_{\mathrm{temp}}. \tag{3.22}$$

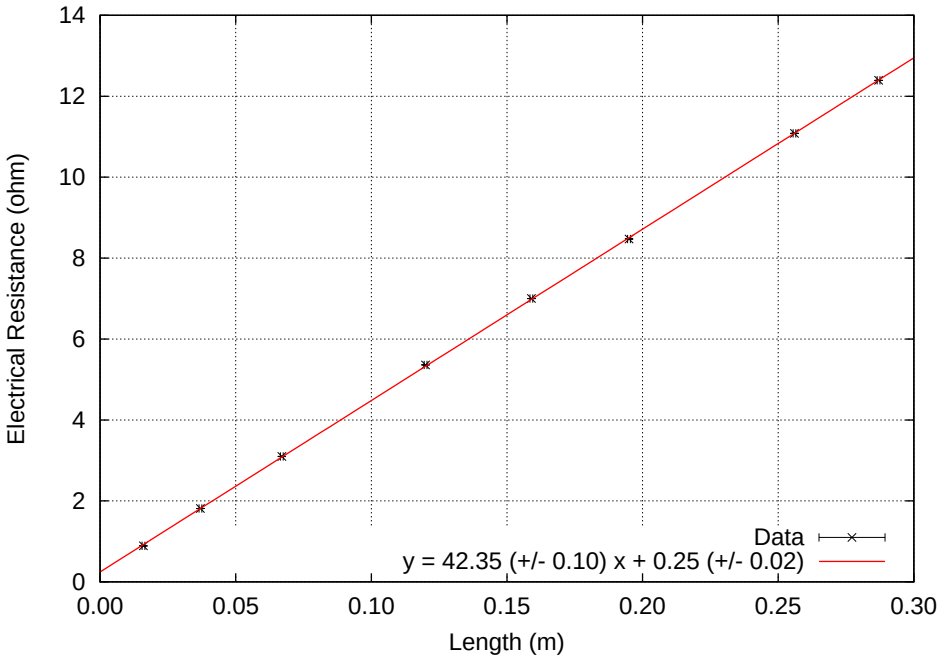

Figure 3.6: A result of electrical resistance measurement of nichrome wire (180 μm in diameter) at ambient temperature of 25 degC.

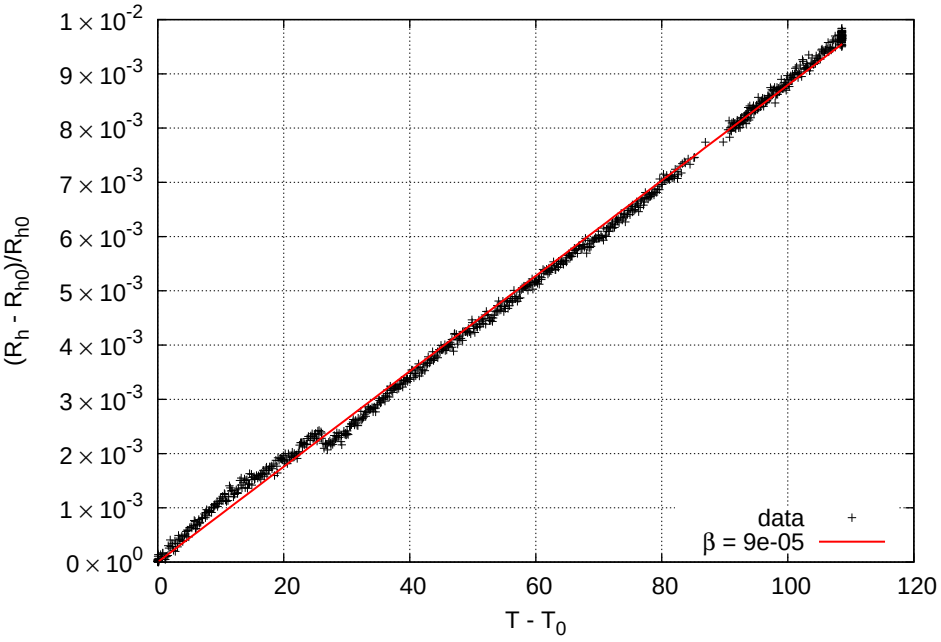

Figure 3.7: Effect of temperature on the electrical resistance of the nichrome wire (180 μm in diameter). The length of the nichrome wire was 29 cm. The standard resistance and temperature were chosen as $R_{h0} = 12.379$ Ω/m and $T_0 = 244$ K (see Equation 3.20).

The uncertainty in the slope s has two sources. One is the deviation of the data from a straight line. The other is how well the linear regime of the curve of temperature versus natural logarithm of time is resolved. The former can be evaluated from the fitting error of the slope, $(\delta s/s)_{\text{fitting}}$. The later is more difficult to quantify. *Presley and Christensen* (1997b) suggested a way to verify this error. That is to divide the linear regime of the curve into smaller segments and compare the resulting slopes with the original one. Here, each of the linear regime was divided into three equal segments by time. Then, the error can be evaluated as,

$$\left(\frac{\delta s}{s}\right)_{\text{segment}} = \frac{1}{3}\left|\sum_{n=1}^{3}\frac{s_{\text{n}}-s}{s}\right|, \tag{3.23}$$

where s is the original slope and s_{n} (n = 1, 2, 3) is the slope of the each segment. For nominal case, the original slope is taken from the linear fitting between 400 and 1000 seconds, and slope of the each segment s_{n} is that of 400-600, 600-800, and 800-1000 seconds. Then, the total error in the slope is taken as the sum of the two errors,

$$\frac{\delta s}{s} = \left(\frac{\delta s}{s}\right)_{\text{fitting}} + \left(\frac{\delta s}{s}\right)_{\text{segment}}. \tag{3.24}$$

The protocol for the thermal conductivity and its error determinations are demonstrated below. As an example data, Figure 3.8 shows temperature data during the measurement of 90-106 μm glass beads at the temperature about 25 degC. This data was obtained when the constant current of 0.02 A was induced to the nichrome wire of 180 μm in diameter, using the sample container A. The sequence of the data analysis is divided by following steps.

1. Determination of original slope.

   The following equation (compared with Equation 3.10) is fitted to the temperature data for time range between 400 to 1000 seconds.

   $$\Delta T = s\ln t + c, \tag{3.25}$$

   The value of slope s and its error are determined. For this example case, $s = 0.600$ and $(\delta s/s)_{\text{fitting}} = 0.08\%$ were obtained.

2. Determination of nichrome wire resistance at initial temperature.

   Since the thermal conductivity measurement are conducted at several temperatures, the electrical resistance per unit length of the nichrome wire at the beginning of the measurement differs from that at room temperature ($R_{\text{h}} = 42.35$ Ω/m). Using Equation (3.20) and giving $R_{\text{h0}} = 42.35$ Ω/m at $T_0 = 25$ degC,

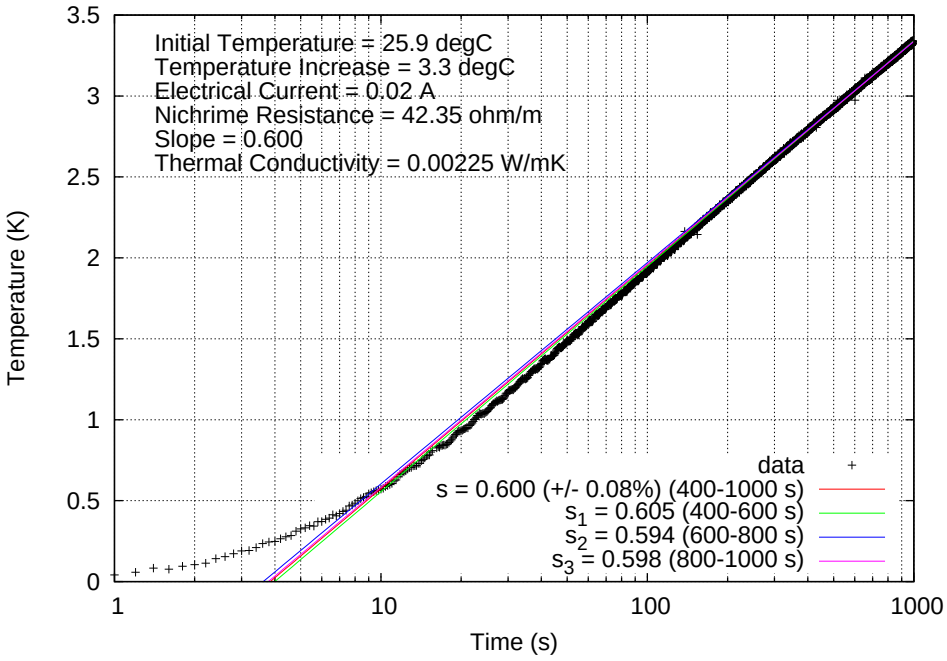

Figure 3.8: An example data of temperature variation of the nichrome wire during the line heat source measurement. A current of 0.02 A was induced to the nichrome wire of 180 μm in diameter. The vertical axis represents the temperature increase from initial temperature. Data processing method is shown in the text.

the resistance is corrected to that at the initial temperature. In Figure 3.8, the initial resistance of the nichrome wire remained $R_{h0} = 42.35$ Ω/m, because the initial temperature of this measurement was 25.9 degC.

3. Calculating the thermal conductivity of sample.

   The thermal conductivity is calculated from Equation (3.16), using the value of nominal slope s, resistance of the nichrome wire at the initial temperature R_h, and induced electrical current I. For the case of this example, $s = 0.600$, $R_h = 42.35$ Ω/m, and $I = 0.02$ A, then the thermal conductivity of $k = 0.00225$ W/mK can be derived.

4. Evaluation of the error in the resistance.

   From the temperature at the beginning and end of the measurements, the resistance error due to temperature variation during the measurements is determined from Equation (3.21). The temperature increase of 3.3 degC caused the error of $(\delta R_h/R_h)_{temp} = 0.03\%$. Then, the total error of the nichrome wire resistance can be calculated from Equation (3.22), as $\delta R_h/R_h = 0.24 + 0.03 = 0.27\%$.

5. Determinations of slopes of small segments and error in the slope value.

   The linear regime is divided into three small segments (400-600, 600-800, and 800-1000 s), and the slopes of these segments s_n (n = 1, 2, 3) were determined by the fitting of Equation (3.25). Then, the slope error relative to the original slope is calculated from Equation (3.23). For the case shown in Figure 3.8, $s_1 = 0.605$, $s_2 = 0.594$, $s_2 = 0.598$, and then, $(\delta s/s)_{segment} = 0.17\%$. The total error in the slope was estimated from Equation (3.24), as $\delta s/s = 0.08 + 0.17 = 0.25\%$.

6. Evaluation of the relative error in measured thermal conductivity.

   Using the error in I, R_h, and s, the error in the resulting thermal conductivity is reduced from Equation (3.19), as,

$$\frac{\delta k}{k} = 2 \times 0.05 + 0.27 + 0.25 = 0.62\%. \tag{3.26}$$

According to this protocol, the thermal conductivity and its error were determined for all data. In the most cases, the maximum error source was $(\delta s/s)_{segment}$.

3.2.3 Protocol for derivation of solid and radiative conductivity

As mentioned in Chapter 2, the thermal conductivity of powdered materials under vacuum contains two contribution of different heat transfer mechanisms; solid conduction through the contact area and thermal radiation between the particle surfaces through the voids. Both contributions depend on several parameters. To understand the heat transfer mechanism and the parameter dependences, the solid and radiative conductivities should be derived from the measured effective thermal conductivity.

Separation of the thermal conductivity into these conductivities was accomplished using temperature-dependent data by the similar method by *Merrill* (1969). In previous studies (e.g. *Merrill*, 1969; *Fountain and West*, 1970; *Cremers et al.*, 1970), it has been assumed that the temperature dependence of the effective thermal conductivity arises from only the radiative conductivity, which is proportional to the temperature cubic. This assumption is approximately approved when the solid conductivity is comparable with or less than the radiative conductivity. In this study, this method is modified by additinally including the temperature dependence of the solid conductivity. The solid conductivity is theoretically proportional to the material thermal conductivity $k_{\mathrm{m}}(T)$. Therefore, the effective thermal conductivity can be written as,

$$k = k_{\mathrm{solid}} + k_{\mathrm{rad}} = Ak_{\mathrm{m}}(T) + BT^3, \tag{3.27}$$

where A and B are solid and radiative coefficients, respectively, which depends on the several parameters other than the temperature. Note that the coefficient A in the following part of this thesis is dimensionless, and differs from a coefficient A appeared in Watson's Equation (2.13).

To determine the values of A and B for all samples listed in Table 3.1, the thermal conductivity was measured as a function of the temperature. For example, Figure 3.9 shows the temperature-dependent thermal conductivity data for EMB-49.5 glass beads (see also Section 3.4). By fitting Equation (3.27) to the data, the values of A and B appropriate for this sample are obtained. If constant material thermal conductivity of 1.56 W/mK (estimated from Equation 3.2) is used, $A = 0.0120$ and $B = 6.56 \times 10^{-11}$ W/mK^4 are obtained, which correspond to $k_{\mathrm{solid}} = 0.0187$ W/mK and $k_{\mathrm{rad}} = 0.0018$ W/mK at temperature of 300 K. On the other hand, when including the temperature dependence of the material thermal conductivity as Equation (3.2), the solid and radiative coefficients are revised to $A = 0.0124$ and $B = 4.28 \times 10^{-11}$ W/mK^4, corresponding to $k_{\mathrm{solid}} = 0.0193$ W/mK and $k_{\mathrm{rad}} = 0.0012$ W/mK at 300 K. Because the thermal conductivity of the glassy material increases with the temperature, the radiative conductivity is revised downward by including the temperature dependence of the solid conductivity.

The solid and radiative coefficients are deduced from the temperature-dependent

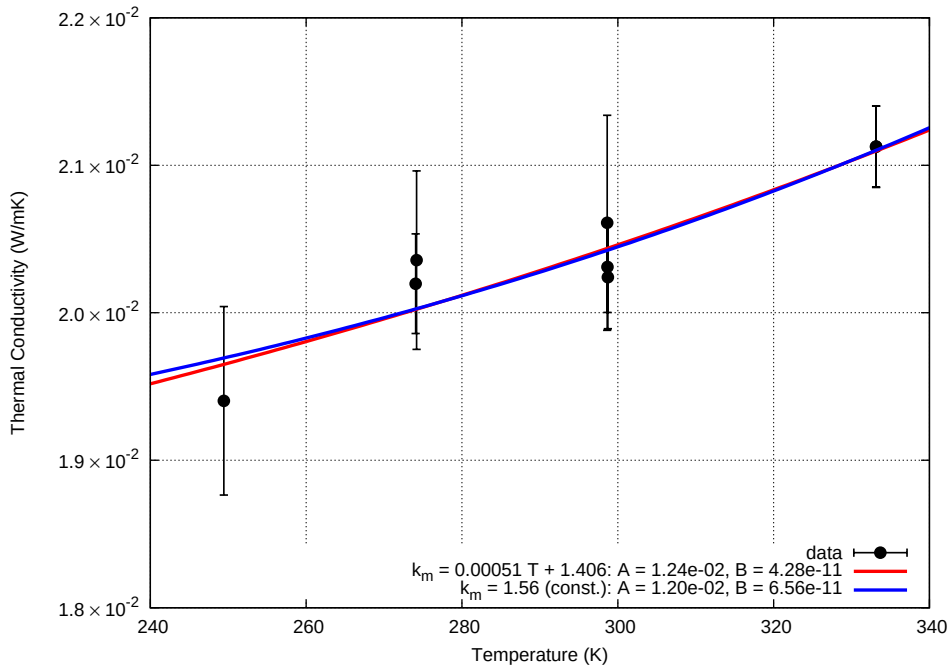

Figure 3.9: Temperature dependence of the thermal conductivity of EMB-49.5 sample and fitting results of Equation (3.27). A red curve represents a fitting result using temperature-dependent material conductivity of $k_{\mathrm{m}} = 5.1 \times 10^{-4} T + 1.406$ W/mK (Equation 3.2). A blue curve shows that using constant material conductivity of $k_{\mathrm{m}} = 1.56$ W/mK, which is calculated at 300 K from Equation (3.2).

thermal conductivity for all samples. The parameter dependences of the conductive and radiative contributions are investigated in subsequent sections.

3.3 Particle size dependence

3.3.1 Experimental method

In order to investigate the particle size dependence of the solid and radiative conductivities, five FGB glass beads (Table 3.1) were measured as a function of the temperature. Figure 3.10 shows the experimental setup. It is important for the line heat source method that there is little temperature gradient within the sample and along the heater line before the measurements. In the experiments in this study, a vacuum chamber was emplaced in a thermostatic chamber, by which the temperature can be controlled and maintained uniformly over the system. The use of the thermostatic chamber enables us to control temperature from low to high temperature without installation of heater and cooler units. The controllable temperature range was beween -25 and 60 degC, which was restricted by operating temperature of silicon and Viton O-ring and of the acrylic sample container.

Each FGB sample was filled in the sample container and tapped. The height of the packed sample was 2 cm above the bottom of the container, or 1 cm above the line heat source sensor. The density and porosity of the sample was estimated from volume and mass of the packed sample. The sample was evacuated by a rotary and turbo molecular pumps down to about 10^{-2} Pa. At the same time, the temperature of the system was raised up to 50 degC or 60 degC (the maximum temperature differed by the measurements). After the temperature equilibrium in the sample, which took typically 2 days, the constant electric current of 20 mA was induced to the nichrome wire and its temperature was recorded for 1000 s. Then the thermal conductivity of the sample and its measurement error were determined by the method described in Section 3.2. After the measurements at maximum temperature, the same procedure was repeated at several lower temperatures down to -25 degC.

To investigate the homogeneity of the measured thermal conductivity of the FGB glass beads, the sample container B was also used (Figure 3.3b).

3.3.2 Results

First, the measurement results by the sample container A are shown. Thermal conductivity of the FGB glass beads at about 25 degC is shown in Figure 3.11. The effective thermal conductivity increased with the particle size. Figure 3.12 shows the thermal conductivity as a function of the temperature. The extraction of the solid and radiative coefficients from these data was addressed, by the method described in Section 3.2. Curves in Figure 3.12 show weighted least-square fitting results of Equation (3.27). The material thermal conductivity k_{m} for FGB glass beads is given by Equation (3.1). Table 3.4 shows the best fitting values and errors of A and B.

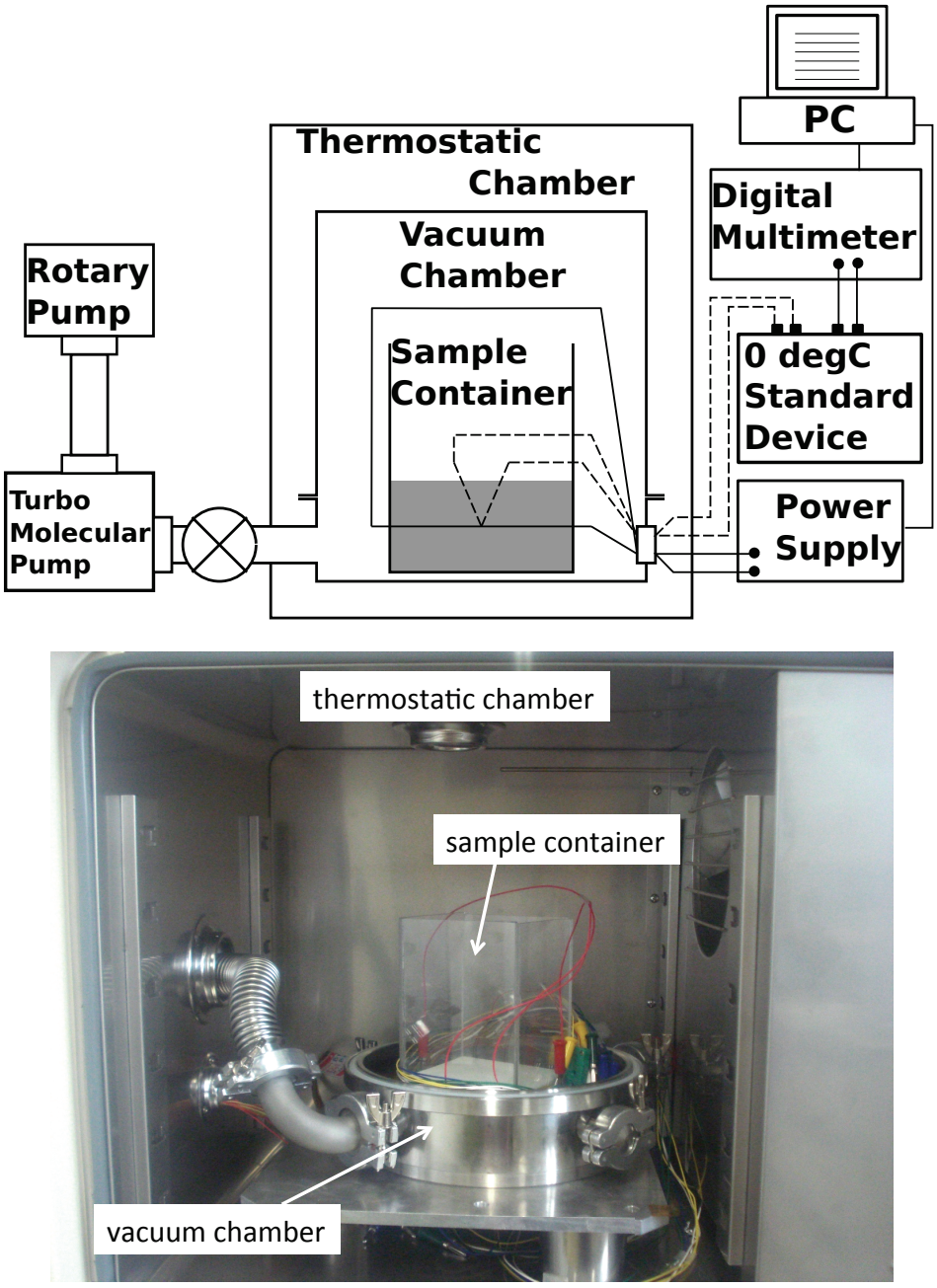

Figure 3.10: Experimental configuration for thermal conductivity measurements of powdered materials under vacuum condition at variable temperature.

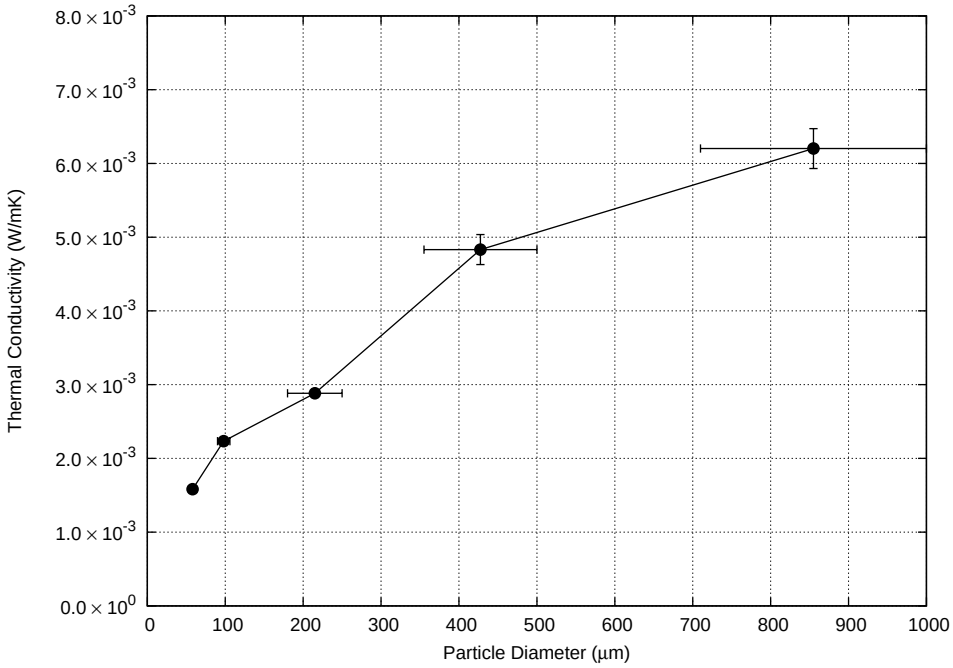

Figure 3.11: Thermal conductivity of five kinds of FGB glass beads at temperature around 25 degC as a function of particle diameter. These data were obtained using the sample container A.

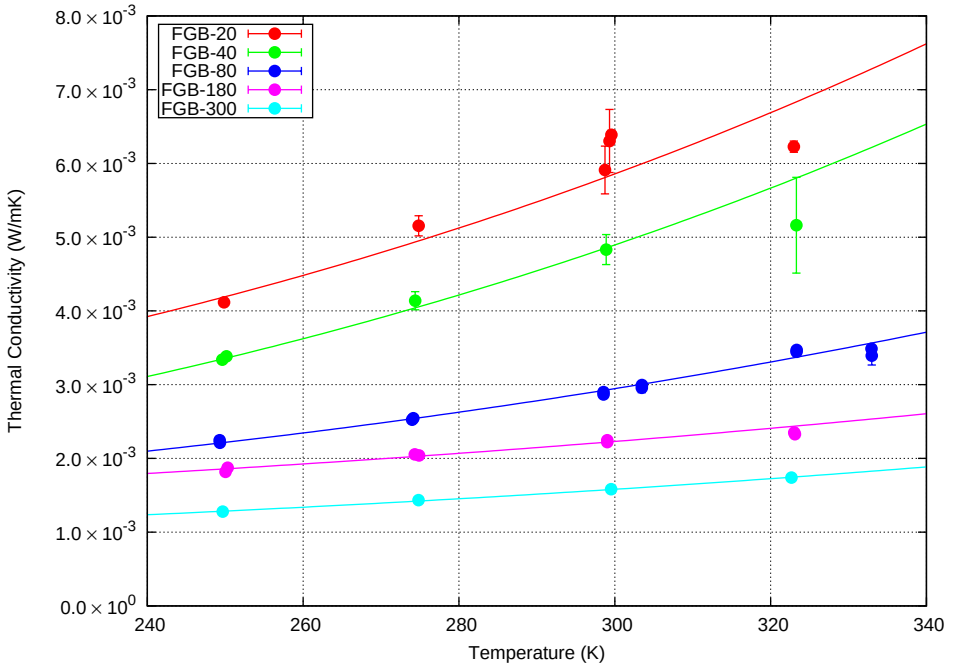

Figure 3.12: Temperature dependence of the thermal conductivity of FGB glass beads using the sample container A. Each curve represents the fitting curve of Equation (3.27).

Table 3.4: Solid and radiative coefficients in Equation (3.27) for FGB glass beads.

Sample	Particle diameter (μm)	Container	Solid coefficient A ($\times 10^{-3}$)	Radiative coefficient B ($\times 10^{-11}$ W/mK^4)
FGB-20	710-1000	A	1.89 ± 0.51	13.9 ± 2.62
		B-ch.1	1.78 ± 0.28	13.2 ± 1.54
		B-ch.2	2.56 ± 0.53	9.90 ± 2.37
		B-ch.3	1.00 ± 0.41	16.1 ± 1.78
FGB-40	355-500	A	1.23 ± 0.18	13.1 ± 1.21
		B-ch.1	0.91 ± 0.07	9.53 ± 0.29
		B-ch.2	1.19 ± 0.06	8.69 ± 0.27
		B-ch.3	2.00 ± 0.22	7.27 ± 0.83
FGB-80	180-250	A	1.21 ± 0.04	5.93 ± 0.20
		B-ch.1	1.11 ± 0.18	5.24 ± 0.83
		B-ch.2	1.34 ± 0.15	4.16 ± 0.57
		B-ch.3	1.42 ± 0.10	5.09 ± 0.52
FGB-180	90-106	A	1.34 ± 0.05	2.76 ± 0.27
		B-ch.1	1.17 ± 0.01	3.67 ± 0.31
		B-ch.2	1.12 ± 0.01	3.54 ± 0.06
		B-ch.3	1.10 ± 0.02	3.98 ± 0.10
FGB-300	53-63	A	0.88 ± 0.02	2.26 ± 0.10
		B-ch.1	0.88 ± 0.03	2.87 ± 0.15
		B-ch.2	0.90 ± 0.04	2.89 ± 0.21
		B-ch.3	1.00 ± 0.04	3.68 ± 0.17

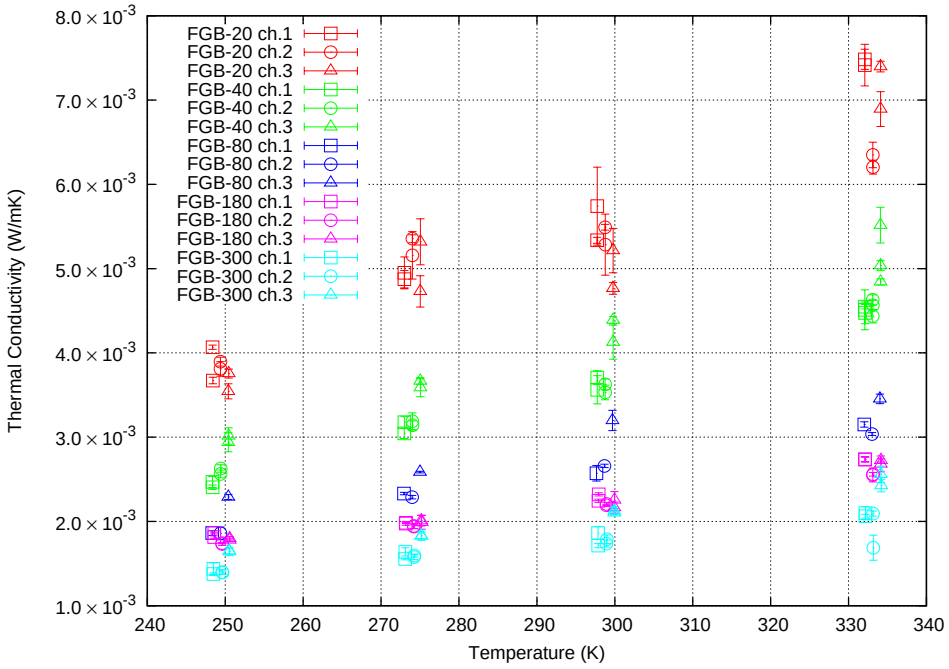

Figure 3.13: Measurement results using container B (Figure 3.3b). Squares, circles, and triangles represent the measurements at ch.1, 2, and 3, respectively. For visualization, data of ch.1 are slided horizontally by -1 K, and for ch.3 by $+1$ K.

Figure 3.13 shows the thermal conductivity of the five FGB glass beads measured with the container B. The measured thermal conductivities by the three line heat source sensors differed by 0.0013 W/mK at maximum. The difference seems to be larger for glass beads with larger particle size. According to Equation (3.14), typical length scale affecting the thermal conductivity measurement by the line heat source measurements for the 1000 seconds heating is from 2 to 5 mm depending on the measured thermal conductivity. Therefore, local heterogeneity, whose typical scale was comparable with the particle size, was likely to affect the heat transfer for the larger beads. The solid and radiative coefficients determined from the measurements in the sample container B are also listed in Table 3.4.

The solid and radiative conductivities at 300 K for the FGB glass beads are plotted in Figure 3.15,. These conductivities are calculated from $k_{\mathrm{solid}} = Ak_{\mathrm{m}}(T)$ and $k_{\mathrm{rad}} = BT^3$ using A and B values in Table 3.4. The mean values in the four measurements are plotted taking lower and higher limits of the vertical errorbars as minimum and maximum values, respectively. Figure 3.15 shows that the radiative conductivity of the powdered materials increases with the particle size and the solid conductivity also increases slightly. The increase in the effective thermal conductivity, as shown in Figure 3.11, was attributed primarily to enhancement of the

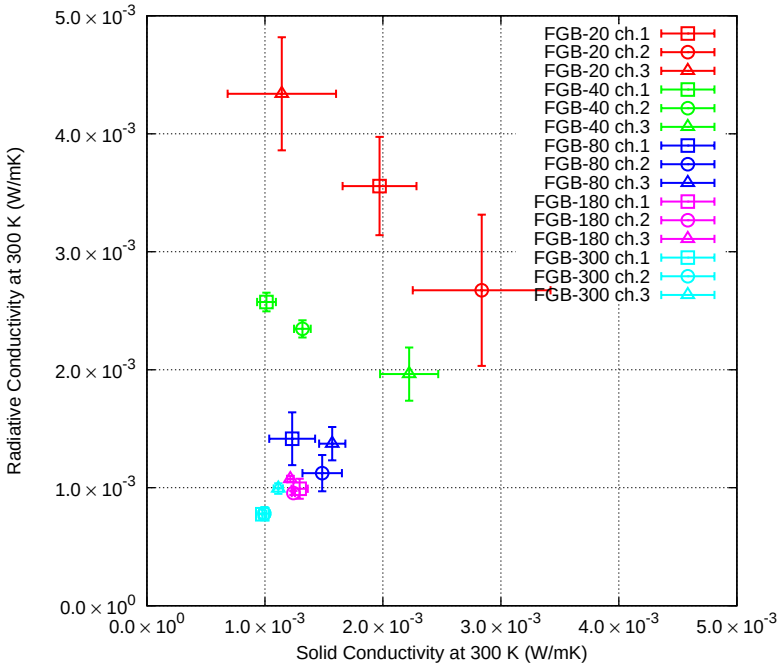

Figure 3.14: Correlation between the solid and radiative conductivity at 300 K measured in the sample container B.

radiative conductivity.

In Figure 3.16, the experimental results in this study are compared with the previous works on the thermal conductivity of glass or SiO_2 beads. The thermal conductivity of the FGB glass beads is higher than that of *Merrill* (1969) and *Wechsler and Simon* (1966), and lower than *Wechsler and Glaser* (1965), *Huetter and Koemle* (2008), and *Gundlach and Blum* (2012). The positive correlation between the effective conductivity and the particle size is consistent with *Wechsler and Glaser* (1965) and *Huetter et al.* (2008).

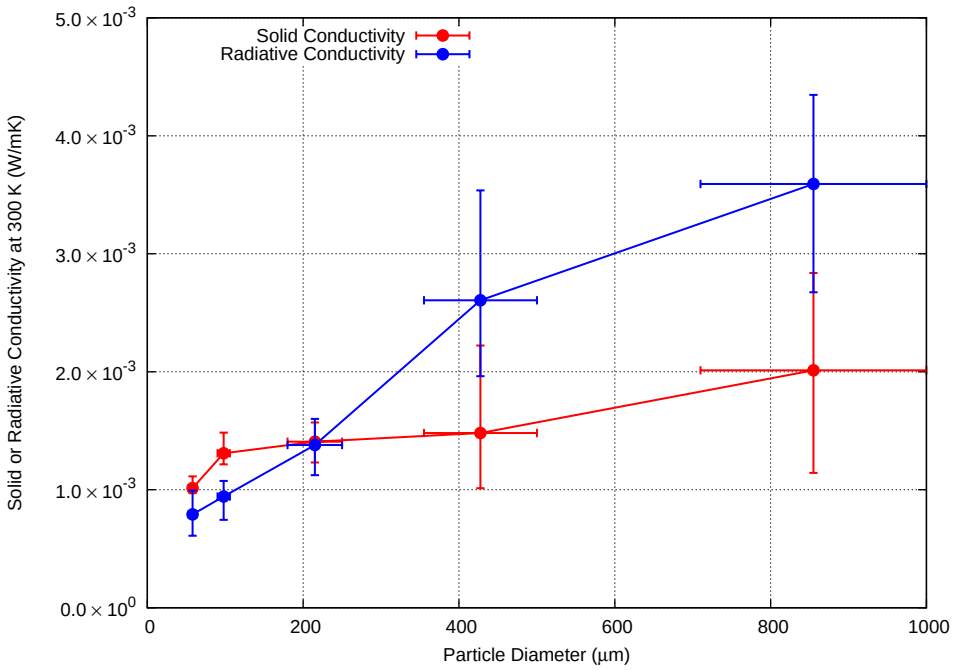

Figure 3.15: Summary of the particle size dependence of solid (red) and radiative (blue) conductivity for the FGB glass beads. The points represent the mean values of the four measurements (the container A and channels 1-3 of the container B). The upper limits of the vertical errorbars are given by the maximum values within the four measurements and the lower limits by the minimum values.

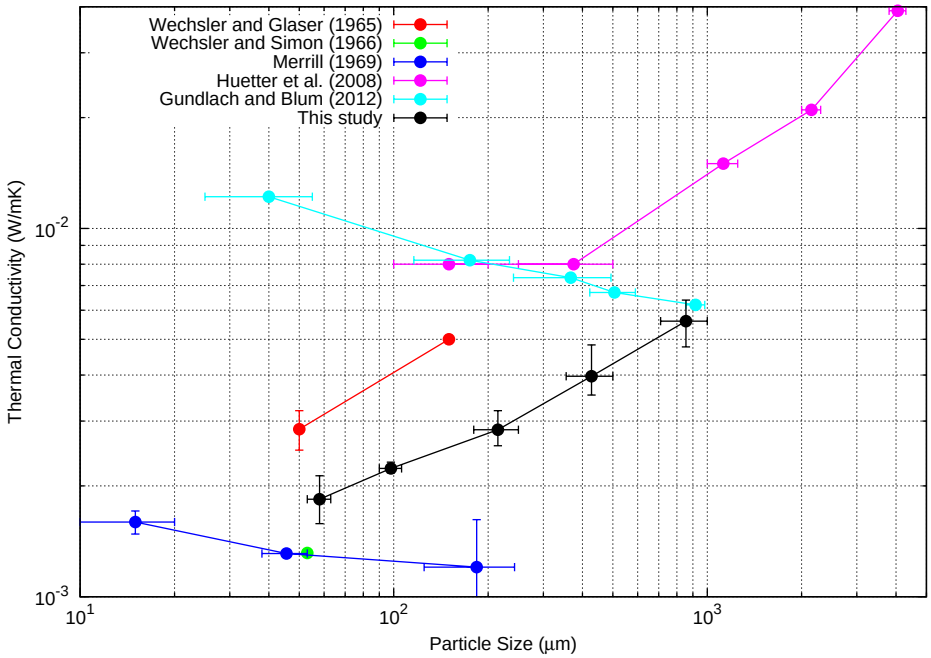

Figure 3.16: Comparison between the effective thermal conductivity obtained in this work (black dots) and previous studies (shown in Figure 2.4).

3.4 Porosity dependence

3.4.1 Experimental method

All FGB glass beads samples had porosity around 0.4. In order to vary the porosity of the powdered materials and to investigate its effect on the thermal conductivity, EMB glass beads with the particle diameter less than 10 μm were used. Since the EMB glass beads had adhesive nature, the sample with higher porosity than 0.4 could be prepared.

The most porous sample was prepared in the sample container A (Figure 3.3a and 3.17) by sieving the EMB glass beads through 53 μm mesh, which produced the maximum porosity of 0.862. The sample was filled in the container to the top, and the porosity was determined from the inner volume of the container and sample weight. The tapping of this sieved sample produced lower porosity of 0.695. By sieving through 500 μm mesh, the porosity of 0.753 was obtained. The compressed sample without the sieving had the porosity of 0.495. These packing procedures are illustrated in Figure 3.18.

In the sample container B (Figure 3.3b), the two samples were prepared by the 53 μm sieve and the compression. The porosities were 0.779 and 0.585, respectively. These samples were used to investigate the heterogeneity in the thermal

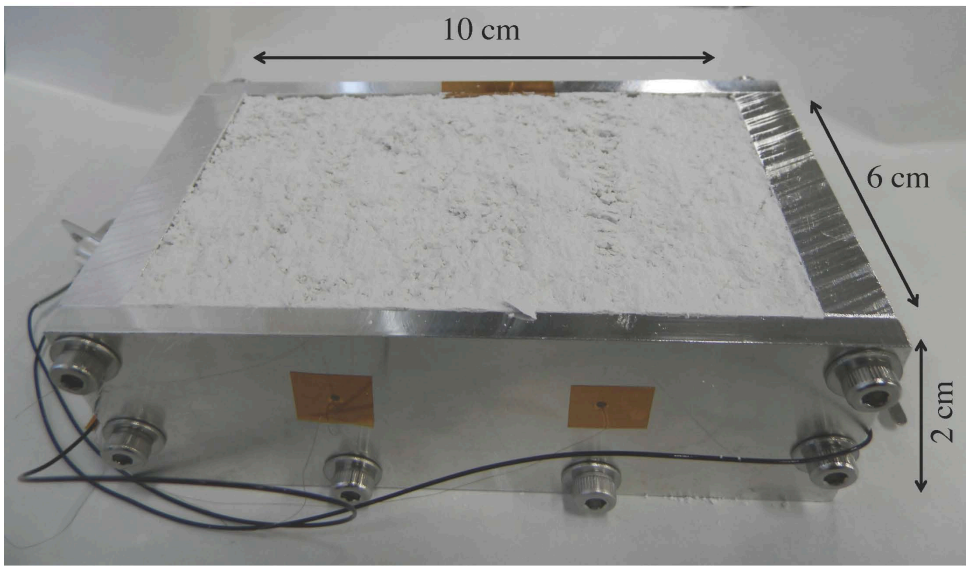

Figure 3.17: Sample container used for investigating porosity dependence of the thermal conductivity of EMB glass beads.

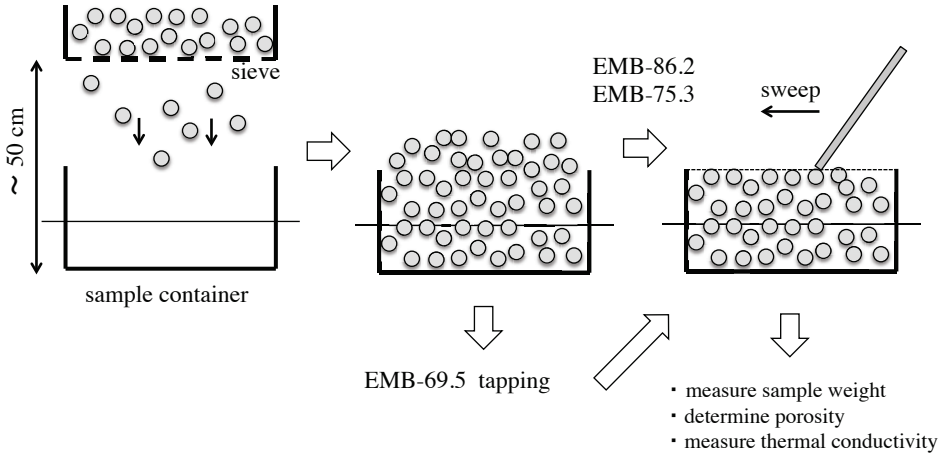

Figure 3.18: Overview of packing procedure for controlling the porosity higher than 0.6. The EMB-49.5 and EMB-58.5 did not sieved and were compressed artificially.

conductivity.

The experimental configuration is the same as shown in Figure 3.10. The sample was evacuated in the vacuum chamber at low exhaust velocity (about 5 hours down to 10 Pa), to avoid blowoff of the fine powders. The test procedures are also the same as those in Section 3.3.

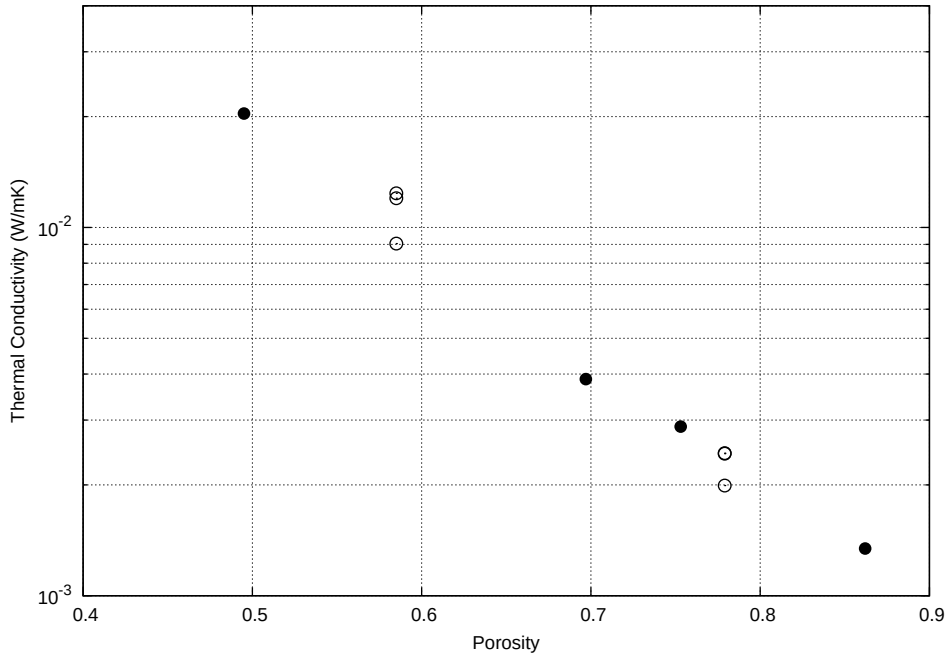

Figure 3.19: Thermal conductivity of EMB glass beads at temperature of about 25 degC as a function of porosity. Filled and hollow circles represent the measurement by the sample container A and B, respectively.

3.4.2 Results

Figure 3.19 and 3.20 show the experimental results. In Figure 3.19, the thermal conductivities at about 25 degC are plotted as a function of the porosity. The thermal conductivity of the EMB glass beads decreased from 0.02 to 0.0013 W/mK with increasing the porosity. For EMB glass beads as well as FGB glass beads, the thermal conductivity was measured at several temperature as shown in Figure 3.20, and the temperature-dependent increase in the thermal conductivity was confirmed.

Similar to the FGB glass beads in Section 3.3, the solid and radiative conductivities are constrained from the temperature-dependent thermal conductivity for EMB glass beads. Equation (3.27) was fitted to the data in Figure 3.20, using Equation (3.2) as EMB material thermal conductivity k_{m}, The resultant solid and radiative coefficients, A and B, are listed in Table 3.5.

From these coefficients, the solid and radiative conductivities at 300 K are plotted in Figure 3.21. The solid conductivity showed a decreasing function of the porosity. When the porosity is higher than about 0.6, the radiative conductivity increased with the porosity. At lower porosity than 0.6, the radiative conductivity was higher than those at higher porosity. The radiative conductivity became more dominate as the porosity is higher.

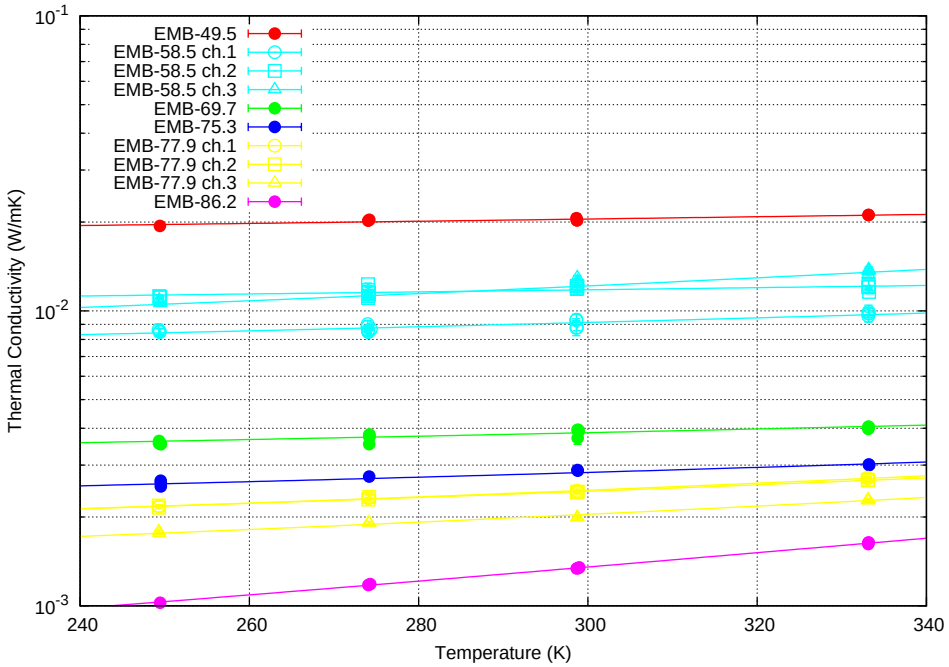

Figure 3.20: Temperature dependence of the thermal conductivity of EMB glass beads of different porosities. Each curve represents fitting result of Equation (3.27).

Table 3.5: Solid and radiative coefficients in Equation (3.27) for EMB glass beads samples.

Sample	Porosity	Container	Solid coefficient	Radiative coefficient
		A ($\times 10^{-3}$)	B ($\times 10^{-11}$ W/mK^4)	
EMB-49.5	0.495	A	12.4 ± 0.02	4.28 ± 0.87
EMB-58.5	0.585	B-ch.1	5.00 ± 0.08	4.92 ± 0.52
		B-ch.2	7.15 ± 0.17	2.34 ± 0.10
		B-ch.3	5.57 ± 0.12	12.8 ± 0.96
EMB-69.7	0.697	A	2.20 ± 0.01	1.61 ± 0.26
EMB-75.3	0.753	A	1.51 ± 0.01	1.74 ± 0.22
EMB-77.9	0.779	B-ch.1	1.19 ± 0.01	2.23 ± 0.08
		B-ch.2	1.22 ± 0.01	2.03 ± 0.08
		B-ch.3	0.93 ± 0.02	2.20 ± 0.10
EMB-86.2	0.862	A	0.40 ± 0.01	2.71 ± 0.04

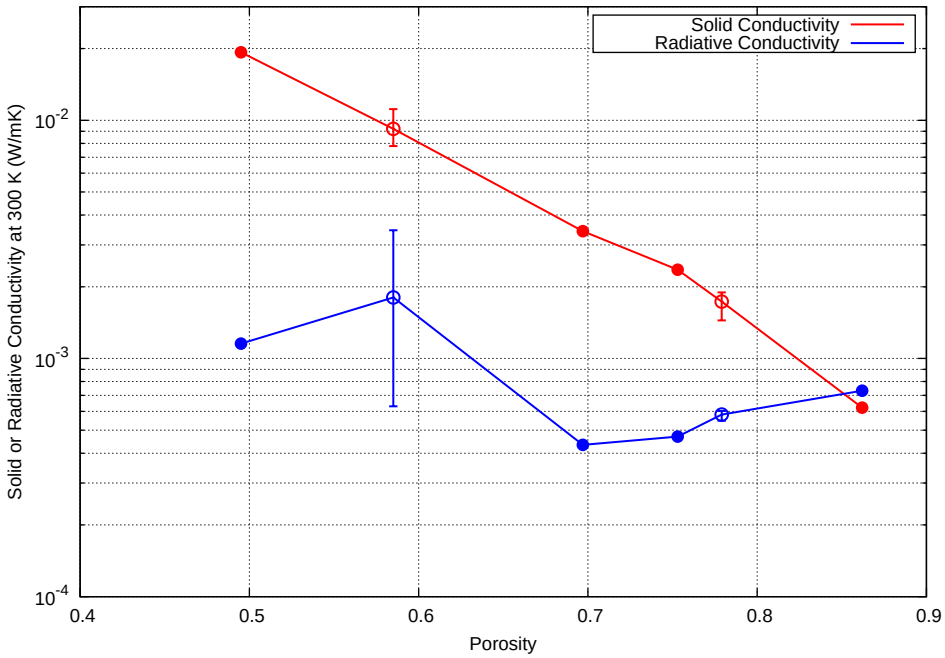

Figure 3.21: Solid and radiative conductivity at 300 K as a function of the porosity. Filled circles represent the measurement by the sample container A. Hollow circles represent the average of the three measurements by the sample container B, with the vertical errorbars being the highest and lowest values among the three measurements.

The radiative conductivity of the EMB-58.5 was significantly scattered. Heterogeneous packing of the particles would cause this scattering, since this sample was not sieved and artificially compressed, as well as EMB-49.5. Moreover, around this porosity, the radiative conductivity is order of magnitude lower than the solid conductivity. Therefore, it is difficult to precisely determine the radiative conductivity. In the subsequent discussion, the radiative conductivities of EMB-49.5 and EMB-58.5 are not included. Note that the solid conductivity of EMB-58.5 was less scattered, which indicate that the solid conductivity is less sensitive to the packing structure.

For the EMB-77.9, the radiative conductivity as well as the solid conductivity showed good agreement among the three measurements. It means that the samples, which were sieved and not compressed can be recognized as homogeneous in the thermal conductivity. Therefore, the results obtained for the sample of EMB-69.7, EMB-75.3, and EMB-86.2, as well as EMB-77.9, would be reliable.

In Figure 3.22, the effective thermal conductivity of the EMB glass beads is compared to the results by *Krause et al.* (2011), who measured spherical SiO_2 powders of 1.5 μm in diameter as a function of the porosity. The result obtained in this study was comsistent with that of *Krause et al.* (2011). Note that *Krause et al.* (2011) did not determine the solid and radiative conductivities of thier samples. They neglected the radiative conductivity and derived an empirical relation between the solid conductivity and the porosity by fitting an exponential function to their data, as $k_{\mathrm{solid}} \propto \exp(-5.88\phi)$, where ϕ is the porosity. This empirical relation has been widely utilized in the model calculation of thermal evolution of porous planetesimals (*Henke et al.*, 2012a; *Neumann et al.*, 2012). This study showed that the radiative conductivity is not negligible component for the higher porosity. At the porosity of 0.862, the solid and radiative conductivities were comparable. Fitting of the same function to the solid conductivity obtained in this study results in $k_{\mathrm{solid}} \propto \exp(-8.24\phi)$. It means that the solid conductivity model empirically derived by *Krause et al.* (2011) might overestimate the solid conductivity at the higher porosity.

3.5 Thermal conductivity of metallic beads and regolith simulant

3.5.1 Experimental method

Regolith simulant, titanium and copper beads were measured by the same method as FGB glass beads using the sample container A. For the measurements of the

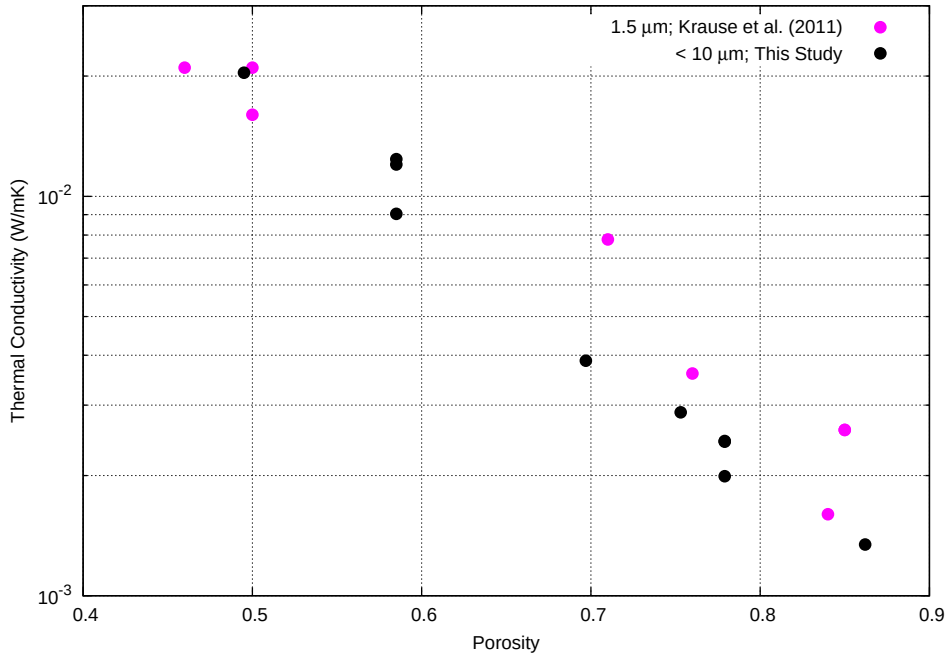

Figure 3.22: Comparison of the effective thermal conductivity obtained in this work and by *Krause et al.* (2011).

metallic beads (FMF-Ti and FMF-Cu), the nichrome wire was coated by enamel for electrical insulating between the wire and the sample. The thermal conductivity for each sample was measured as a function of the temperature using the same experimental system as the FGB glass beads (Figure 3.10). The porosity of the three samples are shown in Table 3.1

3.5.2 Results

The thermal conductivities of the regolith simulant, titanium beads, and copper beads are plotted as a function of the temperature in Figure 3.23. The measurement results of the FGB-180 glass beads (having comparable size to FMF-Ti and FMF-Cu) are also displayed. The thermal conductivity of the regolith simulant slightly increased with the temperature from 0.0040 to 0.0046 W/mK. On the other hand, for the titanium beads it decreases with the temperature from 0.0359 to 0.0140 W/mK. For the copper beads, it seemed to increase with the temperature.

First, the thermal conductivity of the two metallic beads is duscussed. In Figure 3.23, the fitting results of $k = Ak_{\mathrm{m}}(T) + BT^3$ with $k_{\mathrm{m}} = 1587/T + 16.5$ and $k_{\mathrm{m}} = 9784/T + 365$ for titanium and copper beads, respectively (Table 3.2), are drawn. The fitting to the data on the titanium beads gives $A = 2.08 \times 10^{-3}$ and $B = -9.04 \times 10^{-10}$ W/mK^4. A negative value of the radiative conductivity was estimated, which

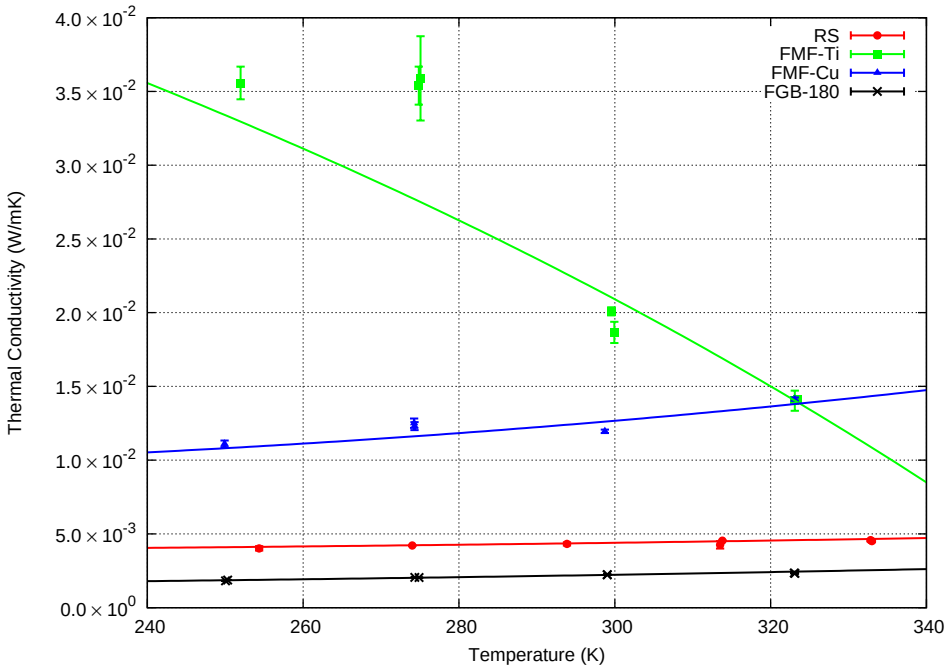

Figure 3.23: Temperature effect on thermal conductivity of regolith simulant (RS), titanium beads (FMF-Ti) and copper beads (FMF-Cu). For comparison, the results for glass beads of 90-106 μm (FGB-180) are also plotted. Solid curves represent fitting results of Equation (3.27) using the material conductivity of each composition shown in Table 3.2.

can not be approved. For the copper beads, $A = 2.00 \times 10^{-5}$ and $B = 1.75 \times 10^{-10}$ W/mK^4 were derived. This radiative conductivity was much higher than that of the FGB-180 glass beads ($B = 2.76 \times 10^{-11}$ W/mK^4). Because the emissivity and resultant radiative transfered energy of the copper beads are lower than the glass beads (Table 3.2), the higher radiative conductivity would be physically impossible. It should be mentioned that the metallic beads possibly had the oxidized layer on the surface. The solid conductivity or thermal conductance at the contacts is sensitive to the thermal property of the surface material. The oxidized metal has different thermal conductivity and its temperature dependence from the pure metal. Then, the use of the material conductivity of $k_{\mathrm{m}}(T)$ for the pure metals might be inadequate.

Next, the result for the regolith simulant is described. The solid and radiative conductivities are deduced by fitting of the Equation (3.27) to the temperature-dependent data. The material conductivity k_{m} is taken as a constant of 2.5 W/mK, as mentioned in Section 3.1. Then, $A = 1.47 \times 10^{-3}$ and $B = 2.63 \times 10^{-11}$ W/mK^4 were obtained for the regolith simulant. In Figure 3.24, the values of A and B are compared to those of FGB glass beads, by taking the particle diameter of the regolith simulant as the mean diameter of 74 μm. The solid coefficient of the regolith simulant was slightly higher than that of the glass beads with comparable size. The cause of this difference is considered to be several factors, such as particle shape and particle size distribution, whose contributions are difficult to be separated in the current status. The radiative coefficient of the regolith simulant was comparable with that of the glass beads. This consistency indicates that the radiative conductivity can be characterized by the mean particle size.

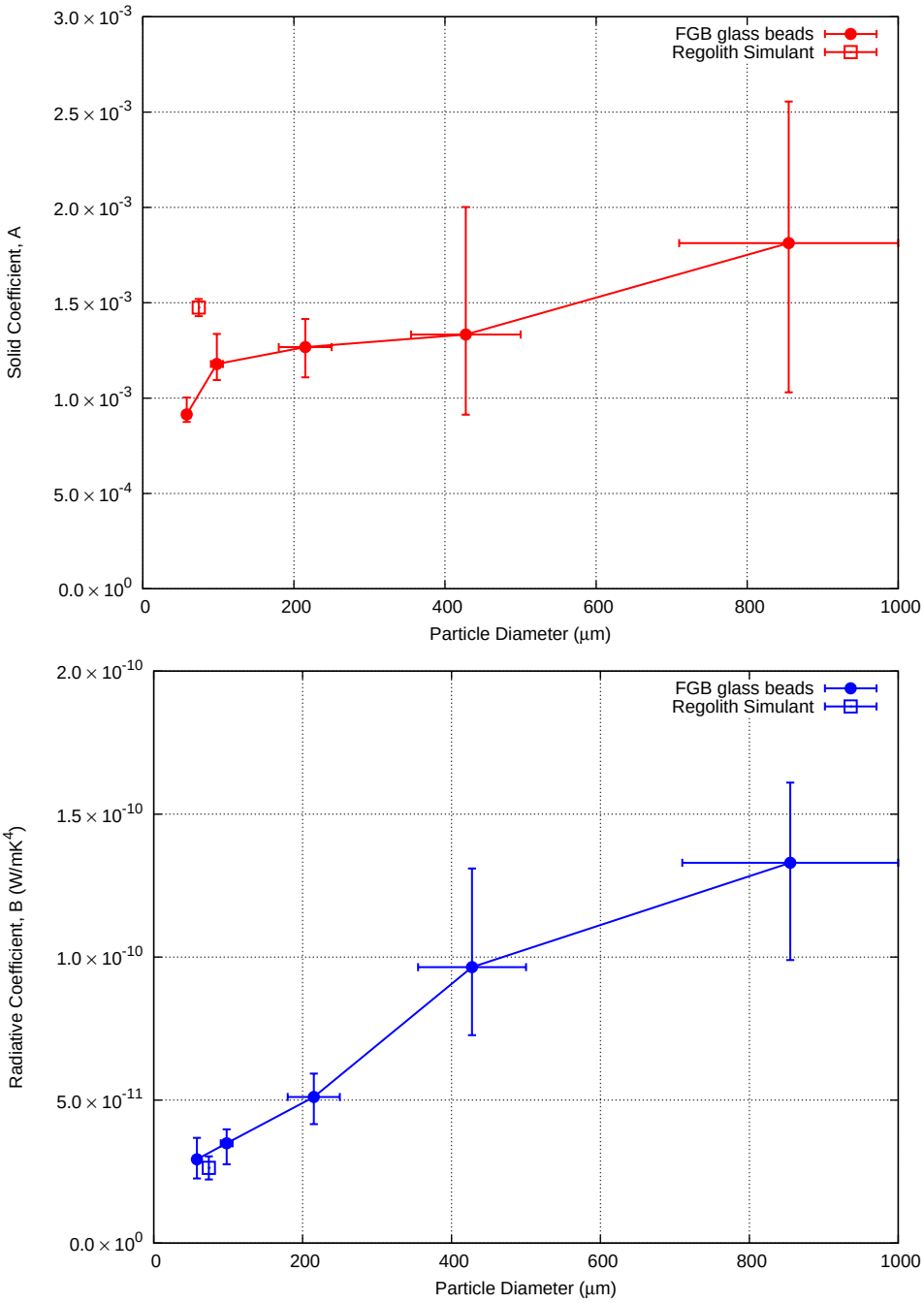

Figure 3.24: Solid (top) and radiative (bottom) coefficients of the regolith simulant (follow squares) compared with those of FGB glass beads (filled circles). The particle size of the regolith simulant is set at the mean size of 74 μm. Note that the vertical error bar for the regolith simulant represents only the fitting error of Equation (3.27). On the other hand, error bars for the FGB glass beads represent the sample heterogeneity (Figure 3.15).

3.6 Compressional stress dependence

3.6.1 Experimental method

The stress dependence was measured for the FGB-20 and FGB-180 glass beads and the regolith simulant. Figure 3.25 shows the experimental configuration developed newly in this study in order to measure the thermal conductivity with external compression. The pressing system consisted of six brass blocks and its driving mechanics. The driving mechanics components were a rotational shaft, rotational bearings, gears, and an ultrasonic motor. The six brass weights (0.2, 0.4, 0.9, 1.2, 1.5, and 3.3 kg, respectively) were suspended by strings in series above a sample container and the strings is fixed at the rotational shaft. The weights can be rolled up and down using the ultrasonic motor. The stress in the sample was controlled by changing the number of weight superimposed onto the top of the sample. The line heat source sensor was strung horizontally in the sample container (40 mm width, 100 mm length, and 60 mm height), 20 mm above the bottom. Two stress transducers (PGM-02KG, Kyowa Electronic Instruments Co., Ltd.) were mounted on the bottom and lateral planes of the sample container, which allowed to directly measure the vertical and horizontal stress in the powder samples.

Sample was poured in the container and packed as densely as possible by tapping the container. Thickness of the sample was 40 mm from the bottom of the container. The system was evacuated in a vacuum chamber (different chamber from used in Section 3.3 and 3.4) down to 10^{-4} Pa. The stress values by the stress transducers started to decrease just after the evacuation, because of the differential pressure between the front and back sides of the detector plane. The gas was gradually evacuated from the inside of the stress transducer, and it needed at least 3 days until the stress value with the transducer on the bottom of the container returned to the original value. Then, constant current of 40 mA was supplied to the nichrome wire and its temperature was recorded for 1000 s. The thermal conductivity was determined by fitting of Equation (3.10) to the temperature data from 400 to 1000 s. At the same time, the output voltages of the two stress transducers were recorded for about 30 seconds with a frequency of 1 Hz. Stress value can be calculated by multiplying a conversion coefficient by the output voltage. The horizontal and vertical stresses were determined by averaging the recorded stress values.

After the thermal conductivity measurements in the uncompressed state, the lowest weight was loaded on the sample. The thermal conductivity and the stresses were measured by the same procedure. Until the all weights were put on the sample, these procedures were repeated. After that, the weights were turned up and the measurements were conducted in order. This cycle was repeated three times. All

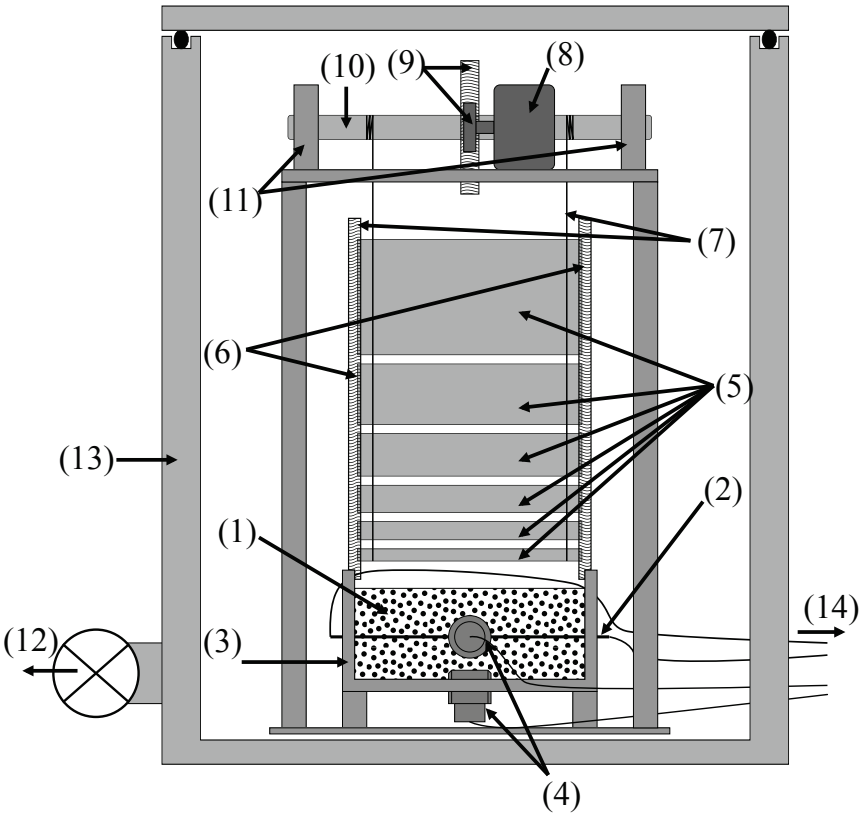

(1) Samples (2) Line Heat Source System (3) Sample Container
(4) Stress Transducers (5) Weights (6) Guides for Weights
(7) Strings (8) Ultrasonic Motor (9) Gears (10) Rotational Shaft
(11) Bearing (12) Exhaust System (13) Vacuum Chamber
(14) Electronic Devices

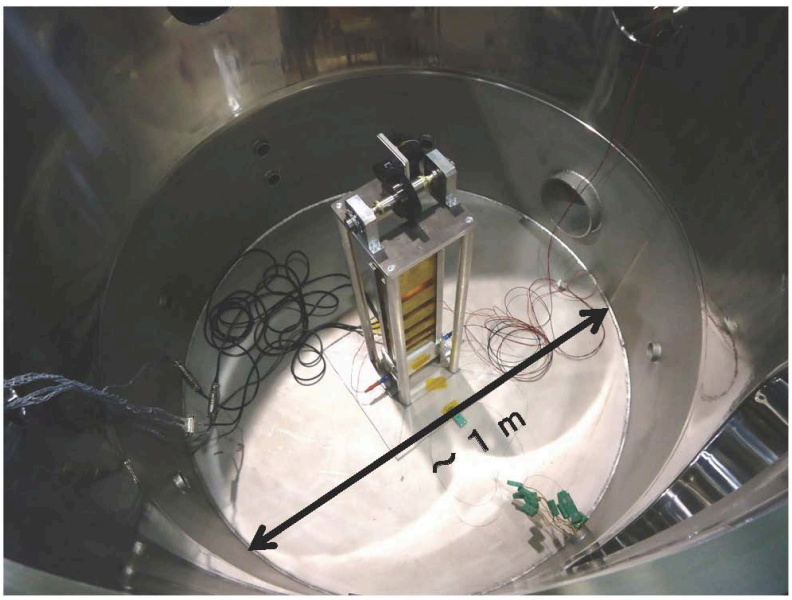

Figure 3.25: Experimental configuration for investigating compressional stress dependence of the thermal conductivity of powdered materials.

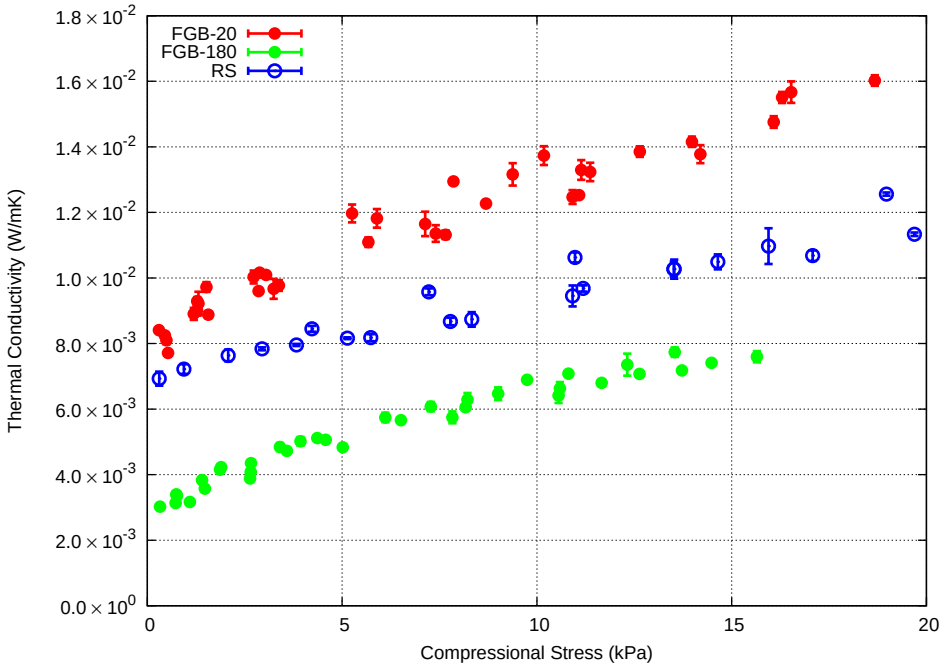

Figure 3.26: Effective thermal conductivity of FGB glass beads and the regolith simulant as a function of the compressional stress. The horizonal axis represents mean stress values of vertical and horizontal stresses shown in Figure 3.27. Errors in the compressional stress are not shown in this figure and the followings, since they are negligible compared to the measured values (see the text).

measurements were conducted at room temperature (about 22 degC).

3.6.2 Results

Figure 3.26 shows thermal conductivity of the two glass beads and the regolith simulant as a function of the compressional stress. The horizontal axis represents averaged value of the vertical and horizontal stresses measured by the stress transducers. Variation in the stress values during the stress measurements for 30 seconds were within 0.05 kPa, so that errors in the horizontal and vertical stress values would be negligibly small compared to the measured values. It was found that the thermal conductivity of the all samples increased with the compressional stress.

In powdered media, it is known that the stress field is heterogeneous due to internal friction of the particles (*Masuda et al.*, 2006). Figure 3.27 shows relations between vertical and horizontal stresses. The glass beads and the regolith simulant had the ratio of the horizontal to vertical stresses about 0.77 and 0.26, respectively. This might indicate that efficiency of heat transport is different in horizontal and vertical directions, especially for the regolith simulant. *Garrett and Ban* (2011)

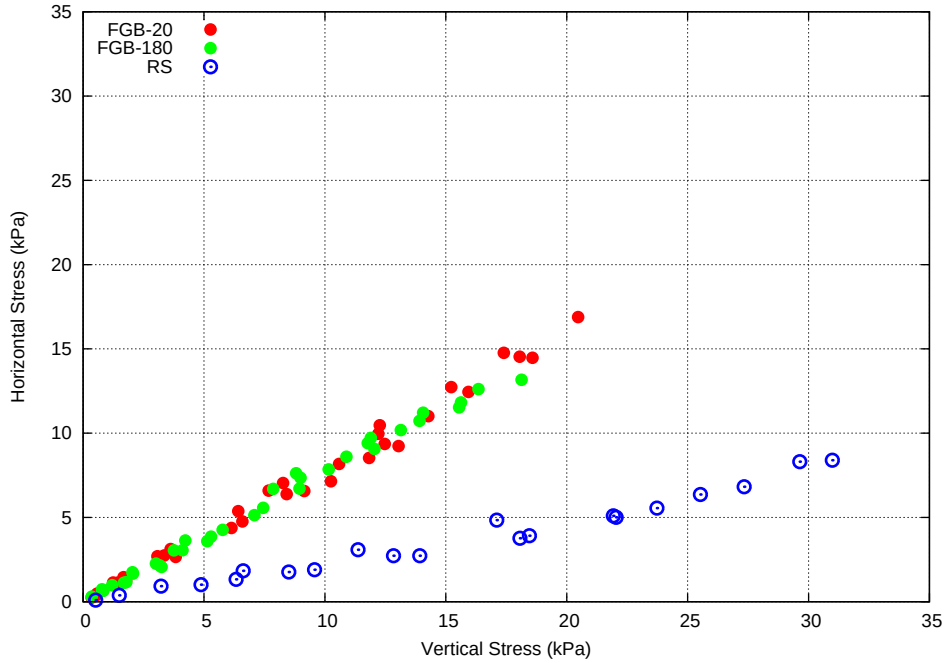

Figure 3.27: Relation between vertical and horizontal stresses during the compression tests for FGB-20 glass beads, FGB-180 glass beads, and regolith simulant.

performed two dimensional finite element simulations and stated that the thermal conductivity measured by the line heat source apparatus placed in the sample horizontally is represented by the average of the horizontal and vertical thermal conductivities. Therefore, the averaged value of the vertical and horizontal stresses would be characteristic quantity of the measured thermal conductivity.

During the compressional tests, the samples would be somewhat densified. After finishing all thermal conductivity measurements, sinking of the sample surface by about 1 mm was observed. This contributes the density increase by about 3% in consideration of original sample height of 40 mm. Therefore, the effect of densification of the samples to the thermal conductivity could be neglected.

When the powdered materials are compressed without re-arrangement of the packed particles, the particles will be deformed elastically and the contact area broadens even without significant change of the bulk density. The broadened contacts provide wide heat paths, through which the heat can efficiently flow between the particles, and therefore, the solid conductivity can increase with the compressional stress. Because of little densification of the samples during the compressional tests, the radiative conductivity would not vary by the compressional stress. By subtracting the radiative conductivity at 22 degC, which can be estimated from the values of B for each sample (Section 3.3 and 3.5), from the measured thermal

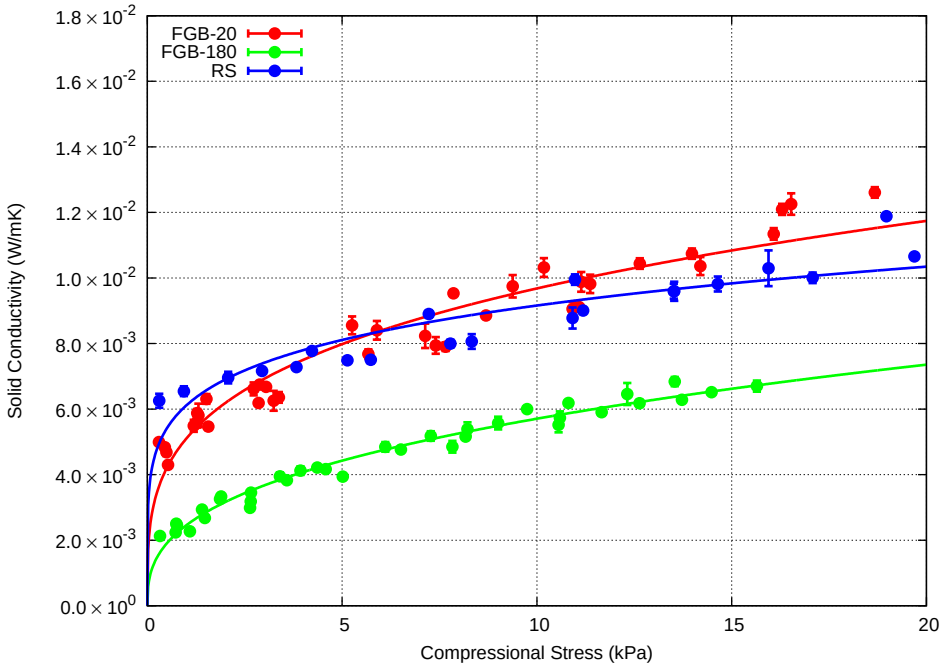

Figure 3.28: Solid conductivity of FGB glass beads and regolith simulant as a function of the compressional stress. The curves represent the fitting curves of Equation (3.28).

conductivity, the compressional stress dependence of the solid conductivity can be deduced as shown in Figure 3.28. The larger solid conductivity of the FGB-20 glass beads than the FGB-180 is consistent with the experiments without the compression (Figure 3.15 in Section 3.3).

If two spheres were compressed by normal force along a line passing through the centers of the spheres, radius of the circular contact area follows Hertzian theory, which expects that the contact radius is proportional to the normal force with an exponent of 1/3. Then, to determine the stress or contact size dependence of the solid conductivity, following exponential function is fitted to the data in Figure 3.28,

$$k_{\mathrm{solid}} = k_{\mathrm{s},0}\sigma^{p}, \tag{3.28}$$

where σ is the compressional stress in kPa unit, $k_{\mathrm{s},0}$ and p is fitting variables. The fitting results are shown in Figure 3.28 and Table 3.6 lists the resultant $k_{s,0}$ and p. For the two glass beads, the exponential coefficients of p = 0.29 and 0.35 were determined. According to the Hertzian contact theory, radius of the contact area is proportional to contact force or applied stress with an exponent of 1/3, which is comparable with the exponent of p for the glass beads. This consistency strongly suggests that the solid conductivity of the glass beads is proportional to the radius of the contact area between the particles.

Table 3.6: Fitting parameters of $k_{s,0}$ and p in Equation (3.28) for two glass beads and regolith simulant, from Figure 3.28.

Sample	$k_{s,0}$	p
FGB-20	0.0051 ± 0.0002	0.29 ± 0.01
FGB-180	0.0026 ± 0.0001	0.35 ± 0.01
RS	0.0061 ± 0.0003	0.18 ± 0.02

On the other hand, the regolith simulant has the smaller value of $p = 0.17$. The difference between the glass beads and regolith simulant might attribute to irregular (not spherical) particle shapes of the regolith simulant. Equation (3.28) implies that the solid conductivity approaches to zero, when no compressional stress including self-weight is applied. However, in practice, finite contact area exists even for such a limited case, due to adhesive force between the particles, which contributes the solid conductivity as an offset value in Figure 3.28. The difference between the fitting curve and measured conductivity could come from this effect. The contribution of the adhesive force to the solid conductivity cannot be constrained by current understandings. If assuming that the solid conductivity of the regolith simulant determined in Section 3.5, $k_{solid} = 0.0037$ W/mK, all corresponds to the contribution of the adhesive force, fitting by Equation (3.28) with including this offset (i.e., fitting by $k_{solid} = k_{s,0}\sigma^p + 0.0037$) gives $p = 0.36$ for the regolith simulant, which is comparable value with that for the glass beads. The smaller adhesive contribution makes the resultant value of p lower. Thus, the difference of the stress dependence might be explained by including the effect of adhesive force on the solid conductivity.

3.7 Effect of particle size distribution

3.7.1 Experimental method

To investigate the effect of the particle size distribution on the thermal conductivity, binary mixture of the glass beads of 90-106 μm (FGB-180) and 180-250 μm (FGB-80) were measured. These mixed samples with the weight ratio of 2:1, 1:1, and 1:2 were prepared. The sample container B shown in Figure 3.3b was used.

The mixed samples were prepared by the following systematic procedure. The larger FGB-80 glass beads with a given mass were put in the sample container, and the smaller FGB-180 glass beads were filled on the FGB-80 beads. This sample container was vertically vibrated using a vibration table (acceleration of about 5 G and frequency of 22 Hz) for 10 minutes. After the mixing by the vertical vibration,

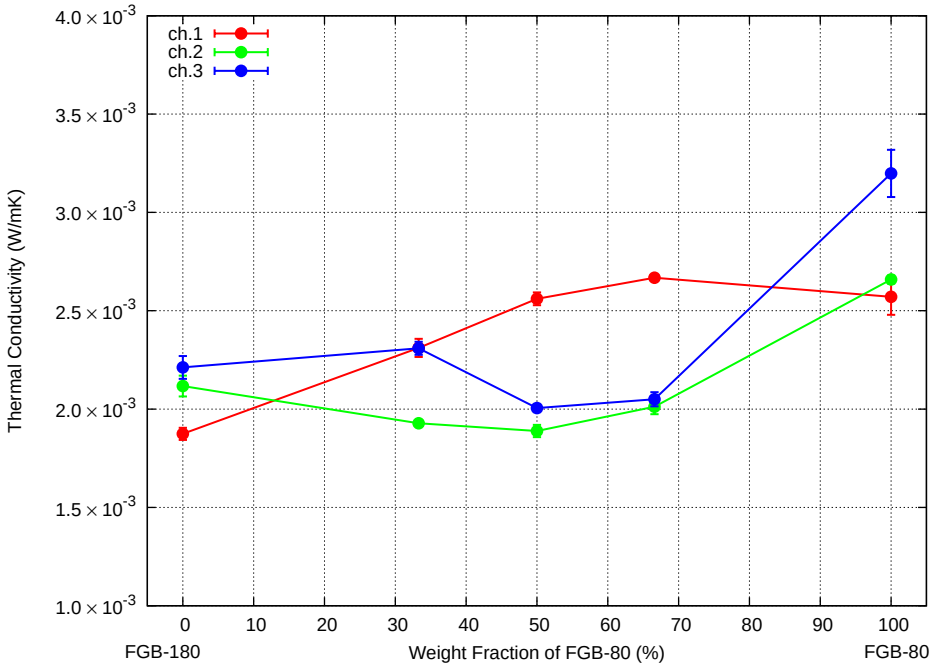

Figure 3.29: Thermal conductivity of binary mixtures of FGB-180 and FGB-80 glass beads at 25 degC. The horizontal axis represents weight fraction of the larger FGB-80 glass beads relative to the total mass. The sample container B (Figure 3.3b) was used.

the volume and porosity of the sample was determined from the height and total mass of the packed beds. The thermal conductivity was measured by the same method described in Section 3.3 as a function of the temperature.

3.7.2 Results

Figure 3.29 shows the thermal conductivity of the binary mixture of the glass beads at 25 degC as a function of weight fraction of the larger (FGB-80) glass beads. The mixed samples had the thermal conductivity ranged from 0.0019 to 0.0027 W/mK, all of which are distributed within the range for the two mono-sized end-members (FGB-180 and FGB-80). The thermal conductivities obtained by the three sensors differed by 0.0007 W/mK at maximum, which is comparable with that observed for mono-sized glass beads (Figure 3.13).

The solid and radiative coefficients were determined from the temperature dependent data (Figure 3.30). These estimated values are listed in Table 3.7 and plotted in Figure 3.31. It was found that both the solid and radiative conductivities were roughly ranged between those of the two end-members, similar to the case for the effective thermal conductivity at 25 degC. However, because of the heterogeneity of the thermal conductivity, the effect of the mixing ratio could not be found out. At

Table 3.7: Solid and radiative coefficients of the binary mixtures of the FGB-180 and FGB-80 glass beads obtained by the fitting of Equation (3.27) to the data in Figure 3.30. In the first column, mixing mass ratio of the FGB-180 and FGB-80 and the bulk porosity of the sample, ϕ, are shown. The second column represents the line heat sensor channels in the sample container (Figure 3.3b).

Mixing ratio FGB-180:FGB-80 (Porosity ϕ)	channel	Solid Coefficient A ($\times 10^{-3}$)	Radiative Coefficient B ($\times 10^{-11}$ W/mK^4)
0:1	ch.1	1.11 ± 0.18	5.24 ± 0.83
($\phi = 0.39$)	ch.2	1.34 ± 0.15	4.16 ± 0.57
	ch.3	1.42 ± 0.10	5.09 ± 0.52
1:2	ch.1	1.29 ± 0.06	4.67 ± 0.25
($\phi = 0.37$)	ch.2	0.91 ± 0.03	3.48 ± 0.15
	ch.3	0.94 ± 0.02	3.87 ± 0.11
1:1	ch.1	1.09 ± 0.06	5.05 ± 0.25
($\phi = 0.35$)	ch.2	0.76 ± 0.07	3.83 ± 0.35
	ch.3	0.88 ± 0.06	3.76 ± 0.29
2:1	ch.1	0.84 ± 0.10	5.61 ± 0.35
($\phi = 0.37$)	ch.2	1.04 ± 0.20	2.74 ± 0.90
	ch.3	0.99 ± 0.13	4.18 ± 0.48
1:0	ch.1	0.98 ± 0.02	2.86 ± 0.10
($\phi = 0.40$)	ch.2	0.75 ± 0.03	3.54 ± 0.15
	ch.3	0.88 ± 0.02	3.16 ± 0.09

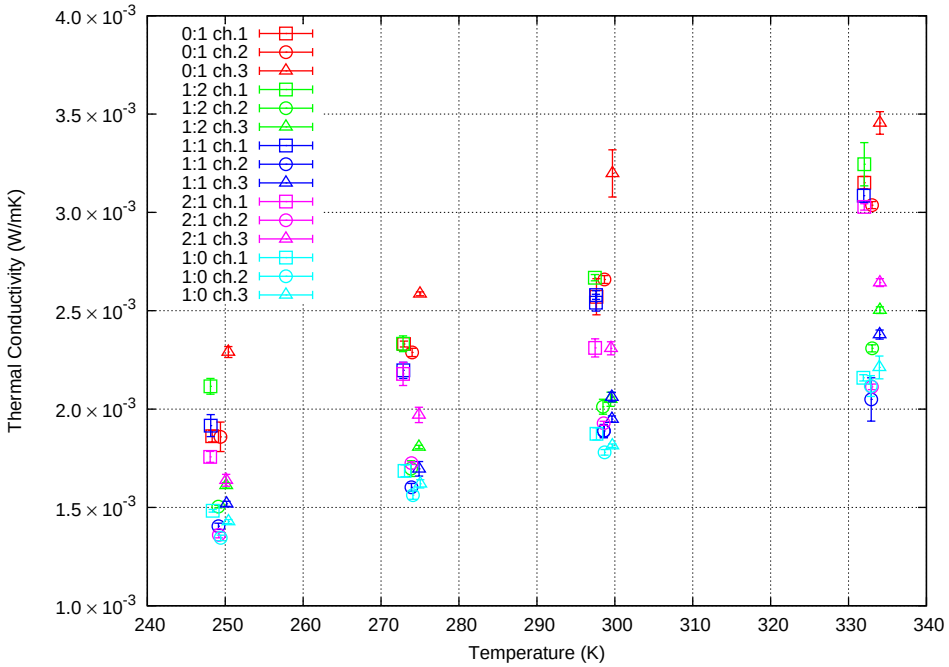

Figure 3.30: Thermal conductivity of binary mixtures of FGB-180 and FGB-80 glass beads as a function of the temperature. 0:1, 1:2, 1:1, 2:1, and 1:0 in the legend are represent the mixing ratio of FGB-180 and FGB-80.

least, it could be stated that the solid and radiative conductivities does not become higher or lower than those of the mono-sized samples.

In Figure 3.32, the solid and radiative conductivities at 300 K of the mixture are compared with the mono-sized FGB glass beads in terms of the average diameter. Overall trends of the particle size dependences are not disturbed, even if the particle size of the mixture is taken as average diameter. It might imply that the thermal conductivity of the mixture of the different sizes can be characterized by the average diameter. Note that the bulk porosity of the mixture prepared in this study was slightly lower than that of the mono-sized glass beads. The lower porosity of the mixtures would make the solid conductivity higher and the radiative conductivity lower.

3.8 Thermal conductivity of sintered glass beads

3.8.1 Experimental method

In Section 3.6, it was found that contact radius between the particles is an essential parameter on the solid conductivity. When the powder beds are heated at high

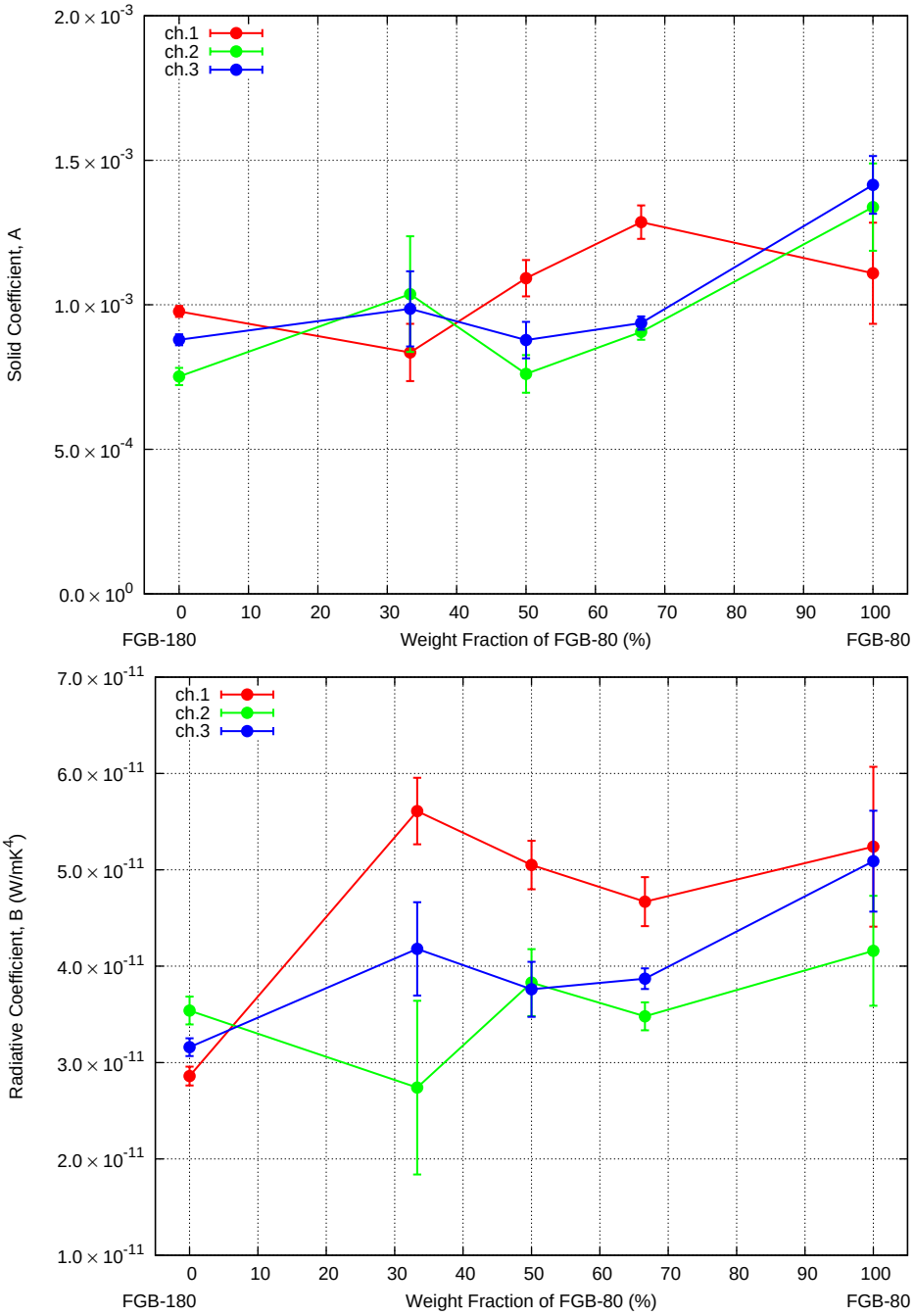

Figure 3.31: The solid (top) and radiative (bottom) coefficients as a function of the mixing ratio, from Table 3.7. The different colors represent the difference in the channels of the sample container B.

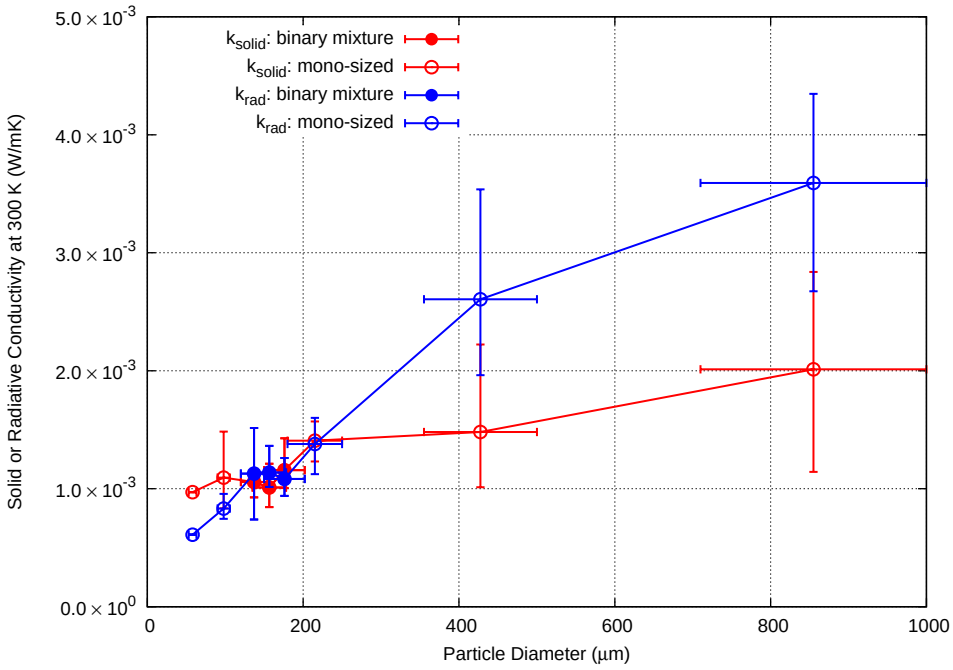

Figure 3.32: Solid (red) and radiative (blue) conductivity of the binary mixture of the glass beads (filled circles) and mono-sized glass beads (hollow circles) as a function of averaged diameter.

temperature below the melting point, particles begin to mechanically connect each other so as to form necks at the contact points of the particles. This irreversible thermodynamic phenomenon is called sintering. Growth of the neck size would make the solid conductivity higher than that of unconsolidated powders. In this section, effect of the sintering on the thermal conductivity is investigated.

The samples used in this experiment were FGB-20, FGB-40, and FGB-80 glass beads. Each sample was filled in an alumina sample container, in which a line heat source sensor was mounted (Figure 3.33). The line heat source sensor consisted of a nichrome wire of 500 μm diameter and three K-type thermocouples fixed by ceramic glue on the nichrome wire. This packed sample was sintered by heating in the electrical furnace at atmospheric pressure. The heating temperature and duration are summarized in Table 3.8. For each FGB glass bead, three sintered samples were made by changing the heating duration with the sintering temperature maintaining a constant.

The thermal conductivity for the nine sintered samples was measured under vacuum condition (10^{-2} Pa) by the line heat source method. Electrical resistance of the 500 μm nichrome wire after the sintering was $R_{\mathrm{h}} = 6.04 \pm 0.03$ Ω/m. By inducing the constant electrical current of 0.25 A, the thermal conductivities were

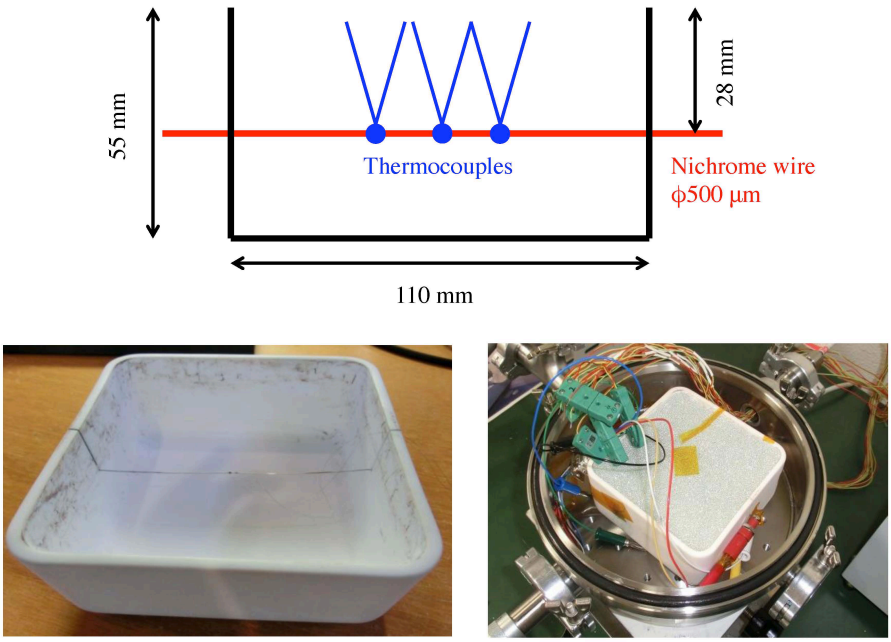

Figure 3.33: Sample container (top and left bottom) and experimental setup (right bottom) for investigating the effect of the sintering on the thermal conductivity.

Table 3.8: Sintering temperature and duration for preparation of sintered glass beads samples.

Sample	Sintering temperature (degC)	Sintering duration (hour)	Degree of sintering
FGB-20	672	2.0	low
		4.0	medium
		8.0	high
FGB-40	645	5.0	low
		9.9	medium
		20.0	high
FGB-80	640	3.4	low
		6.7	medium
		14.0	high

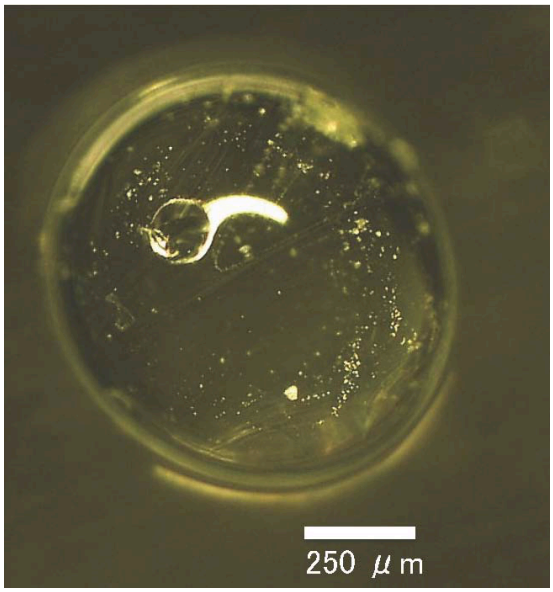

Figure 3.34: A trace of the broken neck on a glass bead.

determined from the temperature data obtained with the three thermocouple, respectively. A time regime from 100 s to 750 s was utilized for the linear fitting. The thermal conductivity was measured only at room temperature. Only the FGB-20 glass beads sintered at temperature of 672 degC for 8 hours was measured at the temperature from -25 to 50 degC to estimate effect of the radiative contribution.

After the thermal conductivity measurement, the individual necks of the sintered sample was broken. An original neck part can be observed as a rounded trace shown in Figure 3.34. For 50 separated particles for every sintered samples, particle diameter, area of the all traces with clear outline larger than 10 μm in diameter, and the distance between center of the trace and center of the particle were measured. The observed region was restricted to the circular area with radius of a half of the particle radius from the center of the particle, which is about 6.7% of the total surface area of a sphere (Figure 3.35). The radius of the trace was calculated from the observed area by approximating it as a circle with equal area.

3.8.2 Results

First, the result of the neck observation is described. Figure 3.36 shows the histogram of the neck-like traces observed on 50 particles for each sintered sample. The horizontal axis, trace radius ratio, means the ratio of radius of the traces to that of the particle. For example, on the sintered FGB-20 glass beads with high degree of the sintering, the number of the observed traces on 50 particles was 196, which is too much if the all traces correspond to the necks.

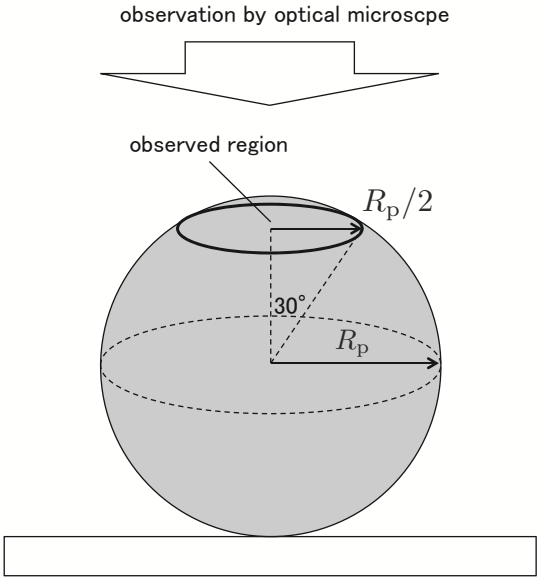

Figure 3.35: Observed region to find the trace of the necks on the glass beads. R_p represents the particle radius.

From geometrical consideration, more than one particles can not contact to a particle within the observed region. Furthermore, the number of the contacting particles on a particle (coordination number) is averagely 6.24 for randomly packed spheres (*Pinson et al.*, 1998), and the observed region corresponds to 6.7% of the whole surface area of a sphere. If the necks are randomly distributed on the particles, the number of necks observed per particle should 0.418 stochastically. Therefore, 21 (= 50 $\times$ 0.418) necks would be observed. The origin of excess number of the observed neck-like traces is considered to be originally existing large-scale roughness and/or dents generated during the breaking of the sintered sample. I assumed that these roughness or dents were smaller than the necks. To extract the necks from the observed traces, a trace with maximum size on individual particles was selected. Among them, the larger 21 traces were taken as the neck traces. This selection gives maximum size of the neck radius. The deduced histogram of the neck radius ratio is shown in Figure 3.37.

Averaged neck radius ratio and porosity of the sintered samples are shown in Table 3.9. The error in the neck radius ratio is taken as standard deviation of the neck radius histogram in Figure 3.37. As a result, the neck radius ratios between 0.075 to 0.30 were attained with the porosity maintaining almost constant around 0.41. The neck radius ratio became larger when increasing the degree of the sintering, as expected.

The measured thermal conductivity of the sintered glass beads are also listed

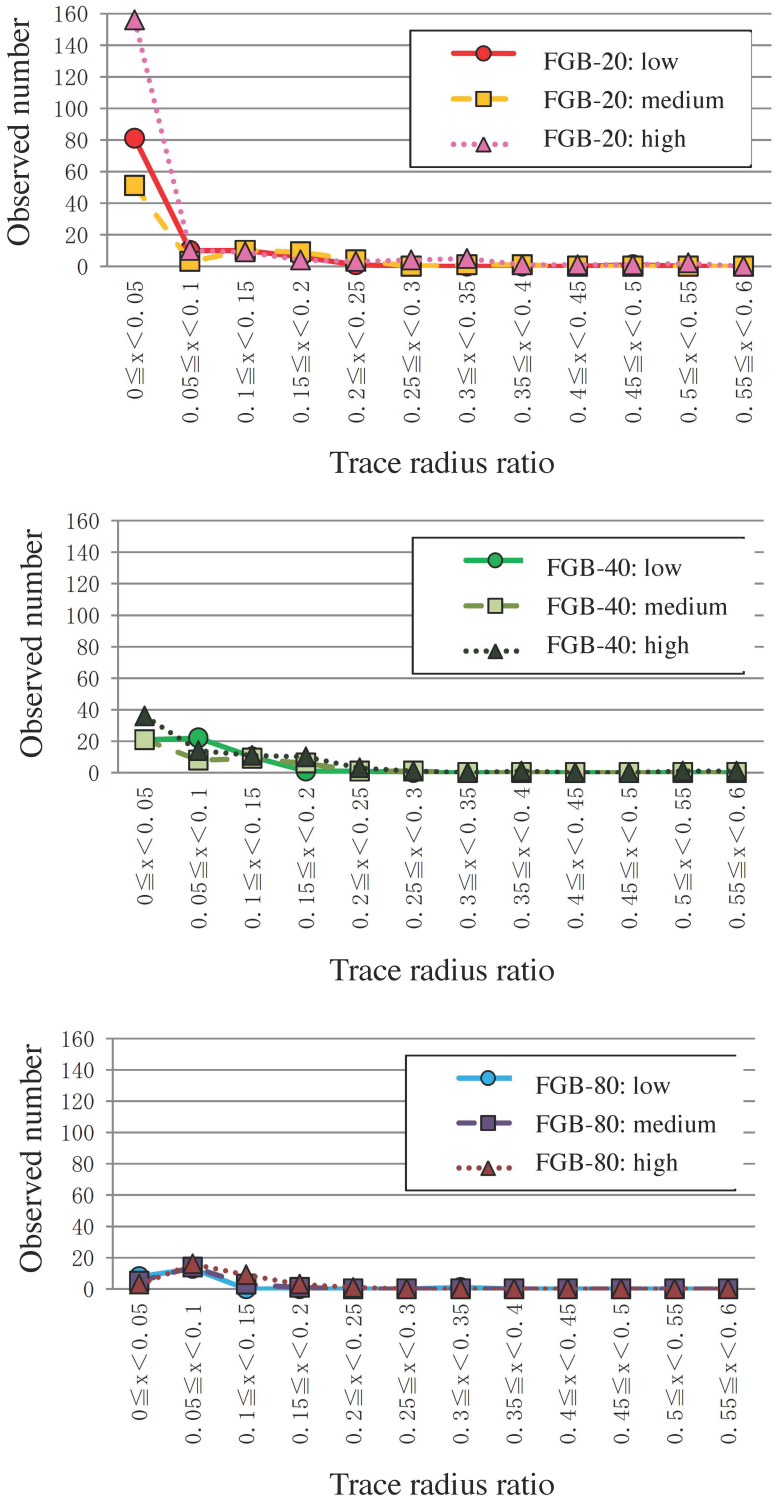

Figure 3.36: Histograms of the observed neck-like trace sizes on 50 particles. The terms of low, medium, and high in the legends represent the degree of the sintering (Table 3.8).

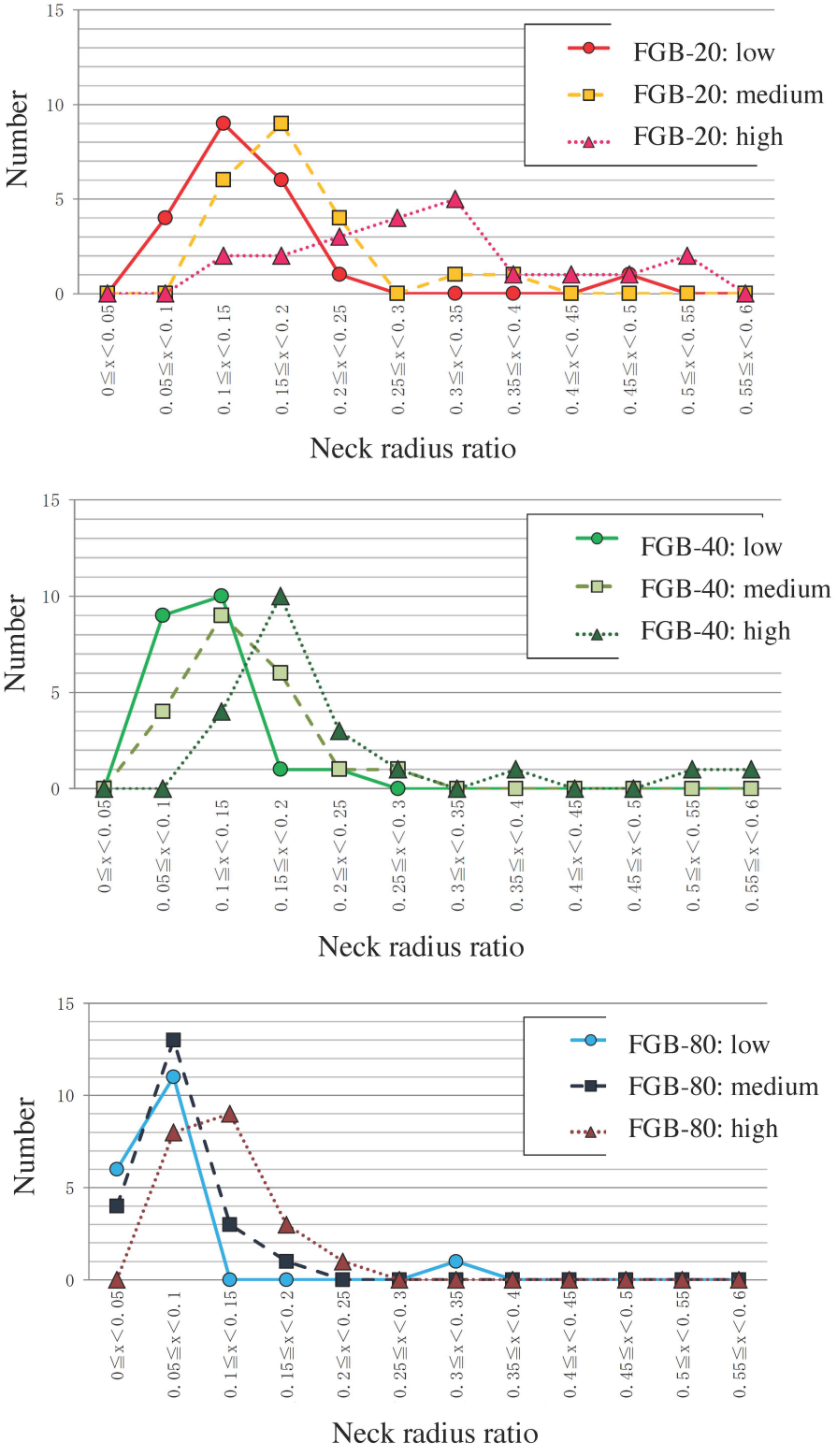

Figure 3.37: Estimated histograms of the neck radius ratio, extracted from Figure 3.36.

Table 3.9: Average neck radius ratio, porosity, and thermal conductivity of the sintered samples. Errors in the neck radius ratio represent standard deviation of the estimated neck size distribution (Figure 3.37). The averaged thermal conductivity values obtained by three points measurements are shown, taking differences of the averaged thermal conductivity from maximum and minimum values as superscript and subscript errors, respectively.

Sample	Degree of sintering	Neck radius ratio	Porosity	Thermal conductivity ($\times 10^{-2}$ W/mK)
FGB-20	low	0.151 ± 0.08	0.42	$8.8^{+0.8}_{-0.8}$
	medium	0.188 ± 0.066	0.44	$15.5^{+0.5}_{-0.5}$
	high	0.300 ± 0.109	0.40	$22.8^{+1.8}_{-2.3}$
FGB-40	low	0.109 ± 0.034	0.42	$6.9^{+0.4}_{-2.3}$
	medium	0.144 ± 0.051	0.41	$8.8^{+0.6}_{-1.2}$
	high	0.223 ± 0.124	0.40	$10.1^{+0.7}_{-0.9}$
FGB-80	low	0.075 ± 0.059	0.41	$4.0^{+0.4}_{-0.3}$
	medium	0.078 ± 0.029	0.40	$5.3^{+0.8}_{-0.9}$
	high	0.119 ± 0.036	0.39	$9.6^{+0.2}_{-0.2}$

in Table 3.9. Figure 3.38 shows the relation between the neck radius ratio and the thermal conductivity. It was found that the thermal conductivity increased with the neck radius ratio for each FGB sample. Although the data had large errors in the neck ratio, a linear relation between the thermal conductivity and neck radius ratio independent of the particle size was appeared, which is represented by,

$$k = 0.671x, \tag{3.29}$$

where x is the neck radius ratio. The proportionality to the neck radius is consistent with the finding from the compressional stress dependence for the unconsolidated glass beads, in which the solid conductivity is proportional to the radius of the contact area between the particles (Section 3.6).

To investigate the radiative contribution on the effective thermal conductivity of the sintered glass beads, the temperature dependence of the thermal conductivity of FGB-20 sintered glass beads with high degree of the sintering, which was prepared separately from the above experiments. The solid and radiative conductivity were separated by fitting the Equation (3.27) using Equation (3.1) as material conductivity k_{m}. This gave the solid coefficient $A = 0.144 \pm 0.003$ and the radiative coefficient $B = (3.53 \pm 14.3) \times 10^{-11}$ W/mK^4. The radiative coefficient was consistent with that of the unconsolidated FGB-20 glass beads (Table 3.4). Since the radiative conductivity at 300 K is about 0.0048 W/mK, the radiative contribution is negligible

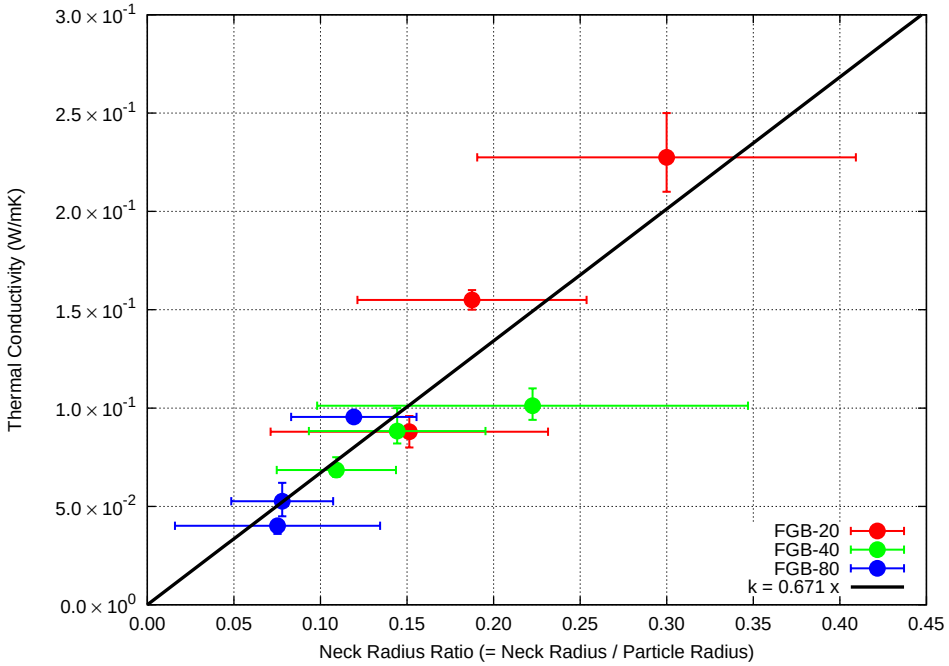

Figure 3.38: Thermal conductivity of the sintered glass beads as a function of the neck radius ratio. A linear fitting for all data is shown as a solid line.

compared with the solid conductivity. The temperature dependence of the effective thermal conductivity mainly attributed to that of the solid conductivity. Therefore, the thermal conductivity data shown in Figure 3.39 approximately represents the solid conductivity.

3.9 Summary of the experimental results

In this thesis, effects of temperature, particle size, porosity, compressional stress, particle size distribution, and degree of sintering, on the thermal conductivity of powdered materials were experimentally examined. The temperature-dependent data were utilized to derive the solid and radiative conductivities for each sample, which enabled us to investigate the parameter dependences of each conductivity.

From the experimental results on the compressional stress dependence for the unconsolidated glass beads and on the neck size dependence for the sintered glass beads, it was found that the solid conductivity is proportional to the radius of the contact area between the particles. Another finding from the measurements for the sintered glass beads was that the solid conductivity can be scaled by the ratio of the contact radius to the particle radius. Then, the solid conductivity is empirically

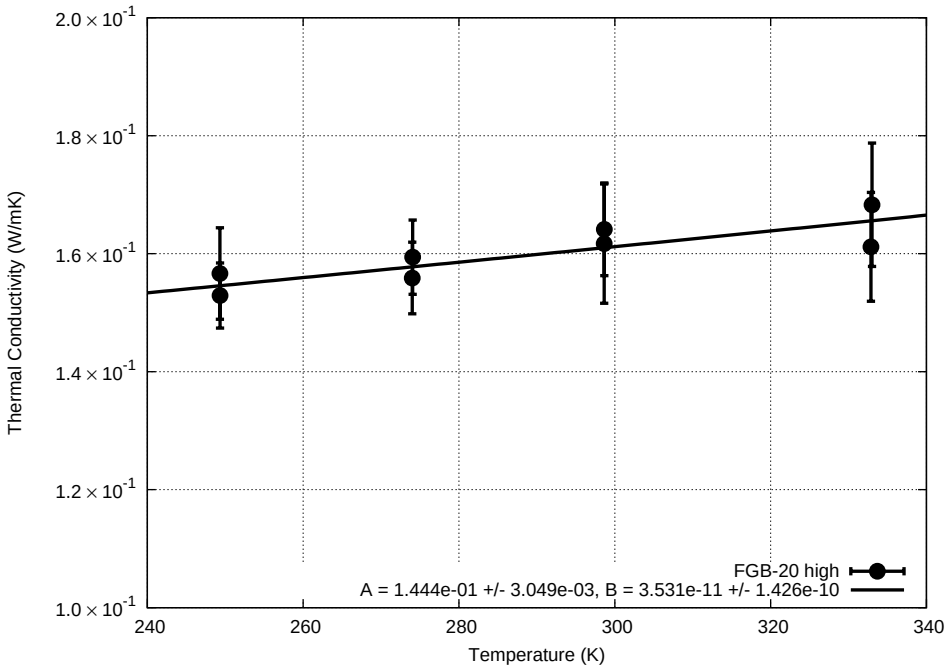

Figure 3.39: Temperature effect on thermal conductivity of highly sintered FGB-20 glass beads. In this experiment, a thermocouple was fixed only at the center of a nichrome wire (see Figure 3.33) and the thermal conductivity was measured twice at each temperature. A fitting result of Equation (3.27) is shown as a solid curve.

expressed as,

$$k_{\text{solid}} \propto \frac{r_c}{R_p}, \tag{3.30}$$

where r_c is the contact radius between the particles, and R_p is the particle radius.

In Figure 3.40, the solid conductivity coefficient A for the five FGB glass beads and EMB-49.5 glass beads is compared in terms of the particle diameter. It was found that the solid conductivity differed by an order of magnitude bewteen the EMB and FGB glass beads. Figure 3.41 shows photographs of the EMB, FGB-20, and FGB-180 glass beads by scanning electron microscope (SEM). The EMB glass beads had smooth surfaces. On the other hand, surfaces of the FGB glass particles were microscopically rough, and degree of the surface roughness seemed to differ by the samples. When the two spheres contact, existence of the surface roughness can reduce the contact area from that without the roughenss. The reduced contact area makes the contact conductance, or the solid conductivity, smaller. Moreover, the adhesive force between particles is weakened by the surface roughness, because of separation between the surfaces of the particles (*Gregory*, 1981; *Perko et al.*, 2001). The weakened adhesive force would also reduce the contact area. Thus, the rapid drop in the solid conductivity from the EMB to the FGB glass beads, as found in Figure 3.40, could be explained by the effects of the surface roughness and the related weakening of the adhesive force. The particle size dependence of the solid conductivity for the five FGB glass beads would be affected by the surface roughness.

As shown in Figure 3.16, the thermal conductivity was greatly scattered by the researchers, even when the particle size is the same. One of the causes of the scattered values might attribute to the difference in the surface roughness of the particles they used, if inherent errors from the experimental method and sample preparation are neglected. As the particles have roguher surfaces, the solid conductivity and resultant effective thermal conductivity become lower.

The radiative conductivity was dependent on the particle size (Figure 3.15) and porosity (Figure 3.21). The radiative conductivity of the powdered materials has been traditionally modeled by thermal radiation between two separated plates, as described in Section 2.2. The modeled radiative conductivity is proportional to effective distance for radiative heat transfer (or mean free path of the photon) L in Equation (2.12) (*Merrill*, 1969; *Gundlach and Blum*, 2012), which is characterized by typical void size between the particles. The void size is proportional to the particle size when the porosity is constant. Therefore, the radiative conductivity would be proprotional to the particle size, as found in Figure 3.15. When the particle size is constant, the void size, and the resultant radiative conductivity, would increase with the porosity, as found in Figure 3.21. Then, the particle size and porosity de-

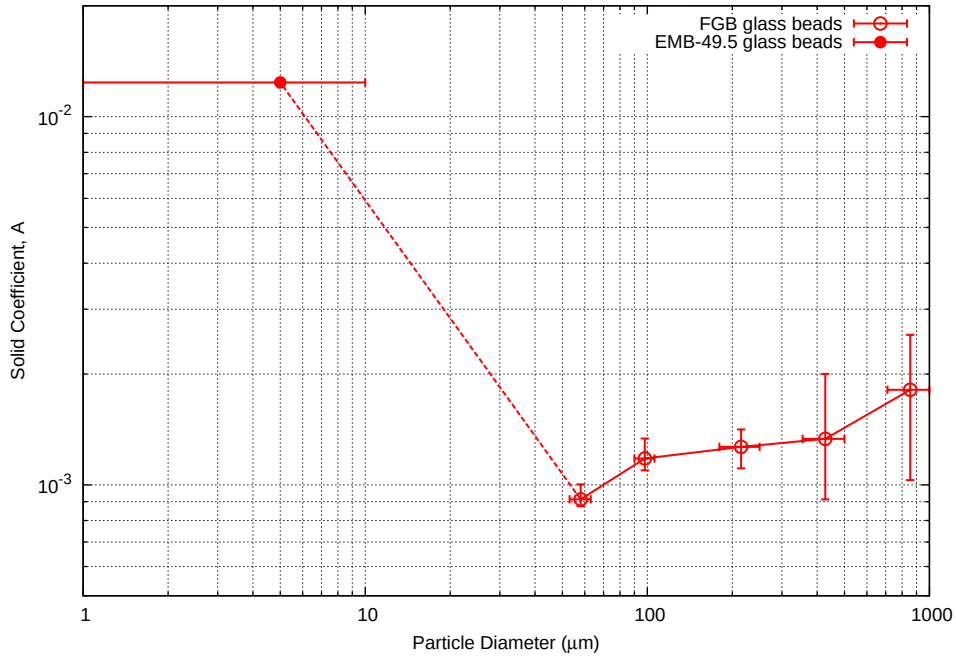

Figure 3.40: Solid coefficients for EMB-49.5 and FGB glass beads as a function of the particle diameter.

pendences of the radiative conductivity are described in terms of these dependences of the void size bewteen the particles.

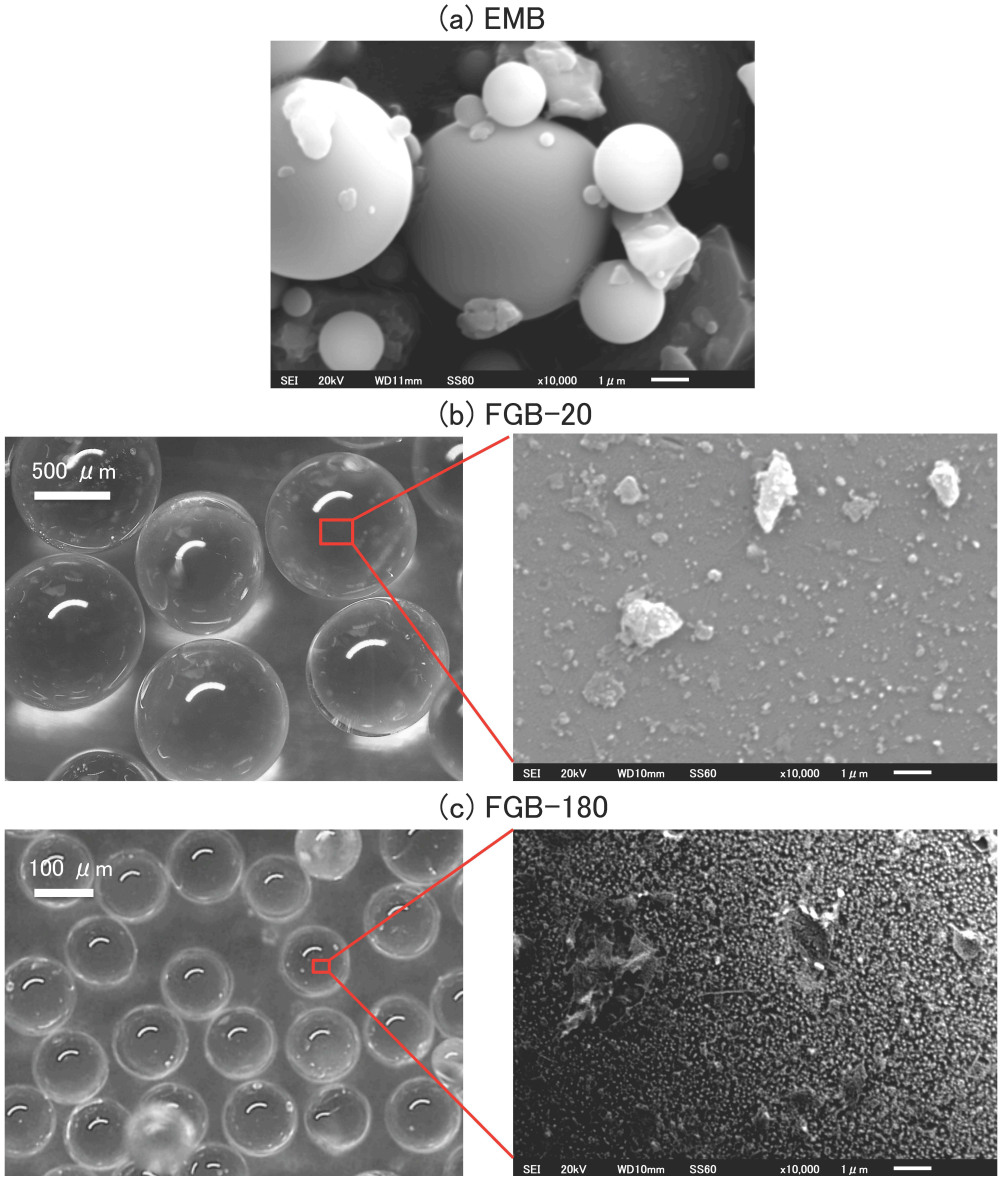

Figure 3.41: SEM images of the surface of the EMB, FGB-20, and FGB-180 glass beads. A scale bar of 1 μm is shown at the right bottom of each SEM image.

Chapter 4

Integrative model of thermal conductivity of powdered materials

In this chapter, a thermal conductivity model for powdered materials under vacuum conditions is developed. The conductive and radiative heat transfers are assumed to take place in parallel, so that the effective thermal conductivity is expressed as the sum of the solid and radiative conductivities as,

$$k = k_{\mathrm{solid}} + k_{\mathrm{rad}}. \tag{4.1}$$

The solid and radiative conductivities are modeled independently.

4.1 Solid conductivity model

Consider equal-sized spheres packed homogeneously in a cubic container with unit length and unit cross-sectional area, as shown in Figure 4.1. One-dimensional heat flow is given from the bottom to the top of the sphere bed. Solid conductivity is equivalent to bulk thermal conductance of the bed, which can be formulated as N_{A} parallel connections and N_{L} serial connections of thermal conductance of single sphere. N_{A} is the number of the spheres per unit area perpendicular to the heat flow direction, and N_{L} is the number of the spheres per unit length along it. Then, the solid conductivity model is given by,

$$k_{\mathrm{solid}} = \frac{N_{\mathrm{A}}}{N_{\mathrm{L}}} H, \tag{4.2}$$

where H is thermal conductance of single particle. It includes the thermal conductance through inter-particle contact points, H'_{c}, and that within a particles, H_{p}, as,

$$H = \frac{1}{\frac{1}{H'_{\mathrm{c}}} + \frac{1}{H_{\mathrm{p}}}}. \tag{4.3}$$

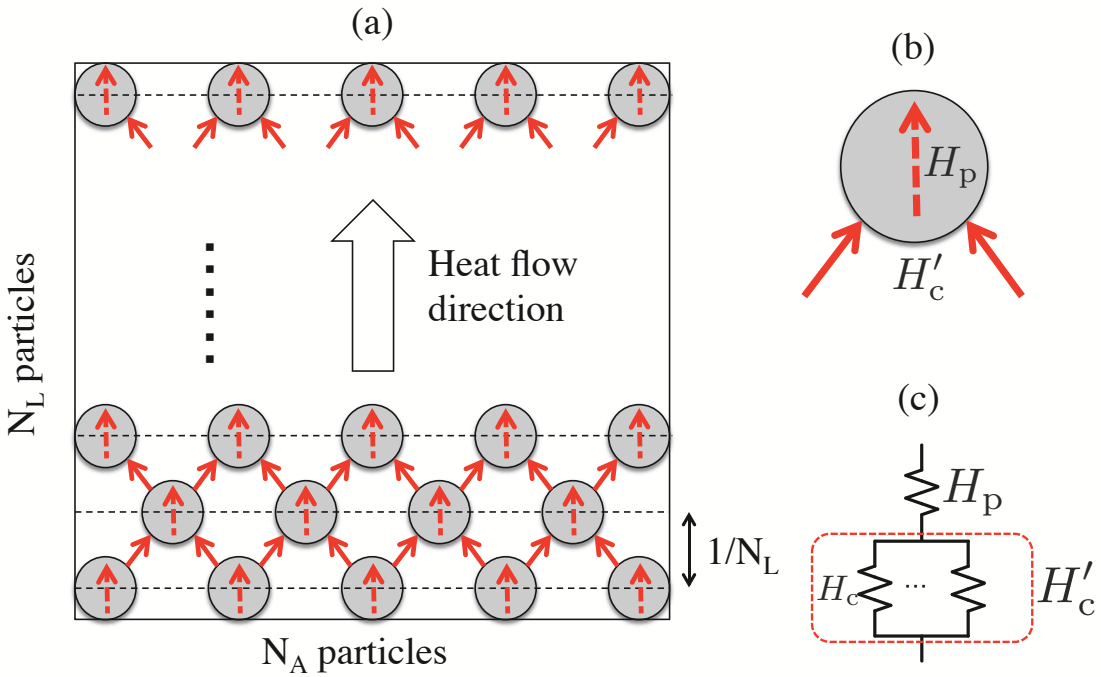

Figure 4.1: (a) Illustration of the solid conductivity model. Thermal conductivity can be formulated by N_L serial and N_A parallel connections of thermal conductance of unit cell (b). H_p shows thermal conductance within a particle and H'_c is total contact conductance, calculated as parallel connection of single contact conductance H_c. A thermal conductance model of the unit cell is shown in the right bottom (c).

Typically for powdered materials, the contribution of H_p is negligible compared with H_c', because $H_c' \ll H_p$. Then, Equation (4.3) can be approximated as,

$$H \approx H_c'. \tag{4.4}$$

H_c' is written by parallel connections of the conductance at the contact points, H_c. Assuming that all contacts have the same thermal conductance (or the same contact area),

$$H_c' = \frac{C}{2}\frac{2}{\pi}H_c, \tag{4.5}$$

where C is the number of particles contacting a particle (coordination number). The factor $2/\pi$ comes from correction of the contact conductance to that along the net heat flow direction (see below). Thus, the solid conductivity of Equation (4.2) reduces to the following equation.

$$k_{solid} = \frac{N_A}{N_L}\frac{C}{2}\frac{2}{\pi}H_c. \tag{4.6}$$

The number of the spheres in unit volume, N, can be written in terms of particle radius R_p and porosity ϕ as,

$$N = \frac{1-\phi}{\frac{4}{3}\pi R_p^3}, \tag{4.7}$$

For a three-dimensionally homogeneous packing, N_L can be expressed as $N^{1/3}$. However, at the porosity larger than 0.476, N_L becomes smaller than $1/2R_p$, which means that the distance between the two adjacent particle layers along the heat flow direction becomes larger than the particle diameter. In such a case, any particles can not contact each other, and the heat can not conduct to the next particles. To avoid this problem, assume that the gravity acts along the heat flow direction and the particle layers does not separate vertically. In this situation, the minimum values of N_L is $1/2R_p$, equivalent to that of the simple cubic packing structure. In this study, N_L for the face centered cubic structure is adopted,

$$N_L = \frac{\sqrt{3}}{2\sqrt{2}R_p}. \tag{4.8}$$

Then, effect of the porosity on the number of particles is imposed on N_A as

$$N_A = \frac{N}{N_L} = \frac{\sqrt{6}(1-\phi)}{2\pi R_p^2}. \tag{4.9}$$

When the porosity increases, N_A and the resultant solid conductivity from Equation (4.6) decrease.

The coordination number C also depends on the porosity. In this study, a result of numerical simulation by *Suzuki et al.* (1980) is used. Their model predicts that the coordination number C decreases with the porosity ϕ as,

$$C = \frac{2.812(1-\phi)^{-1/3}}{f^2(1+f^2)}, \tag{4.10}$$

where $f = 0.07318 + 2.193\phi - 3.357\phi^2 + 3.194\phi^3$.

The contact conductance H_c depends on size of the contact area. When two spheres make a contact by external normal force F, the radius of the contact area follows the Hertzian theory, which predicts that the contact radius r_c is written by,

$$r_{c,\mathrm{hertz}} = \left[\frac{3}{4}\frac{1-\nu^2}{E}FR_p\right]^{1/3}, \tag{4.11}$$

where ν is Poisson's ratio, E is Young's modulus (*Timoshenko and Goodier*, 1951). Beside the external force F, adhesive force can work between the particles, which also make finite contact area. *Johnson et al.* (1971) expanded the Hertzian theory by including the effect of the adhesive force (JKR theory) as,

$$r_c = \left[\frac{3(1-\nu^2)}{4E}\left\{F + 6\pi\gamma R_p + \sqrt{12\pi\gamma R_p F + (6\pi\gamma R_p)^2}\right\}R_p\right]^{1/3}, \tag{4.12}$$

where γ is surface energy of solid materials. When $\gamma = 0$, the JKR theory of Equation (4.12) becomes equivalent to the Hertzian theory of Equation (4.11). The external force F acting on a particle is calculated in terms of the compressional stress σ as,

$$F = \frac{\sigma}{N^{2/3}} = \left(\frac{4\pi}{3(1-\phi)}\right)^{2/3} R^2\sigma. \tag{4.13}$$

The factor $1/N^{2/3}$ corresponds to mean area (including surrounding void space) of a particle. When the compressional stress σ in the powdered media attributes to the self-weight of the particles, it is written as,

$$\sigma = \rho_m(1-\phi)gz, \tag{4.14}$$

where ρ_m is true density of the solid particle, g is gravitational acceleration, and z is depth.

The contact conductance H_c is estimated by approximating two contacting spheres by two circular cylinders with radius of R_p contacting with a circular area of $\pi {r_c}^2$ (Figure 4.2). When heat flux is given perpendicular to the contact face and R_p is sufficiently larger than r_c, the contact conductance H_c is proportional to the radius of contacting area, r_c, as

$$H_c = 2k_m r_c, \tag{4.15}$$

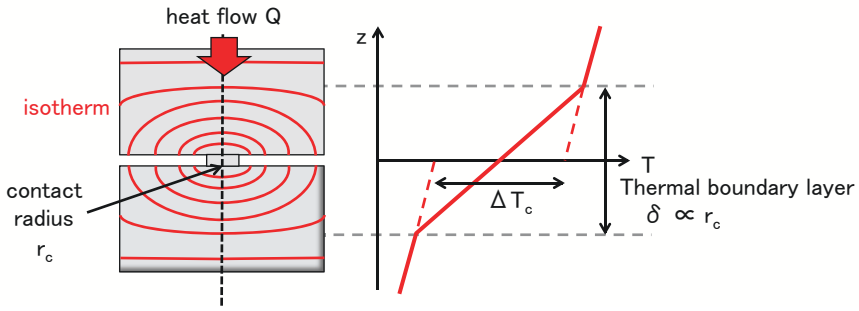

Figure 4.2: Isotherm in the two contacting solids. Right figure shows approximated temperature distribution along the center line perpendicular to the contact face.

where k_{m} is the thermal conductivity of the contacting material (*Cooper et al.*, 1969). The proportionality to the radius, not to the area, can be explained as the following dimensional analysis. The contact thermal conductance is defined as,

$$H_c = \frac{Q}{\Delta T}, \tag{4.16}$$

where Q is heat flow through the bodies, and ΔT is the temperature difference across the contact. The heat flux across the contact is $q = Q/\pi r_{\mathrm{c}}^2$. The thickness of the thermal boundary layer δ can be scaled by the contact radius r_{c} if horizontal scale of the solid bodies is sufficiently larger than the contact area ($R_{\mathrm{p}} \gg r_{\mathrm{c}}$). The temperature difference ΔT is calculated from the Fourier's law as,

$$\Delta T = q\frac{\delta}{k_{\mathrm{m}}} \approx \frac{Q}{\pi r_{\mathrm{c}}^2}\frac{r_{\mathrm{c}}}{k_{\mathrm{m}}} \propto \frac{Q}{r_{\mathrm{c}}}, \tag{4.17}$$

Substituting Equation (4.17) into Equation (4.16), the proportionality of the contact conductance to the contact radius ($H_{\mathrm{c}} \propto r_{\mathrm{c}}$) is proved. This theoretical result is consistent with the experimental results on the compressional stress dependence for the unconsolidated glass beads and on the neck size dependence for the sintered glass beads.

Using the contact radius predicted from Equation (4.12), the contact conductance can be calculated. Note that the JKR and Hertzian theory assumed perfectly smooth surface of the contacting material. In practice, however, particles have rough surfaces as shown in Figure 3.41, which would make the contact area smaller than that for the smooth particles. In order to explain the effect of the surface roughness on the solid conductivity, I introduce a correction factor ξ for the contact radius. For the particles with surface roughness, the contact radius reduces to ξr_{c} ($\xi \leq 1$). For perfectly smooth surface, $\xi = 1$. Using the corrected contact radius, the contact conductance H_{c} is re-written as,

$$H_{\mathrm{c}} = 2k_{\mathrm{m}}\xi r_{\mathrm{c}}. \tag{4.18}$$

This expression for H_c is satisfied when the heat flow direction is perpendicular to the contact face. In the conduction model of the powdered materials, thermal conductance along the heat flow is lower than H_c, since the contact faces tilt against the net heat flow directions. Assuming the contact angle relative to the one-dimensional heat flow direction is randomly distributed surrounding a sphere, the contact conductance is corrected by a factor of $2/\pi (= \int_0^\pi \sin\theta d\theta / \int_0^\pi d\theta)$. For this reason, the factor of $2/\pi$ arose in Equation (4.5).

Using the above equations, one can calculate the solid conductivity by giving the parameters of k_m, R_p, ϕ, E, ν, γ, σ, and ξ. One can calculate the solid conductivity as,

$$k_{solid} = 2k_m(1-\phi)C\frac{\xi r_c}{R_p}. \tag{4.19}$$

The solid coefficient, which is the normalized solid conductivity by the material conductivity, is then,

$$A = 2(1-\phi)C\frac{\xi r_c}{R_p}. \tag{4.20}$$

The effect of the porosity comes from the factor $(1-\phi)C$. The solid conductivity is proportional to the ratio of the inter-particle contact radius to the particle radius. In other words, the solid conductivity is inversely proportional to the particle size, if the contact size stays constant. This dependence comes from the particle size dependence of $N_A(\propto 1/R_p^2)$ and $N_A(\propto 1/R_p)$. This feature is consistent with the experimental result for the sintered glass beads (Figure 3.38 in Section 3.8), by which the solid conductivity was found to be proportional to the neck radius ratio.

For unconsolidated powdered materials, the particle size dependence of the contact size and the resultant solid conductivity differ by what kinds of the contact force acts bewteen the particles. If the particles are not adhesive and the contact force is only the external compressional stress, the contact radius is proportional to the particle radius from Equations (4.11) and (4.13). In this case, the solid conductivity is independent of the particle size. Inversely, giving that the particles are adhesive and external force and/or self-weight are negligible compared to the inter-particle adhesive force, the contact radius is proportional to the particle radius with an exponent of 2/3 from Equation (4.12). In this case, the solid conductivity decreases with the particle size with an exponent of $-1/3$. The highest solid conductivity observed for the smallest μm-sized EMB glass beads (Figure 3.40), would attribute the adhesive force, which is more predominant for the smaller particle size. On the other hand, an increase in the solid conductivity with the particle size observed for the five FGB glass beads (hollow circles in Figure 3.40) cannot be caused by the either effects of the self-weight or the adhesive foce. As discussed in Section 3.9, it would reflect the effect of the surface roughness of individual particles (Figure 3.41). Therefore,

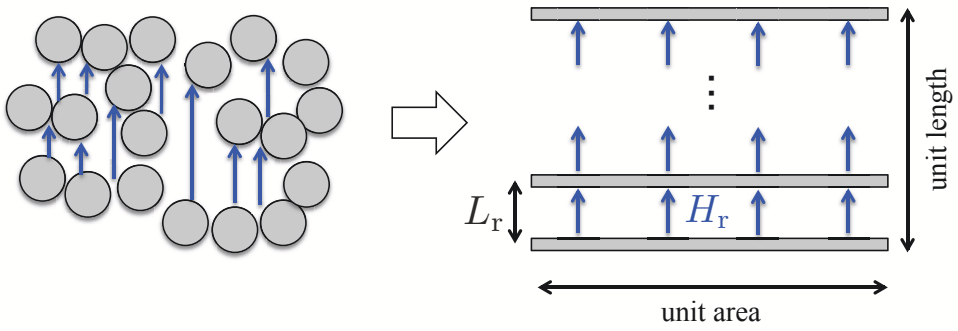

Figure 4.3: Illustration of a radiative conductivity model. L_r is distance between infinitely-thin planes and H_r is thermal conductance by radiative heat transfer between the two adjacent planes.

installation of the factor ξ in the solid conductivity model plays important role in the interpretation of the experimental results for the FGB glass beads.

4.2 Radiative conductivity model

Radiative heat transfer through the volid spaces in the powdered media is modeled by one-dimensional thermal radiation between multiple infinitely-thin parallel planes, as illustrated in Figure 4.3. It is assumed that two adjacent planes have temperature difference of ΔT, and the planes or particles is opaque for the thermal radiation. The thermal conductance between two planes by the thermal radiation, H_r, can be calculated as,

$$H_r = \frac{\varepsilon}{2-\varepsilon}\sigma_{SB}[(T+\Delta T)^4 - T^4]\frac{1}{\Delta T} = 4\frac{\varepsilon}{2-\varepsilon}\sigma_{SB}T^3, \tag{4.21}$$

where ε is emissivity, σ_{SB} is the Stefan-Boltzmann constant, and T is temperature of a colder plane. With L_r being distance between two adjacent planes, the number of the layers in unit length is $1/L_r$. The radiative conductivity of this layered media can be expressed as multiple serial connections of the radiative conductance H_r as,

$$k_{rad} = L_r H_r = 4\frac{\varepsilon}{2-\varepsilon}\sigma_{SB}L_r T^3. \tag{4.22}$$

L_r represents effective distance for the radiative heat transfer. It can be scaled by characteristic length of the void space in the powdered media.

In homogeneous packing of equal-sized spheres, the void volume per particle is calculated from particle radius R_p and porosity ϕ as,

$$V = \frac{\phi}{N} = \frac{4}{3}\pi R_p^3 \frac{\phi}{1-\phi}, \tag{4.23}$$

where N is the number of the spheres in unit volume given by Equation (4.7). By approximating this typical void volume by that of a sphere with the diameter of D_{v}, the typical void length can be formulated as,

$$D_{\mathrm{v}} = 2\left(\frac{\phi}{1-\phi}\right)^{1/3} R_{\mathrm{p}}. \tag{4.24}$$

I introduce a factor ζ to scale the typical void length D_{v} to the effective distance for the radiative heat transfer L_{r}, so that,

$$L_{\mathrm{r}} = \zeta D_v = 2\zeta\left(\frac{\phi}{1-\phi}\right)^{1/3} R_{\mathrm{p}}. \tag{4.25}$$

By substituting Equation (4.25) into Equation (4.22), the radiative conductivity can be formulated as,

$$k_{\mathrm{rad}} = 8\frac{\varepsilon}{2-\varepsilon}\sigma_{\mathrm{SB}}\zeta\left(\frac{\phi}{1-\phi}\right)^{1/3} R_{\mathrm{p}}T^3, \tag{4.26}$$

and the radiative conductivity coefficient becomes,

$$B = 8\frac{\varepsilon}{2-\varepsilon}\sigma_{\mathrm{SB}}\zeta\left(\frac{\phi}{1-\phi}\right)^{1/3} R_{\mathrm{p}}. \tag{4.27}$$

The modeled radiative conductivity is proprotional to the particle size, since the void length (Equation 4.24) is proportional to it. In a similar way, the increase in the radiative conductivity with the porosity attributes the enhancement of the void size. They are consistent with the experimental results (Figure 3.15 and 3.21).

Table 4.1: Parameters used for comparing the model with the experimental data.

Parameter	Symbol	FGB glass beads	EMB glass beads	Regolith simulant
Particle diameter	$2R_p$	855 μm for FGB-20 427.5 μm for FGB-40 215 μm for FGB-80 98 μm for FGB-180 58 μm for FGB-300	5 μm	74 μm
Porosity	ϕ	0.40	0.495-0.862	0.43
True density	ρ_m	2480 kg/m^3	2600 kg/m^3	2990 kg/m^3
Material conductivity at 300 K	k_m	1.11 W/mK	1.56 W/mK	2.5 W/mK
Young's mudulus	E	71.6 GPa	71.6 GPa	78.0 GPa
Poisson's ratio	ν	0.23	0.23	0.25
Surface energy	γ	0.0 J/m^2 for non-adhesive model 0.02 J/m^2 for adhesive model		
Depth	z	1 cm only for the uncompressed experiments		
Emissivity	ε	0.89	0.89	0.9

4.3 Comparison with the experimental results

The effective thermal conductivity of all samples measured in this study, except for the metallic beads, was divided into the solid and radiative conductivities using the temperature-dependent data. In this section, the solid and radiative conductivity models are compared with the experimental results. The parameters used for the model calculation for FGB glass beads, EMB glass beads, and regolith simulant, are listed in Table 4.1.

4.3.1 Solid conductivity

Whether the samples used in this study were adhesive or nonadhesive is unknown. The adhesive force is characterized by the surface energy (Equation 4.12). For the FGB glass beads, EMB glass beads, and regolith simulant, the surface energy of γ = 0.02 J/m^2, which is typical for SiO_2 (*Gundlach et al.*, 2011), is used for the cases of adhesive particles. The nonadhesive case is represented by giving $\gamma = 0$ J/m^2.

The solid conductivity of the FGB glass beads is calculated as a function of the particle diameter in Figure 4.4. The correction factor of the contact radius ξ was set to unity. If the particles are nonadhesive, the constant solid coefficient of 0.0027 is calculated. On the other hand, when the adhesive force is taken into account, the solid coefficient is enhanced up to 0.0084 for the particle diameter of 100 μm. The adhesive force becomes more effective on the solid conductivity for the smaller particles.

It was found that the solid conductivity model was higher than any experimental data for the FGB glass beads. The lower experimental values can be reasonably explained by the effect of the surface roughness observed on the FGB glass particles (Figure 3.41). The roughness makes the contact radius smaller than that of smooth particles, whose effect can be expressed in term of the factor ξ. The values of ξ for respective samples are listed in Table 4.2. If the non-adhesive model is adopted, ξ ranges from 0.33 to 0.96. On the other hand, ξ becomes lower, from 0.09 to 0.56 for the adhesive model. The lower values of ξ are obtained for smaller particles, which might reflect the fact that the smaller beads had more dense roughness (Figure 3.41).

The solid conductivity of the EMB glass beads expected from the model is shown in Figure 4.5 as a function of the porosity. The modeled solid conductivity decreased by two orders of magnitude with the porosity from 0.4 to 0.9. The non-adhesive model was an order of magnitude lower than the experimental values. It can not be explained by the surface roughness, because $\xi \leq 1$. The adhesive model agreed well with the experimental results for the EMB glass beads. The model developed in this study can predict the solid conductivity with uncertainty of

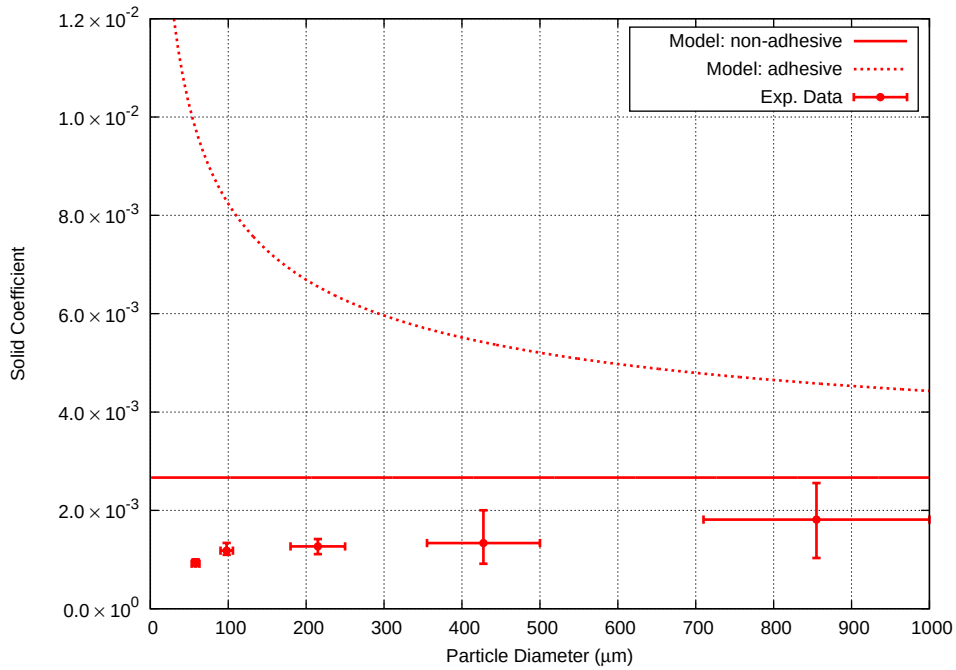

Figure 4.4: Model calculation of the solid coefficient as a function of the particle diameter, compared with the experimental results shown in Figure 3.15. The solid line is for nonadhesive case (γ = 0 J/m^2) and the dashed curve is for adhesive (γ = 0.02 J/m^2), with $\xi = 1$.

Table 4.2: Values of ξ to be matched with the experimental solid coefficients for FGB glass beads determined from Figure 4.4. The ranges shown in parentheses correspond to the experimental error bars shown in Figure 4.4.

	nonadhesive case ξ = 0 J/m^2	adhesive case ξ = 0.02 J/m^2
FGB-20	0.68 (0.39-0.96)	0.40 (0.23-0.56)
FGB-40	0.50 (0.34-0.75)	0.25 (0.17-0.37)
FGB-80	0.48 (0.42-0.53)	0.19 (0.17-0.22)
FGB-180	0.44 (0.41-0.50)	0.14 (0.13-0.16)
FGB-300	0.34 (0.33-0.38)	0.09 (0.09-0.10)

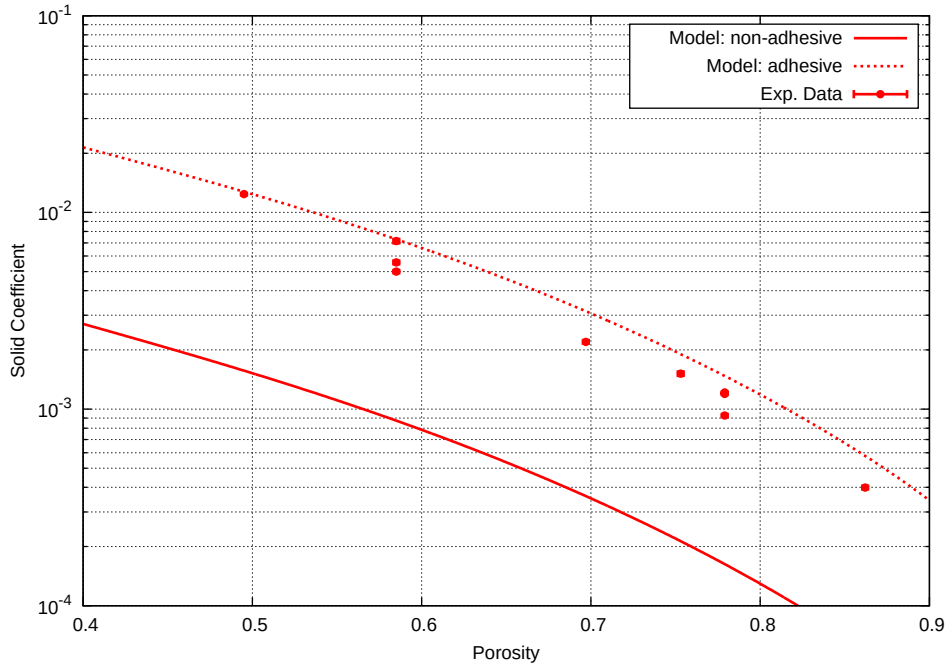

Figure 4.5: Model calculation of the solid coefficient as a function of the porosity, compared with the experimental results shown in Figure 3.21. The solid line is for nonadhesive case ($\gamma = 0$ J/m^2) and the dashed curve is for adhesive ($\gamma = 0.02$ J/m^2), with $\xi = 1$.

Table 4.3: Model estimations of the solid coefficient for the uncompressed regolith simulant. Fitted ξ values are shown in the right column.

Model estimation	Measured	ξ
2.32×10^{-3} (nonadhesive)	1.47×10^{-3}	0.63
7.48×10^{-3} (adhesive)		0.20

less than 50%.

The solid conductivity for the regolith simulant calculated from the non-adhesive and adhesive models are shown in Table 4.3. As is the case for the FGB glass beads, the model estimations were higher than the experimental values. If these differences are assumed to attribute the surface roughness parameter ξ, $\xi = 0.63$ (nonadhesive case) and 0.20 (adhesive case) were obtained.

Figure 4.6, 4.7, and 4.8 show estimations of the compressional stress dependence of the solid conductivity for the FGB-20 glass beads, FGB-180 glass beads, and regolith simulant, respectively. Similar to the uncompressed data, the experimental values were lower than the calculated. The best fitted values of ξ are listed in Table 4.4. For the non-adhesive case, the values of ξ for the FGB-20 and FGB-180 glass beads are consistent with those determined form the uncompressed data

Table 4.4: Values of ξ to fit the compressional stress dependent solid conductivity for the FGB-20, FGB-180, and regolith simulant. See also Figure 4.6, 4.7, and 4.8.

	nonadhesive (ξ = 0 J/m^2)	adhesive (ξ = 0.02 J/m^2)
FGB-20	0.79	0.72
FGB-180	0.47	0.35
Regolith simulant	0.40	0.31

in Table 4.2. On the other hand, if the adhesive model is adopted, the values of ξ are higher than those for the uncompressed data. For the regolith simulant, the adhesive model can be well fitted by giving $\xi = 0.31$ rather than the non-adhesive model.

The thermal conductivity of the sintered glass beads can be also estimated using the solid conductivity model in terms of the contact radius ratio (r_c/R_p) in Equation (4.19). In Figure 4.9, the model calculated form Equation (4.19), are compared to the experimental data (Figure 3.38). It was found that the model showed higher thermal conductivity and larger slope than the experimental data. In the derivation of Equation (4.19), thermal conduction within the particles was neglected, by assuming the contact conductance H_c' is sufficiently lower than the conductance within the particle H_p. This assumption is applicable for the unconsolidated powders. For the sintered powders, the effect of the thermal conductance within the particles can not be neglected compared to the contact conductance, because the neck formation enhances the contact conductance.

Effect of the thermal conductance within the particles H_p on the effective solid conductivity k_{solid} is roughly quantified below. For simplicity, I approximate H_p as the conductance within a cube, whose volume is equivalent to that of a sphere, $V_p = 4\pi R_p^3/3$, with R_p being the particle radius. Then, the following equation on H_p can be derived,

$$H_p = k_m \frac{V_p^{2/3}}{V_p^{1/3}} = \left(\frac{4\pi}{3}\right)^{1/3} R_p k_m. \tag{4.28}$$

Using Equation (4.3), the solid conductivity model including the effect of the intra-particle conduction can be written by,

$$k_{solid} = \frac{N_A}{N_L} H = \frac{N_A}{N_L} \frac{1}{1/H_c' + 1/H_p}. \tag{4.29}$$

By giving the same expressions for N_A, N_L, and H_c' as described in Section 4.1, the revised solid conductivity model is also plotted in Figure 4.9. Since H_p is proportional to the particle radius as well as H_c', the revised solid conductivity model is also independent of the particle radius. If the contact radius ratio is less than about 0.05, the solid conductivity is determined dominantly by the contact conductance.

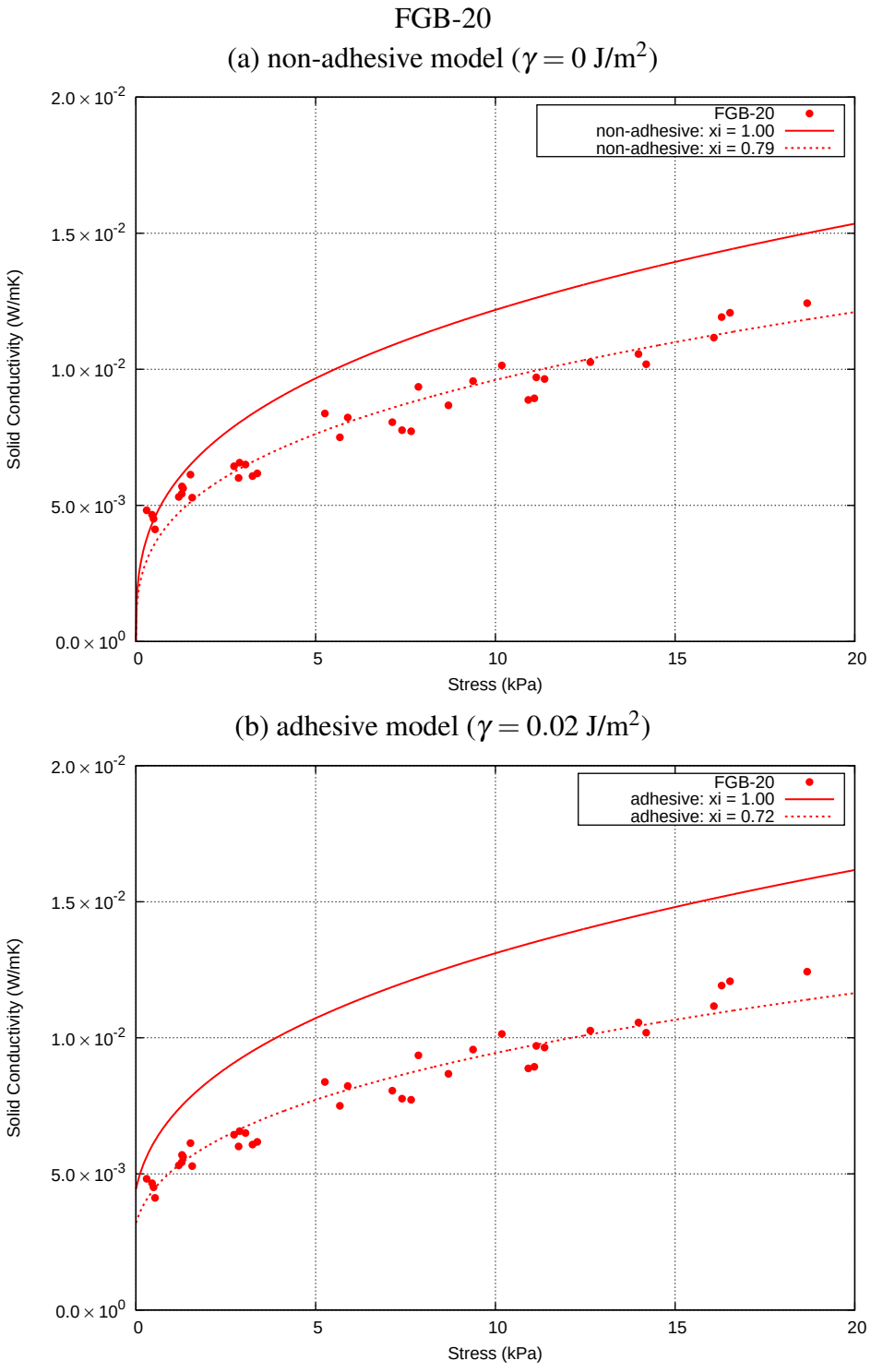

Figure 4.6: Comparison between the solid conductivity models and the experimental results on the compressional stress dependence for the FGB-20 glass beads. The solid curves represent the model with $\xi = 1$. The dashed curves show the fitting result via ξ.

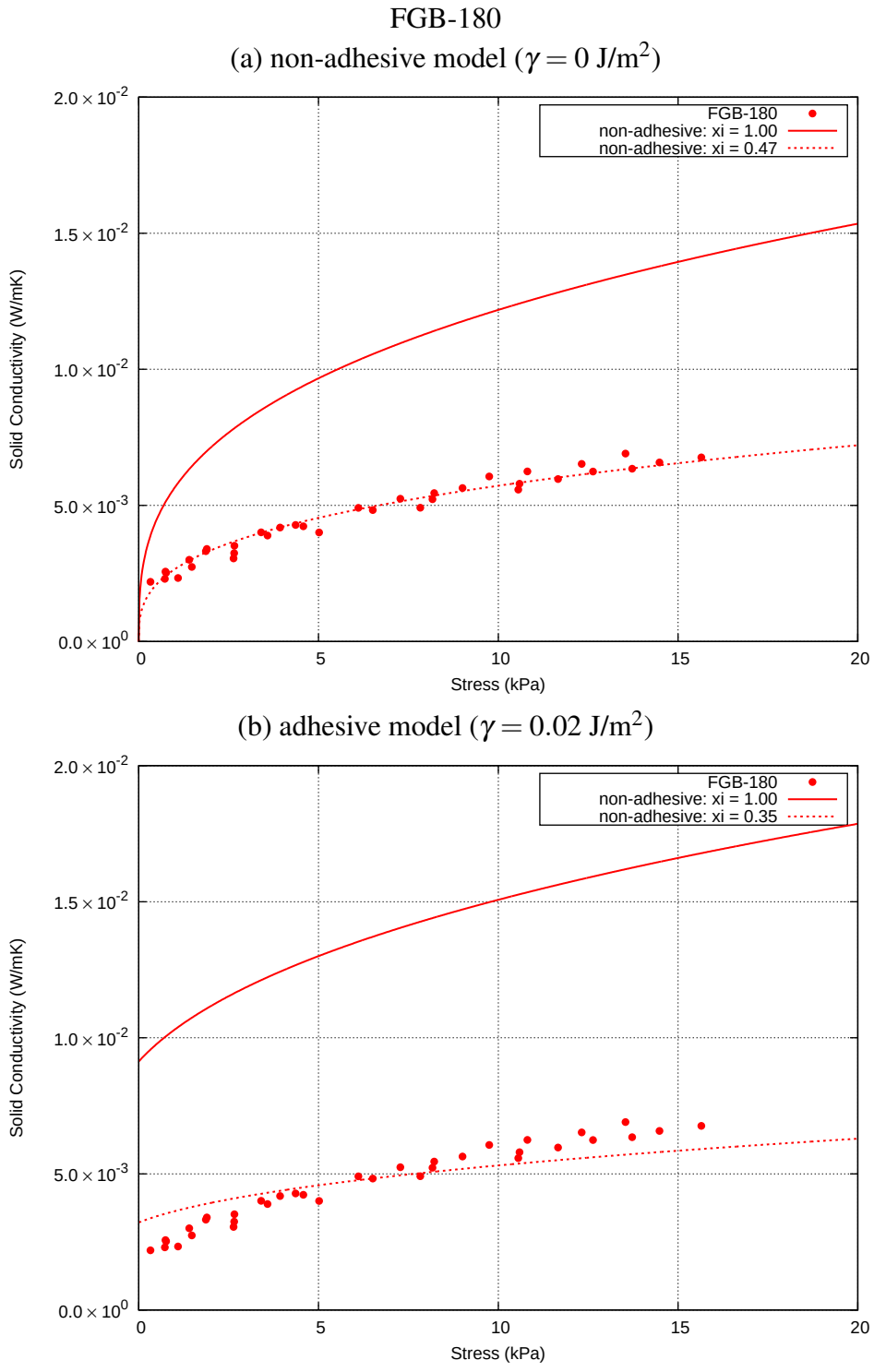

Figure 4.7: Comparison between the solid conductivity model and the experimental results on the compressional stress dependence for the FGB-180 glass beads. The solid curves represent the model with $\xi = 1$. The dashed curves show the fitting result via ξ.

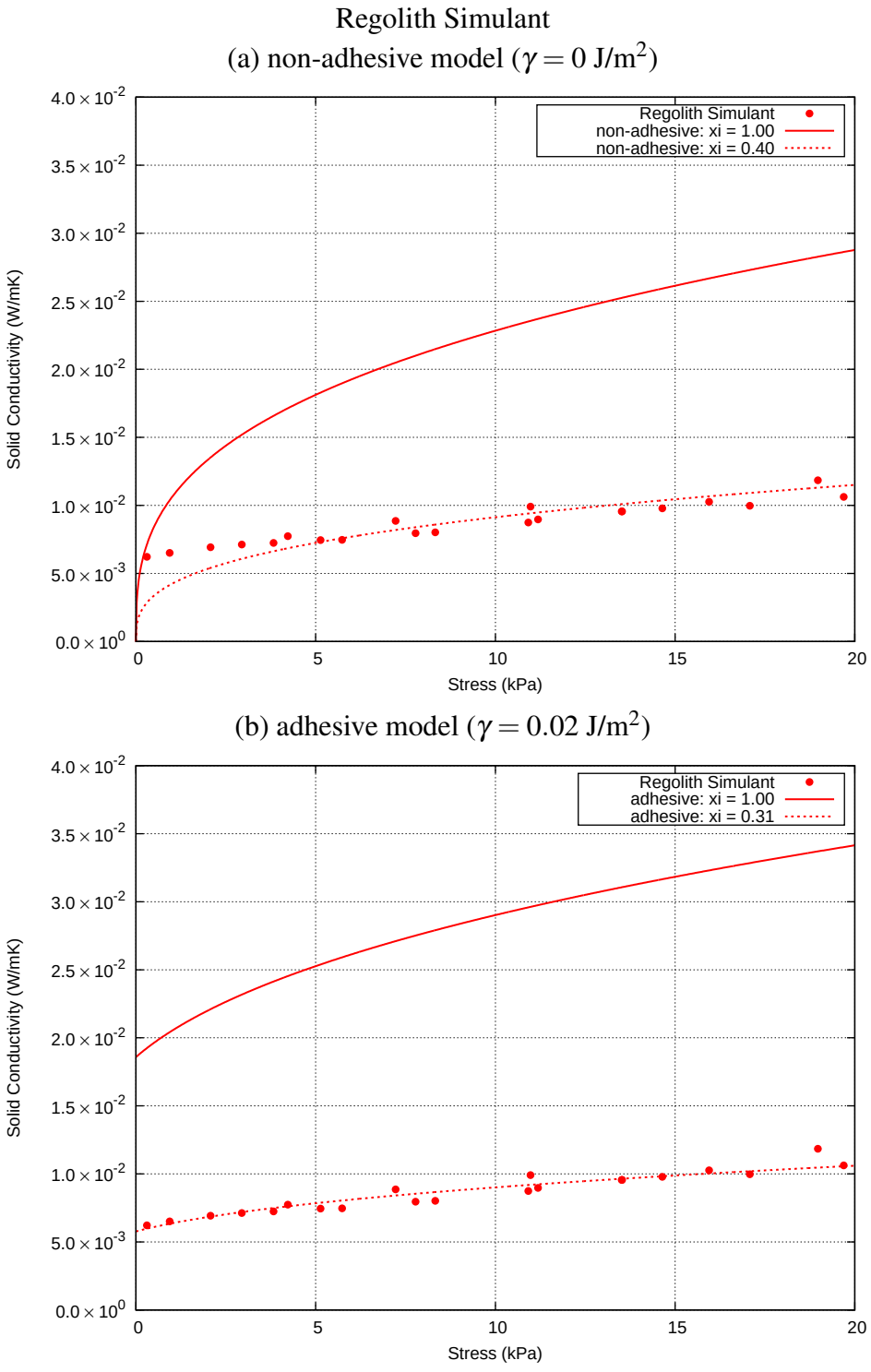

Figure 4.8: Comparison between the solid conductivity model and the experimental results on the compressional stress dependence for the regolith simulant. The solid curves represent the model with $\xi = 1$. The dashed curves show the fitting result via ξ.

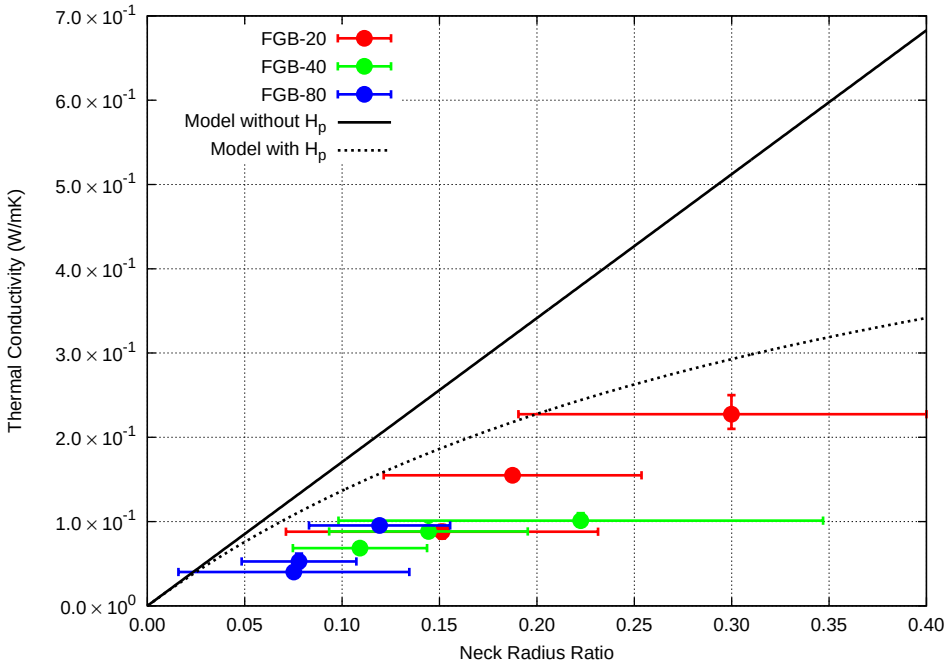

Figure 4.9: Comparison between the solid conductivity model and the experimental data for the sintered FGB glass beads. The radiative conductivity is neglected, since it is sufficiently smaller than the solid conductivity for the sintered sample. Solid line represents the model without the thermal conductance within the particles H_p, calculated from Equation (4.19). Dashed curve represents the model with H_p in addition to the contact conductance H_c', using Equation (4.29).

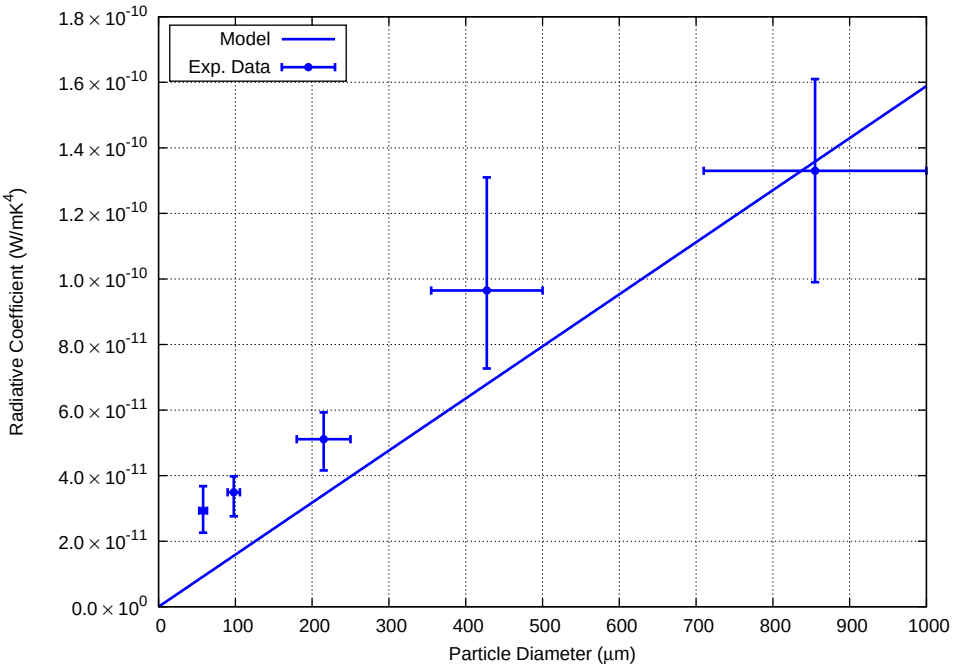

Figure 4.10: Model calculation of the radiative coefficient, with $\zeta = 1$, as a function of the particle diameter, compared with the experimental results shown in Figure 3.15.

The intra-particle conductance becomes more effective as the contact radius ratio (or the contact conductance) increases. Thus, the above mentioned difference between the model and the experimental data for the sintered glass beads would be explained by the non-negligible effect of the conduction within the particles. From Figure 4.9, the revised model is still higher than the experimental values. Note that the effect of the intra-particle conduction depends on the geometrical assumption for the derivation of H_{p}. More realistic assumption will be required in the future work.

4.3.2 Radiative conductivity

The radiative conductivity can be calclated form Equation (4.26) in terms of temperature, particle radius, porosity, and emissivity. Figure 4.10 shows comparison between model and expreimental data on the radiative conductivity at 300 K for the FGB glass beads as a function of the particle diameter, with $\zeta = 1$. The calculated radiative conductivity agreed well with the overall trend of the experimental data. In a strict sense, the value of ζ differed by the particle size. Table 4.5 shows the best fitted values of ζ. It seemed to increase with decreasing the particle size. The cause of this trend is discussed in the next section.

The modeled radiative conductivity for the EMB glass beads is shown in Fig-

Table 4.5: Values of ζ to be matched with the experimental radiative coefficients for FGB glass beads from Figure 4.10. The ranges shown in parentheses represent possible ranges due to the experimental error (or heterogeneity).

Sample	ζ
FGB-20	0.98 (0.73-1.19)
FGB-40	1.42 (1.07-1.93)
FGB-80	1.50 (1.22-1.74)
FGB-180	2.24 (1.77-2.56)
FGB-300	3.18 (2.45-3.99)

ure 4.11 as a function of the porosity. The experimental data are restricted to the sieved samples (EMB-86.2, EMB-77.9, EMB-75.3, and EMB-69.5), because the compressed EMB-49.5 and EMB-58.5 showed significant heterogeneity in the radiative conductivity (Section 3.4). The model with $\zeta = 1$ showed an order of magnitude lower radiative conductivity than the experimental values, which means underestimate of the effective radiative distance. Figure 4.12 shows optical micrographs of the top surface of the EMB glass beads sieved through the 53 μm mesh (corresponding to EMB-86.2, EMB-77.9, and EMB-69.5) and 500 μm mesh (EMB-75.3). As seen in these photos, the individual particles form larger sized aggregates and large voids exist between the aggregates. It is expected that the radiative heat transfer though these larger voids would be effective than that through the smaller voids between the individual particles. Enhancement of the effective radiative distance from the geometrical estimate of the void size, in which the homogeneous packing of the individual particles was assumed, can be expressed by the factor $\zeta = 15$.

Maximum size of the aggregate would be limited by mesh size of the sieve. For the EMB-86.2, EMB-77.9, and EMB-69.5, the size of the aggregates seemed uniform about 50 μm (Figure 4.12a), ten times larger than the EMB particle diameter. Since the ratio of the aggregate size to the particle size (≈ 10) was roguhly consistent with the fitting value of $\zeta = 15$, it is indicated that the effective radiative distance can be characterized by the aggregate size, not by the individual particle size. On the other hand, although the EMB-75.3 sample was sieved through the larger mesh of 500 μm (100 times larger than the individual particle size) its radiative conductivity can be fitted by the same factor of $\zeta = 15$. A photo of 500 μm sieved sample (Figure 4.12b) showed that the size of the aggregates is not uniform, which would make the void size between the aggregates, and therefore the radiative conductivity, smaller.

For the regolith simulant, the radiative coefficient of 1.25×10^{-11} is calculated from the model with $\zeta = 1$. This is slightly lower than the experimentally deter-

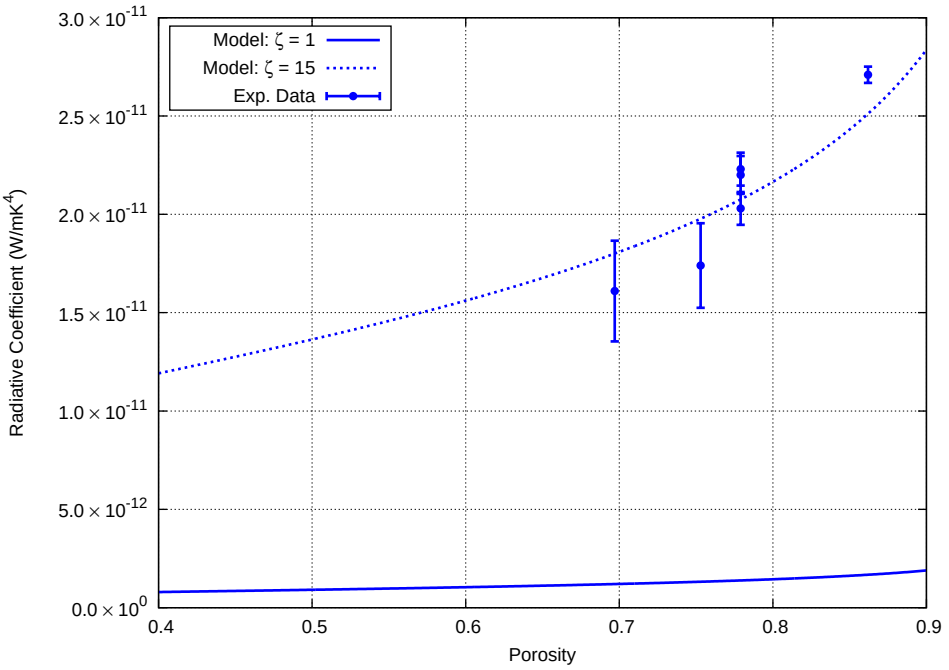

Figure 4.11: Model estimation of the radiative coefficient as a function of the porosity. The compared experimental data are shown in Figure 3.21. Solid curves represents the model with $\zeta = 1$. A radiative conductvity model with $\zeta = 15$ (dashed curve) can be well fitted to the experimental data.

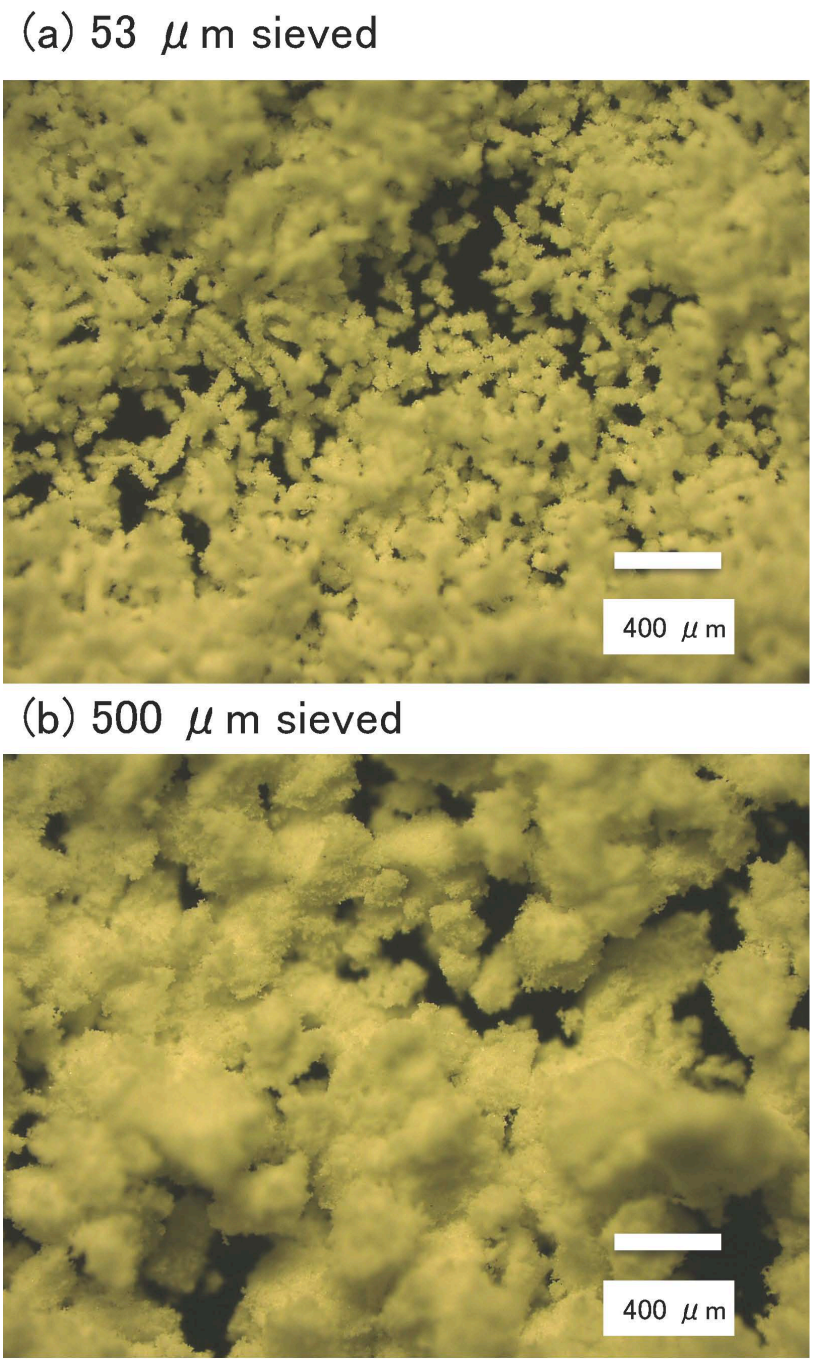

Figure 4.12: Optical micrographs of the sieved EMB samples.

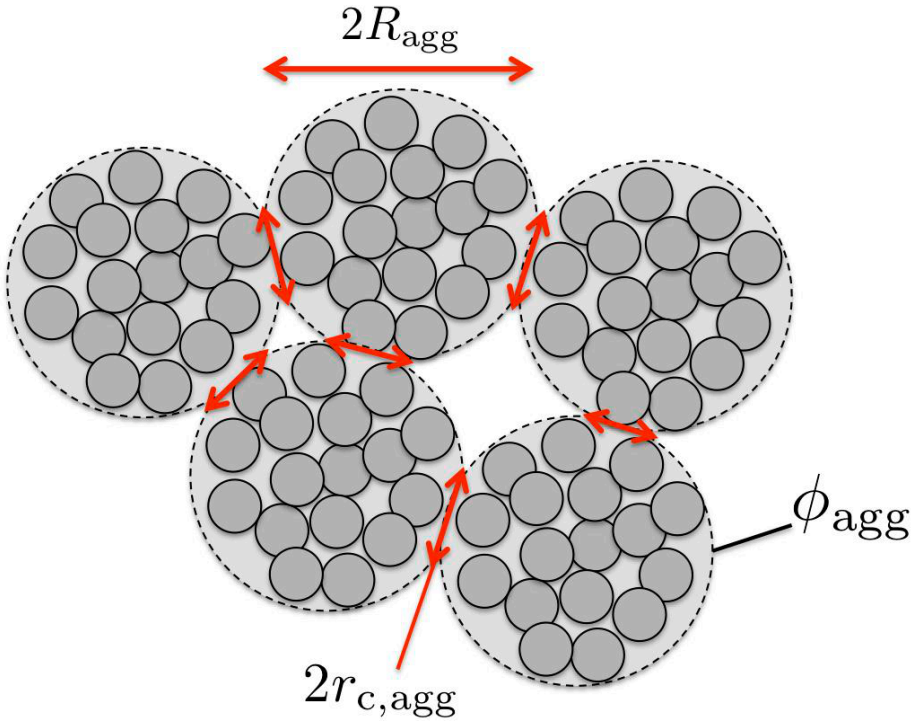

Figure 4.13: Model of a packing of aggregates. R_{agg} is radius of the aggregates, and $r_{\mathrm{c,agg}}$ is contact radius between the aggregates. Porosity of individual aggregates ϕ_{agg} is defined in Figure 4.14.

mined values of $B = 2.63 \times 10^{-11}$ (Section 3.5). $\zeta = 2.1$ is adequate for the regolith simulant.

4.4 Discussion

Effect of the aggregation on the solid conductivity

In Section 4.3.2, it was suggested that the radiative conductivity is affected by the aggregation. On the other hand, the solid conductivity data was well consistent with the model, which assumed homogeneous packing. The aggregation seemed not to affect the solid conductivity significantly.

Figure 4.13, shows a schematic model of packing of the aggregates. The individual aggregates have radius of R_{agg} and porosity of ϕ_{agg}. Difinition of three kinds of the porosity is illustrated in Figure 4.14. The bulk porosity of the powdered materials ϕ is related to the porosity of the individual aggregates ϕ_{agg} and porosity of

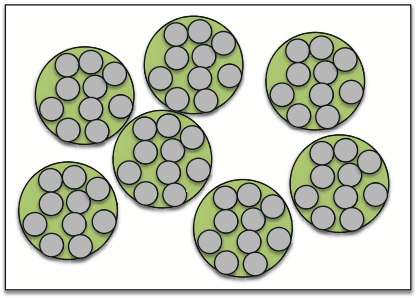

$$(1-\phi) = (1-\phi_{\mathrm{agg}})(\phi_{\mathrm{pack,agg}})$$

bulk porosity

$$\phi = \frac{\square + \square}{\square + \square + \square}$$

porosity of an aggregate

$$\phi_{\mathrm{agg}} = \frac{\square}{\square + \square}$$

porosity of packing structure of aggregates

$$\phi_{\mathrm{pack,agg}} = \frac{\square}{\square + \square + \square}$$

Figure 4.14: Difinition of bulk porosity ϕ, porosity of individual aggregates ϕ_{agg}, and porosity of packing structure of the aggregates $\phi_{\mathrm{pack,agg}}$. Gray; individual particle. Green; void within the aggregates. White; Void between the aggregates.

the packing structure of the aggregates $\phi_{\mathrm{pack,agg}}$ as,

$$(1-\phi) = (1-\phi_{\mathrm{agg}})(1-\phi_{\mathrm{pack,agg}}). \tag{4.30}$$

If the individual aggregates have the solid conductivity of k_{agg}, the effective solid conductivity of the packing of the aggregates can be modeled using Equation (4.19) as,

$$k_{\mathrm{solid}} = 2k_{\mathrm{agg}}(1-\phi_{\mathrm{pack,agg}})C(\phi_{\mathrm{pack,agg}})\frac{r_{\mathrm{c,agg}}}{R_{\mathrm{agg}}}, \tag{4.31}$$

where $r_{\mathrm{c,agg}}$ is the effective contact radius between the aggregates, which includes the void space among aggregate-aggregate contact faces. Above equation indicates that the solid conductivity is independent of the size of the aggregates when the contact radius ratio $r_{\mathrm{c,agg}}/R_{\mathrm{agg}}$ is taken as a constant, similar to the solid conductivity of the sintered glass beads. Let us call this model "structual model" and the original one "homogeneous model".

The porosity and thermal conductivity of the individual aggregates, ϕ_{agg} and k_{agg}, are unknown. Assume that $\phi_{\mathrm{agg}} = 0.495$ (maximum compression of the EMB glass beads attained in this study), and corresponding thermal conductivity of $k_{\mathrm{agg}} = 0.02$ W/mK. In Figure 4.15, the solid conductivity of the aggregates packing is calculated as a function of the bulk porosity by giving the contact radius ratios between the aggregates $r_{\mathrm{c,agg}}/R_{\mathrm{agg}}$ = 0.1, 0.2, and 0.3. The structural model included the effect of the conduction within the aggregates, as done for the sintered glass beads (Equations 4.28 and 4.29). The structual model with $r_{\mathrm{c,agg}}/R_{\mathrm{agg}} = 0.2$ agreed with the experimental values. It was also found that there was less difference between the homogeneous model and the structual model with $r_{\mathrm{c,agg}}/R_{\mathrm{agg}} = 0.2$.

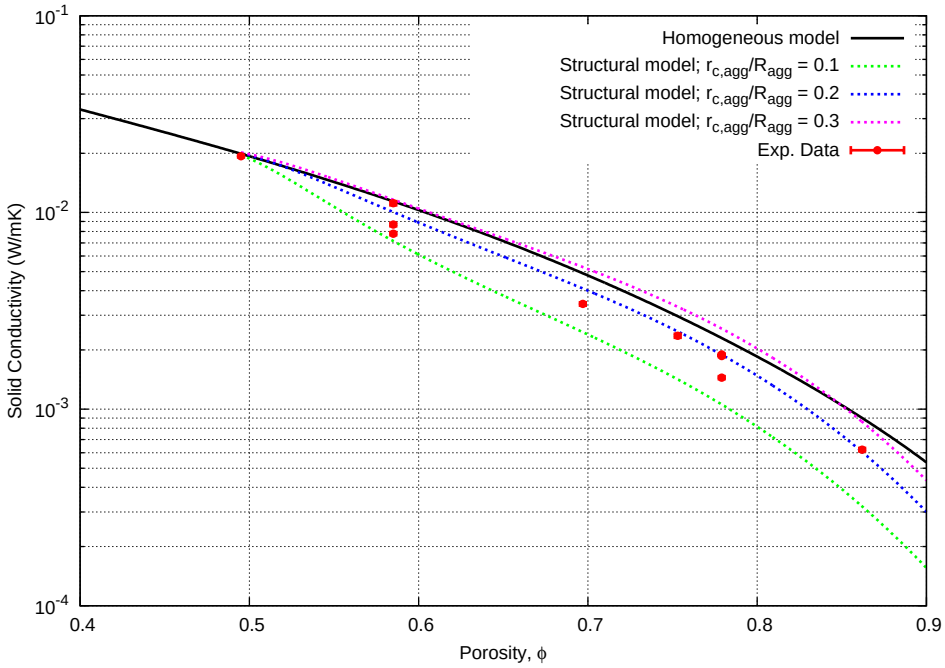

Figure 4.15: The structural solid conductivity models (dashed curve) for the aggregate packing compared to the homogeneous model (solid curve) and the experimental data. In the structural model, $\phi_{\mathrm{agg}} = 0.495$ and $k_{\mathrm{agg}} = 0.02$ W/mK are assumed. Three kinds of the structural models are shown with different contact radius ratios bewteen the aggregates, $r_{\mathrm{c,agg}}/R_{\mathrm{agg}}$ = 0.1, 0.2, and 0.3.

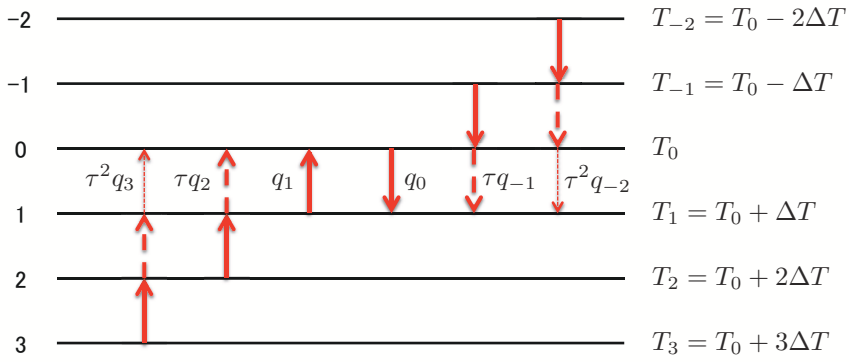

Figure 4.16: Radiative heat transfer in the semi-transparent parallel planes See text for definitions of the parameters.

In practice, the contact radius ratio $r_{\mathrm{c,agg}}/R_{\mathrm{agg}}$ would differ by the aggregate size and structural packing porosity of the aggregates. Whether the ratio of $r_{\mathrm{c,agg}}/R_{\mathrm{agg}} = 0.2$ is realistic is unknown. Moreover, as mentioned before, the aggregates found in the EMB-75.3 sample did not have the uniform size. The effect of the size distribution can not be modeled in the present state.

Effect of particle size on ζ

As mentioned in Section 4.3.2, the scaling factor of the radiative heat transfer distance ζ seemed to increase with decreasing the particle size (Table 4.5). One of the possible examinations of this trend is that the smaller particles are not opaque against the thermal radiation, or electromagnetic wave. For the derivation of the radiative conductivity, the particles were assumed to be completely opaque, i.e., assuming the transmittance τ equals to zero.

First, effect of the semi-transparent nature of the particles on the radiative conductivity is discussed. As a simple example, consider six parallel planes as shown in Figure 4.16. Each plane has the transmittance of τ. By neglecting the reflection on the plane surface, net heat exchange between the plane 0 and 1 is,

$$\begin{aligned} q &= q_1 + \tau q_2 + \tau^2 q_3 - q_0 - \tau q_{-1} - \tau^2 q_{-2} \\ &= (q_1 - q_0) + \tau(q_2 - q_{-1}) + \tau^2(q_3 - q_{-2}), \end{aligned} \tag{4.32}$$

where $q_i = \varepsilon\sigma_{SB}T_i^4$ is the radiative heat flux from the i-th plane. By approximating $(T_0 + n\Delta T)^4 \approx T_0^4 + 4nT_0^3\Delta T$ with n being integers ($\Delta T \ll T_0$), the net heat flux between the two planes can be calculated as,

$$q = 4\varepsilon\sigma_{SB}(5\tau^2 + 3\tau + 1)T_0^3\Delta T. \tag{4.33}$$

The radiative conductivity within the semi-transparent layers is defined by,

$$k_{\mathrm{rad},\tau} = q\frac{L_\mathrm{r}}{\Delta T} = 4\varepsilon\sigma_{SB}(5\tau^2+3\tau+1)L_\mathrm{r}T_0^3, \tag{4.34}$$

where L_r is the distance between the two planes. If the planes are opaque for the thermal radiation, the radiative conductivity is equivalent to the original model of Equation (4.22), except for the term on the emissivity (ε or $\varepsilon/(2-\varepsilon)$). Therefore, the radiative conductivity enhances by a factor of $5\tau^2+3\tau+1$ due to the additional transmitted energy from the other planes. If $2n$ semi-transparent planes are considered, the enhancement factor ζ becomes

$$\zeta = \sum_{i=0}^{n}(2n+1)\tau^n. \tag{4.35}$$

The radiative conductivity of the FGB-300 glass beads, for example, was larger than the opaque model by the factor of 3.18 (ζ in Table 4.5). If this factor is all contributed from the transparent nature of the glass particles, the transmittance of 0.35 is required.

Next, the transmittance of the particles is estimated by approximating a particle by a thin slab, whose thickness is comparable to the particle diameter. When the thermal radiation enters on a semi-transparent slab perpendicular to the slab surface, spectral transmittance of the slab is written by the following equation,

$$\tau_\lambda = \exp(-\frac{4\pi k_\mathrm{a} d}{\lambda}), \tag{4.36}$$

where k_a is a coefficient representing the energy adsorption within the solid material (imaginary part of complex index of refraction), d is thickness of the slab, and λ is wavelength of the incident light (*Modest*, 2013). This relation holds if $d \gg \lambda$ (in the region whose optical characteristics are determined by the geometric optics). Using the data on the values of k_a for soda-lime glass obtained by *Rubin* (1985), the spectral transmittance is plotted in Figure 4.17. As shown in this figure, the transmittance is higher for the thinner slab, or smaller particles. The spectral transmittance strongly depends on the wavelength in the infrared region. Therefore, total or integrated transmittance depends on the incident power spectral.

To estimate the total transmittance, thermal radiation from a slab with the temperature of 300 K emitted into another slab is considered. The emitted powder spectral can be calculated as,

$$I_\lambda(\lambda,T) = \varepsilon_\lambda I_{\mathrm{b},\lambda}(T,\lambda) = \varepsilon_\lambda \frac{2hc^2}{\lambda^5(\mathrm{e}^{hc/\lambda kT}-1)}, \tag{4.37}$$

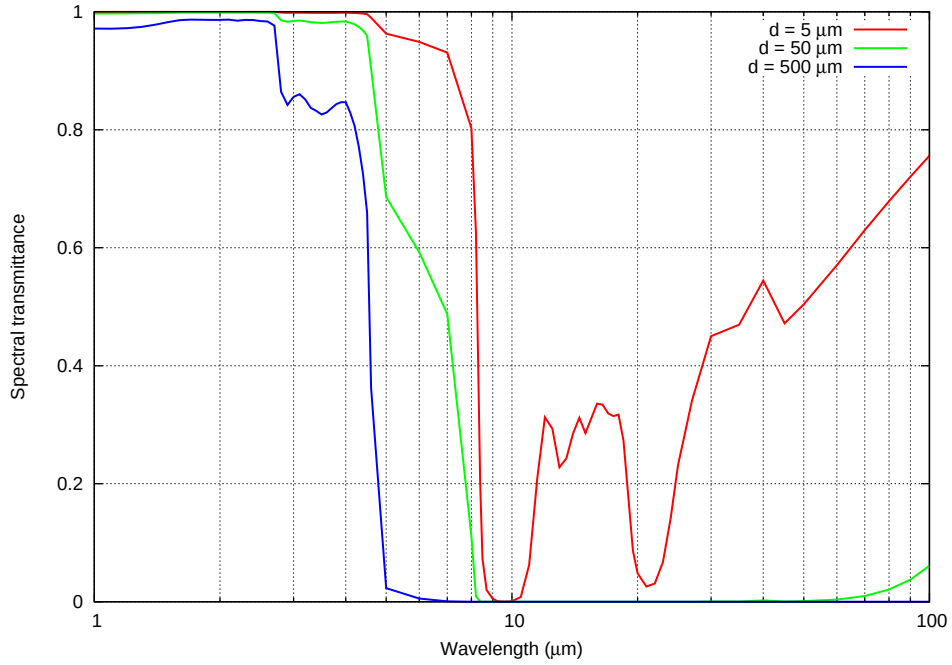

Figure 4.17: Spectral transmittance of soda-lime glass calculated from Equation (4.36) using k_a from *Rubin* (1985). The slab thickness values of d = 5, 50, and 500 μm are given.

where ε_λ is spectral emissivity, $I_{b,\lambda}$ is black body emissive power given by the Plank's law, h is the Plank's constant, c is the speed of light, k_B is the Boltzmann constant. The total transmittance is defined as,

$$\tau = \frac{\int_\lambda \tau_\lambda I_\lambda d\lambda}{\int_\lambda I_\lambda d\lambda}. \tag{4.38}$$

The spectral transmittance τ_λ, adsorptance α_λ, and reflectance ρ_λ are related each other as, $\tau_\lambda + \alpha_\lambda + \rho_\lambda = 1$. For simplicity, the reflectance ρ_λ is set to zero. The Kirchhoff's law states that $\varepsilon_\lambda = \alpha_\lambda$. Therefore, the spectral emissivity is calculated by $\varepsilon_\lambda = 1 - \tau_\lambda$ using the spectral transmittance given by Equation (4.36).

Figure 4.18 shows the total transmittance calculated from Equation (4.38) as a function of the slab thickness. For comparison, the transmittance calculated from Equation (4.35) using experimentally determined values of ζ for the FGB glass beads (Table 4.5) is also plotted. It can be seen that the estimated total transmittance of the glass is lower than the transmittance required to enhance the radiative conductivity by the factor of ζ. It means that the effect of the particle size on the observed values of ζ can not be explained by the semi-transparent nature of the smaller particles.

Note that Equation (4.36) can be adopted in the geometrical optics regime ($d \gg \lambda$). The black body spectral has the peak intensity around the wavelength of 10

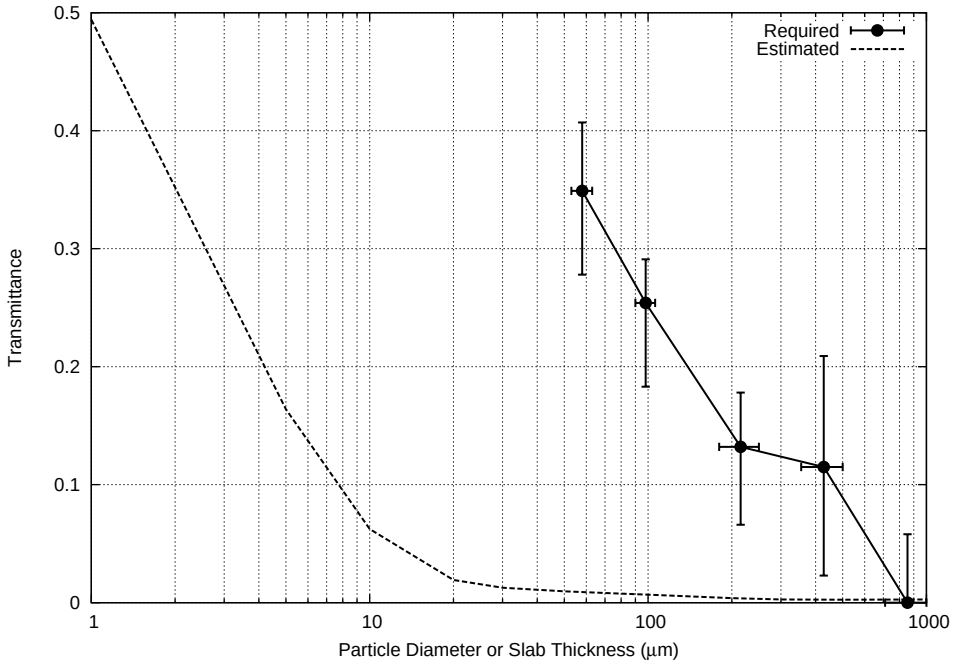

Figure 4.18: Dashed curve: Total transmittance of a slab of soda-lime glass as a function of the slab thickness, calculated from Equation (4.38). Points: Total transmittance required to enhance the radiative conductivity by the factor of ζ (Table 4.5) as a function of the particle diameter, calculated from Equation (4.35).

μm at the temperature of 300 K, so that the estimated transmittance of the small particles (such as FGB-300 glass beads) might not be plausible. When $d \sim \lambda$, Mie scattering theory would be suitable. Because forward scattering is dominant for the Mie scattering, it could make the forward radiative heat flux and resulting radiative conductivity higher.

Thermal conductivity of the sintered glass beads lower than the model

In Figure 4.9, the sintered glass beads had lower thermal conductivity than the model, even when the intra-particle conduction was introduced. Although the quantitative formulation of the intra-particle conductance was not verified in this study, there might be other contributions to cause the disagreement.

The neck sizes of the sintered glass beads were broadly distributed, not uniform (Figure 3.37). In the privious discussion, averaged neck radius was taken as an effective size on the total solid conductivity. If there is size distribution of the necks, the effective neck size possibly becomes lower than the average neck radius. The contact conductance at the neck region is proportional to the neck radius. When parallel connection of the different contact thermal conductances is considered, the effective conductance corresponds to the average contact conductance. On the other hand, when the serial connection is considered, the effective conductance is lower than the average, since the heat flow is constructed at the smaller contacts. Effect of the neck radius distribution on the solid conductivity using the neck radius distribution (Figure 3.37) is discussed.

Let us define the contact conductance per unit neck radius as h, so that the resulting contact conductance at each contact is represented as hr_i, where r_i (i = 1,..., n) is the neck radius at i-th contact. The serial connection of these contact conductances produces the total conductance H_t as,

$$H_\mathrm{t} = \frac{1}{\sum_{i=1}^{n} 1/hr_i}, \tag{4.39}$$

Effective neck radius r_eff is introduced. It is defined as a neck radius whose serial connection results in the same total conductance as H_t,

$$\frac{1}{n/hr_\mathrm{eff}} = H_\mathrm{t}. \tag{4.40}$$

The effective neck radius on the thermal conduction is calculated as,

$$r_\mathrm{eff} = \frac{n}{\sum_{i=1}^{n} 1/r_i}. \tag{4.41}$$

From the neck size distribution shown in Figure 3.37, the calculated effective neck radius ratio is summarized in Table 4.6. As expected, the effective neck radius

Table 4.6: Effective neck radius ratio calculated from Equation (4.41), compared to the average neck ratio.

Sample	Degree of sintering	Average neck ratio	Effective neck ratio
FGB-20	low	0.151	0.129
	medium	0.188	0.172
	high	0.300	0.264
FGB-40	low	0.109	0.101
	medium	0.144	0.131
	high	0.223	0.187
FGB-80	low	0.075	0.060
	medium	0.078	0.070
	high	0.119	0.111

ratio is lower than the average by 20% at the maximum. However, the difference between the experimental data and the model is still exist, even if the average neck radius ratio in Figure 4.9 is replaced by the effective neck ratio.

There are other possible causes for the lower experimental values than the model. A method of the neck selection from the trace of the broken necks (shown in Section 3.8) potentially overestimated the neck radius, because I had assumed that the neck size was larger thant the originally existing roughness and dent generated during the breaking prcedure. The breaking process of the physical contacts could produce the neck traces larger than the original neck size. They can not to be addressed furthermore in this work. Direct measurement of the neck size without the breaking is preferred in the future work.

Chapter 5

Numerical simulation for thermal evolution of planetesimals

5.1 Thermal model

Some different scenarios for planetesimal formation have been suggested. As mentioned in Chapter 1, planetesimal formation via mutual collisional growth of the silicate dust aggregates could not be feasible because of the easy disruption of the dust aggregates by the relatively low speed collisions (*Wada et al.*, 2013). Gravitational instability model would be a feasible scenario for the rocky planetesimal formation.

Dust particles in the nebula settled to the mid-plane in a few thousand years at Earth's orbit (1 AU from the Sun), with coagulation of the particles (*Weidenschilling*, 1980). Based on the gravitational instability model for the planetesimal formation (*Hayashi et al.*, 1985), mass of the primordial planetesimal can be roughly estimated as,

$$m = \pi \left(\frac{G\Sigma_{\rm d}\tau_{\rm K}}{2} \right)^2 \Sigma_{\rm d}, \tag{5.1}$$

where G is the gravitational constant, $\Sigma_{\rm d}$ is surface density of the solid dusts in the early nebula, and $\tau_{\rm K}$ is orbital period of the Kepler motion. The radius of the planetesimal R with the mass m depends on packing porosity of the dust particles. I assume that the planetesimals had uniform porosity of $\phi = 0.9$ (*Kataoka et al.*, 2013). With $\Sigma_{\rm d} = 7.1(a/1\ {\rm AU})^{-3/2}$ ($a < 2.7$ AU), where a is the distance from the central Sun, the size distribution of the primordial planetesimals formed by the gravitational instability is shown in Figure 5.1. The true density of the dust particle is assumed at $\rho_{\rm m} = 3710$ kg/m^3, and compact ($\phi = 0$) and porous ($\phi = 0.9$) cases are shown. For the porous case, the radius of the planetesimal is about 10 km in the inner solar system. In this thesis, the thermal calculation is conducted for the

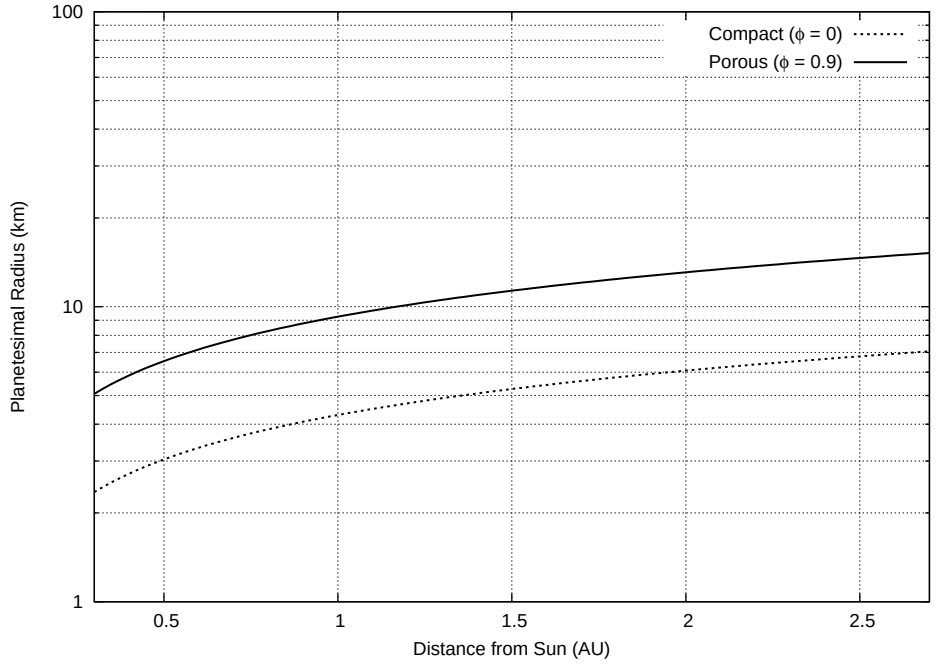

Figure 5.1: Typical radius distribution of the planetesimal formed by the gravitational instability. A solid curve assumed the planetesimal's bulk porosity of 0.9 and a dashed curve assumed non-porous condition.

planetesimals less than 10 km in radius.

The formation age of the planetesimal can be constrained from chronological data of meteorites. ^{182}Hf-^{182}W chronology of iron meteorites showed that the differentiation and core formation in their parent bodies occurred within 1.5 Myr after the CAI formation (*Qin et al.*, 2008; *Kleine et al.*, 2009). Combined with the thermal modelling, they suggested that parent bodies of the iron meteorites were formed within 1 Myr after the CAI formation. The age of the chondrules ranges from 1 to 3 Myrs after the CAI formation. Parent bodies of the chondritic meteorites would be accreted after the chondrule formation. Several studies on the thermal evolution of the meteorites' parent bodies attempted to constrain the time when the planetesimal accretion is completed. Many ordinary chondrite models based on the onion-shell model (e.g. *Miyamoto et al.*, 1981; *Akridge et al.*, 1998; *Harrison and Grimm*, 2010; *Henke et al.*, 2012a,b) showed that the parent body of the ordinary chondrite was formed at about 2 Myr after the CAI formation. Like this, the formation of meteorites' parent bodies, or planeterimals, would be continuous events. In this study, the formation age of the planetesimal is taken as a variable from 0 Myr to 3 Myr relative to the CAI formation. Note that the parent body of the meteorites does not necessarily correspond to the planetesimal formed by the gravitational instability.

The collisional growth of the initial planetesimals would result in the larger parent body.

It is assumed that the rocky planetesimals consist of ordinary chondrites-like silicate particles. Studies on interplanetary dust particles indicated that the size of the pristine dust particles is less than 1 μm (*Rietmeijer*, 1993). I assume that the radius of the dust particles in the planetesimals has is 0.5 μm. Table 5.1 shows parameters used for the calculations.

Table 5.1: Parameters for planetesimal used in the thermal calculations.

Parameter	Symbol	Values	Reference
Parameters of planetesimal			
Planetesimal radius	R	100 m to 10 km	
Formation time	$t_{\rm form}$	0 to 3 Myr	
Porosity	ϕ	0.9	
Initial temperature	T_0	200 K	
Parameters of composite material			
Particle radius	$R_{\rm p}$	0.5 μm	*Rietmeijer* (1993)
True density	$\rho_{\rm m}$	3710 kg/m^3	chondrite (*Yomogida and Matsui*, 1983)
Specific heat	$c(T)$	$800+0.25T-1.5\times10^7/T^2$	chondrite (*Yomogida and Matsui*, 1984)
Material thermal diffusivity	$\kappa(T)$	$6.0\times10^{-7}+2.6\times10^{-4}/T$	chondrite (*Yomogida and Matsui*, 1984)
Material thermal conductivity	$k_{\rm m}$	$\kappa_{\rm m}(T)\rho_{\rm m}c(T)$	
Young modulus	E	78 GPa	basalt (*Schultz*, 1995)
Poisson's ratio	ν	0.25	basalt (*Schultz*, 1995)
Surface energy	γ	0.02 J/m^2	SiO_2 (*Gundlach et al.*, 2011)
Parameters for sintering calculation			
Molecule diameter	d	4.56×10^{-10} m	SiO_2 (*Poppe*, 2003)
Molecule volume	Ω	4.98×10^{-29} m^3	SiO_2 (*Poppe*, 2003)
Surface tension for sintering	γ_s	0.3 N/m	amorphous SiO_2 (*Brinker and Scherer*, 1990)
Constant for surface diffusivity	$D_{\rm s0}$	5.53×10^{11} m^2/s	amorphous SiO_2 (*Poppe*, 2003)
Activation energy for surface diffusion	$A_{\rm s}$	6.43×10^5 J/mol	amorphous SiO_2 (*Poppe*, 2003)
Constant for viscosity	η_0	4.16×10^{-16} Pa·s	Glass (*Kuczynski*, 1949)
Activation energy for viscous flow	$A_{\rm v}$	4.29×10^5 J/mol	Glass (*Kuczynski*, 1949)

5.1.1 Heat conduction equation

Given that the planetesimals were not disturbed by the mutual impacts during the thermal evolution, the following spherically-symmetric heat conduction equation is solved by the explicit finite difference method.

$$\rho c \frac{\partial T}{\partial t} = \frac{1}{r^2}\frac{\partial}{\partial r}\left(r^2 k \frac{\partial T}{\partial r}\right) + \rho Q(t), \tag{5.2}$$

where T is temperature, r is radius from the center, t is time, ρ is bulk density, c is specific heat, Q is heat generation rate per unit mass, and k is thermal conductivity. The central difference equation of Equation (5.2) becomes,

$$T_j^{n+1} = T_j^n + \frac{1}{\rho_j c_j}\left\{\frac{1}{\Delta r_j}\left[\frac{k_{j+1}+k_j}{2}\frac{T_{j+1}-T_j}{(\Delta r_{j+1}+\Delta r_j)/2} - \frac{k_j+k_{j-1}}{2}\frac{T_j-T_{j-1}}{(\Delta r_j+\Delta r_{j-1})/2}\right] + \frac{1}{r_j}k_j\frac{T_{j+1}-T_{j-1}}{\Delta r_j} + \rho_j Q\right\}\Delta t. \tag{5.3}$$

where Δt and Δr are time and radius steps, respectively, with superscript n being the time coordinate and subscript j being the radius coordinate (node number) from the center. For all calculations, the spherical planetesimals were subdivided into 100 spherical shells (i.e. node number is 100). The computational time step Δt was adjusted so that the following Courant-Friedrichs-Lewy condition is satisfied during the calculation.

$$\frac{k}{\rho c}\frac{\Delta t}{\Delta r^2} \leq \frac{1}{2}. \tag{5.4}$$

Initial temperature is assumed to be constant at T_0 as,

$$T = T_0, \qquad \text{at } t = 0. \tag{5.5}$$

The initial temperature of $T = 200$ K is adopted. Surface temperature of the planetesimal maintains at the initial temperature,

$$T = T_0 \qquad \text{at } r = R, \tag{5.6}$$

and there is no point heat source at the center,

$$\frac{\partial T}{\partial r} = 0 \qquad \text{at } r = 0. \tag{5.7}$$

5.1.2 Heat source

Main heat source in the early planetesimal is the energy released by the decay of the radioactive nuclides. The most effective is the decay heat of short-lived isotope ^{26}Al. Other short-lived isotope ^{60}Fe and long-lived isotopes ^{40}K, ^{232}Th, ^{235}U, ^{238}U are also included. The heat generations by these isotopes can be calculated as (*Henke et al.*, 2012a),

$$Q^i = \frac{d}{dt}\left(X^i \frac{E^i_{\rm r}}{m^i} f^i\right) = X^i \frac{E^i_{\rm r}}{m^i} f^i_{\rm t_0} \exp\left(-\lambda^i t\right), \tag{5.8}$$

where $E^i_{\rm r}$ is heat energy released by decay of a nuclide i with mass of m^i, X^i is mass fraction of the element i in the material, $f^i_{\rm t_0}$ is isotope ratio at the time of the planetesimal formation, and λ^i is decay constant. $f^i_{\rm t_0}$ can be written in terms of the formation time relative to the solar system (CAI) formation, t_0, and the isotope ratio at the solar system formation, $f^i_{\rm CAI}$,

$$f^i_{\rm t_0} = f^i_{\rm CAI} \exp\left(-\lambda^i t_0\right). \tag{5.9}$$

The total heat generation is calculated as,

$$Q(t) = \sum_i \left[X^i \frac{E^i_{\rm r}}{m^i} f^i_{\rm CAI} \exp\left\{-\lambda^i (t + t_0)\right\}\right]. \tag{5.10}$$

The decay constant is related to the half-life $\tau^i_{1/2}$,

$$\lambda = \frac{\ln 2}{\tau_{1/2}}. \tag{5.11}$$

The parameters for this heat source are shown in Table 5.2.

5.1.3 Sintering of dust particles

The sintering of dust particles in the planetesimals would occur at high temperature, after which physical properties of the planetesimal would change drastically due to resulted mechanical connection of the particles. The neck growth during the sintering proceeds by several modes; viscous flow, surface diffusion, volume diffusion, grain boundary diffusion, and evaporation-condensation (*Rockland*, 1967). For μm-sized pure SiO_2 particles, the surface diffusion is considered to be dominant mechanism (*Poppe*, 2003). The neck growth for glass particles by *Kuczynski* (1949) was well represented by the viscous flow theory. In this study, the neck growth of the dust particles is calculated by combination of both the surface diffusion and viscous flow.

Table 5.2: Parameters for radioactive heat generation.

Isotope	$f_{\rm CAI}$	$E_{\rm r}$ (MeV)	$\tau_{1/2}$ (Myr)	X
^{26}Al	^{26}Al/^{27}Al = 5.1×10^{-5} (1)	3.19 (2)	0.73 (1)	9.03×10^{-3} (3)
^{60}Fe	^{60}Fe/^{56}Fe = 1.15×10^{-8} (4)	2.89 (2)	2.6 (5)	2.60×10^{-1} (3)
^{40}K	^{40}K/^{39}K = 1.5×10^{-3} (6)	0.69 (2)	1.2×10^{3} (7)	7.07×10^{-4} (3)
^{232}Th	^{232}Th/Th = 1 (6)	40.4 (2)	1.4×10^{4} (7)	5.44×10^{-8} (3)
^{235}U	^{235}U/U = 0.24 (6)	44.4 (2)	7.0×10^{2} (7)	3.02×10^{-8} (3)
^{238}U	^{238}U/U = 0.76 (6)	47.5 (2)	4.5×10^{3} (7)	3.02×10^{-8} (3)

References: (1) *Nyquist et al.* (2009). (2) *Henke et al.* (2012a). (3) Typical chondritic values from *Henke et al.* (2012a). (4) *Tang and Dauphas* (2012). (5) *Rugel et al.* (2009). (6) Calculated from Table 3 in *Anders and Grevesse* (1989). (7) *Hays* (1972).

The sintering can be subdivided into two stages. In the early stage of sintering, the neck grows without the porosity reduction, until the neck radius ratio reaches about 0.3. In this stage, neck growth by the surface diffusion is represented by the following equation (*Nochols and Mullins*, 1965),

$$\frac{r_{\rm n}}{R_{\rm p}} = \left(\frac{25\gamma_{\rm s} d\Omega D_s}{k_B T R_{\rm p}^4} t \right)^{1/6}, \tag{5.12}$$

where $r_{\rm n}$ is neck radius, $R_{\rm p}$ is particle radius, $\gamma_{\rm s}$ is surface tension proceeding the sintering, d and Ω are diameter and volume of the molecule, k_B is the Boltzmann constant, T is temperature, and t is time. Surface diffusion coefficient $D_{\rm s}$ strongly depends on temperature as,

$$D_{\rm s} = D_{\rm s0} \exp\left(-\frac{A_{\rm s}}{R_{\rm g} T} \right), \tag{5.13}$$

where $D_{\rm s0}$ and $A_{\rm s}$ are constants depending on the material types, and $R_{\rm g}$ is the gas constant. For the viscous flow sintering, the neck growth follows,

$$\frac{r_{\rm n}}{R_{\rm p}} = \left(\frac{3\gamma_{\rm s}}{2\eta R_{\rm p}^4} t \right)^{1/2}, \tag{5.14}$$

where η is viscous coefficient given by,

$$\eta = \eta_0 \exp\left(\frac{A_{\rm v}}{R_{\rm g} T} \right), \tag{5.15}$$

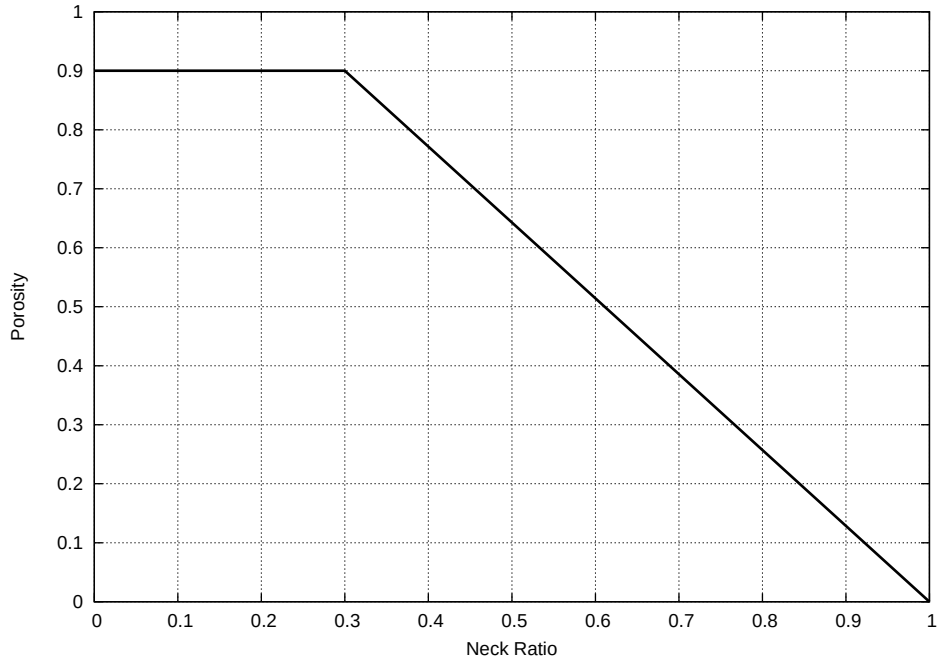

Figure 5.2: Assumed relation between the porosity and the neck radius ratio. The neck radius ratio is calculated from Equation (5.12) and (5.14).

where η_0 and A_v are constants (*Kuczynski*, 1949). The increase in the neck radius during the finite time step Δt is calculated for each mode. Adding these increment radii, total neck growth for Δt can be calculated. The initial neck radius is set at zero.

It is empirically known that the porosity starts to decrease and the void space between the particles diminishes when the neck radius ratio exceeds 0.3 (late stage of sintering). In this stage, formulation of the sintering process has not been established. Therefore, Equations (5.12) and (5.14) are used to calculate the neck radius even in the late stage. The porosity is assumed to be related linearly to the neck radius ratio. When the neck radius ratio exceeds 0.3, the porosity linearly decreases from the initial porosity so as to make the porosity zero at the neck radius ratio of 1 (Figure 5.2).

The parameters used for the sintering calculation are listed in Table 5.1.

5.1.4 Thermal conductivity

The thermal conductivity of initial state of the planetesimal is calculated from the thermal conductivity model developed in Chapter 4 in terms of dust size, porosity, physical properties of composite material, and temperature. Because of the low mass of the planetesimals, compressional stress attributing to the self-weight

is neglected. Using the parameters shown in Table 5.1, the thermal conductivity of the planetesimals is calculated from the models given by Equation (4.20) and (4.27). The resulting solid and radiative coefficients are $A = 5.68 \times 10^{-4}$ and $B = 4.72 \times 10^{-13}$ W/mK^4, if $\xi = 1$ and $\zeta = 1$.

As mentioned in Section 4.3, the solid conductivity decreases due to particle surface roughness via ξ parameter, and the radiative conductivity enhances due to large scale void structure via ζ parameter. It is assumed that the dust particles have perfectly smooth surfaces, so that ξ = 1 is adopted for the solid conductivity. Before the planetesimal formed, the individual dust particles were settled in the mid-plane of the disk with undergoing the aggregation. The planetesimal formed from these aggregates is expected to have macroscopic structure (packing of the aggregates, as shown in Figure 4.12). Although the void size enhancement factor ζ is not known exactly, the experimentally determined value of $\zeta \approx 10$ is adopted. Therefore, the radiative coefficient $B = 4.20 \times 10^{-12}$ W/mK^4 is utilized for the calculations. In this situation, the solid conductivity $k_{\rm solid}$ is 1.90×10^{-3} W/mK (using the material conductivity $k_{\rm m} = 3.35$ W/mK, see below) and the radiative conductivity is 3.36×10^{-5} W/mK at the initial temperature of 200 K. This means that the solid conduction is dominant heat transfer mode in the planetesimals.

The solid conductivity enhances by the sintering. Evolution of the solid coefficient as a function of the neck radius ratio is shown in Figure 5.3. While the neck is smaller than a critical value, the thermal conductivity maintains at the unconsolidated value of $A = 5.68 \times 10^{-4}$. The critical values, after which the solid conductivity is switched to that of sintered materials, is calculated so that the solid coefficient of the sintered materials, given by Equation (5.17) (see below), becomes equivalent to the unconsolidated value of $A = 5.68 \times 10^{-4}$. As the neck grows above the critical value, the solid conductivity starts to increase linearly with the neck radius ratio. This linear relation is based on the experimental results for the sintered FGB glass beads. The empirical relation between the solid conductivity and the neck radius ratio is given by Equation (3.29) for the porosity of 0.4, which is experimentally verified at the neck ratio less than 0.3. This equation is independent of the particle size. By dividing Equation (3.29) by the material conductivity of the FGB glass at normal temperature ($k_{\rm m} = 1.11$ W/mK), the solid coefficient can be obtained as,

$$A = 0.605 \frac{r_{\rm n}}{R_{\rm p}} \quad \text{at } \phi = 0.4, \tag{5.16}$$

In order to correct the solid conductivity at $\phi = 0.4$ into that at $\phi = 0.9$, the solid conductivity model as described by Equation (4.20) can be used. The porosity-dependent term in this equation is $(1-\phi)C$. At $\phi = 0.4$, $(1-\phi)C = 3.8$, and $(1-\phi)C = 0.059$ at $\phi = 0.9$. The solid coefficient of the sintered dust particles at

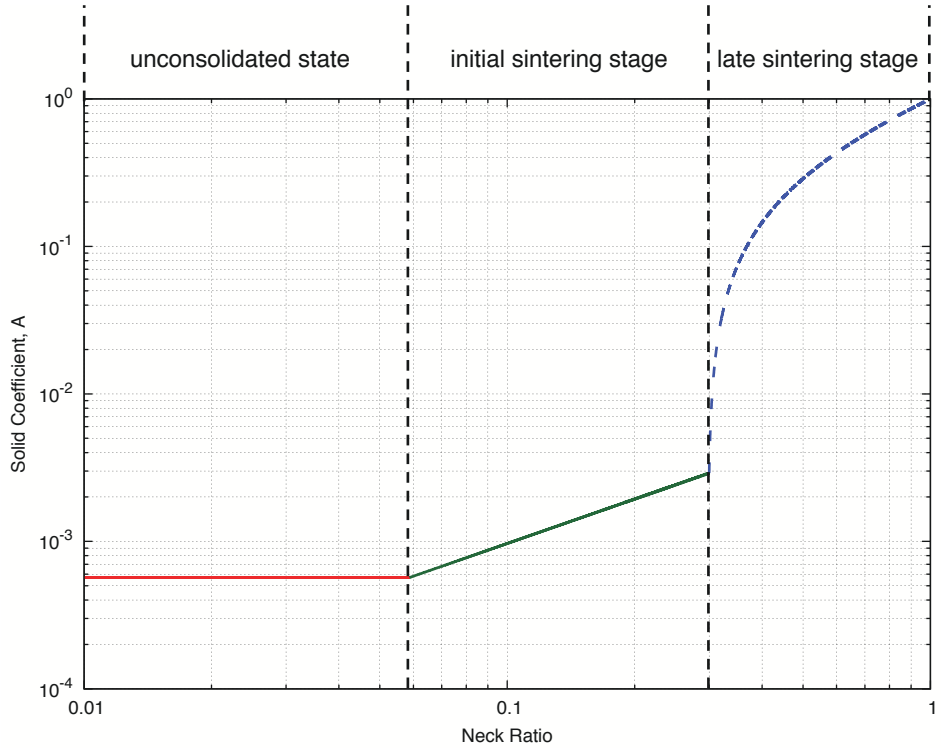

Figure 5.3: Solid coefficient as a function of the neck radius ratio of the planetesimal. The red horizontal line is given by the solid conductivity model of Equation (4.20). The green line represents Equation (5.17). At higher neck ratio than 0.3, a relation represented by the blue dashed curve is assumed.

the porosity of 0.9 is estimated by multiplying a factor of $0.016 (= 0.059/3.8)$ by the Equation (5.16),

$$A = 0.00968 \frac{r_{\rm n}}{R_{\rm p}} \quad \text{at } \phi = 0.9, \tag{5.17}$$

This relation is drawn as the line in the neck radius ratio range between 0.059 and 0.3 in Figure 5.3. At the neck ratio larger than 0.3, the relationship is unknown because the porosity is expected to start reducing. The relation in the neck ratio range between 0.3 to 1 is approximated by a linear relation as to reach $A = 1$ at maximum neck ratio of 1.

The solid conductivity is calculated by multiplying the solid coefficient A by the material conductivity $k_{\rm m}$. The intrinsic material conductivity of natural ordinary chondritic meteorites is difficult to determine experimentally, because of the presence of voids or cracks in the meteorite samples, which makes the thermal conductivity lower than intrinsic value. *Yomogida and Matsui* (1983) measured the thermal diffusivity of 26 chondritic meteorites under vacuum. They approximated the thermal diffusivity κ of the meteorites as a function of the porosity ϕ and temperature

T as (*Yomogida and Matsui*, 1984),

$$\kappa(T,\phi) = \left(6\times10^{-7} + \frac{2.6\times10^{-4}}{T}\right)(1-1.13\phi^{0.33}). \tag{5.18}$$

The intrinsic thermal diffusivity without the voids $\kappa_{\rm m}(T)$ is approximately estimated by giving $\phi = 0$ in Equation (5.18). The thermal conductivity can be calculated from

$$k_{\rm m}(T) = \kappa_{\rm m}(T)\rho_{\rm m}c(T), \tag{5.19}$$

where $\rho_{\rm m} = 3710$ kg/m^3 is true density and $c(T) = 800 + 0.25T - 1.5\times10^7/T^2$ is the specific heat for chondritic composition (*Yomogida and Matsui*, 1984).

The radiative conductivity is calculated by the product of the radiative coefficient times temperature cubic, as Equation (4.26). When the porosity decreases by the sintering, the radiative conductivity is expected to be reduced. The linear relation between the radiative coefficient and the porosity is assumed so as to reach $B = 0$ at zero porosity.

5.2 Thermal evolution of planetesimals

For instance, two results of the thermal calculations of the planetesimals are shown below. Figure 5.4 shows thermal evolution of a planetesimal of 2 km in radius formed at 2.5 Myr after CAI formation. The temperature at the center of this planetesimal increases up to 600 K, and the peak temperature gradually decreases from the center to the surface. During the temperature evolution, the neck begins to grow at about 1 Myr after the planetesimal formation only near the center. The porosity does not change, because the neck ratio does not exceed 0.3. The thermal conductivity at the center enhances immediately after the neck growth.

For comparison, the calculation result for a planetesimal with R = 5 km and $t_{\rm form}$ = 2 Myr is shown in Figure 5.5. The evolution is remarkably different from the model in Figure 5.4, although the peak temperatures at the centers differ by only 50 K. After the sintering starts, the neck radius ratio rapidly increases up to 1, which causes enhancement of the thermal conductivity by three orders of magnitude. If the thermal conductivity of the inner region increases by the sintering, the heat energy generated by radioactive decay efficiency conducts to upper not-sintered layer. The low-conductive nature of the non-sintered layer makes its temperature higher by the heat flow from the inside, and then, the sintering occurs. This is seen as the abrupt increase in the temperature and neck ratio at $r = 0.95R$ (purple curves in Figure 5.5). As a result, the peak temperature becomes homogeneous. Note that it depends on the functional equation of the neck growth and resultant solid conductivity variation in the neck ratio range larger than 0.3.

(a)

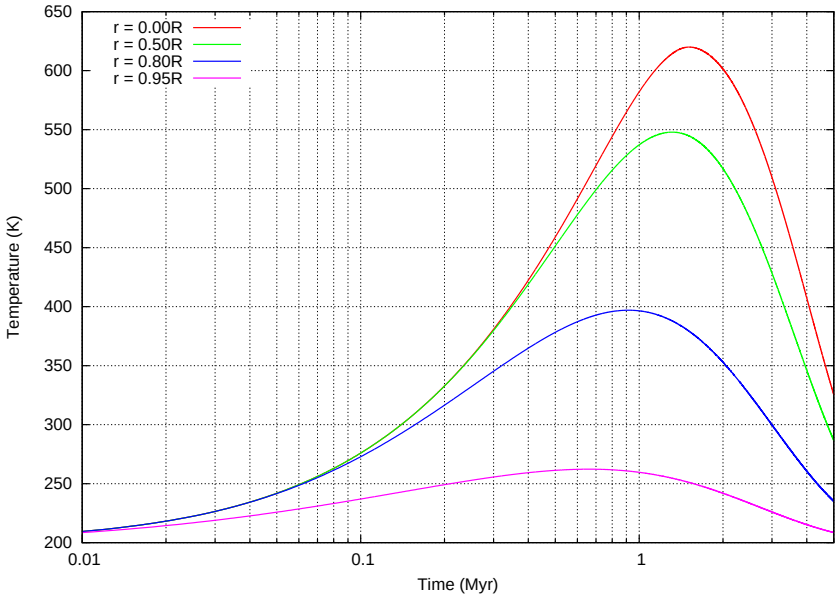

(b)

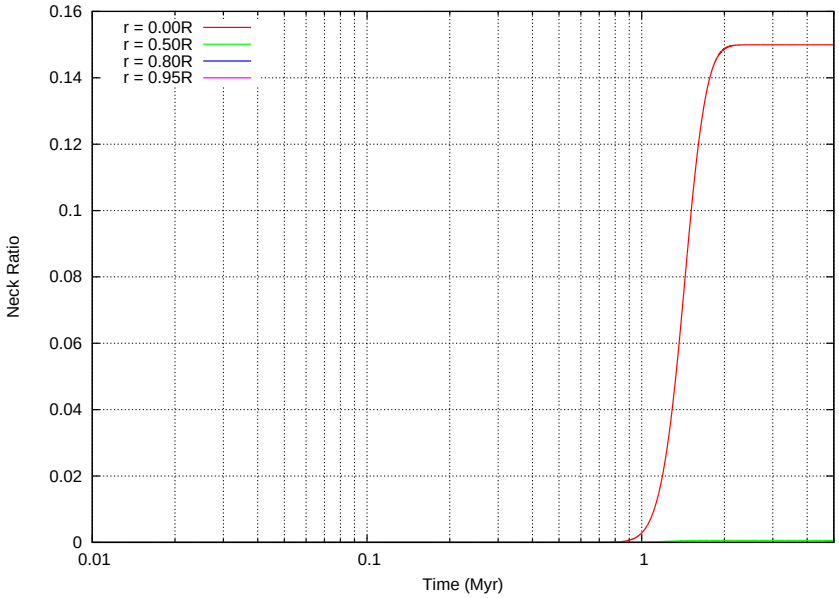

Figure 5.4: (a) Temperature, (b) neck ratio, (c) porosity, and (d) thermal conductivity evolutions inside a planetesimal of 2 km in radius (R = 2 km) formed at 2.5 Myr after the CAI formation ($t_{\rm form}$ = 2.5 Myr). Red curves represent the temporal evolutions at the center ($r = 0.0R$). Green, blue, purple curves are the evolutions at the radius of $0.5R$, $0.8R$, and $0.95R$ from the center, respectively. Panel (e) shows the peak temperature distribution in the planetesimal. (In panel (b), the curves of $r = 0.50R$, $0.80R$, and $0.95R$ are lapped over at the bottom of this figure. Sililarly, the porosity evolitions (c) at all positions maintains at initial porosity of 0.9.)

(c)

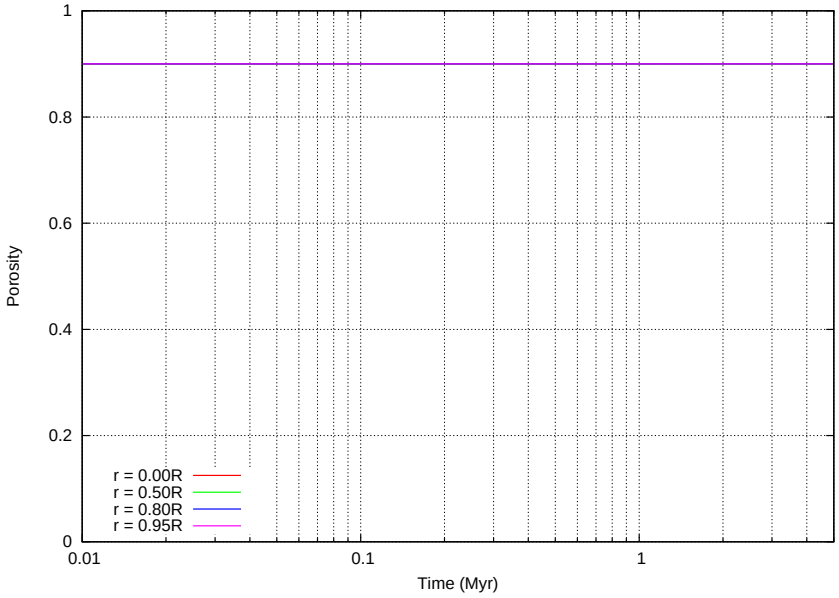

(d)

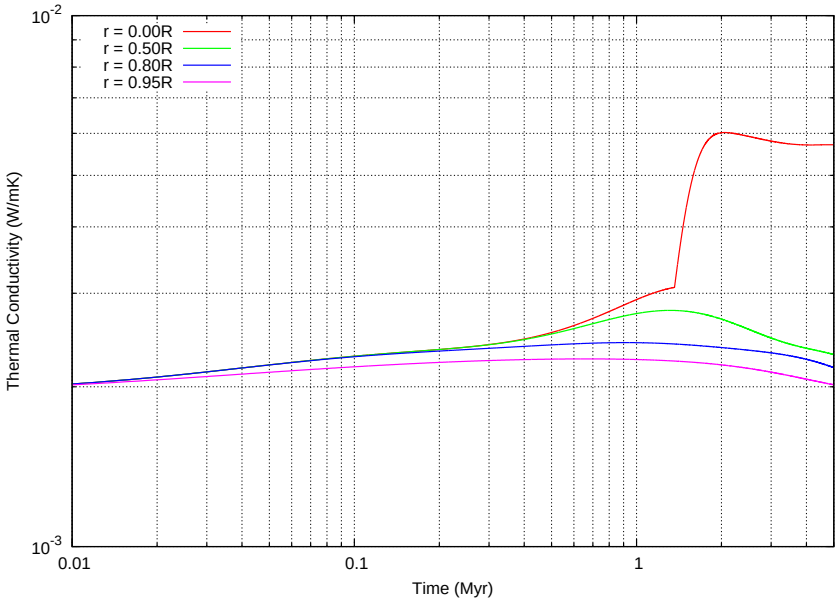

Figure 5.4: Continued.

(e)

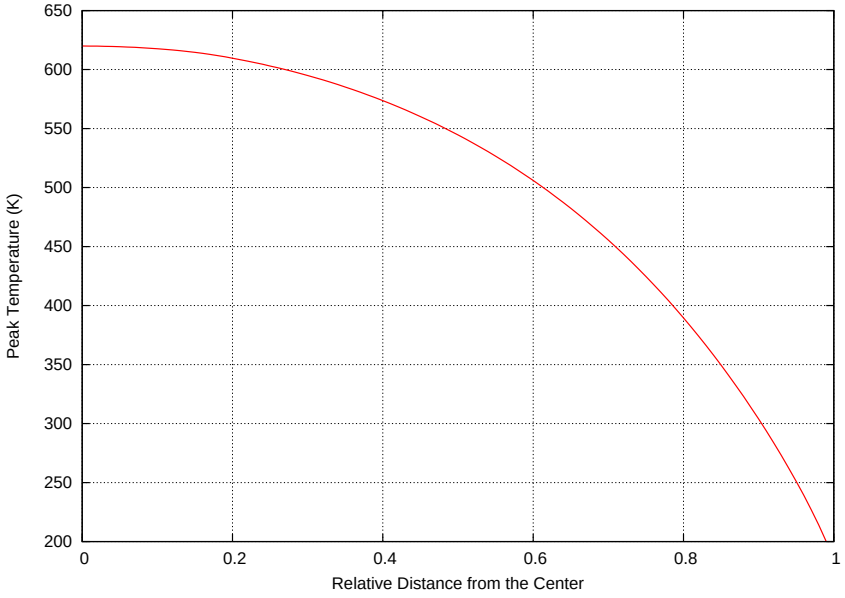

Figure 5.4: Continued.

5.3 Sintering condition of the planetesimals

Whether the sintering occurs and how degree the neck growth proceeds are important problems for thermal and collisional evolution of the planetesimals. In this section, conditions required for the sintering of planetesimals are organized in terms of the size and formation age of the planetesimals. Before the sintering, the dust particles adhesively contact each other with contact radius ratio of 0.027 relative to the particle radius, calculated from JKR theory (Equation 4.12) for dust particles of 0.5 μm in radius. When the neck radius ratio, calculated from the sintering equations (5.12) and (5.14), exceeds the original value of 0.027, physical properties of the planetesimals would change. Therefore, the neck radius ratio of 0.027 is chosen as a criterion for determining occurrence of the sintering. If the neck radius ratio becomes higher than 0.3, the porosity starts to reduce and the planetesimal shrinks.

Figure 5.6 graphically summarizes the sintering condition at the center of the planetesimals. The final neck radius ratio is divided into three regions; $r_{\rm n}/R_{\rm p} < 0.027$, $0.027 < r_{\rm n}/R_{\rm p} < 0.3$, and $r_{\rm n}/R_{\rm p} > 0.3$. Planetesimals with the later two cases are interpreted as sintered and consolidated planetesimals. As the formation age is later, the minimum planetesimal size needed for the sintering becomes larger. This figure indicates that the planetesimals larger than 400 m in radius can undergo the sintering or neck formation between the dust particles. Another speculation is that almost the sintered planetesimals has the neck ratio larger than 0.3, which

(a)

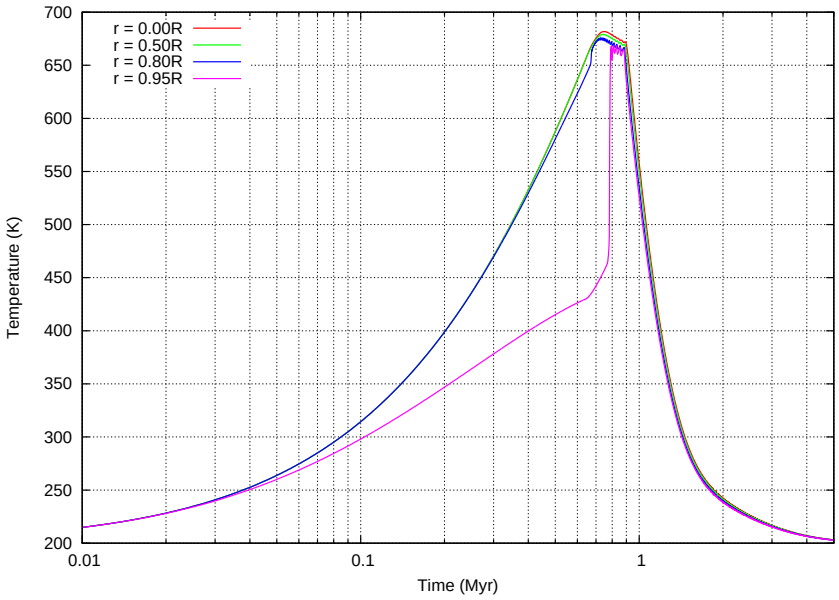

(b)

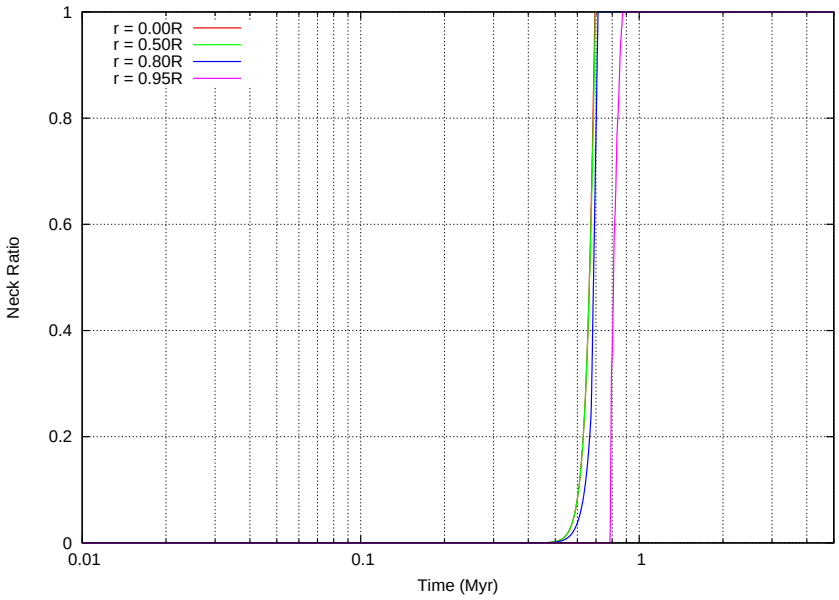

Figure 5.5: (a) Temperature, (b) neck ratio, (c) porosity, and (d) thermal conductivity evolutions inside a planetesimal of 5 km in radius (R = 5 km) formed at 2 Myr after the CAI formation ($t_{\rm form}$ = 2 Myr). Panel (e) shows the peak temperature distribution in the planetesimal.

(c)

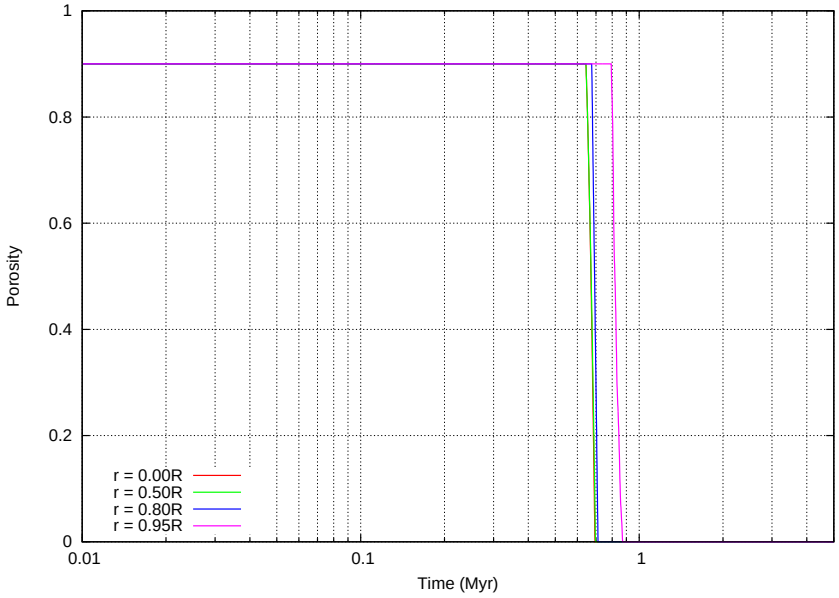

(d)

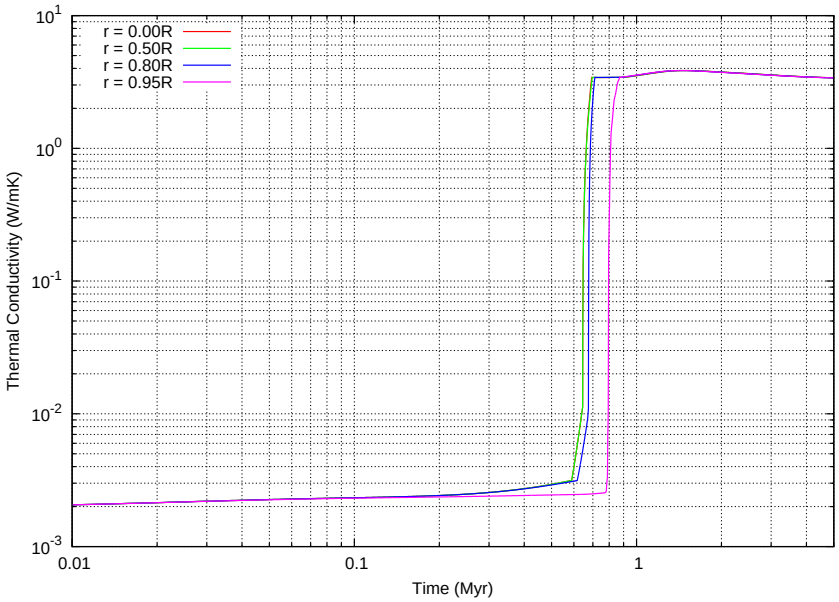

Figure 5.5: Continued.

(e)

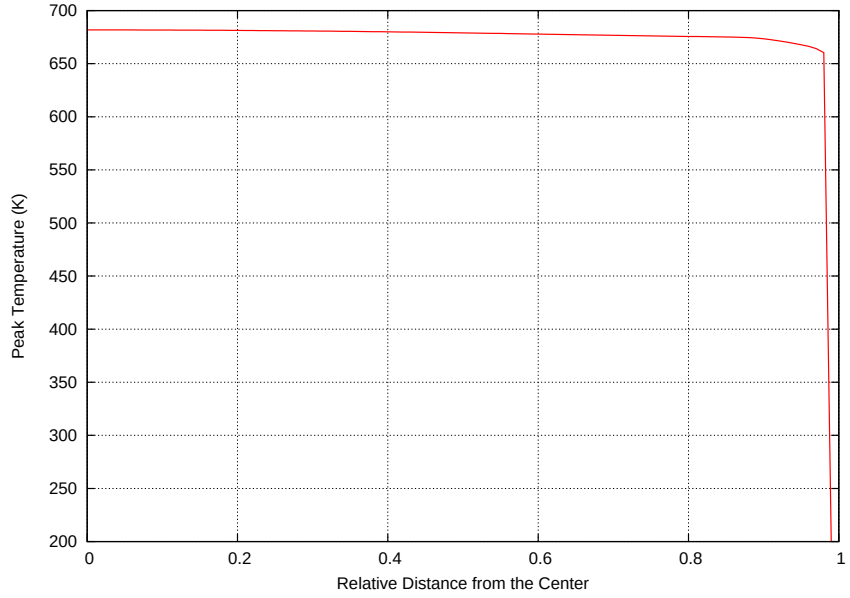

Figure 5.5: Continued.

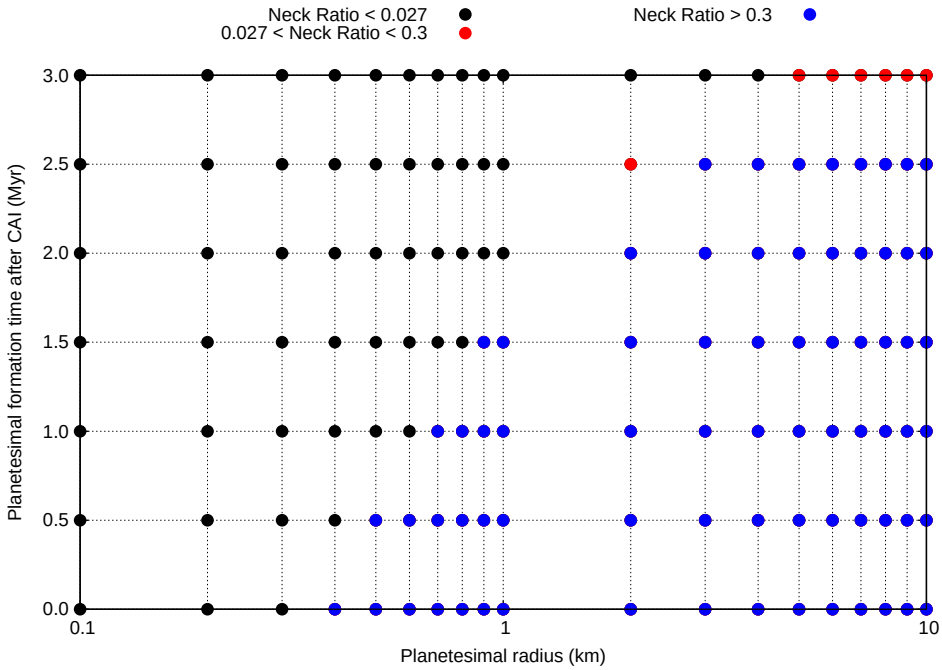

Figure 5.6: Summary of sintering conditions at the center of planetesimals. Black, red, and blue dots are categorized by the final neck radius ratio less than 0.027, larger than 0.027, and larger than 0.3, respectively.

results in decrease of the porosity and shrinkage of the radius.

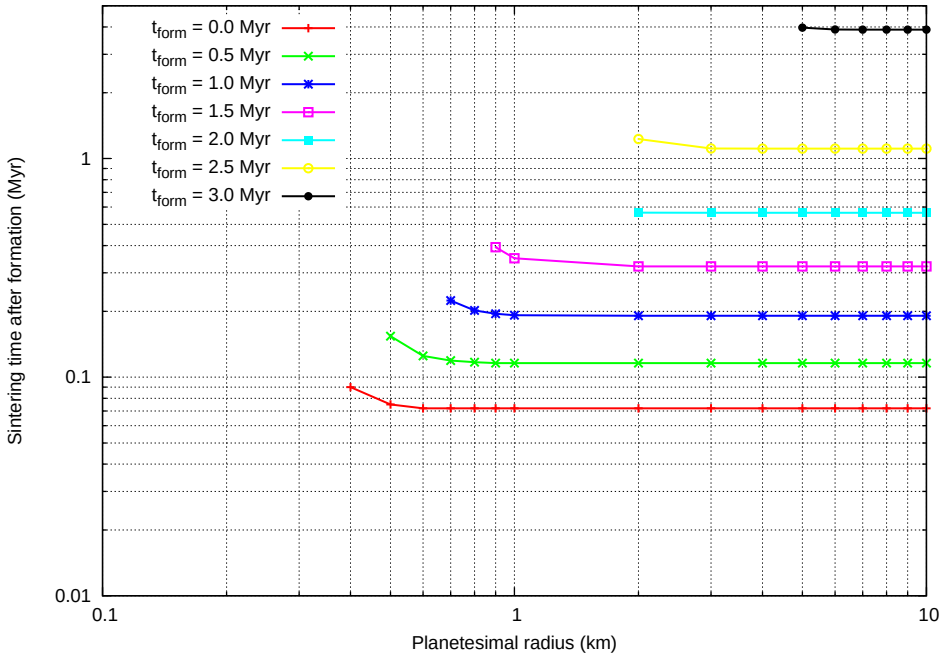

Figure 5.7: Sintering time (when the neck radius ratio becomes higher than 0.027) at the center of planetesimal as a function of the radius and the formation time of the planetesimal.

There is time lag between the planetesimal formation and the sintering. This time lag is shown in Figure 5.7. For example, at the center of a planetesimal of 10 km radius formed at 2 Myr after the CAI formation, the sintering occurs at 0.57 Myr after the planetesimal formation. The time lag is primarily determined by the planetesimal's formation age. As the planetesimal formed later relative to the CAI formation, the time lag for the sintering becomes longer. It needs at least 0.07 Myr after the planetesimal formation.

5.4 Implication to collisional process of planetesimals

The sintering of the dust particles would drastically change the mechanical strength of the planetesimal, which would affect outcome of the mutual collisions. In this section, collisional evolution of the thermally evolving planetesimal is discussed, by comparing the sintering time and collisional timescale relative to the planetesimal's formation age.

Assume that the planetesimals have the same mass m at a given distance from the Sun, as given by Equation (5.1). When the mutual collision of two equal-sized planetesimals occurs and they merges completely, the collisional growth rate of the

planetesimal can be written by,

$$\frac{dm}{dt} = mn\sigma_{\rm col}v, \tag{5.20}$$

where n is number density of the planetesimals, $\sigma_{\rm col}$ is collisional cross section, and v is their relative velocity. The collisional timescale can be defined as,

$$\tau_{col} = \frac{m}{dm/dt} = \frac{1}{n\sigma_{\rm col}v}. \tag{5.21}$$

According to *Hayashi et al.* (1985), the collisional timescale can be approximated as,

$$\tau_{col} = \frac{\rho R}{3\pi\Sigma_{\rm d}}\frac{\tau_{\rm K}}{1+2\theta}. \tag{5.22}$$

where $\rho = (1-\phi)\rho_m$ is the bulk density of the planetesimals, R is the radius of the planetesimals, and $\theta = 2Gm/Rv^2$ is the Safronov number which represents the increase in the collisional cross section due to gravitational focusing. Using Equation (5.22), we can calculate the collisional timescale as a function of the planetesimal radius R and orbital radius a.

Figure 5.8 shows comparison between the collisional timescale calculated from Equation (5.22) and the sintering time shown in Figure 5.7. The safronov number is set at zero (i.e., neglecting runaway growth), because the gravitational focusing is not so effective for the initial planetesimals with the mass of 10^{18} g formed at the Earth's orbit (*Hayashi et al.*, 1985). In the following discussion, let us assume that the radius of the planetesimal is 10 km uniformly over the nebula (Figure 5.1). It is found that the collisional timescale at the Earth's and Mars' orbit is shorter than the sintering time, which means that collisions between the unconsolidated planetesimals occurred dominantly in the early stage of the planetary accretion. On the other hand, in the asteroid source region, the collisional timescale is comparable to or longer than the sintering time if the initial planetesimals are formed immediately (typically $t_{\rm form} < 0.5$ Myr) after the CAI formation. Therefore, the collisions between the consolidated planetesimals would be dominant in this region. Figure 5.8 shows that internal structure of the planetesimals, when the mutual collision occurs, is different by the orbital distance. As a result, the collisional outcome would differ.

The thermal evolution and the collisional process are simultaneous event. At the Earth's orbit, the collision between 10 km-sized planetesimals takes place within 6,000 years (Figure 5.8). After 6,000 years from the formation, the temperature of the planetesimal heated up only by less than 50 K at the center. Therefore, the thermal evolution before the collisions can be neglected. On the other hand, the heating prior to the collisional growth is significant at the asteroid region, since the collisional timescale is comparable to the heating timescale. The typical temperature of

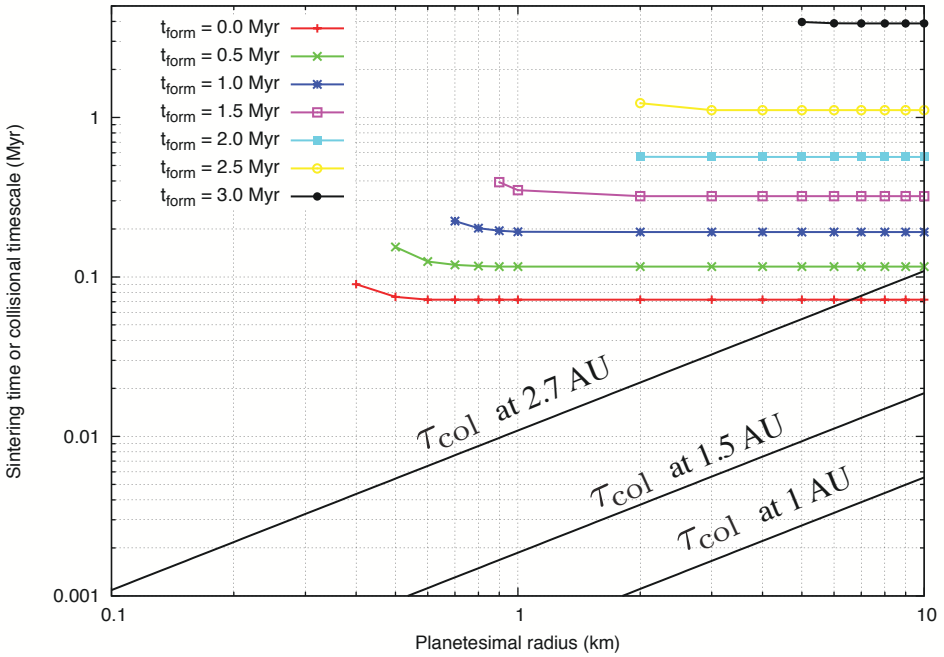

Figure 5.8: Comparison between the sintering times (the same as in Figure 5.7) and collisional timescales (solid black lines) calculated from Equation (5.22) with $\theta = 0$. The collisional timescales at the Earth's orbit (1 AU), Mars' orbit (1.5 AU), and asteroid region (2.7 AU) are shown.

the colliding planetesimals can be characterized by the temperature averaged by the volume as,

$$T_{\rm ave} = \frac{\sum_i T_i v_i}{\sum_i v_i} \tag{5.23}$$

where T_i and v_i are the temperature and volume of the spherical shell of i-th node. Figure 5.9 shows increase in the temperature relative to the initial temperature of 200 K at the center (red) and averaged by the volume (blue) at 0.1 Myr after the formation (typical collisional timescale at 2.7 AU) for the 10 km planetesimal as a function of the formation age relative to the CAI formation. For example, the temperature in the planetesimals with 10 km radius increases by 400 K at the maximum when the collision occurs. If such thermally evolving planetesimals coalesce by the collision, the resulting larger planetesimal, or parent body of the meteorites and asteroids, has higher initial temperature than the equilibrium temperature with the nebula. Many studies on the thermal evolution of the meteorite's parent bodies did not take into account the pre-heating before the collisional growth (e.g. *Miyamoto et al.*, 1981; *Akridge et al.*, 1998; *Harrison and Grimm*, 2010; *Henke et al.*, 2012a). Considering the pre-heating of the primordial planetesimals, the temperature in the parent body should be revised upward by several hundred Kelvins from their calculated results.

In the previous studies, the thermal and collisional processes are independently studied. However, as shown above, they are closely related each other. Comparison between their timescales, as done in this study, are of great importance for appreciating the collisional and thermal evolutions of the planetesimals. In the future work, it is of importance to investigate the effect of the internal structure (unconsolidated or consolidated) of the planetesimals on the collisional outcome. By combining with the thermal model of the planetesimals constructed in this study, the evolution of the planetary bodies will be able to be understood well with linkage between the collisional and thermal processes.

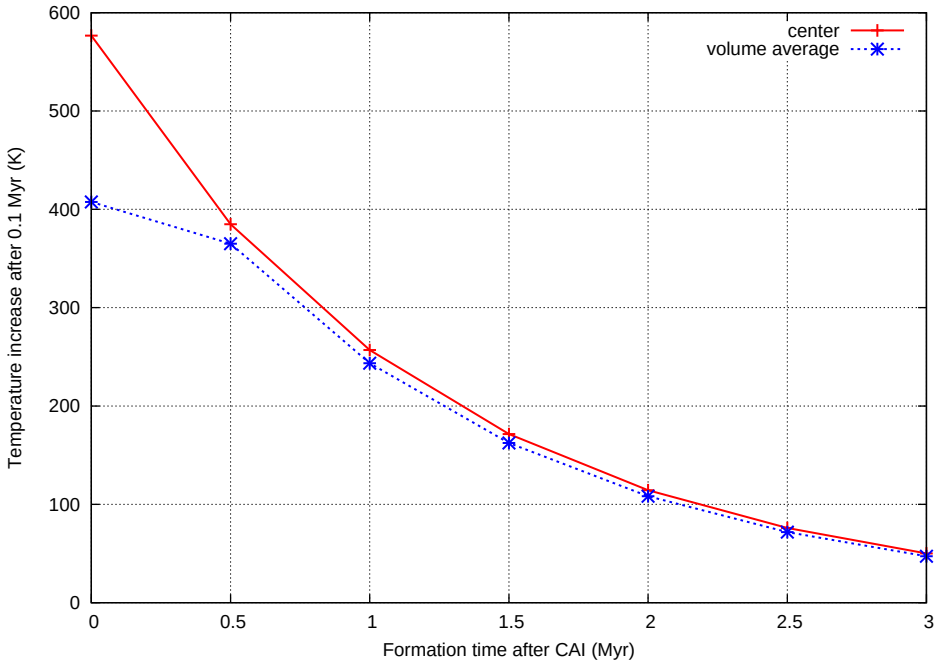

Figure 5.9: Temperature variation relative to the initial temperature in the planetesimal with the radius of 10 km at 0.1 Myr after the planetesimal formation. The central temperature (red) and volume averaging temperature (blue) are plotted as a function of the formation age after the CAI formation.

Chapter 6

Summary and conclusion

In this study, the parameter dependence of the thermal conductivity of the powdered materials was investigated by the experiments under vacuum condition. The most importance of this study, compared to the previous study, is comprehensive and systematic investigations of the thermal conductivity using the same experimental configuration and method. Numerous data sets were obtained, which can be compared with each other. Systematic acquisition of the temperature-dependent data, which were utilized to separate the effective thermal conductivity into the solid and radiative contributions, enabled us to comprehend the parameter dependences of each contribution.

Parameters whose dependence of the thermal conductivity were investigated in this study are temperature (250 - 330 K), particle size (5 μm - 1 mm), porosity (0.40 - 0.86), material type (glass, titanium, copper), compressional stress (¡ 20 kPa), particle size distribution (binary mixture of glass beads), and neck size ratio (¡ 0.3). Especially, the compressional stress and neck size dependences were measured for the first time. Using the data for the glass beads, the heat transfer mechanism in the powdered materials was considered. It was found that the solid conductivity is characterized by the contact radius and number of the contacts per unit area and length. Moreover, the microscopic roughness on the particle surfaces would reduce the solid conductivity. The radiative conductivity could be expressed in terms of the void size between the particles.

The solid and radiative conductivities were modeled based on the heat transfer mechanism inferred from the experimental results. The models were constructed on the assumptions that (1) the particles have uniform size and spherical shapes, (2) packing of the particles is homogeneous, (3) one-dimensional heat flows in the direction of the gravity, and (4) the particles are opaque for the thermal radiation. This is the first quantitative model for the powdered materials under vacuum constructed in accordance with the physical mechanism successfully. The model integratively

describes the parameter dependences, such as particle size, porosity, compressional stress, etc. By giving values of these parameters, one can estimate the thermal conductivity of powdered materials with various physical conditions. As an unprecendented idea, the factor ξ, which represents reduction of the contact radius due to the surface roughness ($\xi \leq 1$), is included in the solid conductivity model. For the glass beads measured in this study, the empirical values of ξ ranged from 0.33 to 0.97, depending on the particle size and surface roughness. The radiative conductivity model contains the factor ζ in order to scale the geometrical void size between the particles to the effective distance of the radiative heat transfer. By comparing the experimental results for the radiative conductivity, the empirical values of ζ increased with the particle size, up to 15. The largest ζ value for the smallest glass beads would attribute the aggregation, which enhanced the void size effective on the radiative heat transfer through the void spaces between the aggregates.

As an application of the thermal conductivity model, the thermal conductivity of the planetesimal was estimated, and the thermal evolution of the planetesimal was numerically calculated. The calculation results were utilized to constrain the sintering (neck formation) conditions of the planetesimals. The center of the planetesimal as small as 1 km in radius (depending on the formation age) could undergo high temperature above 600 K due to low thermal conductivity of the powdered materials, and the sintering occurred. The minimum radius of the planetesimal required to cause the sintering was found to be 400 m. The minimum radius becomes larger for the planetesimal formed later. Furthermore, time delay at which the sintering starts was also determined. It takes 0.07 Myr to 4 Myr, sensitive to the formation age. Comparison between the sintering and collisional timescales revealed that the collisional process in the early stage of the planetary accretion proceeded by the collision between unconsolidated planetesimals at the Earth's orbit. In the region of the asteroids, these timescales are comparable, so that the collisions between the consolidated planetesimals could be dominate. It is indicated that the collisional outcome differs by the orbit due to the difference in the internal structure of the colliding planetesimals.

There still remain some unsolved problems in quantitative interpretation of the discrepancy between the experimental and modeled conductivity. Although the value of ξ seemed to depend on the surface roughness, its dependence can not be formulated. It should be also noted that ξ is only a factor which represents the deviation of the experimental data from the model. It is not clear whether ξ represents the effect of the surface roughness alone. To answer this question, powder samples without the surface roughness should be prepared and measured in the future work, although the solid conductivity of the EMB glass beads with smooth surface was consistent with the model of $\xi = 1$. The values of ζ were larger than unity, up to 4,

even for the glass beads without the aggregation (FGB glass beads). Although the semi-transparent nature of the small particles was discussed according to the geometrical optics theory as a possible cause of the enhanced radiative conductivity, the empirical values of ζ could not be quantitatively explained. It will be preferred to model the radiative heat transfer in the powdered materials using the Mie scattering theory.

Effect of the particle size distribution and shapes of the particles on the thermal conductivity is also important issue for modelling the thermal conductivity of the natural samples such as the regolith on the planetary surface. Although binary mixtures of the glass beads with the different particle sizes were measured in this study, the solid and radiative conductivities were so heterogeneous that the dependence could not be resolved. The method of the sample preparation has to be re-considered. Enhancement of the heat transfer distance during the line heat source measurement by making the heating duration longer may avoid the effect of the local heterogeneity. To investigate the effect of the particle shape, the particles, whose shapes are well-characterized (such as ellipsoidal particles or cubes), should be measured.

In this study, the basic formulation of the thermal conductivity of powdered materials under vacuum was performed. In the future work, the model will be upgraded by formulating ξ and ζ in terms of roughness parameters (amplitude and/or wavelength) and scattering properties, respectively. In order to apply the model to the natural regolith on the planetary bodies, some parameters, which suitably represent the effects of the particle size distribution and particle shape, should be introduced, based on the future experimental results.

Appendix A

Thermal conductivity structure in lunar regolith layer

As shown in Section 1.3, the thermal conductivity of the lunar regolith was in-situ measured in Apollo missions as part of the Heat Flow Experiments. The thermal conductivity values reported in literature were scattered from 0.009 to 0.03 W/mK, depending on the depth, measurement sites, and methods for estimating the thermal conductivity *Langseth et al.* (1973, 1976). The resulting crustal heat flow value on the Moon is uncertain. For the future landing missions on the Moon, the thermal conductivity of the surface regolith layer is a fundamental knowledge. In this Appendix, the thermal conductivity model presented in Chapter 4 is utilized to estimate the thermal conductivity structure in the lunar regolith layer. The modeled result is compared to the data obtained in Apollo missions.

For the calculation, it is assumed that the all physical and chemical parameters other than the porosity and compressional stress (temperature, particle size, composition, etc.) are uniform along the depth. The density distribution of the lunar surface regolith was constrained by lunar core samples collected in Apollo 15 to 17 missions. An approximate relation between the density and the depth was proposed as,

$$\rho = \rho_0 \frac{z + z_1}{z + z_2}, \tag{A.1}$$

where ρ is density, z is depth, and $\rho_0 = 1920$ kg/m^3, $z_1 = 0.122$ m, and $z_2 = 0.18$ m are empirical constants (*Carrier et al.*, 1991). The porosity is calculated by assuming the true density of 3100 kg/m^3, recommended for the lunar soil by *Carrier et al.* (1991). The stress field in the regolith is given by hydrostatic pressure, as,

$$\sigma = \int_0^z \rho(z') g dz', \tag{A.2}$$

where g is the gravitational acceleration at the lunar surface. Using the density

Table A.1: Parameters for the thermal conductivity calculation of the lunar regolith.

Parameter	Values	Note
Material conductivity, k_m	2.5 W/mK	basalt (*Clauser and Huenges*, 1995)
Particle Diameter, D_p	74 μm	regolith simulant we measured
Young modulus, E	78 GPa	basalt (*Schultz*, 1995)
Poisson's ratio, ν	0.25	basalt (*Schultz*, 1995)
Surface energy, γ	0.02	SiO_2 (*Gundlach et al.*, 2011)
Temperature, T	250 K	*Langseth et al.* (1976)
Emissivity, ε	1	-
Contact radius correction factor, ξ	0.31	This study for regolith simulant

distribution of Equation (A.1) and gravity on the lunar surface ($g = 1.6$ m^2/s), one can analytically calculate the self-weighted stress distribution in the lunar regolith (Figure A.1).

The parameters for the thermal conductivity calculation of the lunar regolith is shown in Table A.1. Mean particle size of the lunar regolith particles is assumed to be the same as the lunar regolith simulant used in this study, which is within the range of the mean particle size for the lunar regolith samples (45 to 100 μm *McKay et al.*, 1991). The subsurface temperature of 250 K measured by Apollo Heat Flow Experiments (*Langseth et al.*, 1972, 1973) is used. The contact radius correction factor ξ is set at 0.31, which is determined from the data for the compressional stress dependence of the regolith simulant (Table 4.4). The uncompressed sample has lower ξ of 0.20, which would be suitable for the top surface of the regolith. The value of ζ in the radiative conductivity model is set at 2.1, which is also determined for the regolith simulant. However, the radiative conductivity is not dominant compared to the solid conductivity of the compressed subsurface regolith.

Figure A.2 shows the thermal conductivity calculated from the thermal conductivity model using the porosity and stress distribution in Figure A.1. The modeled thermal conductivity increases with the depth from 0.003 W/mK at the top surface to 0.01 at the depth of 2 m. The thermal conductivity deduced from the in-situ heater-activated measurements (*Langseth et al.*, 1973), which measured local conductivity near the heat flow probe, is significantly higher than the model. This difference would represent the effect of the regolith compaction near the probe, caused by the drilling process. The compaction means enhancement of the density and the stress from the undisturbed original ones. The compression tests of Apollo 12 regolith samples by *Carrier* (1972); *Carrier et al.* (1973) showed possible maximum density of 2000 kg/m^3 (corresponding to the minimum porosity of

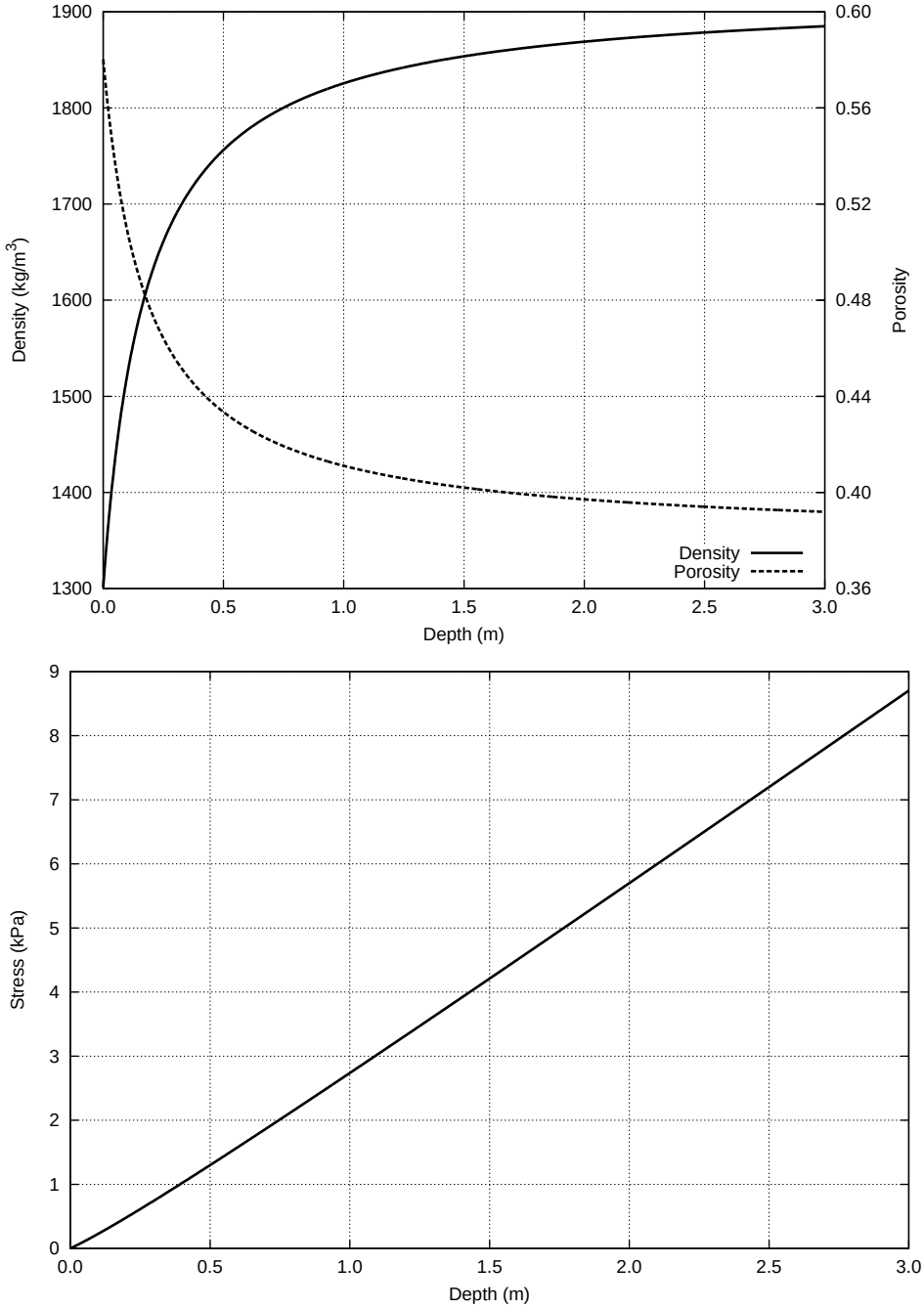

Figure A.1: Density, porosity and hydrostatic pressure distribution in the lunar regolith. The porosity is calculated from the density distribution (Equation A.1) assuming true density of 3100 kg/m^3.

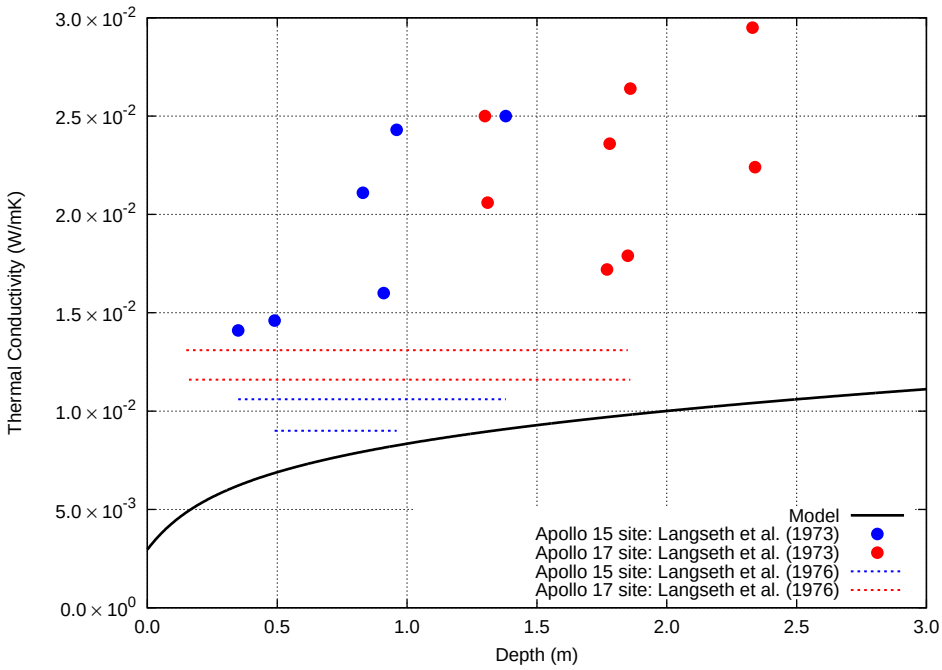

Figure A.2: Thermal conductivity estimation in the lunar regolith (black curve), compared to the in-situ measurements. The points represent the heater-activated estimation for Apollo 15 (blue) and 17 (red) sites. The horizontal lines represent the thermal conductivity estimation from the thermal diffusivity deduced from the attenuation of annual temperature variations propagating into the lunar regolith (from *Grott et al.*, 2010).

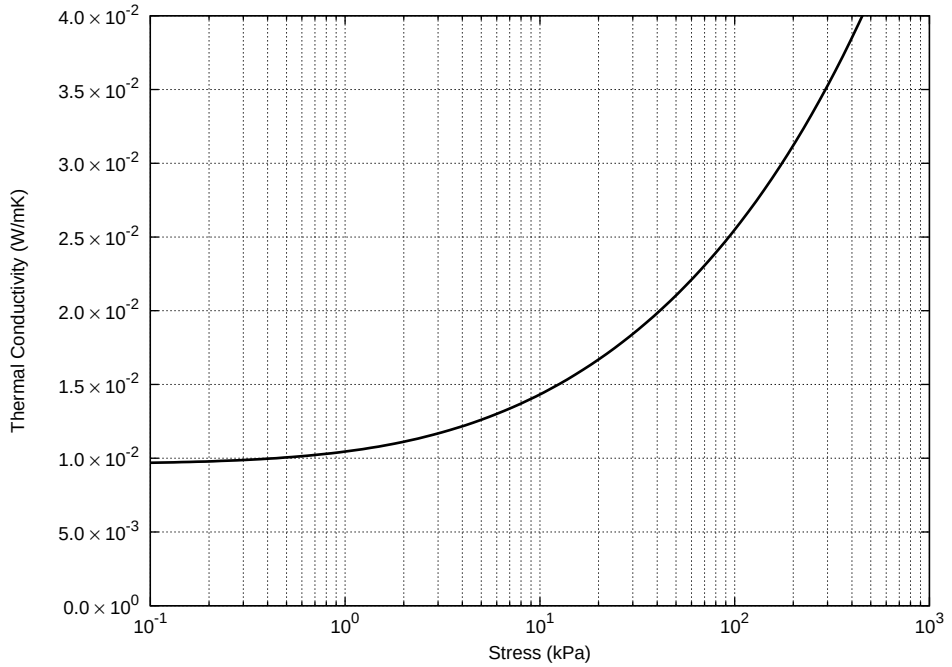

Figure A.3: Compressional stress dependence of modeled thermal conductivity for the regolith simulant with the closest packing density of 2000 kg/m^3 (porosity of 0.35). The parameters listed in Table A.1 are used.

0.35) under one-dimensional compression of 70 kPa. If the regolith maintains this minimum porosity of 0.35, the compressional stress from 10 to 200 kPa is needed so as to enhance the thermal conductivity up to 0.014 to 0.03 W/mK (Figure A.3). Penetration experiments were carried out during the Apollo 15 and 16 missions (*Mitchell et al.*, 1972a,b; *Carrier et al.*, 1991). The recorded stress applied by the astronauts during the penetration were ranged from 10 to 1000 kPa depending on the penetration sites and depth, part of which would be stored in the regolith layer. It could enhance the local thermal conductivity of the regolith.

On the other hand, the thermal conductivity reported by *Langseth et al.* (1976), which was estimated from thermal diffusivity measurements using annual temperature variation, is also higher than the model at shallower depth. They stated that the regolith compaction near the probe could be neglected for the estimation of the regolith's thermal property from the long-term temperature variation, though without quantitative validation. One of the possible causes of the higher thermal conductivity is that higher stress than the hydrostatic pressure is applied on the subsurface regolith particles, which might be accomplished by the hysteresis of the compressional stress due to global long-term bombardments of meteorites on the lunar surface. In order to enhance the thermal conductivity of the regolith at 50 cm

depth up to 0.01 W/mK without the density increase, the additional stress about 15 kPa is required. This stress might reflect the history of compaction and relaxation process by meteorite impact on the Apollo 15 and 17 sites.

There are less experimental and theoretical evidences for supporting the results of Apollo Heat Flow Experiments. In this thesis, by focusing on the deviation of the compressional stress from the hydrostatic pressure in the lunar regolith layer, its values required for reproducing the reported thermal conductivity of the lunar regolith were estimated. Whether these compressional stress values are proper should be addressed in the future work. Note that the model calibration (determination of ξ and ζ) was conducted using only a simulant. Since actual lunar regolith could have the different properties from the simulant (particle shape, composition, etc.), the thermal conductivity measurements and the model calibration using the lunar regolith samples are necessary. Especially, compressional sress dependent data must be obtained.

Appendix B

Physical properties of regolith on small bodies inferred from thermal inertia

Asteroids, for example Ida (*Belton et al.*, 1994) and Itokawa (*Miyamoto et al.*, 2007), as well as the Moon, are considered to be covered with regolith. The thermal inertia I (J/m^{2}Ks$^{0.5}$) is defined as,

$$I = \sqrt{k\rho c} = \sqrt{k\rho_{\rm m}(1-\phi)c}, \tag{B.1}$$

where k is thermal conductivity, c is specific heat, and $\rho = \rho_{\rm m}(1-\phi)$ is bulk density with $\rho_{\rm m}$ being true density of the material and ϕ porosity. The values of the thermal inertia of many asteroids has been estimated from infrared observations (*Delbo' et al.*, 2007). Since the thermal conductivity depends on the physical properties of the regolith (such as particle size, temperature, porosity, and composition), these physical parameters of the surface regolith may be estimated from the inferred thermal inertia value. The knowledge of the physical properties of the surface regolith helps us to understand its origin. Moreover, global mapping of the thermal inertia and the physical condition of the surface regolith of an asteroid from the remote sensing observation from an orbiter can provide the helpful information for selecting landing or sample-return sites. In this chapter, I attempt to constrain the physical parameters of the regolith on asteroid (162173) 1999JU3, target asteroid of Japanese asteroid explorer Hayabusa 2. Hayabusa 2 lunched on December 3, 2014. It equips a thermal infrared imager, named TIR, which images thermal emission from the surface.

Figure B.1 shows the relation between the thermal inertia, thermal conductivity, and porosity, assuming the specific heat of 700 J/kgK and the true density of 3000 kg/m^3. The thermal inertia values of the powdered samples, whose thermal con-

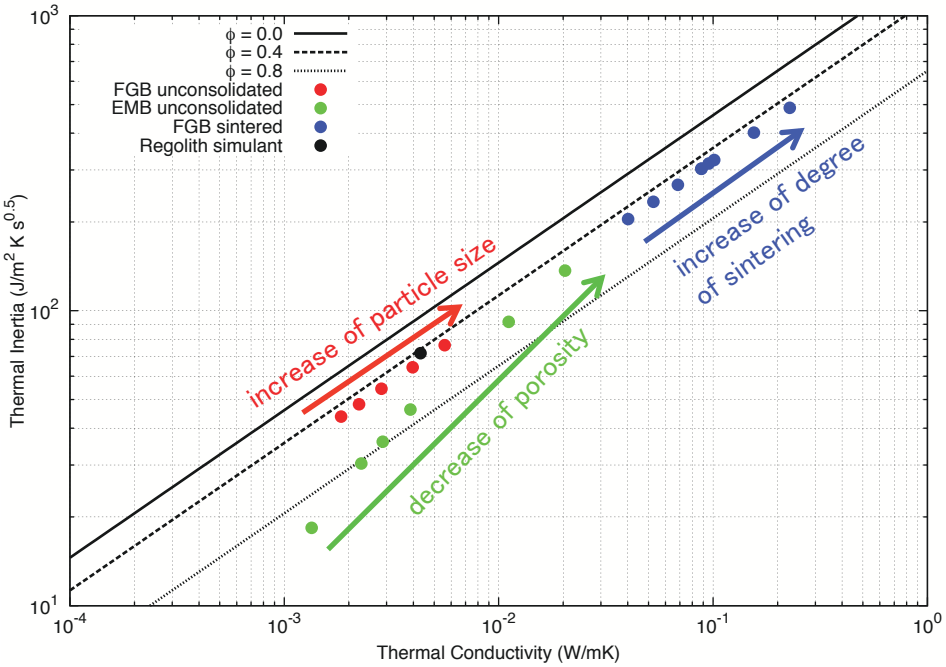

Figure B.1: Relation between thermal inertia and thermal conductivity calculated from Equation (B.1) with true density $\rho_{\rm m} = 3000$ kg/m^3 and specific heat $c = 700$ J/kgK. Three different porosities of 0.0, 0.4, and 0.8 are given. The experimental data at 300 K for the FGB glass beads, EMB glass beads, and regolith simulant are also plotted, whose thermal inertia is calculated using their bulk density and assuming $c = 700$ J/kgK.

ductivity was measured in this study, are also plotted. The thermal conductivity and resulting thermal inertia increase with increasing the particle size and/or decreasing the porosity. The unconsolidated glass beads used in this study have the thermal inertia less than 135 J/m^{2}Ks$^{0.5}$. The higher thermal inertia up to 500 J/m^{2}Ks$^{0.5}$ was obtained for the sintered glass beads.

The thermal inertia estimated for 1999JU3 ranges from 200 to 600 J/m^{2}Ks$^{0.5}$ (constrained by the ground-based and space telescope observations, *Müller et al.*, 2011). This thermal inertia range is consistent with that of the sintered powders, rather than the unconsolidated powders (Figure B.1). If the 1999JU3 is covered with the unconsolidated regolith, one of the possible examinations of the higher inertia, or higher thermal conductivity, is that the regolith has the particle size larger than 1 mm. The larger particle size makes the thermal conductivity higher by increase of the radiative contribution. Alternatively, the lower porosity could make the thermal inertia higher due to higher solid conductivity and higher density in Equation (B.1). Now, taking the particle size and porosity as variables and using the thermal conductivity model shown in Chapter 4, the thermal inertia can be calculated as a function of these parameters. The particle size and porosity of the

regolith on 1999JU3 are constrained.

The physical properties of the regolith on the asteroids are assumed to be identical to the lunar regolith simulant used in this study (Table 3.2). The specific heat of the meteorites $c = 800 + 0.25T - 1.5 \times 10^7/T^2$ is used (*Yomogida and Matsui*, 1984). For simplicity, the temperature of the surface regolith is fixed at 300 K. The contact force between the regolith particles contains only the adhesive force using the surface energy of 0.02 J/m^2, since the gravitational force is small on the surface of small bodies. I used the correction factors for the solid and radiative conductivities of the regolith simulant without the compression, $\xi = 0.20$ and $\zeta = 2.1$, respectively. Substituting the calculated thermal conductivity k into Equation (B.1), the thermal inertia can be calculated as a function of the particle size and porosity. It is assumed that the average size of the surface regolith is representative of the particle size effective on the thermal conductivity.

Figure B.2 shows the variation of the thermal inertia with the particle radius and porosity. In the region 1 shown in Figure B.2, the solid conductivity is the dominant contribution on the effective thermal conductivity. In this region, the thermal inertia decreases with increasing the particle size, because the contact radius ratio by the adhesive force becomes smaller for the larger particles. On the other hand, the radiative conductivity is dominant and the thermal inertia increases with the particle size in the region 2. The thermal inertia is sensitive to the particle size rather than the porosity as long as it is higher than roughly 200 J/m^{2}Ks$^{0.5}$.

The thermal inertia between 200 and 600 J/m^{2}Ks$^{0.5}$ for the asterid 1999JU3 corresponds to the particle radius from a few milimeters to several tens milimeters. For example, if the thermal inertia is 200 J/m^{2}Ks$^{0.5}$ and the porosity of the surface regolith ranges from 0.3 to 0.9, the particle size can be restricted from 1.6 mm to 4.3 mm. Thus, from the global distirbution of the thermal inertia by TIR on-board Hayabusa 2, the order estimation of the regolith's particle size can be performed even though the porosity is unknown. Note that if the thermal inertia is as small as 100 J/m^{2}Ks$^{0.5}$, or less, the possible particle size is widely distributedin in Figure B.2, because the thermal inertia is also sensitive to the porosity. Therefore, it is difficult to constrain the particle size. Only the maximum size of the regolith particles could be estimated.

Above discussion is based on the assumption that the regolith on the asteroid has the thermophysical properties similar to the lunar regolith simulant. Moreover, the effects of the particle size distribution and particle shape on the thermal conductivity have not been sufficiently understood. Future works on these parameter dependence are required to apply the thermal conductivity model to the natural regolith layer on the terrestrial bodies.

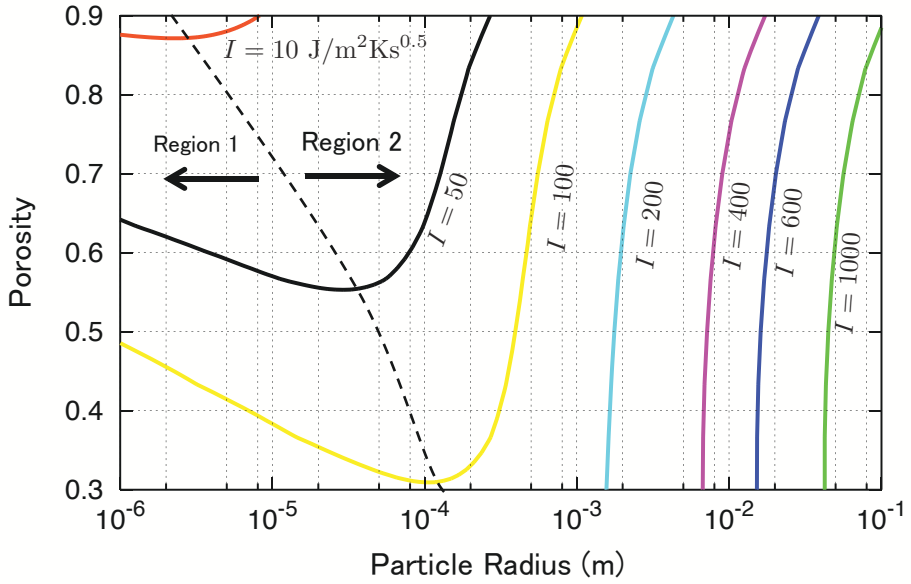

Figure B.2: Contour map of the thermal inertia as a function of the particle radius and porosity. The thermal conductivity is calibrated by the uncompressed lunar regolith simulant measured in this study. In the region 1, the solid conductivity is dominant. Inversely, the radiative conductivity is dominant in the region 2. The boundary of these region is defined by the local minimum point on each contour.

Acknowledgments

My heartfelt appreciation goes to Assoc. Prof. Satoshi Tanaka of Institute of Space and Astronautical Science for his useful advice and constant encouragement of my work. I would like to express my great appreciation to Dr. Kazunori Ogawa of Japan Aerospace Exploraton Agency, who taught me the basic knowledge and skills for the experiments and continuously discussed my experimental results. I greatly appreciate Assoc. Prof. Rie Honda of Kochi University for her constructive comments on interpretation of the experimental results and numerical method for thermal evolution of planetesimal. Discussion with Prof. Masahiko Arakawa of Kobe University about the results of my experiments and application of thermal calculation of planetesimal was very beneficial to my research. This work could not be completed without their guidance and continuous supprots on my research.

I would like to thank Ms. Shoko Tsuda for her support of the experiments for the sintered glass beads. Ms. Maho Ogawa first utilized my experimental results for calculation of planetesimal's thermal evolution. I appreciate Dr. Koji Wada of Chiba Institute of Technology and Akimasa Kataoka of Tokyo Institute of Technology for the discussion about formation and collisional evolution of planetesimals. SEM imaging of the samples was supported by Dr. Yuzuru Karouji of Japan Aerospace Exploraton Agency.

Constructive and critical comments on this thesis by Prof. Hajime Hayakawa, Assoc. Prof. Takahiro Iwata, and Assoc. Prof. Hiroyuki Ogawa of Institute of Space and Astronautical Science were greatly helpful.

I thank my wife and family for their warm encouragement of my research life.

Finally, I am deeply grateful to Dr. Yu-ichi Iijima for proposing my reserch plan and earnest guidance until passing away on December 7, 2012. This thesis is dedicated to him.

References

Akridge, G., P. H. Benoit, and D. W. G. Sears (1998), Regolith and megaregolith formation of h-chondrites: Thermal constraints on the parent body, *Icarus*, *132*, 185–195.

Amelin, Y., A. N. Krot, I. D. Hutcheon, and A. A. Ulyanov (2002), Lead isotopic ages of chondrules and calcium-aluminum-rich inclusions, *Science*, *297*, 1678–1683, doi:10.1126/science.1073950.

Anders, E., and N. Grevesse (1989), Abundances of the elements: Meteoritic and solar, *Geochimica et Cosmochimica Acta*, *53*, 197–214.

Andersson, P., and G. Bäckström (1976), Thermal conductivity of solids under pressure by the transient hot wire method, *Review of Scientific Instruments*, *47*(2), 205–209.

Belton, M. J. S., C. R. Chapman, J. Veverka, K. P. Klaasen, A. Harch, R. Greeley, R. Greenberg, J. W. H. III, A. McEwen, D. Morrison, P. C. Thomas, M. E. Davies, M. H. Carr, G. Neukum, F. P. Fanale, D. R. Davis, C. Anger, P. J. Gierasch, A. P. Ingersoll, and C. B. Pilcher (1994), First image of asteroid 243 Ida, *Science*, *265*, 1543–1547.

Blackwell, J. H. (1954), A transient-flow method for determination of thermal constants of insulating materials in bulk, *Journal of Applied Physics*, *25*(2), 137–144.

Blum, J., and G. Wurm (2008), The growth mechanisms of macroscopic bodies in protoplanetary disks, *Annual Review of Astronomy and Astrophysics*, *46*, 21–56, doi:10.1146/annurev.astro.46.060407.145152.

Bouvier, A., J. Blichert-Toft, F. Moynier, J. D. Vervoort, and F. Albarede (2007), Pbpb dating constraints on the accretion and cooling history of chondrites, *Geochimica et Cosmochimica Acta*, *71*, 1583–1604, doi:10.1016/j.gca.2006.12.005.

Brinker, C. J., and G. W. Scherer (1990), *Sol-gel science - the physics and chemistry of sol-gel processing*, Academic Press, San Diego.

Carr, M. H., R. L. Kirk, A. McEwen, J. Ververka, P. Thomas, J. W. Head, and S. Murchie (1994), The geology of Gaspra, *Icarus*, *107*, 61–71.

Carrier, W. D. (1972), Strength and compressibility of returned lunar soil, *Proceedings of the Third Lunar Science Conference*, *3*, 3223–3234.

Carrier, W. D., L. G. Bromwell, and R. T. Martin (1973), Behavior of returned lunar soil in vacuum, *Journal of the Soil Mechanics and Foundations Division*, *99*(11), 979–996.

Carrier, W. D., G. R. Olhoeft, and W. Mendell (1991), Physical properties of the lunar surface, in *Lunar sourcebook, A User's Guide to the Moon*, edited by G. H. Heiken, D. T. Vaniman, and B. M. French, chap. 9, Cambridge University Press.

Carslaw, H. S., and J. C. Jaeger (1959), *Conduction of Heat in Solid*, second ed., Oxford University Press, London.

Chambers, J. (2006), Meteoritic diversity and planetesimal formation, in *Meteorites and the Early Solar System II*, edited by D. S. Lauretta and H. Y. McSween, pp. 487–497, University of Arizona Press, Tucson.

Clauser, C., and E. Huenges (1995), Thermal conductivity of rocks and minerals, in *Rock Physics and Phase Relations, A Handbook of Physical Constants*, edited by T. J. Ahrens, AGU Reference Shelf 3, Americal Geophysical Union.

Cooper, M. G., B. B. Mikic, and M. M. Yovanovich (1969), Thermal contact conductance, *International Journal of Heat and Mass Transfer*, *12*, 279–300.

Cremers, C. J. (1971), Density, pressure, and temperature effects on heat transfer in Apollo 11 fines, *AIAA Journal*, *9*(11), 2180–2183.

Cremers, C. J. (1972a), Thermal conductivity of Apollo 12 fines at intermediate density, *The Moon*, *4*, 1694–1696.

Cremers, C. J. (1972b), Thermophysical properties of Apollo 12 fines, *Icarus*, *18*, 294–303.

Cremers, C. J. (1972c), Thermal conductivity of Apollo 14 fines, *Pcoceedings of the Third Lunar Science Conference*, *3*, 2611–2617.

Cremers, C. J. (1975), Thermophysical properties of Apollo 14 fines, *Journal of Geophysical Research*, *80*(32), 4466–4470.

Cremers, C. J., and R. C. Birkebak (1971), Thermal conductivity of fines from Apollo 12, *Pcoceedings of the Second Lunar Science Conference*, *3*, 2311–2315.

Cremers, C. J., and H. S. Hsia (1973), Thermal conductivity and diffusivity of Apollo 15 fines at low density, *Pcoceedings of the Fourth Lunar Science Conference*, *3*, 2459–2464.

Cremers, C. J., and H. S. Hsia (1974), Thermal conductivity of Apollo 16 lunar fines, *Pcoceedings of the Fifth Lunar Science Conference*, *3*, 2703–2708.

Cremers, C. J., R. C. Birkebak, and J. P. Dawson (1970), Thermal conductivity of fines from Apollo 11, *Pcoceedings of the Apollo 11 Lunar Science Conference*, *3*, 2045–2050.

Delbo', M., A. dell'Oro, A. W. Harris, S. Mottola, and M. Mueller (2007), Thermal inertia of near-Earth asteroids and implication for the magnitude of the Yorkovsky effect, *Icarus*, *190*, 236–249, doi:10.1016/j.icarus.2007.03.007.

Delbo, M., G. Libourel, J. Wilkerson, N. Murdoch, K. T. Ramesh, C. Ganino, C. Verati, and S. Marchi (2014), Thermal fatigue as the origin of regolith on small asteroids, *Nature*, *508*, 233–236.

Fountain, J. A., and E. A. West (1970), Thermal conductivity of particulate basalt as a function of denisity in simulated lunar and martian environments, *Journal of Geophysical Research*, *75*(20), 4063–4069.

Fountain, J. A., and E. A. West (1974), Thermal measurements on lunar simulants in support of core tube studies, *Pcoceedings of the Fifth Lunar Science Conference*, *5*, 242–244.

Fountain, J. A., and E. A. West (1975), Thermal conductivity of particulate basalt: sample size ¡ 38 μ - 5 mm, *Pcoceedings of the Sixth Lunar Science Conference*, *6*, 268–270.

Fountain, J. A., and E. A. West (1978), Thermal conductivity, thermal diffusivity, and specific heat of lunar sample 15031, 38, *Pcoceedings of the Ninth Lunar Science Conference*, *9*, 344–346.

Garrett, D., and H. Ban (2011), Compressive pressure dependent anisotropic effective thermal conductivity of granular beds, *Granular Matter*, *13*, 685–696, doi:10.1007/s10035-011-0273-4.

Gregory, J. (1981), Approximate expressions for retarded van der waals interaction, *Journal of Colloid and Interface Science*, *83*, 138–145.

Grott, M., J. Knollenberg, and C. Krause (2010), Apollo lunar heat flow experiment revisited: A critical reassessment of the in situ thermal conductivity determination, *Journal of Geophysical Research*, *115*(E11005), doi:10.1029/2010JE003612.

Gundlach, B., and J. Blum (2012), Outgassing of icy bodies in the solar system - II: Heat transport in dry, porous surface dust layers, *Icarus*, *219*, 618–629, doi:10.1016/j.icarus.2012.03.013.

Gundlach, B., S. Killias, E. Beitz, and J. Blum (2011), Micrometer-sized ice particles for planetary-science experiments - I. preparation, critical rolling friction force, and specific surface energy, *Icarus*, *214*, 717–723, doi:10.1016/j.icarus.2011.05.005.

Halajian, J. D., and J. Reichman (1969), Correlation of mechanical and thermal porperties of the lunar surface, *Icarus*, *10*, 179–196.

Harrison, K. P., and R. E. Grimm (2010), Thermal constraints on the early histroty of the h-chondrite parent body reconsidered, *Geochimica et Cosmochimica Acta*, *74*, 5410–5423.

Hayashi, C., K. Nakazawa, and Y. Nakagawa (1985), Formation of the solar system, in *Protostars and Planets II*, edited by D. C. Black and M. S. Matthews, pp. 1100–1153, The University of Arizona Press, Tucson.

Hays, J. F. (1972), Radioactive heat sources in the lunar interior, *Physics of the Earth and Planetary Interiors*, *5*, 77–84.

Henke, S., H. P. Gail, M. Trieloff, W. H. Schwarz, and T. Kleine (2012a), Thermal evolution and sintering of chondritic planetesimals, *Astronomy & Astrophysics*, *537*(A45), doi:10.1051/0004-6361/201117177.

Henke, S., H. P. Gail, M. Trieloff, W. H. Schwarz, and T. Kleine (2012b), Thermal history modelling of the H chondrite parent body, *Astronomy & Astrophysics*, *545*(A135), doi:10.1051/0004-6361/201219100.

Herbert, F. (1989), Primoridal electrical induction heating of asteroid, *Icarus*, *78*, 402–410.

Horai, K. (1981), The effect of interstitial gaseous pressure on the thermal conductivity of a simulated Apollo 12 lunar soil sample, *Physics of the Earth and Planetary Interiors*, *27*, 60–71.

Horai, K., J. L. Winkler, S. J. Keihm, M. G. Langseth, J. A. Fountain, and E. A. West (1980), Thermal conduction in a composite circular cylinder: A new technique for thermal conductivity measurements of lunar core samples, *Philosophical Transactions of the Royal Society of London. Series A, Mathematical and Physical Sciences*, *293*(1406), 571–598.

Huetter, E. S., and N. I. Koemle (2008), Determination of the radiative contribution to the thermal conductivity to the effective thermal conduc- tivity of a granular medium under vacuum conditions, *Proceedings of the Fifth European Thermal-Science Conference*.

Huetter, E. S., N. I. Koemle, G. Kargl, and E. Kaufmann (2008), Determination of the effective thermal conductivity of granular materials under varying pressure conditions, *Journal of Geophysical Research: Planets*, *113*(E12004), doi: 10.1029/2008JE003085.

Johnson, K. L., K. Kendall, and A. D. Roberts (1971), Surface energy and the contact of elastic solids, *Proceedings of the Royal Society of London. Series A, Methematical and Physical Sciences*, *324*, 301–313.

Jones, B. W. (1988), A transient-flow method for determination of thermal constants of insulating materials in bulk, *Journal of Physics E: Science Instruments*, *21*, 832–839.

Kataoka, A., H. Tanaka, S. Okuzumi, and K. Wada (2013), Fluffy dust forms icy planetesimals by static compression, *Astronomy & Astrophysics*, *557*(L4), doi: 10.1051/0004-6361/201322151.

Kaviany, M. (1998), Heat transfer in porous media, in *Hondbook of Heat Transfer*, edited by W. M. Rohsenow, J. P. Hartnett, and Y. I. Cho, third ed., chap. 9, McGraw-Hill, New York.

Keihm, S. J., and M. G. Langseth (1973), Surface brightness temperature at the apollo 17 heat flow site: Thermal conductivity of the upper 15 cm of regolith, *Proceedings of the Fourth Lunar Science Conference*, *3*, 2503–2513.

Kleine, T., M. Touboul, B. Bourdon, F. Nimmo, K. Mezger, H. Palme, S. B. Jacobsen, Q.-Z. Yin, and A. N. Halliday (2009), Hf-W chronology of the accretion and early evolution of asteroids and terrestrial planets, *Geochimica et Cosmochimica Acta*, *73*, 5150–5188, doi:10.1016/j.gca.2008.11.047.

Krause, M., J. Blum, Y. Skorov, and M. Trieloff (2011), Thermal conductivity measurements of porous dust aggregates: I. Technique, model and first results, *Icarus*, *214*, 286–296, doi:10.1016/j.icarus.2011.04.024.

Kuczynski, G. C. (1949), Study of the sintering of glass, *Journal of Applied Physics*, *20*, 1160–1163.

Langseth, M. G., S. P. Clark, J. L. Chute, S. J. Keihm, and A. E. Wechsler (1972), Heat-flow experiment, in *Apollo 15 Preliminary Science Report*, chap. 11.

Langseth, M. G., S. J. Keihm, and J. L. Chute (1973), Heat-flow experiment, in *Apollo 17 Preliminary Science Report*, chap. 9.

Langseth, M. G., S. J. Keihm, and K. Peters (1976), Revised lunar heat-flow values, *Proceeding of the Seventh Lunar Science Conference*, pp. 3143–3171.

Masuda, H., K. Higashitani, and H. Yoshida (2006), *Powder Technology Handbook*, 3 ed., CRC Press, London.

McKay, D. S., G. Heiken, A. Basu, G. Blanford, S. Simon, R. Reedy, B. M. French, and J. Papike (1991), The lunar regolith, in *Lunar sourcebook, A User's Guide to the Moon*, edited by G. H. Heiken, D. T. Vaniman, and B. M. French, chap. 7, Cambridge University Press.

McSween, H. Y., A. Ghosh, R. E. Grimm, L. Wilson, and E. D. Young (2002), Thermal evolution models of asteroids, in *Asteroids III*, edited by W. F. B. Jr., A. Cellino, P. Paolicchi, and R. P. Binzel, chap. 4-3-1, pp. 559–571, University of Arizona Press, Tucson.

Merrill, R. B. (1969), Thermal conduction through an evacuated idealized powder over the temperature range of 100° to 500 °K, *Tech. rep.*, National Aeronautics and Space Administration, Washington, D. C.

Mitchell, J. K., L. G. Bromwell, W. D. Carrier, N. C. Costes, W. N. Houston, and R. F. Scott (1972a), Soil-mechanics experiments, in *Apollo 15 Preliminary Science Report*, chap. 7.

Mitchell, J. K., W. D. Carrier, W. N. Houston, R. F. Scott, L. G. Bromwell, H. T. Durgunoglu, H. J. Hovland, D. D. Treadwell, and N. C. Costes (1972b), Soil mechanics, in *Apollo 16 Preliminary Science Report*, chap. 7.

Miyamoto, H., H. Yano, D. J. Scheeres, S. Abe, O. Barnouin-Jha, A. F. Cheng, H. Demura, R. W. Gaskell, N. Hirata, M. Ishiguro, T. Michikami, A. M. Nakamura, R. Nakamura, J. Saito, and S. Sasaki (2007), Regolith migration and sorting on asteroid Itokawa, *Science*, *316*, 1011–1014.

Miyamoto, M., N. Fujii, and H. Takeda (1981), Ordinary chondrite parent body: An internal heating model, *Proceeding of the Lunar and Planetary Science*, *12*, 1145–1152.

Modest, M. F. (2013), *Radiative Heat Transfer*, 3 ed., Academic Press, New York.

Müller, T. G., J. Ďurech, S. Hasegawa, M. Abe, K. Kawakami, T. Kasuga, D. Kinoshita, D. Kuroda, S. Urakawa, S. Okumura, Y. Sarugaku, S. Miyasaka, Y. Takagi, P. R. Weissman, Y. J. Choi, S. Larson, K. Yanagisawa, and S. Nagayama (2011), Thermo-physical properties of 162173 (1999 ju3), a potential flyby and rendezvous target for interplanetary missions, *Astronomy and Astrophysics*, *525*, A145, doi:10.1051/0004-6361/201015599.

Nagashima, A., N. Araki, and T. Baba (2008), *Thermophysical Properties Handbook*, Yokendo, Tokyo.

Neumann, W., D. Breuer, and T. Spohn (2012), Differentiation and core formation in accreting planetesimals, *Astronomy & Astrophysics*, *543*(A141), doi:10.1051/0004-6361/201219157.

Nochols, F. A., and W. W. Mullins (1965), Morphological changes of a surface of revolution due to capillarity induced surface diffusion, *Journal of Applied Physics*, *36*(6), 1826–1835.

Nyquist, L. E., T. Kleine, C.-Y. Shih, and Y. D. Reese (2009), The distribution of short-lived radioisotopes in the early solar system and the chronology of asteroid accretion, differentiation, and secondary mineralization, *Geochimica et Cosmochimica Acta*, *73*(17), 5115–5136, doi:10.1016/j.gca.2008.12.031.

Okuzumi, S., H. Tanaka, H. Kobayashi, and K. Wada (2012), Rapid coagulation of porous dust aggregates outside the snow line: A pathway to successful icy planetesimal formation, *The Astrophysical Journal*, *752*(106), doi:10.1088/0004-637X/752/2/106.

Perko, H. A., J. D. Nelson, and W. Z. Sadeh (2001), Surface cleanliness effect on lunar soil shear strength, *Journal of Geotechnical and Geoenvironmental Engineering*, *127*, 371–383.

Pilbeam, C. C., and J. R. Vaišnys (1973), Contact thermal conductivity in lunar aggregates, *Journal of Geophysical Research*, *78*(23), 5233–5236.

Pinson, D., R. P. Zou, A. B. Yu, P. Zulli, and M. J. McCarthy (1998), Coordination number of binary mixture of spheres, *Journal of Physics D: Applied Physics*, *31*, 457–462.

Piqueux, S., and P. R. Christensen (2009), A model of thermal conductivity for planetary soils: 1. theory for unconsolidated soils, *Journal of Geophysical Research*, *114*(E09005), doi:10.1029/2008JE003308.

Poppe, T. (2003), Sintering of highly porous silica-particle samples: analogues of early solar-system aggregates, *Icarus*, *164*, 139–148, doi:10.1016/S0019-1035(03)00137-4.

Presley, M. A., and P. R. Christensen (1997a), Thermal conductivity measurements of particulate materials: 1. A review, *Journal of Geophysical Research*, *102*(E3), 6535–6549.

Presley, M. A., and P. R. Christensen (1997b), Thermal conductivity measurements of particulate materials: 2. Results, *Journal of Geophysical Research*, *102*(E3), 6551–6566.

Qin, L., N. Dauphas, M. Wadhwa, J. Masarik, and P. E. Janney (2008), Rapid accretion and differentiation of iron meteorite parent bodies inferred from ^{182}Hf-^{182}W chronometry and thermal modeling, *Earth and Planetary Science Letters*, *273*, 94–104, doi:10.1016/j.epsl.2008.06.018.

Ratcliffe, E. H. (1963), A survey of most probable values for the thermal conductivities of glasses between about -150 and 100 degc, including new data on twenty-two glasses and a working formula for the calculation of conductivity from composition, *Glass Technology*, *4*(4), 113–128.

Rietmeijer, F. J. M. (1993), Size distributions in two porous chondritic micrometeorites, *Earth and Planetary Scienece Letters*, *117*, 609–617.

Rockland, J. G. R. (1967), The determination of the mechanism of sintering, *Acta Metallurgica*, *15*, 277–286.

Rubin, A. E. (1995), Petrologic evidence for collisional heating of chondritic asteroids, *Icarus*, *113*, 156–167.

Rubin, M. (1985), Optical properties of soda lime silica glasses, *Solar Energy Materials*, *12*, 275–288.

Rugel, G., T. Faestermann, K. Knie, G. Korschinek, M. Poutivtsev, D. Schumann, N. Kivel, I. Gunther-Leopold, R. Weinreich, and M. Wohlmuther (2009), New measurement of the ^{60}Fe half-life, *Physical Review Letters*, *103*, 072,502, doi: 10.1103/PhysRevLett.103.072502.

Sakatani, N., K. Ogawa, Y. Iijima, R. Honda, and S. Tanaka (2012), Experimental study for thermal conductivity structure of lunar surface regolith: Effect of compressional stress, *Icarus*, *221*, 1180–1182.

Schultz, R. A. (1995), Limits on strength and deformation properties of jointed basaltic rock masses, *Rock Mechanics and Rock Engineering*, *28*(1), 1–15.

Sierks, H., P. Lamy, C. Barbieri, D. Koschny, H. Rickman, R. Rodrigo, M. F. AHearn, F. Angrilli, M. A. Barucci, J.-L. Bertaux, I. Bertini, S. Besse, B. Carry, G. Cremonese, V. Da Deppo, B. Davidsson, S. Debei, M. De Cecco, J. De Leon, F. Ferri, S. Fornasier, M. Fulle, S. F. Hviid, R. W. Gaskell, O. Groussin, P. Gutierrez, W. Ip, L. Jorda, M. Kaasalainen, H. U. Keller, J. Knollenberg, R. Kramm, E. Khrt, M. Kppers, L. Lara, M. Lazzarin, C. Leyrat, J. J. L. Moreno, S. Magrin, S. Marchi, F. Marzari, M. Massironi, H. Michalik, R. Moissl, G. Naletto, F. Preusker, L. Sabau, W. Sabolo, F. Scholten, C. Snodgrass, N. Thomas, C. Tubiana, P. Vernazza, J.-B. Vincent, K.-P. Wenzel, T. Andert, M. Ptzold, and B. P. Weiss (2011), Images of asteroid 21 Lutetia: A remnant planetesimal from the early solar system, *Science*, *334*, 487–490.

Suzuki, M., K. Makino, M. Yamada, and K. Iinoya (1980), A study of coordination number in a romdom packed system of monosized sphere particles (in japanese), *Kagaku Kogaku Ronbunshu*, *6*(1), 59–64.

Tang, H., and N. Dauphas (2012), Abundance, distribution, and origin of ^{60}Fe in the solar protoplanetary disk, *Earth and Planetary Science Letters*, *359*, 248–263, doi:10.1016/j.epsl.2012.10.011.

Timoshenko, S. P., and J. N. Goodier (1951), *Theory of Elasticity*, McGraw-Hill Book Company, Inc., New York.

Urey, H. C. (1955), The cosmic abundances of potassium, uranium, and thorium and the heat balances of the Earth, the Moon and Mars, *Proceedings of the National Academy of Sciences of the United States of America*, *41*(3), 127–144.

Vasavada, A. R., J. L. Bandfield, B. T. Greenhagen, P. O. Hayne, M. A. Siegler, J.-P. Williams, and D. A. Paige (2012), Lunar equatorial surface temperatures and regolith properties from the diviner lunar radiometer experiment, *Journal of Geophysical Research*, *117*(E00H18), doi:10.1029/2011JE003987.

Wada, K., H. Tanaka, T. Suyama, H. Kimura, and T. Yamamoto (2007), Numerical simulation of dust aggregate collisions. i. compression and disruption of two-dimensional aggregates, *The Astrophysical Journal*, *661*, 320–333.

Wada, K., H. Tanaka, S. Okuzumi, H. Kobayashi, T. Suyama, H. Kimura, and T. Yamamoto (2013), Growth efficiency of dust aggregates through collisions with high mass ratios, *Astronomy & Astrophysics*, *559*(A62), doi:10.1051/0004-6361/201322259.

Watson, K. (1964), I. the thermal conductivity measurements of selected silicate powders in vacuum from 150° - 350 °K, ii. an interpretation of the moon's eclipse and lunartion cooling as observed through the earth's atmosphere from 8-14 microns, Ph.D. thesis, California Institute of Technology, Pasadena, California.

Wechsler, A. E., and P. E. Glaser (1965), Presure effects on postulated lunar materials, *Icarus*, *4*(4), 335–352.

Wechsler, A. E., and I. Simon (1966), Thermal conductivity and dielectric constant of silicate materials, *Tech. rep.*, NASA.

Wechsler, A. E., P. E. Glaser, and J. A. Fountain (1972), Thermal properties of granulated materials, in *Thermal Characterictics of the Moon*, *Progress in Astronautics & Aeronautics*, vol. 28, edited by J. W. Lucas, chap. 3a, MIT Press.

Weidenschilling, S. J. (1977), Aerodynamics of solid bodies in the solar nebula, *Monthly Notices of the Royal Astronomical Society*, *180*, 57–70.

Weidenschilling, S. J. (1980), Dust to planetesimals: Settling and coagulation in the solar nebula, *Icarus*, *44*, 172–189.

Wesselink, A. F. (1948), Heat conductivity and nature of the lunar surface material, *Bulletin of the Astronomical Institutes of the Netherlands*, *10*(390), 351–363.

Yomogida, K., and T. Matsui (1983), Physical properties of ordinary chondrites, *Journal of Geophysical Research*, *88*, 9513–9533.

Yomogida, K., and T. Matsui (1984), Multiple parent bodies of ordinary chondrites, *Earth and Planetary Science Letters*, *68*, 34–42.

Youdin, A. N., and F. H. Shu (2002), Planetesimal formation by gravitational instability, *The Astrophysical Journal*, *580*, 494–505.